



Optimization of THz detection by two dimensional plasmons in heterostructures and THz propagation in planar waveguides

Lei Cao

► To cite this version:

Lei Cao. Optimization of THz detection by two dimensional plasmons in heterostructures and THz propagation in planar waveguides. Other [cond-mat.other]. Université Paris Sud - Paris XI, 2013. English. <NNT : 2013PA112014>. <tel-00794896>

HAL Id: tel-00794896

<https://tel.archives-ouvertes.fr/tel-00794896>

Submitted on 26 Feb 2013

HAL is a multi-disciplinary open access archive for the deposit and dissemination of scientific research documents, whether they are published or not. The documents may come from teaching and research institutions in France or abroad, or from public or private research centers.

L'archive ouverte pluridisciplinaire **HAL**, est destinée au dépôt et à la diffusion de documents scientifiques de niveau recherche, publiés ou non, émanant des établissements d'enseignement et de recherche français ou étrangers, des laboratoires publics ou privés.

THÈSE DE DOCTORAT

UNIVERSITE PARIS-SUD

ÉCOLE DOCTORALE : STITS

Institut d'Électronique Fondamentale

DISCIPLINE PHYSIQUE

soutenue le 01/02/2013

Présentée par :

Lei CAO

Sujet :

**Optimisation de la détection THz par plasmons
bidimensionnels dans des hétérostructures et de la
propagation THz dans des guides d'onde planaires**

Directeur de thèse :

Frédéric Aniel

IEF, UPSUD

Co-encadrant de thèse :

Anne-sophie Grimault-Jacquin

IEF, UPSUD

Composition du jury :

Rapporteurs :

Dominique Coquillat

L2C, Université Montpellier 2

Jean-François Lampin

IEMN, Université Lille 1

Examinateurs :

Philippe Ferrari

IMEP-LAHC, Grenoble

Béatrice Dagens

IEF, UPSUD

PhD Thesis

UNIVERSITE PARIS-SUD

DISCIPLINE PHYSICS

Lei CAO

February 1 2013

**Optimization of THz detection by two dimensional plasmons
in heterostructures and THz propagation in planar
waveguides**

Résumé de la thèse

0.1 Introduction et Objectif

Les sources et les détecteurs couramment utilisés en optique et en électronique présentent une chute de leurs performances dans la gamme de fréquence térahertz (THz). Il apparaît aujourd’hui que ce type de dispositifs présente un intérêt fort pour des domaines tels que la physique, la chimie, la biologie et l’astronomie. Mon travail de thèse s’inscrit dans le cadre du développement de composants THz peu onéreux, compacts, accordables en fréquence et facile à intégrer. Ce travail comprend deux parties: 1/ Une analyse et une optimisation de la détection d’ondes THz et 2/ une optimisation de la propagation THz dans des guides planaires dans la bande [10-1000] GHz. Chacune de ces études a un volet de modélisation, de fabrication et de caractérisation.

0.2 Optimisation de la détection THz Résonante en utilisant les Plasmon-Polariton dans des puits quantiques (QWs)

0.2.1 Principe : couplage entre radiation THz (photon) et plasmon 2D

Un plasmon correspond à des oscillations collectives de charges dans un environnement à trois ou deux dimensions (3D ou 2D). Nous avons analysé les plasmons issus d’un gaz 2D d’électrons (2DEG) dans des hétérostructures semi-conductrices. Dans la limite des grandes longueurs d’onde ($k < \sqrt{2\pi N_s}$), la dispersion des plasmons 2D dans un diélectrique homogène infini (permittivité ϵ_s) est dérivée de la relation suivante [Stern1967]: $k^2 = \frac{\epsilon_s \omega^2}{c^2} + \left(\frac{2\epsilon_s \epsilon_0 m * \omega^2}{N_s e^2} \right)^2$, $f = \frac{\omega}{2\pi}$,

où k est le vecteur d’onde de plasmon et ω est la fréquence de plasmon. La dispersion de la radiation THz est $f = \frac{1}{2\pi} \frac{c}{\sin \theta} k$. À 1 THz, le vecteur d’onde est d’environ 4.10^5 m^{-1} pour plasmon 2D dans GaN ($\epsilon_s = 9.7$, $N_s = 1.7.10^{16} \text{ m}^{-2}$), tandis que le photon incident présente un vecteur d’onde incident d’environ 2.10^4 m^{-1} . Par conséquent, le couplage ne peut avoir lieu. Pour compenser le décalage du vecteur d’onde, un réseau métallique de période L et de largeur de ruban métallique W est placé au-dessus de l’hétérostructure (Figure 1).

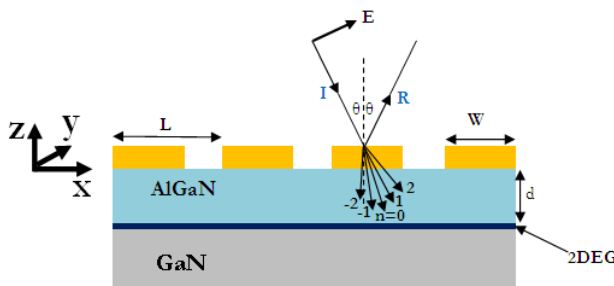


Figure 1: Réseau métallique sur hétéro-jonction AlGaN/GaN

Ainsi, l’onde diffractée par le réseau présente un vecteur d’onde de $k_{xn} = k_x + \frac{2\pi n}{L}$, $n = 0, \pm 1, \pm 2, \dots$. Si la période du réseau L est de l’ordre du micromètre alors le vecteur d’onde k_{xn} est de l’ordre de 10^5 ou 10^6 m^{-1} , ce qui rend possible l’existence d’un plasmons-polaritons (PP, couplage de l’onde avec le plasmon 2D). Le champ électrique de l’onde incidente doit suivre une polarisation transverse magnétique (TM), qui est une condition nécessaire au couplage PP. Pour traiter ce type

d'hétérostructure corruguée, nous avons développé sous Matlab un code numérique basé sur la méthode des ondes couplées (CWM, coupled wave method) [Wendler1999, Wendler2005]. Le 2DEG y est modélisé par une conductivité de type Drude soit quasi 2D si on le considère comme une couche mince, soit 2D si on le considère d'épaisseur nulle. Ceci nous permet de calculer les spectres de transmission, de réflexion et d'absorption des hétérostructures en tant que systèmes multicouches et de déceler les résonances de PP à partir desquelles nous avons tracé la dispersion de PP. Un autre moyen pratique pour modéliser ces dispositifs est d'utiliser le logiciel commercial Ansoft HFSS. Les deux méthodes de calculs (CWM et HFSS) ont été comparées validant ainsi l'utilisation de notre code écrit sous Matlab pour ce type d'application.

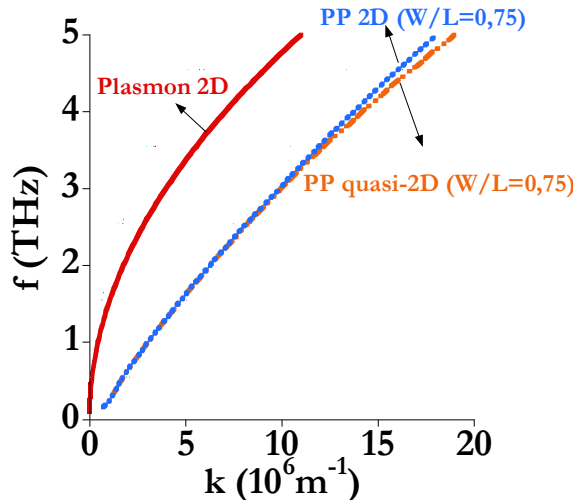


Figure 2: Comparaison entre la dispersion de plasmon 2D dans le GaN et les dispersions des PP ($W/L = 0,75$) sur une hétérostructure d'AlGaN/GaN avec 2DEG quasi-2D ($d_{2\text{DEG}} = 12 \text{ nm}$) et 2D. $N_s = 1,2 \times 10^{17} \text{ m}^{-2}$, $L = 2,2 \mu\text{m}$, et $d = 25 \text{ nm}$.

A titre d'illustration sur la Figure 2, la dispersion de plasmon 2D dans le GaN et du PP dans le cas d'un puits quantique d'AlGaN/GaN avec réseau avec $W/L = 0,75$ ont été tracées. Les métallisations sont en or, leur épaisseur est fixée à $t = 200 \text{ nm}$ et la conductivité vaut $\sigma_{\text{or}} = 4,1 \cdot 10^7 \text{ S/m}$. On peut voir que le vecteur d'onde de PP est plus grand que celui de plasmon 2D dans le GaN à la même fréquence.

De plus, nous pouvons constater que la prise en compte (ou non) de l'épaisseur du gaz 2D, ($d_{2\text{DEG}} = 12 \text{ nm}$ et $d_{2\text{DEG}} = 0$) n'induit pas de modifications remarquables de la courbe de dispersion du PP et $k \cdot d_{2\text{DEG}} \ll 1$. Le modèle simple du gaz ($d_{2\text{DEG}} = 0$) peut donner des résultats satisfaisants. La dispersion d'un PP avec $W/L = 0,75$ a un comportement proche de celle du PP dans le cas d'un QW recouvert d'un film métallique ($W/L = 1$).

Les courbes de dispersions de PP avec un réseau métallique 2D (sans épaisseur, $t = 0$) sont équivalentes à celles obtenues avec un réseau métallique 3D (épaisseur de métal finie fixée à $t = 200 \text{ nm}$) pour le rapport $W/L = 0,75$ et ce quel que soit le modèle du gaz 2D choisi (quasi-2D ou 2D).

Seuls les résultats du puits quantique d'AlGaN/GaN sont présentés, les mêmes conclusions ont été vérifiées pour trois autres hétérostructures qui sont décrites dans la section suivante.

0.2.2 Description des structures étudiées

Les hétérostructures étudiées sont : AlGaN/GaN, InAlN/GaN et AlGaAs/GaAs SiGe/Si/SiGe. Pour cette dernière structure, le silicium (Si) est contraint biaxiallement en tension sur une couche de silicium germanium (SiGe) relaxée. Les matériaux de substrats GaN, GaAs ou SiGe sont modélisés comme des semi-conducteurs semi-infinis sans pertes (les tangentes de pertes sont nulles). Le Tableau 1 présente les paramètres géométriques du réseau (L) pour obtenir une résonance PP à 1 THz et les caractéristiques des matériaux pour chaque hétérostructure. Si les paramètres dans les simulations ne sont pas mentionnés explicitement, leurs valeurs par défaut sont : l'épaisseur de la couche 2DEG $d_{2\text{DEG}} = 12 \text{ nm}$, angle d'incidence $\theta = 0^\circ$, épaisseur du métal $t = 200 \text{ nm}$, conductivité du métal $\sigma_{\text{Or}} = 4,1 \times 10^7 \text{ S/m}$.

Tableau 1: Paramètres des quatre hétérostructures nominales dans la simulation

Matériel	m^*/m_0	N_s (10^{16} m^{-2})	L (μm)	d (nm)	$\mu_{2\text{DEG}}$ à 300K (m^2/Vs)	$\mu_{2\text{DEG}}$ à 77K (m^2/Vs)
AlGaN/GaN	0,22	12	2,2	25	0,2	1,0
InAlN/GaN	0,22	12	1,55	10	0,11	0,33
SiGe/Si/SiGe	0,19	5	1,3	25	0,3	3,2
AlGaAs/GaAs	0,063	1	1,0	25	0,8	5

0.2.3 Etude paramétrique pour l'optimisation de la détection THz pour un gaz d'électrons 2D de concentration de porteurs homogène

La Figure 3 montre le spectre d'absorption PP (courbe noire) pour la structure AlGaN / GaN. Il est obtenu en soustrayant l'absorption normale (courbe solide) par les contributions de 2DEG (courbe brisée) et le réseau (courbe discontinue). De manière générale, trois, parfois quatre pics de résonance PP apparaissent sur les spectres d'absorption. L'amplitude de PP (A_1, A_2 et A_3) à la fréquence de résonance (f_1, f_2 et f_3) est utilisée comme un paramètre clé pour évaluer l'efficacité du couplage PP et pour comparer les performances des différentes structures.

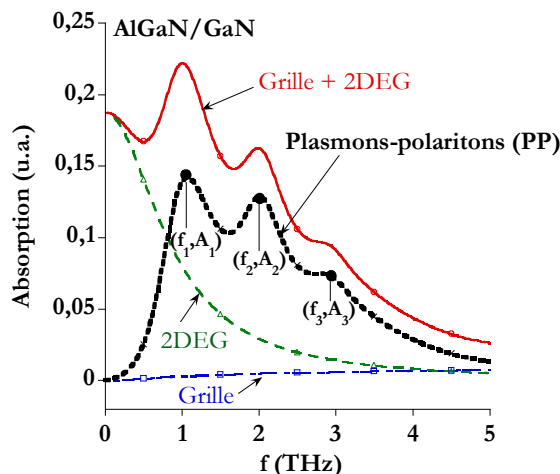


Figure 3: Spectres d'absorption de PP pour la structure AlGaN/GaN à 300 K modélisés avec Ansoft HFSS.

Afin de définir la meilleure hétérostructure, la résonance de PP a été analysée en terme d'amplitude, de position en fréquence, de largeur à mi-hauteur (FWHM : Full Width at Half Maximum en anglais) en fonction de plusieurs paramètres: la période du réseau L, l'angle d'incidence θ , la température, la concentration d'électrons N_s, l'épaisseur de la barrière d et le rapport du réseau W/L.

0.2.3.1 Influence de la période L et de l'angle d'incidence θ sur le spectre d'absorption

La Figure 4 (a) représente la position en fréquence f_1 en fonction de la période L pour les quatre matériaux nominaux à 300K. La relation $f_1 \sim 1/L$ [Muraviov2010, Hirakawa1995] est vérifiée pour W/L = 0,75.

Les résonances d'ordre plus élevé (f_2 ou f_3) peuvent également être adaptées en fonction de la période du réseau L ou par un vecteur d'onde d'ordre élevé $k_{xn} = kx + 2\pi n/L$ (n = 2 ou 3). Dans la plupart des cas, la résonance PP à f_1 est la plus intense en amplitude. L'ajustement de la fréquence de résonance dans la gamme THz [0,3-3] THz s'effectue par le choix de L comprise entre 0,5 et 5 μm . Les périodes du réseau pour chacune des quatre hétérostructures correspondant à une résonance PP f_1 fixée à 1 THz sont énumérées dans le Tableau 1.

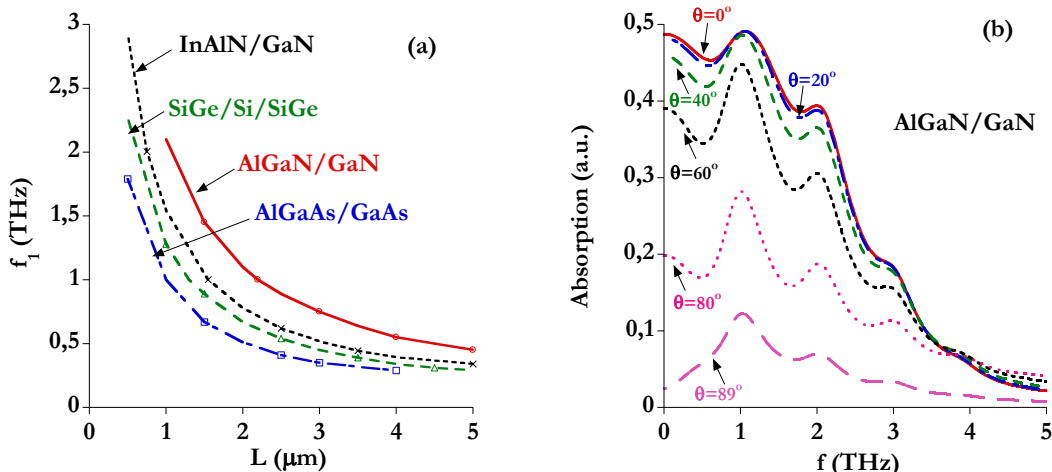


Figure 4: (a) Accordabilité en fréquence f_1 de la première résonance PP en fonction de la période du réseau L pour les quatre hétérostructures à 300 K et pour W/L = 0,75. (b) Spectres d'absorption pour la structure AlGaN/GaN à 300 K avec différents angles d'incidence modélisés avec Ansoft HFSS.

Cependant, deux cas limites pour la période L doivent être distingués et discutés:

- (1) Lorsque L est extrêmement faible ($\leq 0,5 \mu\text{m}$), les champs évanescents seront plus confinés au voisinage de l'interface métal/barrière, rendant inefficace le couplage entre l'onde et le plamson 2D. Par exemple, si L = 0,1 μm , le vecteur d'onde de la première onde évanescante dans la

direction x s'écrit $k_{x1} = 2\pi/L = 2\pi \times 10^7 \text{ m}^{-1}$. La composante du vecteur d'onde dans la direction z est égale à $\sqrt{\epsilon_b \omega^2 / c^2 - k_{x1}^2} \approx jk_{x1} \text{ m}^{-1}$, où ϵ_b est la permittivité de la barrière. Ainsi, la profondeur de propagation est $D_1 = |k_{z1}|^{-1} = 16 \text{ nm}$. Elle est plus petite voire comparable à l'épaisseur de la barrière $d=10 \text{ nm}$ (InAlN/GaN) ou 25 nm pour les trois autres matériaux. Pour des ondes d'ordres supérieurs ($n > 1$), la profondeur de propagation D_n est encore plus petite et l'observation des résonances PP devient difficile.

(2) Lorsque L est supérieure ou égale à $5 \mu\text{m}$, aucun résonance sur le spectre n'apparaît. La raison est liée à la condition de détection de résonance [Knap2002-1] $\omega\tau \gg 1$ (où ω est la pulsation et τ est le temps de relaxation). Cette relation n'est plus satisfaite lorsque ω est petite. Par exemple, pour AlGaN/GaN à 300 K, si $L = 5 \mu\text{m}$, $f_1 = 0,34 \text{ THz}$, et $\tau = 2,5 \times 10^{-13} \text{ s}$, ce qui donne le facteur $\omega\tau = 0,5$ qui bien inférieur à 1.

La Figure 4 (b) représente les spectres d'absorption pour la structure AlGaN/GaN avec θ compris entre 0° et 89° . Le champ électrique E_x qui est essentiel pour l'interaction avec les plasmons longitudinaux 2D, est maximale lorsque que $\theta = 0^\circ$. Ce qui permet d'obtenir les résonances les plus élevées en amplitude. Si on s'intéresse au premier pic de résonance celui-ci passe de 0,48 en incidence normale à 0,12 à 89° . Par conséquent, pour la suite de l'étude nous avons travaillé exclusivement en incidence normale.

La fréquence $f_1 = 1 \text{ THz}$ ne varie quasiment pas du fait que le vecteur d'onde incident ($\omega \sin \theta / c$) reste inférieur à $2\pi/L$.

0.2.3.2 Influence de la température sur le spectre PP

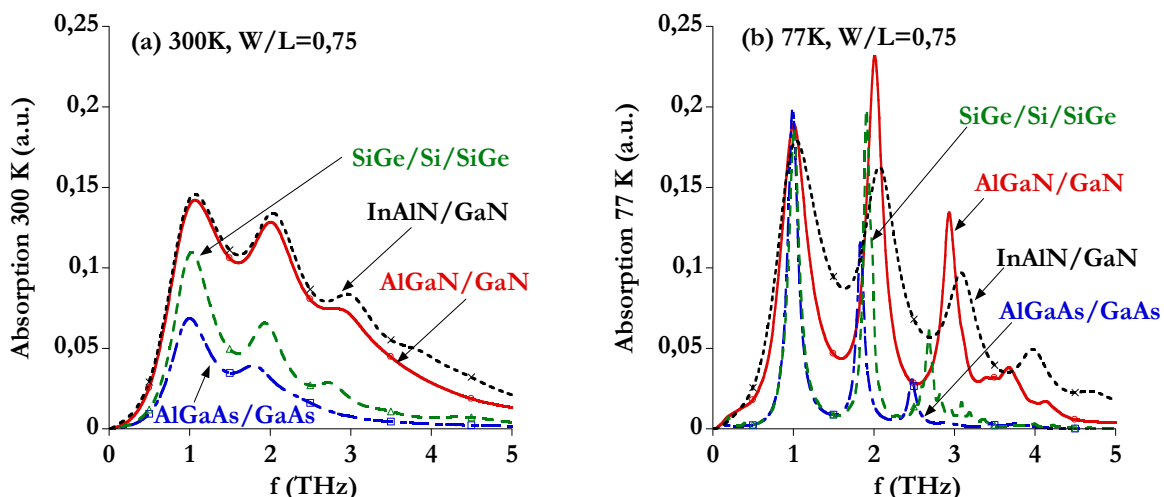


Figure 5: Spectre d'absorption pour les quatre hétérostructures étudiées avec $W/L = 0,75$ à (a) 300 K et (b) 77 K.

La Figure 5 montre les spectres d'absorption PP pour les quatre matériaux à température ambiante (300 K) et cryogénique (77 K) pour $W/L=0,75$. A basse température, les résonances PP sont plus étroites et d'amplitude plus élevée. Par exemple pour AlGaN/GaN, les deux premières résonances PP (A₂ et A₃) augmentent respectivement leur amplitude de 20 % et 40 %. Ceci est

attribué à l'absorption de type Drude du 2DEG qui diminue à basse température. Aux résonances PP (f_n), l'absorption dans le matériau SiGe/Si/SiGe et AlGaAs/GaAs augmentent rapidement en raison de la forte augmentation de la mobilité des électrons à 77 K. À 300 K, les matériaux à base de nitride ont les amplitudes A_n maximales quelque soit l'ordre de la résonance (f_n). L'hétérostructure d'InAlN/GaN apparaît comme optimale en raison de sa grande concentration d'électrons et sa petite épaisseur de barrière comparé à celle d'AlGaN/GaN. Cependant, AlGaAs/GaAs et SiGe/Si/SiGe présentent des absorptions aussi intéressantes notamment à basse température.

À certaines conditions, l'amplitude d'absorption PP (A_n) d'ordre supérieur ($n > 1$) peut devenir plus grande que celle d'ordre 1 (A_1). Le spectre d'absorptions d'AlGaN/GaN et SiGe/Si/SiGe à 77 K vérifient cette observation où l'amplitude $A_2 > A_1$. Ceci peut s'expliquer avec deux hypothèses : 1/Lorsque le facteur W/L augmente, le champ électrique (E_s) pour l'onde avec $n>1$ a une amplitude comparable, voire supérieure au champ E_x pour l'onde avec $n=1$. 2/Deuxièmement, E_x à basse température peut également être plus fort par référence à leur valeur à 300 K.

Un rapport W/L élevé et une température cryogénique sont deux critères spécifiques et favorables pour intensifier fortement les amplitudes A_n des résonances PP ($n>1$).

0.2.3.3 Influence de N_s , d et W/L sur le spectre PP

Dans cette section on étudie, la variation des amplitudes (A_1 , A_2 , A_3) (Figure 6 (a)) des résonances PP en fonction de la la concentration N_s . Une forte absorption s'obtient à partir de l'augmentation du nombre d'électrons par unité de surface qui intéragissent davantage avec les ondes évanescentes. Avec la même N_s (par exemple, 10^{16} m^{-2}), la structure AlGaAs/GaAs présente une amplitude de maximale A_1 en raison de la grande mobilité des électrons.

En ce qui concerne la fréquence PP (f_1 , f_2 et f_3), elle suit une loi en racine carrée qui peut être prédite par la dispersion d'un plasmon 2D recouvert d'un réseau (souvent noté « gated » dans les articles en anglais) $f = \frac{1}{2\pi} \sqrt{\frac{e^2 N_s k}{m^* \epsilon_0 (\epsilon_s + \epsilon_b \coth(kd))}} [Eguiluz1975]$.

L'influence de l'épaisseur de la barrière (d) sur la fréquence PP peut également prédite par $f = \frac{1}{2\pi} \sqrt{\frac{e^2 N_s k}{m^* \epsilon_0 (\epsilon_s + \epsilon_b \coth(kd))}} [Eguiluz1975]$. Lorsque $kd \ll 1$, f est proportionnelle à la racine carrée de l'épaisseur d .

Sur la Figure 6 (b), l'amplitude des résonances PP diminue lorsque d est au-delà de 50 nm. L'amplitude² maximale A_1 a été obtenue avec $d_{opt} = 50 \text{ nm}$ pour AlGaN/GaN et $d_{opt} = 25 \text{ nm}$ pour InAlN/GaN. Pour les deux autres matériaux, A_1 ne fait que décroître en fonction de d . A ces distances optimales, le facteur $\omega\tau$ est de 1,98 (AlGaN/GaN), 1,2 (InAlN/GaN). Quand $d < d_{opt}$, $\omega\tau$ chute rapidement et devient inférieure à 1 d'après la dispersion PP. La détection deviendra le type non résonant [Knap2002-2], résultant de l'amortissement de l'oscillation de plasma, en particulier lorsque la concentration d'électrons est élevée. Si N_s augmente jusqu'à 5.10^{16} m^{-2} dans AlGaAs/GaAs (ce qui n'est pas physiquement possible !), une distance optimale ($d_{opt} = 20 \text{ nm}$) apparaitrait également.

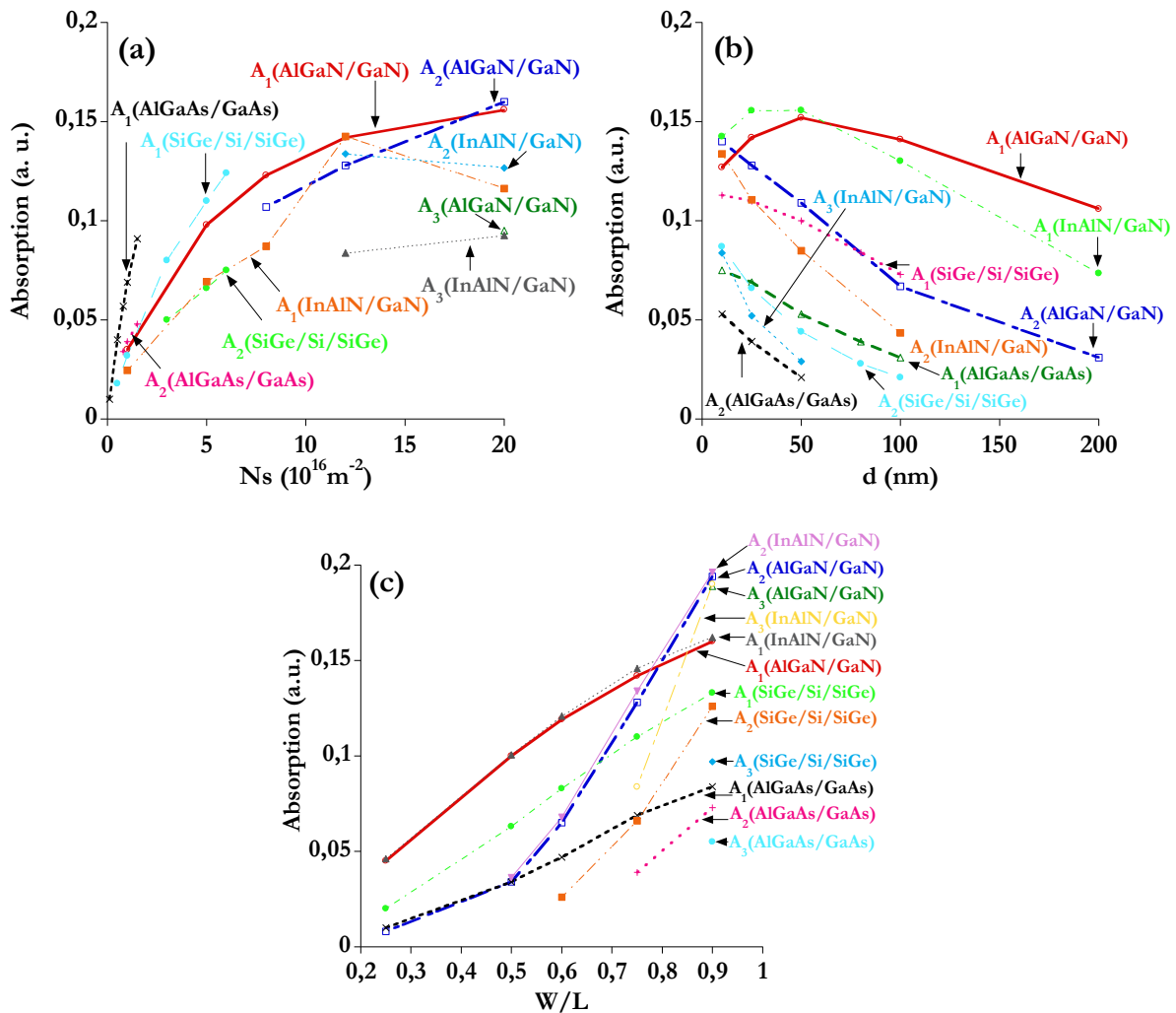


Figure 6: Influences de (a) la concentration homogène N_s , (b) l'épaisseur de la barrière d et (c) le rapport W/L sur des amplitudes (A_1 , A_2 , A_3) des résonances PP à 300 K.

Avec la même valeur de d (par exemple, 50 nm), la structure GaN présente l'amplitude de maximale A_1 en raison de sa grande concentration d'électrons N_s .

La Figure 6 (c) représente la variation des amplitudes (A_1 , A_2 , A_3) des résonances PP en fonction du rapport W/L du réseau.

A_n ont tendance à augmenter significativement avec W/L en raison de l'amélioration du champ électrique longitudinal E_x . Par exemple, A_1 est de 0,045 pour $W/L=0,25$ et de 0,16 pour $W/L=0,9$. Nous avons calculé E_x au voisinage du réseau avec W/L variant de 0.25 à 0.95 pour une période de réseau L fixée à 1 μm . Avec la diminution de la largeur du gap entre deux métallisations successives, E_x devient plus intense à l'interface air/hétérostructure et il s'étend plus profondément vers l'hétérostructure, ce qui rend le couplage avec les plasmons 2D plus fort.

Quand W/L augmente de 0.25 à 0.9, la position en fréquence de la résonance PP décroît de façon monotone. Au-delà de 0,6, f_n est quasiment constante. Par exemple, f_1 est de 1.76, 1.16, 1.06, 1.0 et 1.0 THz pour $W/L=0.25$, 0.5, 0.6, 0.75 et 0.9, respectivement.

Pour la même valeur de W/L (par exemple, 0,75), la structure basée sur nitride présente l'amplitude de maximale A_1 en raison de sa grande concentration d'électrons Ns.

0.2.4 Résonances PP : comparaison modélisation/mesure

Un échantillon $\text{Al}_{0.25}\text{Ga}_{0.75}\text{N}/\text{GaN}$ sur substrat saphir avec réseau périodique métallique a été mesurée par spectroscopie infrarouge à transformée de Fourier (Fourier Transform Infrared en anglais -FTIR-) à température ambiante et cryogénique. Ce travail a été réalisé en collaboration avec Marie-Antoinette Poisson de III/V Lab à Marcoussis qui nous a fourni l'hétérostructure et Isabelle Sagnes et Luc Le Gratiet du Laboratoire de Photonique et Nanostructures (LPN) à Marcoussis qui ont réalisé le dépôt des réseaux métalliques par lithographie électronique. Les spectres de transmission expérimentaux ont ainsi pu être comparés à ceux obtenus numériquement pour différentes valeurs du rapport $W/L = [0.25, 0.5, 0.6, 0.75]$ de 0.6 à 1.8 THz.

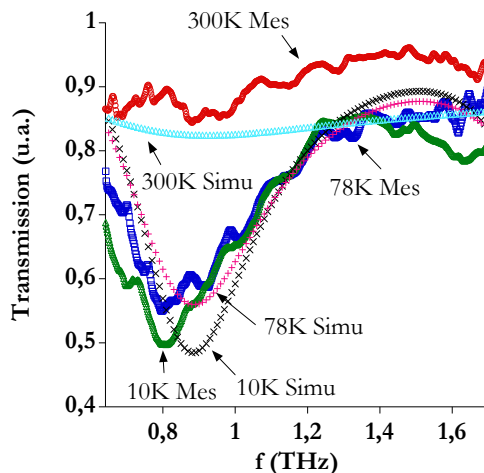


Figure 7: Comparaison des spectres de transmission mesurés (Mes) et modélisés via la méthode CWM (Simu) à 300, 78 et 10 K pour la structure $\text{Al}_{0.25}\text{Ga}_{0.75}\text{N}/\text{GaN}$ ($W/L = 0,6$, $N_s = 8.10^{16} \text{ m}^{-2}$)

Sur la Figure 7 sont montrés les spectres de transmission simulés (Simu) et mesurés (Mes) de 0,6 à 1,7 THz à différentes températures (300 K, 78 K et 10 K) pour un rapport $W/L = 0,6$. Lorsque la température baisse de 300 K à 10 K, l'amplitude de la première résonance apparaît de plus en plus. A température ambiante, la faible absorption est liée principalement à la faible mobilité des électrons, on ne peut distinguer précisément en amplitude et fréquence la première résonance. Les mobilités des électrons dans la simulation ont été fixées à $0.1 \text{ m}^2/\text{Vs}$ pour 300 K, $0.35 \text{ m}^2/\text{Vs}$ pour 78 K et $0.45 \text{ m}^2/\text{Vs}$ pour 10 K. La position en fréquence notée f_1 de cette résonance PP se situe à 0.81 THz (± 0.05 THz comme la résolution de la fréquence dans la mesure) expérimentalement alors qu'elle était prédictive à 0.88 THz numériquement à 10K. La fréquence et l'amplitude en transmission T_1 relevée expérimentalement est équivalente à celle calculée. L'amplitude descend jusqu'à 0.5 en unité arbitraire à 10 K et 0.55 à 300 K. Comme la mobilité est plus importante à 10 K, un second pic de résonance PP commence à se dessiner sur le spectre de transmission, avec une position en fréquence f_2 égale à 1.6 THz et une amplitude en transmission T_1 à 0.8. On ne la distingue pas à 78 K et 300 K sur la gamme de fréquence choisie. Cette confrontation modélisation/expérience se montre très prometteuse pour l'optimisation de la détection THz notamment dans la prédiction des résonances PP à des fréquences THz prédéfinies.

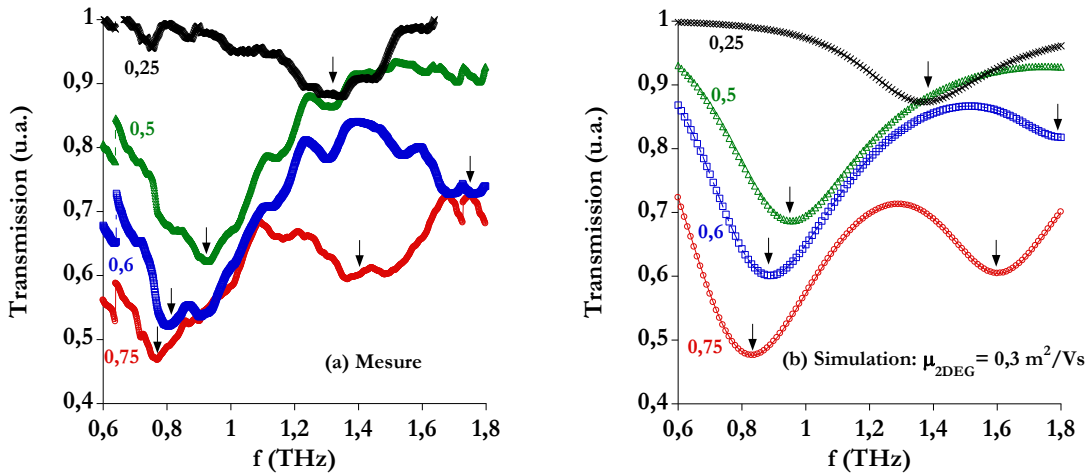


Figure 8: Spectres de transmission avec différents rapport W/L pour la structure $\text{Al}_{0.25}\text{Ga}_{0.75}\text{N}/\text{GaN}$ ($N_s = 8. 10^{16} \text{ m}^{-2}$) à 78 K, (a) mesure et (b) simulation avec $\mu_{2\text{DEG}} = 0,3 \text{ m}^2/\text{Vs}$ avec la méthode CWM

La Figure 8 représente les spectres de transmission mesurés (a) et modélisés (simulation) (b) pour différents rapport W/L à 78 K, avec $\mu_{2\text{DEG}} = 0,3 \text{ m}^2/\text{Vs}$ sur l'intervalle de fréquence [0.6 - 1.8] THz. Expérimentalement, lorsque le rapport W/L croît, la position en fréquence f_1 du premier pic de résonance se déplace vers les basses fréquences. On a une diminution de 0.5 THz entre la position obtenue pour le rapport W/L=0.25 et celui de 0.75. Une deuxième résonance PP n'est observable que pour les deux plus grands rapports W/L c'est-à-dire 0.75 et 0.6 dont les positions en fréquences respectives sont $f_2 = 1.40$ THz et 1.76 THz. De plus, lorsque le rapport W/L augmente on s'aperçoit que l'amplitude T_1 du premier pic de résonance s'accentue atteignant une valeur minimale de 0.48 pour W/L = 0.75. Si on compare ces données avec celles calculées numériquement, on retrouve un bon accord entre les positions en fréquence et les amplitudes des résonances. Par conséquent, l'utilisation d'une fonction de distribution homogène pour la concentration des porteurs dans la direction x, $N_s(x) = N_s$ semble être une hypothèse raisonnable dans le cas d'une hétérostructure de type AlGaN/GaN.

0.2.5 Modélisation d'un gaz d'électron 2D héterogène

Dans les sections qui vont suivre, nous allons aborder l'influence de la modulation d'un gaz d'électron 2D par l'intermédiaire de la modification de la concentration des porteurs en-dessous (N_1) et entre (N_2) les métallisations du réseau ; notamment, sous l'effet d'une polarisation en tension appliquée sur les métallisations. Nous n'aborderons ici que le cas de l'hétérostructure d'AlGaAs/GaAs. Ceci est dû à la différence entre la hauteur de barrière à l'interface métal/semi-conducteur et le niveau de Fermi à l'interface air/semi-conducteur, qui conduit à $N_1 \neq N_2$. A chaque variation de la concentration N_1 correspond une tension de polarisation notée V_G qui est appliquée sur le réseau métallique. La méthode CWM et le logiciel HFSS d'Ansoft peuvent être utilisés pour calculer les spectres d'absorption de ce type de configurations où $N_1 \neq N_2$.

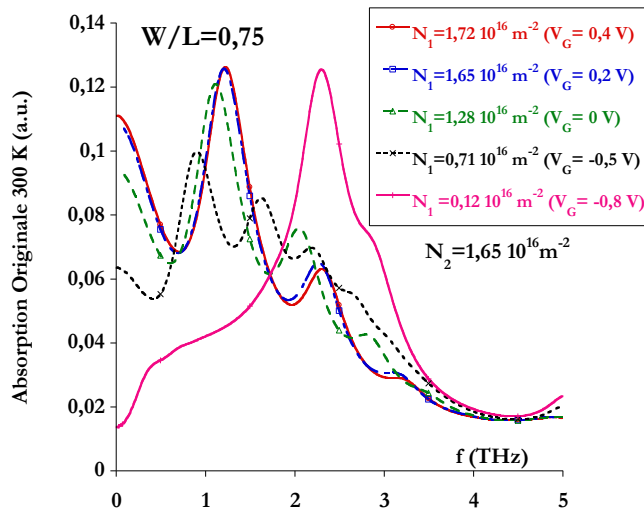


Figure 9 : Spectre d'absorption de la structure AlGaAs/GaAs pour différentes concentrations d'électron N_1 à 300 K et $W/L = 0,75$ avec N_2 fixée à $1,65 \cdot 10^{16} \text{ m}^{-2}$.

Sur la Figure 9, est représentée l'influence de la concentration N_1 (respectivement V_G) sur le spectre d'absorption pour une hétérostructure d'AlGaAs/GaAs à température ambiante avec $W/L = 0,75$ et une concentration N_2 fixée à $1,65 \cdot 10^{16} \text{ m}^{-2}$.

En fixant la concentration N_2 , un peu plus élevé (inférieur) N_1 décale l'amplitude et la fréquence de résonance à haute (basse) valeur. L'accordabilité en fréquence est possible par la tension.

Pour la plus petite des concentrations $N_1 = 0,12 \times 10^{16} \text{ m}^{-2}$ ($N_1 \ll N_2$), la forme du spectre d'absorption est complètement modifiée : on ne retrouve pas de minimum d'absorption à 0,3 THz. En revanche, nous observons un seul pic de résonance qui est décalé vers les hautes fréquences à 2,3 THz avec une amplitude de 0,12. Avec ce fort contraste entre N_1 et N_2 , l'absorption présente une amplitude comparable avec le cas homogène ($N_1 = N_2$). Le pic de résonance est due à l'oscillation dipolaire fondamentale lorsque la répartition de densité d'électrons est antisymétrique des deux côtés de la fente $W_G = L-W$ [Alsmeier1989, Matov2002, Popov2003]. La simulation montre que la fréquence et l'amplitude de l'absorption peut également être modifiées par le rapport W/L .

0.2.6 Conclusion

L'hétérostructure à base de III - Nitrure a l'absorption PP maximale en raison des grandes polarisations spontanées et piézoélectriques.

La fréquence et l'amplitude de résonance peuvent être contrôlées dans la gamme de fréquences THz à la fois par la période du réseau (L), la largeur du métal (W) et la tension (V_G).

Des mesures ont été réalisées sur l'échantillon AlGaN/GaN. Les modélisations se comparent favorablement aux mesures.

Dans la région de forte modulation où la concentration d'électrons $N_1 \ll N_2$, la grille métallique est indispensable pour l'accordabilité en fréquence et prometteuse pour la détection THz.

0.3 Optimisation de la transmission THz dans les guides d'onde planaires

La deuxième partie de ce travail de thèse concerne l'optimisation de la transmission THz via l'étude de la dispersion et de l'atténuation de quatre types de guide d'ondes (coplanaire (CPW), microruban, Slotline et triplaqué) en fonction des dimensions géométriques, des propriétés des matériaux (diélectriques et métallisation) avec des logiciels commerciaux Ansoft HFSS ® (<http://www.ansys.com/>) et MWS CST ® (<http://www.cst.com/>). Une comparaison de leurs pertes et de leur dispersion pour une même impédance caractéristique de 100Ω à 20 GHz est aussi présentée. Les avantages et les limites de chaque guide sont présentés afin de proposer une structure optimale. Une comparaison des résultats numériques avec des mesures électriques réalisées en Allemagne à l'institut Fraunhofer de Fribourg a pu être effectuée entre 340-500 GHz.

L'étude des guides a été réalisée principalement sur substrat polymère : le benzocyclobutène (BCB). Elle s'inscrit dans la continuité d'une première analyse appliquée à la transmission THz via des lignes coplanaires sur substrat semi-conducteur semi-isolant de phosphure d'indium (InP) utilisées pour des photocommutateur d'InGaAs qui fût effectuée dans notre groupe [Grimault 2012].

0.3.1 CPW

Un guide coplanaire (CPW) est défini par trois rubans métalliques : deux plans de masse externes et un ruban central (Figure 10). Chaque ruban est espacé de la dimension W . Les plans de masse sont supposés infinis et le ruban central de dimension finie notée S_1 . L'ensemble repose sur substrat diélectrique. Le guide CPW sur InP ($\epsilon_r=12,5$) avec $W = 6,6 \mu\text{m}$ a une impédance caractéristique (Z_c) de 50Ω . L'influence de W sur la dispersion et les pertes a été analysée. Dans le cas avec le substrat BCB ($\epsilon_r=2,42$), les mêmes dimensions de W sont utilisées pour étudier l'influence de la nature du substrat.

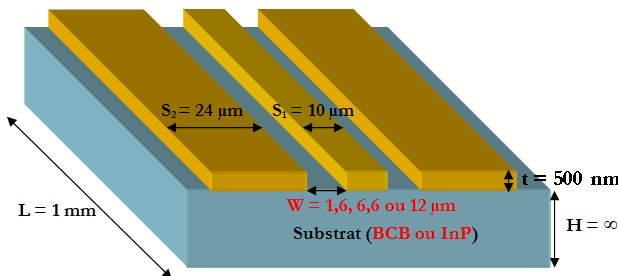


Figure 10: Configuration de CPW

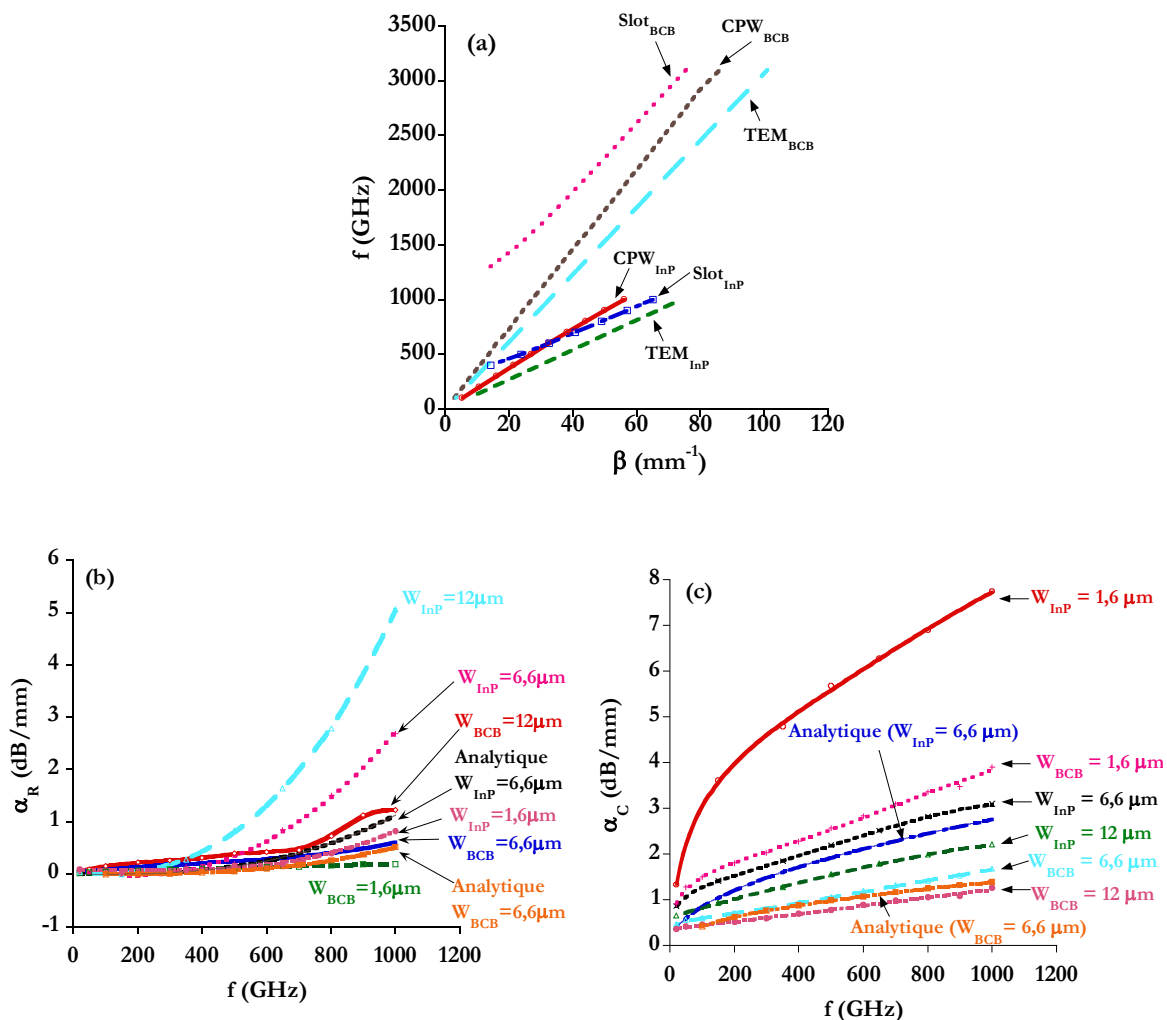
0.3.1.1 Dispersion

La Figure 11 (a) représente la dispersion des deux modes (symétrique (CPW) et antisymétrique (Slotline)) qui se propagent dans la structure CPW sur BCB et InP en fonction de la fréquence pour $W = 6,6 \mu\text{m}$. La ligne TEM représente la dispersion de l'onde de type transverse électromagnétique (TEM) dans substrat semi-infini.

Pour la ligne CPW sur BCB, la courbe de dispersion du mode CPW ne croise pas celle du mode slotline sur toute la gamme de fréquence considérée et ce jusqu'à 3 THz. Contrairement au cas du CPW sur InP, pour lequel le mode CPW peut transférer de l'énergie au mode slotline à partir de 600 GHz. Il convient de noter également que pour la structure sur InP un mode d'ordre supérieur apparaît avec une fréquence de coupure de 800 GHz, il n'est pas représenté ici. Pour le BCB, le premier mode d'ordre supérieur apparaît au-delà de 1,5 THz.

Le coefficient de couplage est calculé à 0,0033 à 3 THz pour CPW sur BCB, tandis que pour CPW sur InP, la courbe de dispersion du mode Slotline couple celle du mode CPW à 0,6 THz. Ceci confirme la possibilité d'échange d'énergie entre les deux modes, car le coefficient de couplage vaut 0,2764 à 600 GHz et augmente ensuite.

D'autre part, le mode CPW peut rayonner vers le substrat parce que la vitesse de phase du mode CPW est toujours plus grande que l'onde TEM dans le substrat [Kasilingam1983]. Plus l'angle de radiation (Ψ) est élevé, plus le rayonnement augmente. Ψ est calculée à 33,87° pour CPW sur BCB et 40,62° pour CPW sur InP.



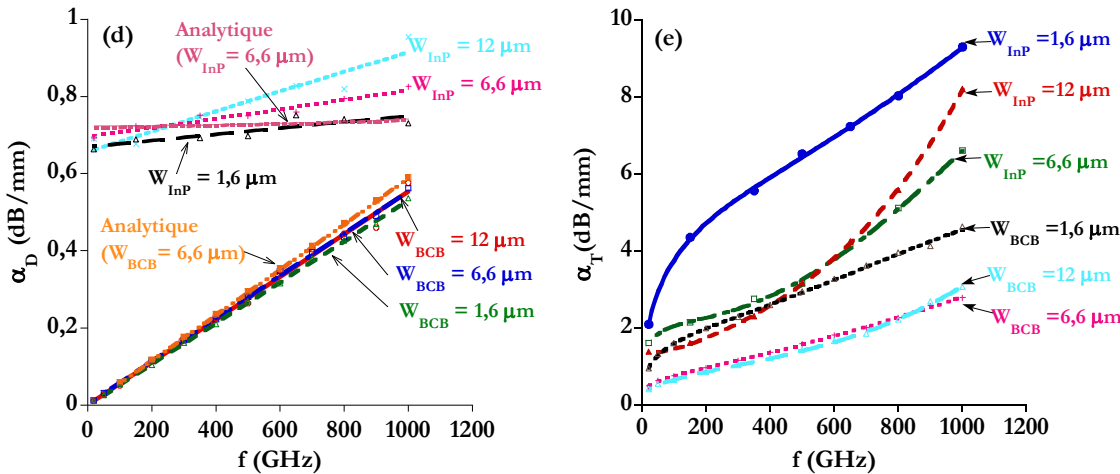


Figure 11: Comparaisons pour la configuration, CPW (AB/BC) pour différents substrats BCB et InP: (a) dispersion avec $W = 6,6 \mu\text{m}$, (b) perte par rayonnement, (c) perte métallique ($\sigma_{or} = 4,1 \cdot 10^7 \text{ S/m}$), (d) perte diélectrique ($\tan\delta_{BCB}=0,007$ et $\sigma_{InP}=2,4 \text{ S/m}$), et (e) pertes totales.

0.3.1.2 Perte par rayonnement α_R

D'après la littérature, deux principaux effets contribuent aux pertes par rayonnement. Le premier est le transfert d'énergie de l'onde guidée dans le substrat telle une onde de choc [Kasilingam1983].

Le second effet est dû au couplage entre l'onde guidée et d'autres ondes comme on le voit dans les courbes de dispersion, lorsque cela est possible. Plusieurs modes peuvent se propager dans le guide CPW il est dit multi-modes. Le coefficient de couplage entre le mode CPW et le mode Slotline est cent fois plus petit que dans le cas d'un CPW sur InP.

La Figure 11 (b) montre les pertes par rayonnement par rapport à la fréquence avec les deux types de substrats. Pour une fréquence située en-dessous de 400 GHz, la dépendance des pertes en fonction de la fréquence est faible, alors qu'au-delà, les pertes suivent une relation polynomiale dépendant du cube de la fréquence f^3 . La courbe analytique a été reportée sur la figure dans le cas de $W = 6,6 \mu\text{m}$ pour les deux substrats. Les pertes calculées suivent globalement la tendance de la courbe analytique à basse fréquence (<400 GHz) mais on s'aperçoit qu'au-delà de 400 GHz les pertes par rayonnement d'une ligne coplanaire sur substrat InP sont sous estimées npar ces relations quasi statiques et que seules des mesures ou des modélisations électromagnétiques 3D sont pertinentes.

Les pertes par rayonnement dépendent également de la géométrie de la ligne et elles sont proportionnelles au facteur $(S_1+2W)^2$. La perte de rayonnement augmente drastiquement avec W . L'avantage du substrat BCB est sa permittivité faible dans la gamme de fréquence THz, ce qui conduit à des plus faibles pertes.

Nous verrons par la suite que les pertes par rayonnement contribuent significativement dans les pertes totales notamment à hautes fréquences.

0.3.1.3 Perte de conduction α_C

Dans la Figure 11 (c), les pertes de conduction ($\sigma_{Or} = 4,1 \cdot 10^7 \text{ S/m}$) sont tracées en fonction de la fréquence pour différents W. L'expression analytique a également été ajoutée pour W = 6,6 μm , et on peut remarquer qu'elle sous-estime les pertes par conduction. Quand W diminue, la densité de courant parasite circule dans une section plus limitée dans le ruban central, entraînant l'augmentation des pertes ohmiques (α_C) qui évoluent en $1/\sigma\delta$ où δ est l'épaisseur de peau qui est proportionnelle à la racine carrée de la fréquence ($\delta=79 \text{ nm à 1 THz}$). Pour un même espace W, si l'on compare le CPW sur InP avec le CPW sur BCB on s'aperçoit que les pertes par conduction sont atténuées en raison de la nature du substrat. Cela confirme encore une fois l'avantage d'utiliser le BCB. Les pertes par conduction sont les pertes qui contribuent le plus aux pertes totales dans un guide CPW à basse fréquence. Les pertes par rayonnement prennent le relais, ensuite, à plus haute fréquence.

0.3.1.4 Perte diélectrique α_D

Les pertes diélectriques sont proportionnelles au facteur ($f \tan \delta$). Comme le montre la Figure 11 (d), les pertes diélectriques calculées pour un guide CPW sur BCB et InP présentent des caractéristiques différentes. Ceci car nous avons modélisé les pertes dans chacun des substrats de manière différente. Les pertes sur InP restent toujours supérieures à celles obtenues sur BCB. Les pertes diélectriques restent toutefois très faibles par rapport aux deux autres pertes que sont le rayonnement et la conduction. L'approche analytique sous-estime les valeurs calculées numériquement à hautes fréquences.

Un modèle précis de la tangente de perte du BCB (4026-46 Cyclotene résines de Dow Chemical Company) a été introduit dans nos modèles à partir de mesures de membranes de BCB dans la gamme THz au FTIR réalisées dans notre groupe en 2008 [Perret2008]. On a de ce fait comparé les pertes diélectriques du CPW sur BCB avec le modèle de tangente de perte suivant ($\tan \delta = 0,0073 + 0,0017 \times f$ (en THz)) et la valeur constante ($\tan \delta = 0,007$) qui a toujours été utilisée jusqu'à présent dans nos modélisations. Le modèle qui dépend de la fréquence produit plus de pertes à hautes fréquences. L'augmentation maximale des pertes diélectriques est d'environ 0,3 dB / mm à 1500 GHz pour W = 12 um. Lorsque l'on compare avec les autres types de pertes dans une structure CPW, cette perte supplémentaire reste cependant négligeable.

0.3.1.5 Pertes totales α_T

L'atténuation totale du mode CPW dans la Figure 11 (e) est considérée comme la somme des trois types de pertes ($\alpha_T = \alpha_R + \alpha_D + \alpha_C$). Pour un même espace W et à une même fréquence, un guide CPW sur BCB présente le moins de pertes et sera plus performant pour la transmission THz. Un guide CPW avec un faible espace W = 1,6 μm est celui qui a le plus de pertes par conduction alors que le guide large avec W=12 μm est celui qui a le plus de pertes par rayonnement. La structure optimale (pertes totales minimales) est celle dont W = 6,6 μm et ce pour les deux substrats, même si le guide avec W = 12 um a des pertes légèrement inférieures à certaines fréquences c'est-à-dire 800 GHz pour BCB et 600 GHz pour InP où un compromis peut être établi pour choisir ce guide.

0.3.2 Structure optimale entre guides d'onde THz sur BCB à Z_c fixée

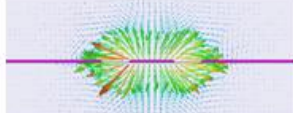
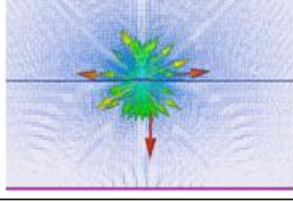
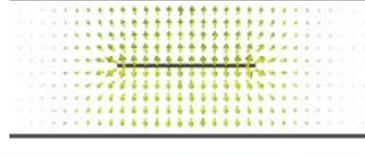
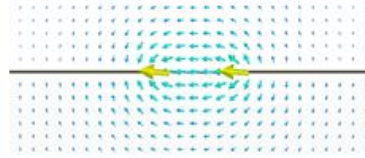
Guide	Dimensions à 100 Ω	Mode Dominant (Champ E)	Z_c (Ω) à 20 GHz
CPW	$W = 6,6 \mu\text{m}$ $S_1 = 10 \mu\text{m}$ $S_2 = 24 \mu\text{m}$ $t = 500 \text{ nm}$ $L = 1 \text{ mm}$ $H = \infty$		73-123 Ω ($W = 1,6-12 \mu\text{m}$)
Microruban	$W = 25 \mu\text{m}$ $H = 30 \mu\text{m}$ $t = 500 \text{ nm}$ $L = 1 \text{ mm}$		210-93 Ω ($W = 5-30 \mu\text{m}$)
Triplaqué	$W = 7,3 \mu\text{m}$ $H = 30 \mu\text{m}$ $t = 500 \text{ nm}$ $L = 1 \text{ mm}$		120-45 Ω ($W = 5-30 \mu\text{m}$)
Ligne à fente (Slotline)	$W = 6 \mu\text{m}$ $S = 240 \mu\text{m}$ $t = 500 \text{ nm}$ $L = 1 \text{ mm}$ $H = \infty$		95-160 Ω ($W = 5-30 \mu\text{m}$)

Figure 12: Dimensions des guides d'onde à 100 Ω .

Dans le cadre de cette étude, on a comparé le guide CPW avec trois autres guides d'ondes (microruban, triplaqué et slotline) pour une même impédance caractéristique fixée à 100 Ω à basse fréquence (20 GHz). Leurs dimensions géométriques sont indiquées sur la Figure 12.

Du point de vue de la dispersion, la ligne triplaqué possède une vitesse de phase égale à la vitesse de phase de l'onde TEM qui se propage dans le substrat polymère BCB. La vitesse de phase des guides CPW et triplaqué est quasi-constante avec la fréquence. Les quatre types de guides d'ondes peuvent être triés en fonction de leur dispersion croissante comme suit : Slotline > Microruban > CPW > Triplaqué.

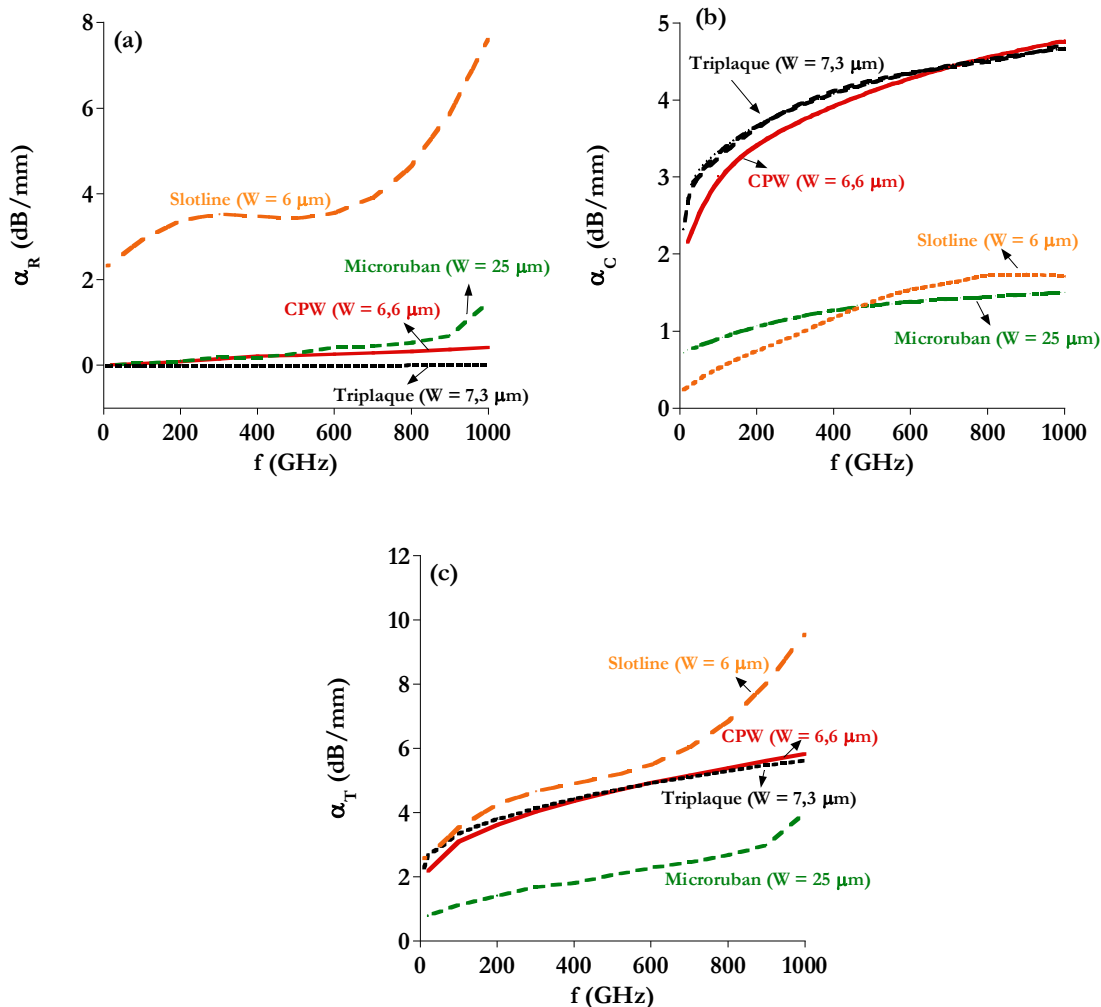


Figure 13: Pertes dans les quatre types de guide d'onde. (a) perte par rayonnement, (b) perte métallique ($\sigma_{0r} = 5.10^6 \text{ S/m}$) et (c) pertes totales ($\sigma_{0r} = 5.10^6 \text{ S/m}$)

0.3.2.1 α_R

Pour les pertes par rayonnement (Figure 13 (a)), la ligne Slotline présente la plus grande atténuation de 7,63 dB/mm à 1 THz bien au-dessus des trois autres lignes à cause de sa grande dispersion. Sans surprise, celles de la ligne triplaqué sont quasi nulles de l'ordre de 0,006 dB/mm pour la même fréquence. Microruban et CPW présentent également des performances satisfaisantes, avec 1,48 dB/mm et 0,43 dB/mm respectivement à 1 THz.

0.3.2.2 α_D

Pour les quatre types de guides d'ondes, les pertes diélectriques maximales observées restent inférieures à 1 dB/mm à 1 THz. Les pertes diélectriques sont faibles et comparables aux pertes par rayonnement dans les lignes CPW et microruban.

0.3.2.3 α_C

Les lignes qui présentent le moins de pertes par conduction sont les guides slotline et microruban environ 1,6 dB/mm à 1 THz (Figure 13 (b)). La ligne CPW et la ligne triplaqué ont une valeur relativement élevée de l'ordre de 4,7 dB/mm à 1 THz.

0.3.2.4 α_T

Les pertes totales sont illustrées sur la Figure 13 (c). La ligne microruban est la ligne de transmission THz optimale montrant une atténuation de 4,0 dB/mm à 1 THz. Les pertes liées aux différents guides sont répertoriées dans le Tableau 2.

Tableau 2: Atténuation dans les quatre types de guide à 1 THz.

	α_R (dB/mm)	α_D (dB/mm)	α_C (dB/mm)	α_T (dB/mm)
CPW	0,43	0,59	4,77	5,84
Microruban	1,48	0,82	1,63	4,00
Triplaqué	0,006	1,00	4,68	5,64
Slotline	7,63	0,94	1,71	9,60

L'atténuation dans CPW et triplaqué est limitée par la perte par conduction. Elle peut être réduite en choisissant la combinaison optimale de S_1/W pour CPW et W/H pour triplaqué à $Z_c = 100 \Omega$. Dans le guide slotline, les pertes par rayonnement sont le plus importantes. En déposant une couche de BCB au-dessus de la structure, la réduction du rayonnement et de la dispersion est possible.

Les pertes par conduction des guides triplaqué et CPW peuvent être réduites en jouant sur les dimensions pour une impédance caractéristique fixée.

0.3.3 Résultats de la mesure CPW sur BCB

Suite à cette étude paramétrique réalisée via de multiples modélisations sous HFSS et CST, nous avons décidé de fabriquer des échantillons en salle blanche de la centrale de technologie Minerve de l'IEF. Nous avons mis en place l'ensemble des étapes technologiques pour élaborer des guides coplanaires en vue de les mesurer expérimentalement avec un analyseur de réseau vectoriel dans la gamme de fréquence [340 – 500] GHz. Ces mesures ont été effectuées à l'Institut Fraunhofer IAF (Allemagne). Les dimensions S_1/W que nous avons fixées pour fabriquer et mesurer des lignes CPW sur BCB (30 μm) sur wafer de Si sont énumérées dans le titre de la Figure 14.

Sur les Figures 14 (a) et (b) sont représentées les atténuations mesurées et modélisées. Un bon accord entre les données numériques et expérimentales a été trouvé pour les cinq dimensions de guide. Si la largeur du ruban central reste fixée à $S_1 = 36 \mu\text{m}$, et que l'espacement W augmente de 3 à 10 μm , l'atténuation augmente. Les pertes évoluent en fonction du cube de la fréquence laissant supposer qu'elles sont directement liées à la croissance des pertes par rayonnement. Par rapport à la confrontation avec les mesures le choix d'une conductivité pour le métal de $\sigma_{Or} = 4,1 \cdot 10^7 \text{ S/m}$ dans les modélisations demeure toutefois raisonnable et relativement adaptée.

Si $S_1 > 36 \mu\text{m}$ alors nous obtenons des pertes totales plus importantes qui peuvent atteindre 16 dB/mm à 500 GHz avec $S_1 = 100 \mu\text{m}$. Ceci est cohérent avec la littérature. L'augmentation des dimensions du guide a une répercussion directe sur les pertes métalliques et/ou sur des pertes par rayonnement. Les fluctuations des données expérimentales sont attribuées aux incertitudes de mesures mais également à la réalisation technologique. Pour résumer, la structure la plus satisfaisante au regard de ses pertes est celle dont les dimensions sont $S_1 = 36 \mu\text{m}$ et $W = 3 \mu\text{m}$ car nous obtenons une atténuation de 2,7 dB/mm à 400 GHz et 3,5 dB/mm à 500 GHz. Ce qui constitue l'état de l'art actuel pour des guide d'onde dans cette gamme de fréquence.

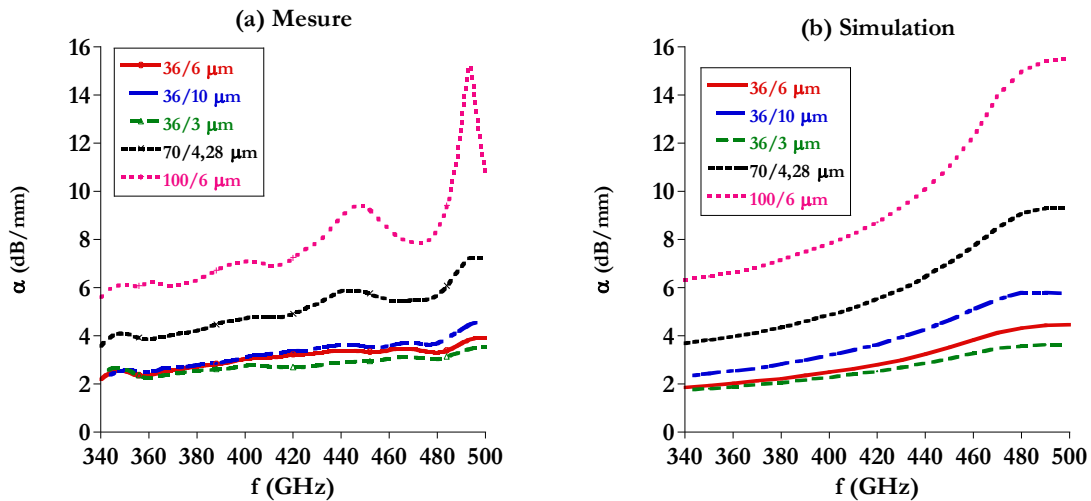


Figure 14: Constante d'atténuation α (dB/mm) mesurée (a) et simulée (b) de CPW avec différentes dimensions (S_1/W) : 36/6, 36/10, 36/3, 70/4,28 et 100/6 μm . Échantillon : Métal (500 nm)/BCB ($\sim 30 \mu\text{m}$)/substrat Si (300 μm), Modèle: $\sigma_{\text{or}} = 4,1 \cdot 10^7 \text{ S/m}$, $\tan\delta(\text{BCB}) = 0,007$, $\epsilon_{\text{BCB}} = 2,42$, 30 μm BCB sur substrat de Si semi-infini ($\epsilon_{\text{Si}} = 11,9$, $\sigma_{\text{Si}} = 10 \text{ S/m}$).

0.4 Conclusion

Le CPW sur BCB est meilleur que le CPW sur InP pour une même dimension.

La perte par rayonnement augmente avec W (la largeur du ruban ou l'espacement entre deux rubans) et la perte par conduction diminue avec W. La perte diélectrique est quasiment constante en fonction de W pour tous les guides ($\leq 1 \text{ dB/mm}$ à 1 THz).

Nous avons comparé les quatre familles de guide d'onde étudié pour une même impédance caractéristique. A $Z_c = 100 \Omega$, la ligne triplaqué n'est quasiment pas dispersive, et la perte par rayonnement est quasiment nulle. La ligne microruban a le minimum d'atténuation ($H = 30 \mu\text{m}$). La ligne microruban semble le meilleur compromis.

Une atténuation expérimentale de 2,7 dB/mm à 400 GHz est obtenue pour la ligne CPW sur BCB. Les modélisations sont en bon accord avec les mesures. Ces mesures constituent l'état de l'art.

Contents

<i>Contents</i>	<i>xxi</i>
List of Tables	xxv
List of Figures	xxvii
Acknowledgements	1
Abstract.....	1
General Introduction.....	3
<i>Chapter 1 Introduction.....</i>	<i>5</i>
1.1 THz applications.....	5
1.1.1 THz time domain spectroscopy (THz TDS).....	5
1.1.2 THz Imaging (T-ray)	6
1.1.3 Telecommunication.....	7
1.2 Terahertz sources.....	7
1.3 Terahertz detectors.....	8
1.3.1 Detector figures of merit.....	9
1.3.2 THz detection methods	9
1.4 Terahertz waveguide.....	13
1.4.1 Free space and dielectric waveguide	13
1.4.2 Planar on-chip waveguide.....	14
<i>Chapter 2 Modeling and Measurement of Plasmon-Polariton for Resonant Terahertz Detection.....</i>	<i>19</i>
2.1 Introduction.....	19
2.2 Plasma in semiconductor	21
2.2.1 3D plasma in bulk semiconductor	21
2.2.2 Heterojunctions and two dimensional electron gas 2DEG	22
2.3 Dispersion and spectrum of Plasmon-Polariton (PP)	31
2.3.1 Dispersion of 2D plasmon.....	32

2.3.2 Grating assisted coupling.....	32
2.3.3 Modeling of PP spectrum.....	33
2.3.4 Results and discussions.....	46
2.3.5 Conclusions	49
2.4 Optimization of resonant THz detection of PP in the heterojunctions III-V and IV-IV	49
2.4.1 Parameters of the studied structures.....	49
2.4.2 Absorption of PP.....	50
2.4.3 Tunability of the resonant frequency versus the grating period	51
2.4.4 Influence of incident angle θ	52
2.4.5 Influence of the metal thickness, the conductivity and the QW width	53
2.4.6 Influence of temperatures on the PP resonances	55
2.4.7 Influences of the electron concentration and the geometric parameters on PP resonances at 300 K.....	58
2.4.8 Conclusions	64
2.5 Measurement of the transmission spectrum of PP in AlGaN/GaN by FTIR	64
2.5.1 Sample fabrication	65
2.5.2 Introductin to FTIR	65
2.5.3 Transmission spectrum excited by TM polarized FIR laser beam	67
2.6 Modeling of non homogeneous 2DEG	72
2.6.1 Non homogeneous electron concentration	72
2.6.2 Variation of electron concentration N_1 below biased metals.....	75
2.6.3 Strongly modulated 2DEG	78
2.6.4 Conclusions	80
2.7 Conclusions of Chapter 2	81
Chapter 3 3D Electromagnetic Modeling and Measurements of Planar Waveguides in THz Frequency.....	83
3.1 Introduction.....	83

3.1.1 Electromagnetic modeling methods	84
3.1.2 Dispersions and losses of a waveguide.....	84
3.2 Harmonic analysis of CPW on BCB at THz frequency with HFSS	88
3.2.1 Simulated CPW structures.....	91
3.2.2 Role of the air-bridges (ABs) on effective permittivity and total losses.....	92
3.2.3 Modal dispersions, coupling effect, phase and group velocities.....	96
3.2.4 Influence of the gap width on the losses	101
3.2.5 Conclusion.....	114
3.3 HFSS analysis of microstrip line on 30 μm BCB	115
3.3.1 Microstrip structure.....	116
3.3.2 Dispersions	117
3.3.3 Losses	119
3.3.4 Conclusions	121
3.4 CST MWS analysis of stripline.....	121
3.4.1 Stripline structure.....	122
3.4.2 Dispersions and losses	123
3.4.3 Conclusions	127
3.5 CST MWS analysis of slotline on substrate BCB.....	127
3.5.1 Slotline structure	128
3.5.2 Modal dispersions and losses	129
3.5.3 Conclusions	135
3.6 Optimal THz planar waveguide.....	135
3.6.1 Comparison criteria.....	135
3.6.2 Dispersion and losses.....	137
3.6.3 Optimization of the performances of waveguides on BCB at 100 Ω	140
3.6.4 Conclusions	142
3.7 Transition design, sample fabrication and measurements	142

3.7.1 Design of coupling transitions.....	142
3.7.2 Technologies of sample fabrication	146
3.7.3 Measurements results in the frequency range [340-500] GHz.....	150
3.7.4 Conclusions concerning measurement.....	160
3.8 Conclusions of Chapter 3	161
Chapter 4 Conclusions and Perspectives.....	165
4.1 Conclusions	165
4.1.1 THz detection	165
4.1.2 THz transmission	166
4.2 Future Work	167
Appendix A: Surface waves in a planar waveguide	169
A.1 Air/dielectric	169
A.2 Air/ dielectric slab/Air	170
A.3 Air/ dielectric slab back conducted	172
Appendix B: Coupling coefficients in CPW.....	173
References	175
Publications and Conferences	191

List of Tables

Tableau 1: Paramètres des quatre hétérostructures nominales dans la simulation	v
Table 1-1: Performances of THz direct detectors.....	10
Table 1-2: Performances of THz free space and dielectric waveguide (1 N _p = 8.686 dB)....	14
Table 1-3: Performances of THz planar waveguide.....	16
Table 2-1: Spontaneous and piezoelectric parameters of III-Nitride wurtzite binary materials	26
Table 2-2: Simulation parameters for the four nominal heterostructures	50
Table 2-3: Simulated range of N _s , d and W/L based on the four nominal structures	59
Table 2-4: Calculated concentration at 300 K by a self consistent 1D Poisson- Schrödinger solver.....	73
Table 2-5: Electron sheet concentration N ₁ in the screened region with applied voltage V _G (V) for AlGaAs/GaAs structure, where N ₂ = 1.65 × 10 ¹⁶ m ⁻²	75
Table 3-1: Dielectric and conductor parameters for the losses calculation	87
Table 3-2: The cutoff frequencies of surface waves in the structure air/conductor backed dielectric (thickens h = 30 μm, ε _{BCB} = 2.42, ε _{InP} = 12.5)	99
Table 3-3: Resonant frequencies (GHz) in HFSS simulations and f _{0n} calculated by theoretical formula (thickness h = 30 μm, ε _{BCB} = 2.42) for the conductor backed CPW	110
Table 3-4: Phase velocities and attenuation properties of the four types of waveguides at 1 THz. Phase velocity in BCB is 1.93 × 10 ⁸ m/s.	139
Table 3-5: Dimensions of CPW and Microstrip.....	143
Table 3-6: Etching and passivation processes for deep holes in silicon by ICP	147
Table 3-7: Soft cure of BCB	148
Table 3-8: Hard cure of BCB	149
Table 3-9: Au etching by IBE.....	149

List of Figures

Figure 1: Réseau métallique sur hétéro-jonction AlGaN/GaN	iii
Figure 2: Comparaison entre la dispersion de plasmon 2D dans le GaN et les dispersions des PP ($W/L = 0,75$) sur une hétérostructure d'AlGaN/GaN avec 2DEG quasi-2D ($d_{2DEG} = 12 \text{ nm}$) et 2D. $N_s = 1,2 \times 10^{17} \text{ m}^{-2}$, $L = 2,2 \mu\text{m}$, et $d = 25 \text{ nm}$	iv
Figure 3: Spectres d'absorption de PP pour la structure AlGaN/GaN à 300 K modélisés avec Ansoft HFSS.....	vi
Figure 4: (a) Accordabilité en fréquence f_1 de la première résonance PP en fonction de la période du réseau L pour les quatre hétérostructures à 300 K et pour $W/L = 0,75$. (b) Spectres d'absorption pour la structure AlGaN/GaN à 300 K avec différents angles d'incidence modélisés avec Ansoft HFSS.....	vi
Figure 5: Spectre d'absorption pour les quatre hétérostructures étudiées avec $W/L = 0,75$ à (a) 300 K et (b) 77 K.....	vii
Figure 6: Influences de (a) la concentration homogène N_s , (b) l'épaisseur de la barrière d et (c) le rapport W/L sur des amplitudes (A_1, A_2, A_3) des résonances PP à 300 K.....	ix
Figure 7: Comparaison des spectres de transmission mesurés (Mes) et modélisés via la méthode CWM (Simu) à 300, 78 et 10 K pour la structure $\text{Al}_{0,25}\text{Ga}_{0,75}\text{N}/\text{GaN}$ ($W/L = 0,6$, $N_s = 8.10^{16} \text{ m}^{-2}$)	x
Figure 8: Spectres de transmission avec différents rapport W/L pour la structure $\text{Al}_{0,25}\text{Ga}_{0,75}\text{N}/\text{GaN}$ ($N_s = 8. 10^{16} \text{ m}^{-2}$) à 78 K, (a) mesure et (b) simulation avec $\mu_{2DEG} = 0,3 \text{ m}^2/\text{Vs}$ avec la méthode CWM	xi
Figure 9 : Spectre d'absorption de la structure AlGaAs/GaAs pour différentes concentrations d'électron N_1 à 300 K et $W/L = 0.75$ avec N_2 fixée à $1,65.10^{16} \text{ m}^{-2}$	xii
Figure 10: Configuration de CPW	xiii
Figure 11: Comparaisons pour la configuration, CPW (AB/BC) pour différents substrats BCB et InP: (a) dispersion avec $W = 6,6 \mu\text{m}$, (b) perte par rayonnement, (c) perte métallique ($\sigma_{Or} = 4,1.10^7 \text{ S/m}$), (d) perte diélectrique ($\tan\delta_{BCB}=0,007$ et $\sigma_{InP}=2,4 \text{ S/m}$), et (e) pertes totales.....	xv
Figure 12: Dimensions des guides d'onde à 100 Ω	xvii
Figure 13: Pertes dans les quatre types de guide d'onde. (a) perte par rayonnement, (b) perte métallique ($\sigma_{Or} = 5.10^6 \text{ S/m}$) et (c) pertes totales ($\sigma_{Or} = 5.10^6 \text{ S/m}$)	xviii
Figure 14: Constante d'atténuation α (dB/mm) mesurée (a) et simulée (b) de CPW avec différentes dimensions (S_1/W) : 36/6, 36/10, 36/3, 70/4,28 et 100/6 μm . Échantillon : Métal (500 nm)/BCB ($\sim 30 \mu\text{m}$)/substrat Si (300 μm), Modèle: $\sigma_{Or} = 4,1.10^7 \text{ S/m}$, $\tan\delta$	

(BCB) = 0,007, $\epsilon_{\text{BCB}} = 2,42$, 30 μm BCB sur substrat de Si semi-infini ($\epsilon_{\text{Si}} = 11,9$, $\sigma_{\text{Si}} = 10 \text{ S/m}$).....	xx
Figure 1-1: Schematic representation of a THz system.....	5
Figure 1-2: THz time domain spectroscopy (TDS) system using photoconductive (PC) antenna as a THz source and detector.....	6
Figure 1-3: Attenuation constant of THz radiation propagated in free space versus the frequency and the transmitted distance [Thomas2011].....	7
Figure 1-4: Emission power versus frequency [Tonouchi2007].....	8
Figure 1-5: Noise temperature of heterodyne THz detectors [Hübers2008].....	13
Figure 1-6: Standard planar waveguides.....	15
Figure 2-1: The three types of heterojunctions: type I (straddling gap), type II (staggered gap) and type III (broken gap).....	22
Figure 2-2: AlGaN/GaN heterojunctions (a) and the conduction band diagram (b).....	23
Figure 2-3: Polarization bound surface charge and 2DEG in pseudomorphic heterojunction with Ga-face wurtzite polarity	24
Figure 2-4: Conduction band profile and electron concentration for pseudomorphic heterojunctions $\text{Al}_{0.3} \text{Ga}_{0.7} \text{As}/\text{GaAs}$ with (solid line) and without (broken line) modulation doping. The donor concentration is $N_D = 2 \times 10^{19} \text{ cm}^{-3}$	26
Figure 2-5: Conduction band profile and electron concentration for pseudomorphic heterojunctions $\text{Al}_{0.25} \text{Ga}_{0.75} \text{N}/\text{GaN}$ without (a) and with modulation doping (b). The donor concentration is 10^{19} cm^{-3} . In each plot, the polarization effect is compared (solid line stands for the case with polarizations, broken line for the case without polarizations).....	27
Figure 2-6: Calculated temperature dependence of the mobility of electrons in a $\text{Al}_{0.15} \text{Ga}_{0.85} \text{N}/\text{GaN}$ modulation doped heterojunctions. The residual ionized impurity concentration in this calculation is $4 \times 10^{15} \text{ cm}^{-3}$ and the doping level 10^{18} cm^{-3} corresponds to a electron gas density of $1.59 \times 10^{12} \text{ cm}^{-2}$. [Hsu1997]	30
Figure 2-7: Spectrum analysis for a multi-layers system containing 2DEG layer.....	31
Figure 2-8: Dispersion of 2D plasmon buried in GaN and light line	32
Figure 2-9: Grating coupler on top of the heterojunction AlGaN/GaN.....	33
Figure 2-10: Periodic grating with finite thickness t.....	34
Figure 2-11: HFSS model for a heterostructure with periodic metallic grating	38

Figure 2-12: HFSS simulated distribution of electric field E_x and E_z in the vicinity of metal grating, $f = 1$ THz, $L = 1$ μm , $W/L = 0.75$, TM polarization and normal incidence ...	39
Figure 2-13: Screened and unscreened multi-layers structure with finite thickness 2DEG ...	40
Figure 2-14: Screened and unscreened multi-layers structure with zero thickness 2DEG	43
Figure 2-15: Comparisons of HFSS (FEM) and CWM calculated dispersions of (a) plasmon-polariton and (b) spectra ($L = 2.2$ μm , $k = 2.86 \cdot 10^6$ m^{-1} , TM and TE polarizations) for AlGaN/GaN heterostructure at 300K, $N_s = 1.2 \times 10^{17}$ m^{-2} , $W/L = 0.75$, and $d = 25$ nm.....	46
Figure 2-16: Dispersions of PP for screened ($W/L = 1$), unscreened ($W/L = 0$) and partially screened ($W/L = 0.75$) heterostructure AlGaN/GaN with 12nm thickness (quasi-2D) and zero thickness (2D) 2DEG layer. $N_s = 1.2 \times 10^{17}$ m^{-2} , $L = 2.2$ μm , and $d = 25$ nm. Dispersion of 2D plasmon in infinite GaN dielectric is plotted for reference (expression (2-14), $N_s = 1.2 \times 10^{17}$ m^{-2})	48
Figure 2-17: Separated different types of absorptions in the nominal heterostructure AlGaN/GaN at room temperature with $W/L = 0.75$ by HFSS	50
Figure 2-18: Tunability of the grating period L on the first resonant peak f_1 for the four heterostructures at 300 K and $W/L = 0.75$	51
Figure 2-19: Original absorption of the heterostructure AlGaN/GaN (3 μm) at room temperature with different incident wave angles by HFSS	53
Figure 2-20: Original absorption of the heterostructure AlGaN/GaN at room temperature with different metal thicknesses (a) and conductivities (b) by HFSS	54
Figure 2-21: Original absorption spectrum of the nominal AlGaN/GaN structure calculated by CWM at 300 K, where $L = 2.2$ μm , $W/L = 0.75$ and $N_s = 1.2 \times 10^{17}$ m^{-2} . (a) Conduction losses due to finite conductivity of grating ($\sigma_{\text{Au}} = 4.1 \times 10^7$ and 5×10^6 S/m) at different grating thicknesses. No 2DEG layer exists. The case with perfect grating is plotted for reference. (b) Absorptions at different 2DEG layer thicknesses. Grating parameters: $t = 200$ nm, $\sigma_{\text{Au}} = 4.1 \times 10^7$ S/m.....	54
Figure 2-22: PP absorption spectrum of the four nominal structures with $W/L = 0.75$ at (a) 300 K and (b) 77 K	55
Figure 2-23: Absorption spectrum of the four nominal structures without grating at (a) 300 K and (b) 77 K.....	56
Figure 2-24: Amplitude of electric field E_x of different scattered waves versus W/L (0.25-0.9) at the plane of 2DEG layer (a distance of 25 nm from the surface) in AlGaN/GaN structure. (a) $n = 1$, (b) $n = 2$, (c) $n = 3$ at 300 K, and (d) $n = 2$ at 77 K. They were calculated by CWM. $L = 2.2$ μm	57

Figure 2-25: PP absorption spectrum of the four structures. (a) 300 K, W/L = 0.6, (b) 77 K, W/L = 0.6, (c) 300 K, W/L = 0.9, and (d) 77 K, W/L = 0.9.....	58
Figure 2-26: Influences of carrier surface concentration N_s on PP absorption spectrum of the four nominal structures at 300 K with W/L = 0.75. (a) resonant frequency and (b) absorption amplitude.....	59
Figure 2-27: Influences of barrier thickness d on PP absorption spectrum of the four nominal structures at 300 K with W/L = 0.75. (a) resonant frequency and (b) absorption amplitude.....	60
Figure 2-28: (a) Original absorption with 2DEG and grating, (b) Absorption without grating, and (c) PP absorption (A_1) of the four nominal structures versus barrier thickness d (1-100 nm) at the first resonant frequency (f_1) at 300 K with W/L = 0.75. A_1 for AlGaAs/GaAs at $N_s = 5.10^{16} \text{ m}^{-2}$ is superimposed in (c) for comparison.....	61
Figure 2-29: Influences of filling factor W/L (0.25-0.9) on PP absorption spectrum of the four nominal structures at 300 K. (a) resonant frequency and (b) absorption amplitude	62
Figure 2-30: Electric field E_x distribution in the vicinity of metal grating at 1 THz by HFSS. L = 1 μm and W/L = 0.25-0.95	63
Figure 2-31: Influences of filling factor W/L (0.25-1) on PP absorption spectrum of nominal structure AlGaAs/GaAs at 300 K	63
Figure 2-32: Microscopic image of the Au gratings on top of the sample AlGaN/GaN, L = 2.2 μm , W/L = 0.75.....	65
Figure 2-33: Schema of the standard FTIR setup	65
Figure 2-34: Experimental setup of the FTIR measurement with a bolometer detector.....	67
Figure 2-35: CWM simulated transmission spectrum for AlGaN (25 nm)/GaN (3 μm)/Sapphire (330 μm) at 300 K: (a) without grating, $N_s = 1.2 \times 10^{17} \text{ m}^{-2}$, (b) with grating, L = 2.2 μm , and W/L = 0.75. Dotted red curve: original spectrum, solid blue curve: averaged spectrum without Fabry-Pérot resonances	68
Figure 2-36: Measured transmission spectrum at different temperatures for $\text{Al}_{0.25}\text{Ga}_{0.75}\text{N}/\text{GaN}$ (W/L = 0.6, $N_s = 8.10^{16} \text{ m}^{-2}$).....	70
Figure 2-37: Transmission spectrum with different ratio W/L for $\text{Al}_{0.25}\text{Ga}_{0.75}\text{N}/\text{GaN}$ (78 K, $N_s = 8.10^{16} \text{ m}^{-2}$), (a) measurement and (b) simulation with $\mu_{2\text{DEG}} = 0.3 \text{ m}^2/\text{Vs}$	71
Figure 2-38: Non homogeneous distribution of electron concentration	73
Figure 2-39: Comparison of the two numerical methods: Absorption spectrum of the nominal AlGaN/GaN structure with different concentration N_2 at 300 K, where W/L	

$= 0.75$, $N_1 = 1.2 \times 10^{17} \text{ m}^{-2}$ (solid line: HFSS (FEM), $\Delta S=0.005$. broken line: Matlab (CMW), $n_{\max}=20$).....	74
Figure 2-40: Comparison of the absorption spectrum with the three types of 2DEG density distribution functions (step, linear and parabolic) for AlGaAs/GaAs at 300 K, where $N_1 = 1.28 \times 10^{16} \text{ m}^{-2}$, $N_2 = 1.65 \times 10^{16} \text{ m}^{-2}$, $t_1 = 20 \text{ nm}$, $L = 1 \mu\text{m}$ and $W = 0.75 \mu\text{m}$	74
Figure 2-41: Calculated wave function and energy bands in AlGaAs/GaAs for the two cases: $V_G = 0$ and $V_G = -0.8 \text{ V}$	75
Figure 2-42: Absorption spectrum of the AlGaAs/GaAs structure with different 2DEG concentration N_1 at 300 K, where the metal width (a) $W = 0.75 \mu\text{m}$ and (b) $W = 0.5 \mu\text{m}$. The step function model is used with the parameters $N_2 = 1.65 \times 10^{16} \text{ m}^{-2}$ and $L = 1 \mu\text{m}$	77
Figure 2-43: Schema of strongly modulated 2DEG in AlGaAs/GaAs structure: (a) with metallic grating, and (b) without metallic grating	78
Figure 2-44: Original absorption spectrum of the strongly modulated AlGaAs/GaAs structure with and without metallic grating at 300 K. $N_1 = 0$, $N_2 = 1.65 \times 10^{16} \text{ m}^{-2}$, $L = 1 \mu\text{m}$, $W = 0.75 \mu\text{m}$ and $d = 25 \text{ nm}$	78
Figure 2-45: (a) Frequency and (b) amplitude of original absorption spectrum of the strongly modulated AlGaAs/GaAs structure versus the filling factor ($W/L = 0.02-0.98$) with and without metallic grating at 300 K. $N_1 = 0$, $N_2 = 1.65 \times 10^{16} \text{ m}^{-2}$, $L = 1 \mu\text{m}$ and $d = 25 \text{ nm}$. Simulated by CWM.....	80
Figure 3-1: Schematic of a coplanar waveguide (CPW) on a dielectric substrate	88
Figure 3-2: Vector electric field distribution of the two principle modes in a conventional CPW structure, (a) Symmetric CPW mode and (b) Asymmetric slotline mode. The highlighted parts correspond to metals.....	89
Figure 3-3: Vector electric field distribution of the three propagating modes in a conductor backed CPW (CB-CPW) structure: (a) CPW mode, (b) Slotline mode, and (c) Microstrip mode. The highlighted parts correspond to metals.....	90
Figure 3-4: Four types of CPW configurations in the numerical simulation (BC: Baked Conductor)	91
Figure 3-5: (a): HFSS 3D model of CPW with airbridges and backed conductor (Figure 3-4 (d)) and (b): Dimensions of the 3D airbridges (AB) in the simulation	92
Figure 3-6: Influences of airbridges (AB) on the effective permittivity of the mode CPW and slotline for CPW on semi-infinite BCB	93
Figure 3-7: Influences of airbridges (AB) on the total attenuation of CPW mode and Slotline (SL) mode for CPW on semi-infinite BCB: (a) $W = 1.6 \mu\text{m}$, (b) $W = 6.6 \mu\text{m}$ and (c) $W = 12 \mu\text{m}$	94

Figure 3-8: Influences of airbridges (AB) on the effective permittivity of the mode CPW, slotline and microstrip for CPW on 30 μm BCB with backed conductor at different W	95
Figure 3-9: Influences of airbridges (AB) on the total attenuation of mode CPW, Slotline (SL) and Microstrip (MS) for CPW on 30 μm BCB with backed conductor: (a) W = 1.6 μm , (b) W = 6.6 μm and (c) W = 12 μm	96
Figure 3-10: Comparison of dispersion curves for conventional CPW on semi-infinite substrate BCB and InP with airbridges ($S_1 = 10 \mu\text{m}$, $S_2 = 24 \mu\text{m}$, W = 6.6 μm)	97
Figure 3-11: Phase (solid) and group (broken) velocities of CPW mode in conventional CPW on BCB substrate with ABs	98
Figure 3-12: Dispersion curves of the three supported modes for conductor backed CPW on 30 μm BCB substrate with airbridges ($S_1 = 10 \mu\text{m}$, $S_2 = 24 \mu\text{m}$, W = 12 μm).....	99
Figure 3-13: Phase (solid) and group (broken) velocities of CPW mode in conductor backed CPW on BCB substrate with (b) airbridges	100
Figure 3-14: Effective dielectric constant of CPW mode on the substrate BCB with airbridges ($S_1 = 10 \mu\text{m}$, $S_2 = 24 \mu\text{m}$).....	100
Figure 3-15: Comparison of radiation losses for the CPW configuration AB/BC on BCB and InP	103
Figure 3-16: Comparison of conduction losses for the CPW configuration AB/BC on BCB and InP ($\sigma_{\text{Au}} = 4.1 \times 10^7 \text{ S/m}$)	105
Figure 3-17: Comparison of dielectric losses for the CPW configuration AB/BC on BCB and InP	106
Figure 3-18: HFSS calculated dielectric losses for the mode CPW in configuration AB/BC on BCB with a constant and a frequency-dependant loss tangent $\tan\delta$ (W = 12 μm)	107
Figure 3-19: Comparison of total losses for the mode CPW in configuration AB/BC on BCB and InP	107
Figure 3-20: Influences of backed conductor (BC) on the radiation loss of the CPW mode for CPW on 30 μm BCB: (a) W = 1.6 μm , (b) W = 6.6 μm and (c) W = 12 μm	109
Figure 3-21: Electric field distribution along BC CPW propagation direction at the center plane in dielectric BCB and at the profile plane (thickness h = 30 μm , gap width W = 12 μm): (a) f = 550 GHz, (b) f = 600 GHz (f_{06}) and (c) f = 790 GHz (f_{08})	112
Figure 3-22: Radiation loss (dB) of the CPW mode versus the line length L (0.2 - 1 mm) for conductor backed CPW on 30 μm BCB.....	112

Figure 3-23: Influences of backed conductor (BC) on the total losses of the mode CPW for CPW on 30 μm BCB. (a) Conduction loss ($\sigma_{\text{Au}} = 5.10^6 \text{ S/m}$), (b) Dielectric loss, and (c) Total losses ($\sigma_{\text{Au}} = 5.10^6 \text{ S/m}$)	113
Figure 3-24: Microstrip line on a dielectric substrate of thickness H	116
Figure 3-25: Electromagnetic vector field distribution in a microstrip line. Left: Electric field, Right: Magnetic field. The highlighted part represents metals	116
Figure 3-26: (a) Phase constant, (b) effective dielectric constant, and (c) phase and group velocities of microstrip line on 30 μm BCB, W is the signal trace width	118
Figure 3-27: HFSS calculated losses of microstrip line on 30 μm BCB, (a) Radiation loss, (b) Dielectric loss, (c) Conduction loss and (d) Total losses.....	119
Figure 3-28: Schematic of the stripline surrounded by homogenous dielectric (left), and two layered dielectric with equal thickness (right).....	122
Figure 3-29: Electric vector field distributions of a stripline in homogeneous BCB. (a) Symmetric stripline mode, and (b) Asymmetric parallel plate mode.....	123
Figure 3-30: Phase constant (a) and effective dielectric constant (b) of stripline in homogeneous BCB, W is the central strip width	124
Figure 3-31: CST calculated losses of stripline in homogeneous 30 μm BCB, (a) Radiation loss, (b) Dielectric loss, (c) Conduction loss ($\sigma_{\text{Au}} = 5.10^6 \text{ S/m}$) and (d) Total losses ($\sigma_{\text{Au}} = 5.10^6 \text{ S/m}$)	124
Figure 3-32: Dispersion (a) and radiation loss (b) of stripline ($W = 30 \mu\text{m}$) in homogeneous 30 μm BCB, GaAs and Ge	126
Figure 3-33: Dispersion (a) and radiation loss (b) of stripline ($W = 30 \mu\text{m}$) in non homogeneous 30 μm dielectric (15 μm air and 15 μm BCB)	127
Figure 3-34: Schematic of a conventional slotline on a semi-infinite dielectric substrate (left), and a conductor backed slotline on a finite substrate (right).....	128
Figure 3-35: Electromagnetic vector field distribution of the dominant slotline mode in a conventional slotline. (a): Electric field and (b): Magnetic field	129
Figure 3-36: Phase constant (a), effective permittivity (b), phase and group velocities (c) of a slotline on semi-infinite BCB at different slot width W (5-30 μm)	130
Figure 3-37: CST calculated losses of slotline on semi-infinite BCB, (a) Radiation loss, (b) Dielectric loss, (c) Conduction loss ($\sigma_{\text{Au}} = 5.10^6 \text{ S/m}$) and (d) Total losses ($\sigma_{\text{Au}} = 5.10^6 \text{ S/m}$)	131
Figure 3-38: Electromagnetic vector field distribution of the parasitic Microstrip mode in a conductor backed slotline. (a): Electric field and (b): Magnetic field	133

Figure 3-39: Phase constant (a), and effective permittivity (b) of slotline mode and microstrip mode in conductor backed (BC) slotline on 30 μm BCB. Cases of conventional slotline (BC) are also shown for comparisons in (b).....	133
Figure 3-40: CST calculated losses of conductor backed (BC) slotline on 30 μm BCB, (a) Radiation loss and (b) Total losses. Cases of conventional slotline (BC) are also shown for comparisons.....	134
Figure 3-41: Dimensions of different 100 Ω waveguides for comparisons	136
Figure 3-42: Phase constant (a), effective permittivity (b), phase (c) and group (d) velocities of the fundamental mode in the four types of waveguides. Phase constant of TEM wave in BCB is also plotted for reference	137
Figure 3-43: Losses of the four types of waveguides: (a) Radiation loss, (b) Dielectric loss, (c) Conduction loss ($\sigma_{\text{Au}} = 5.10^6 \text{ S/m}$), and (d) Total losses ($\sigma_{\text{Au}} = 5.10^6 \text{ S/m}$)	138
Figure 3-44: (a) Total losses of CPW (BC) at 100 Ω with different combinations of S_1 and W, (b) Conduction loss of stripline at 100 Ω with different combinations of W and H ..	140
Figure 3-45: (a) Deposition of BCB (thickness h) on top of the slotline. (b) and (c) are the phase velocity and radiation loss of slotline at 100 Ω with different combinations of W and h. (d) is the total losses of microstrip at 100 Ω with different combinations of W and H	141
Figure 3-46: Design transitions for (a) CPW-CPW, and (b) CPW-Microstrip. Line dimensions are indicated	143
Figure 3-47: Electric field distribution along the propagation direction (white arrow) for 1 mm length of CPW ($S_1 = 70 \mu\text{m}$) with transitions at two ends.....	144
Figure 3-48: (a) Reflection (S_{11}) and transmission (S_{21}) of a 1 mm CPW with two transitions at both ends, and (b) Insertion losses in different sections of a transition (Figure 3-46 (a)).....	144
Figure 3-49: Electric field distribution along the propagation direction (white arrow) for 1 mm length of Microstrip line ($W = 20 \mu\text{m}$) with transitions at two ends	145
Figure 3-50: (a) Reflection (S_{11}) and transmission (S_{21}) of a 1 mm Microstrip line with two transitions at both edges, and (b) Insertion losses in different sections of a transition (Figure 3-46 (b)).....	145
Figure 3-51: Arrangement of waveguide motif centered on a 2 inch silicon wafer.....	146
Figure 3-52: Flow chart for realization of waveguide on thick BCB with an underlying conductor layer on silicon wafer. Procedure details are described in the text	147
Figure 3-53: Scanning electron microscopy (SEM) image of thick BCB (60-70 μm) deposited on Si substrate.....	148

Figure 3-54: Optical microscopy images of wafer after the removal of photo resist: (a) Waveguides on thin BCB without underlying Au layer, (b) waveguides on thick BCB with underlying Au layer. The enlarged part corresponds to the designed waveguides	150
Figure 3-55: Short circuited CPW ($S_1 = 36 \mu\text{m}$, $W = 3 \mu\text{m}$) for de-embedding (length of the short circuited part = $35 \mu\text{m}$) and the equivalent electrical circuit model of B31 (left length = $50 \mu\text{m}$, right length = $250 \mu\text{m}$).....	152
Figure 3-56: Electrical model and symbol of the access region for CPW structure.....	152
Figure 3-57: 1 mm CPW line ($S_1 = 36 \mu\text{m}$, $W = 3 \mu\text{m}$, $L = 1000 \mu\text{m}$) with two transitions and its equivalent circuit model.....	153
Figure 3-58: Fitting results of the reflection coefficients for the short circuited CPW (B31, B32, and B33). (a) Reflection coefficient in smith chart, phase of $50 \mu\text{m}$ (b), $150 \mu\text{m}$ (c) and $250 \mu\text{m}$ (d) short circuited CPW. The thick smooth curves represent the modeling (modeling and experiment are displayed in the same color). B31-L250 stands for the $250 \mu\text{m}$ short circuited part in B31. The rest may be deduced by analogy.....	154
Figure 3-59: Fitting results of the transmission and reflection coefficients of CPW line ($S_1 = 36 \mu\text{m}$, $W = 3 \mu\text{m}$) at different lengths. (a) $L = 500 \mu\text{m}$, (b) $L = 1 \text{ mm}$ and (c) $L = 2 \text{ mm}$. The thick smooth curves represent the modeling (modeling and experiment are displayed in the same color)	155
Figure 3-60: Circuit model for extracting the S parameters of CPW line ($S_1 = 36 \mu\text{m}$, $W = 3 \mu\text{m}$) based on measurement results and fitted transition models.....	155
Figure 3-61: De-embedded S parameters of CPW ($S_1 = 36 \mu\text{m}$, $W = 3 \mu\text{m}$) at different lengths. (a) $L = 500 \mu\text{m}$, (b) $L = 1 \text{ mm}$ and (c) $L = 2 \text{ mm}$	156
Figure 3-62: (a) Measured and (b) modeled attenuation constant α (dB/mm) of CPW without backed conductor at different dimensions (S_1/W) : $36/6$, $36/10$, $36/3$, $70/4.28$ and $100/6 \mu\text{m}$. Sample: Metal (500 nm)/BCB ($\sim 30 \mu\text{m}$)/Si substrate (300 μm), Model: $\sigma_{\text{Au}} = 4.1 \cdot 10^7 \text{ S/m}$, $\tan\delta$ (BCB) = 0.007, $\epsilon_{\text{BCB}} = 2.42$, $30 \mu\text{m}$ BCB on semi-infinite Si ($\epsilon_{\text{Si}} = 11.9$, $\sigma_{\text{Si}} = 10 \text{ S/m}$). (c) is the calculated radiation loss. (d) is the simulated attenuation with $\sigma_{\text{Au}} = 5 \cdot 10^6 \text{ S/m}$	157
Figure 3-63: Optical microscopy images of a fabricated CPW ($S_1 = 70 \mu\text{m}$, $W = 4.28 \mu\text{m}$, $L = 500 \mu\text{m}$).....	158
Figure 3-64: Measured (a/c) and modeled (b/d) attenuation constant α (dB) of 1/2 mm CPW with backed conductor at different dimensions (S_1/W) : $36/6$, $36/10$, $36/3$, $70/4.28$ and $100/6 \mu\text{m}$. Sample: Metal (500 nm)/BCB ($\sim 60 \mu\text{m}$)/Metal (500 nm)/Si substrate (300 μm), Model: $\sigma_{\text{Au}} = 4.1 \cdot 10^7 \text{ S/m}$, $\tan\delta$ (BCB) = 0.007, $\epsilon_{\text{BCB}} = 2.42$, BCB thickness is assumed to be $60 \mu\text{m}$. (e) and (f) are the simulated attenuation for a 1 mm and 2 mm conductor backed CPW at $\sigma_{\text{Au}} = 5 \cdot 10^6 \text{ S/m}$, respectively	160

Figure 3-65: (a) Effective permittivity, (b) phase and group velocities of microstrip ($W = 30 \mu\text{m}$) with signal line buried in different thickness of BCB ([10-30] μm) by HFSS. 0 corresponds to conventional microstrip with signal line in air162

Acknowledgements

I would like to take this opportunity to express many sincere thanks to all the people who have offered me helps, advices, supports and suggestions during the three-year PhD work at IEF (Institut d'électronique Fondamentale).

First of all, I would like to thank my supervisor Professor Frédéric Aniel. Without his encouragement and guidance, this work will not be initiated and proceeded. I am very grateful for his patience, motivation, enthusiasm and in-depth understanding of physical knowledge. All of these make him a great advisor. At the same time, many thanks to my thesis co-advisor Ms. Anne-sophie Grimault-Jacquin, who taught me the basic technologies in the clean room and introduced me to the modeling method of planar waveguides by HFSS. Her hospitality gave me the feeling of being at home during my thesis. She has always been ready to listen to any problems on both scientific research and administrative procedures and try to help me out. Thanks to the help of Mr. Nicolas Zerounian in our group, who made the spectrum measurement of heterostructures by FTIR possible. His contributions in the de-embedding work of CPW structures in ADS were also appreciated. I am also grateful to Ms. Angelina Chavez for her accomplishments in the simulations of Slotline and stripline by HFSS during the six-month master internship. Her work made the modeling of planar waveguides in Chapter 3 complete. Many valuable discussions also came from both present and past PhD students in the group: Hamzeh Hani, Eric Tea and Eloy Ramirez Garcia.

Many engineers in the clean room IEF/MINERVE (CTU) have assisted me with great experiences and patience in the realization of waveguide samples. Thanks to Sylvain David for his suggestions on the etching of silicon by ICP and etching of BCB by RIE, to François Maillard for the assistances in the etching of gold by IBE, to David Bouville for cutting the sapphire substrate, to Jean-René Coudeville for his training and advices on photolithography, to Fabien Bayle for characterizing the samples by SEM, to Marie-Paule Plante for the observation of sample surface by profilometer, to José Palomo for his help on gold deposition by ion gun, and to Cédric Villebasse for informations on chemical etching by Hydrofluoric acid (HF). I am also indebted to Ms. Marie-Antoinette Poisson (Alcatel/Thales III-V lab) for offering nitride based heterostructures and Ms. Isabelle Sagnes (LPN) for realizing micrometer gold grating on heterostructure by e-beam lithography.

Finally, I must thank my parents (Cao Guodong and Yan Kailin) and brothers (Cao Liang and Cao Wei) for their supports and encouragement throughout the period of my education. And I would also like to acknowledge the financial support of China Scholarship Council (CSC).

Abstract

In the Terahertz (THz) frequency gap between electronics and optics, the development of compact, tunable, less costly and room temperature operating sources, detectors, amplifiers and passive devices is growing. Electronic devices based on two dimensional (2D) plasmons in heterostructures open up the possibility of tunable emission and detection of THz radiation. For short distance THz transmission, the increased radiation loss as well as other types of loss (dielectric and ohmic loss) may handicap the applications of conventional planar waveguides well studied in the microwave band. Reevaluation of their propagation properties and comprehension of the physical nature of each kind of loss are necessary.

This work is divided into two main sections. The first part deals with the optimization of THz resonant detection by quasi 2D plasmons-polaritons (PP) in the quantum wells (QW) among four heterostructures: III-V (AlGaN/GaN, InAlN/GaN, AlGaAs/GaAs) and IV-IV (SiGe/Si/SiGe). With the aid of metallic grating coupler, both ANSOFT HFSS and an indigenously developed program are used to investigate quantitatively the influences of structural parameters (grating period, metal strip width and thickness of barrier layer) and natural properties of 2D plasmons (electron concentration and mobility) on the PP resonances (frequency and amplitude) up to 5 THz. Transmission spectra of sample AlGaN/GaN have been measured by Fourier Transform Infrared Spectroscopy (FTIR) in 0.6-1.8 THz for various metal filling factor and at different temperatures to compare with the simulated results. At last, two types of modulated 2D electron gas in AlGaAs/GaAs are analyzed. One is the natural electron variation below and between metal fingers due to the difference between the barrier height at the interface metal/semiconductor and Fermi level pinning at the interface air/semiconductor. The other type is the forced modulated 2DEG by biasing voltage on metal fingers. These two parametric studies allow us to analyze and tune the frequency and amplitude of the THz detection.

The second part separately studies the dispersions and attenuations of four waveguides (Coplanar waveguide (CPW), Microstrip, Stripline and Slotline) with the variation of geometric dimensions and properties of dielectric and metal by ANSOFT HFSS and CST MWS. Their performances are compared until 1 THz based on the same characteristic impedance. The advantages and the limitations of each waveguide are outlined and an optimal THz transmission line is proposed. Furthermore, preliminary measured attenuation of CPW in the frequency range 340-500 GHz are demonstrated and compared with numerical results. The design of transitions for adapting experimental probes by HFSS and the de-embedding method for extracting scattering and attenuation parameters of CPW by Agilent Advanced Design System (ADS) are also presented.

General Introduction

The electronic and optical devices like sources (photoconductive switch, diodes, quantum cascade lasers) and detectors (transistors) need to be improved in the terahertz (THz) range due to the lack of output power and the lack of understanding on some physical processes in this frequency domain. Currently, the increasing potential applications in physical, chemical, astronomical and biological disciplines have driven the advancement of THz technology, notably by integrating emitters, detectors, amplifiers based on semiconductor heterostructures, and passive elements (transmission lines and antennas). The objective of these researches is to realize THz components which are cheap, compact, tunable and easily integrated.

THz radiation lies between microwave and far infrared frequencies in the electromagnetic spectrum. It is broadly referred to the sub-millimeter wave which fills the wavelength range 1-0.1 mm (0.3-3 THz). The border between THz and far infrared is still blurry.

More efforts are still needed from the research side to improve the emission power and detection efficiency at room temperature, as well as to reduce the attenuation of THz signal propagation. This work aims to optimize THz detection and transmission based on compact semiconductor materials and passive devices.

The objective of this thesis contains two distinct parts: (1) to develop original compact plasmonic devices as the THz detectors and (2) to study the transmission performances of some planar waveguides in the THz frequency range. Numerical modeling for the optimization of THz detection device is conducted with both a commercial code (HFSS) and an indigenously developed solver. Moreover, parametric simulations are scheduled to evaluate the losses (dielectric, conduction and radiation) and dispersion in the THz transmission line. The two both studies contain a technological part. For THz detection, samples provided by III/V lab have been processed in the clean room of Laboratoire de Photonique et de Nanostructures (LPN). For the passive transmission devices, the fabrication has been performed in totality in the clean room MINERVE/CTU at Institut d'Electronique Fondamentale (IEF). The experiments on THz detection were realized at IEF whereas waveguides were measured at Fraunhofer Institute for Applied Solid State Physics (Fraunhofer IAF) in Germany.

The content of the manuscript is organized as follows.

Chapter 1 introduces the state-of-the-art THz sources, detectors and wave guiding structures. THz applications are reviewed. Then the performances of existing THz detectors and waveguides are summarized and compared.

In Chapter 2, we present an analysis of resonant THz detection of the 2D plasmon in four types of heterostructures (AlGaN/GaN, InAlN/GaN, AlGaAs/GaAs, and SiGe/Si/SiGe) by periodic metal grating coupler with both ANSOFT HFSS and an indigenous developed code in between 0 and 5 THz. Spectroscopy measurements have been made on the basis of the best simulated material structure analyzed for THz detection. A good agreement between the modeled and experimental transmission results has been achieved. Inhomogeneous electron distribution modulated both by the existence of metal grating and the biasing voltage on the metal is also considered in the numerical work for AlGaAs/GaAs structure in the last section.

Chapter 3 deals with the dispersions and losses of four types of planar waveguide (Coplanar waveguide (CPW), microstrip line, Slotline and stripline) with commercial code ANSOFT HFSS and CST MWS in THz frequency range (20 GHz-1.0 THz). Optimal structure is proposed by comparing the dispersions and losses of the studied four waveguides on the same substrate based on the same characteristic impedance. Some preliminary measurement data of CPW will be compared with the simulated results.

Finally, Chapter 4 gives the general conclusions and perspectives.

Chapter 1 Introduction

The sub-millimeter wavelength range (1 mm-100 μm) or the terahertz frequency band (0.3 THz-3 THz) is sandwiched between microwave and far infrared wave in the electromagnetic spectrum. One terahertz corresponds to a wavelength of 300 μm (wave number of 33 cm^{-1} , or photon energy of 4.1 meV). In this "THz gap", the demand of sources, detectors and amplifiers, which are tunable, coherent, compact, less costly and operational at room temperature, is growing. A typical THz system is composed by the sources, the detectors and the waveguides, as shown in Figure 1-1.

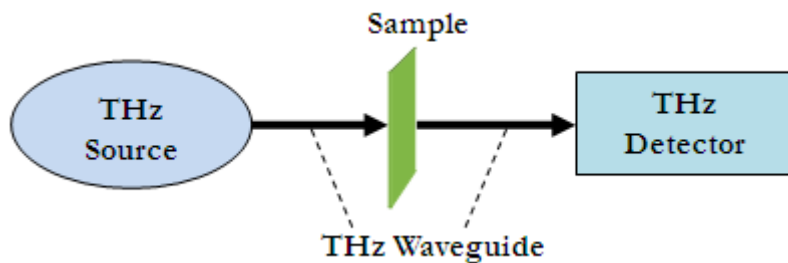


Figure 1-1: Schematic representation of a THz system

1.1 THz applications

Recently, with the fast development of semiconductor fabrication technology, the THz frequency receives considerable attentions in many applications like spectroscopy, imaging and ultrahigh speed wireless communications.

THz radiation have many unique features in the electromagnetic spectrum [Kemp2006]: short wavelength to satisfy the spatial resolution for imaging purposes, penetration into those non-polar substances to show the concealed objects, non-ionizing radiation to ensure the safety of people with moderate intensities... Here, some representative application areas among medical, material, physical, chemical, biological, spatial and communication domains are briefly introduced. The terahertz technology has been reviewed in detail from other contributions [Siegel2002, Dragoman2004, Chamberlain2004].

1.1.1 THz time domain spectroscopy (THz TDS)

The basic THz spectroscopy optical setup is schematically represented in Figure 1-2, with photoconductive (PC) antenna as the emitter and detector. The femtosecond duration pulses emitted from a laser is separated by a beamsplitter into two beams going to the THz source and detector with equivalent power. THz sub-picosecond pulse is produced by the dipole antenna at the emission side excited by one half of the optical pulse, then is focused and directed to the sample under test. The transmitted THz pulse shape will be changed after passing through the sample. At the detection side, THz pulse is mapped out by changing the delay time between the THz radiation and the other half of the optical pulse. Similarly, the detected THz signal without sample in the same configuration is also recorded as the reference pulse. The frequency spectrum of the transmitted and reference pulse is obtained by Fourier transformation. The material properties (refractive index $n'(\omega)$ and the absorption coefficient $k(\omega)$) can be calculated by analyzing the spectroscopic information of the transmittance signal.

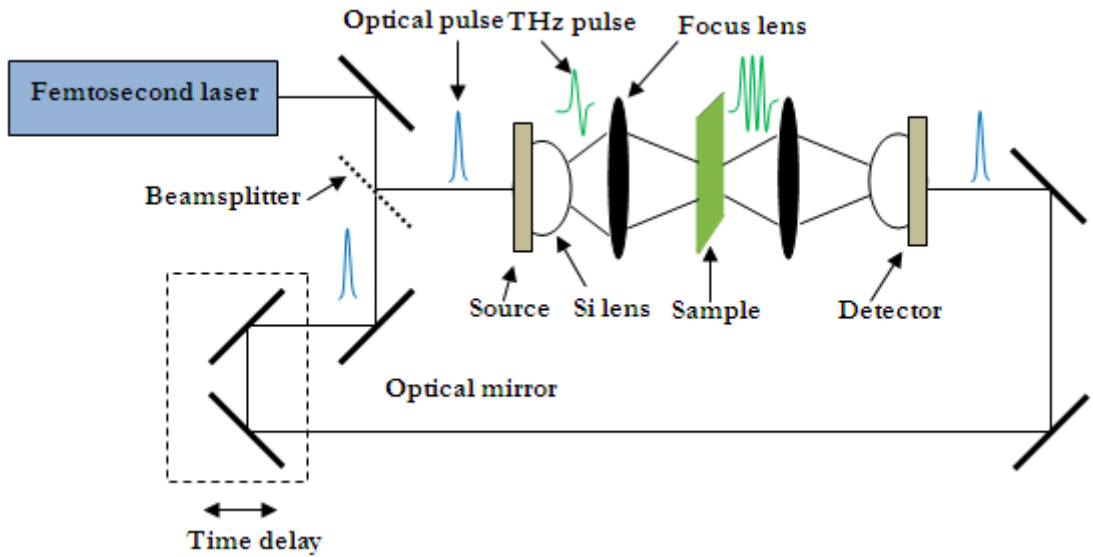


Figure 1-2: THz time domain spectroscopy (TDS) system using photoconductive (PC) antenna as a THz source and detector

$$\frac{E_{sample}(\omega)}{E_{reference}(\omega)} = \left| \sqrt{T(\omega)} \right| e^{-j(\phi(\omega) - \omega d/c)} = \frac{4n(\omega)}{(1+n(\omega))^2} \frac{e^{-j(n(\omega)-1)\omega d/c}}{1 - \frac{(1-n(\omega))^2}{(1+n(\omega))^2} e^{-j2n(\omega)\omega d/c}} \quad (1-1)$$

Where $n(\omega) = n'(\omega) - jk(\omega)$ is the complex material refractive index, d is the sample thickness, $T(\omega)$ and $\phi(\omega)$ are the measured amplitude and phase shift of the relative transmission power signal in the frequency domain. In some cases, the reflection THz pulse from the sample can be detected and analyzed to obtain material permittivity. Besides the PC antenna, nonlinear electrooptic (EO) crystals are also frequently used as the emission and detection elements [Zhao2002].

1.1.2 THz Imaging (T-ray)

Most insulators are transparent to THz radiation, making its convenient application in checking baggage at airports, scanning letters for drugs and screening persons for weapons. To accomplish the process of imaging, CCD (Charge Coupled Device) cameras are needed to collect optical intensity and map the sample object with lens on one or an array of photo-detectors when the sample is scanned in two dimensions vertical to the THz beam. Based on PC antennas technologies, an imaging system at NiCT, Japan has realized a THz imaging of a structure of 3×2 apertures with a spatial resolution in the sub-millimeter range, while another group at the Rensselaer Polytechnic Institute has shown the possibility of real time THz imaging using two dimensional EO sampling technologies [Wu1996]. The minimum spatial resolution of these pulses THz imaging systems are mainly limited by the diffraction of THz radiation. Recent development of field effect transistor (FET) based on the nonlinearity of two dimensional plasmons in the channel also demonstrated the experimental transmission imaging of metals with a GaAs nanometric transistor responded to continuous THz radiations at 1.63 THz and 2.54 THz at room temperature, where the resolution is achieved at $300 \mu\text{m}$ [Nadar2010].

1.1.3 Telecommunication

The frequency band [275-3000] GHz has not been allocated for specific use, and presents great interests for future wireless telecommunications with ultrahigh data rate of 10 Gbit/s or even higher, which is higher needed in high resolution television signal transition and the future personal communication. The main problem is associated with the strong interaction of THz radiation with the polar molecules H_2O in the atmosphere. Figure 1-3 shows the attenuation constant of THz transmission in free space in function of frequency and propagation distances. Some transmission windows which have local minimum attenuation are located around 300 GHz, 350 GHz, 410 GHz, 670 GHz and 850 GHz. At 300 GHz, for an indoor distance of 10 m, the overall attenuation reaches 102 dB, while it is 100 dB/km for outdoor environment due to scattering on hydrometeors. In practical application, the high gain antennas and amplifiers are indispensable to enhance the detected signal between the transmitter and receiver. A wireless link has achieved error free transmission of over 10 Gbit/s data signals in a distance about 1 km at 200 GHz for broadcast live TV programs during Beijing Olympic Games [Hirata 2009]. Towards 100 Gbit/s wireless communications, larger bandwidth is appreciated. The development in the 300 to 500 GHz frequency range is now possible thank to the increasing cutoff frequency of semiconductor devices and circuits.

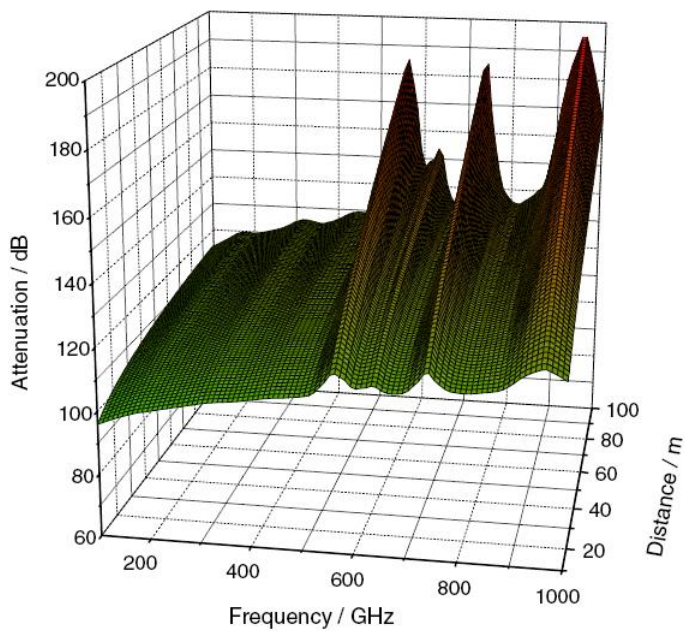


Figure 1-3: Attenuation constant of THz radiation propagated in free space versus the frequency and the transmitted distance [Thomas2011]

1.2 Terahertz sources

Various kinds of sources exist, and here you will find an exhaustive list. At the aspect of optics, different lasers, such as the p-type germanium (Ge) lasers [Hübers2005] and the THz quantum cascade lasers (QCLs) [Williams2007] begin to operate as THz sources. CW QCL operates at cryogenic temperature. Below 1.5-2 THz, it does not seem realistic to develop CW QCL at room temperature.

From the side of electronics, both the two-terminal diodes and three-terminal transistors have been extensively researched. Among the diodes, IMPATT (Impact Ionization Avalanche Transit Time Diodes) [Mishra1997], TUNNETT (Tunneling Transit Time Diodes) [Nishizawa1979], Gunn diodes [Yilmazoglu2008] or RTDs (Resonant Tunneling Diodes) [Asada2008] are the typical examples. Although the room temperature operation is realized, their output frequency range needs to be further pushed into THz range. Figure 1-4 illustrates the emission power of different sources in function of the frequency. In these sources, the tunability of frequency is hard to achieve. Two dimensional (2D) plasmons oscillation near the surface of semiconductors seems to be a candidate for tunable solid state far infrared source, where the tunability is allowed by the variation of carrier concentration. Coupling component, like metallic grating is required to couple out the radiation. The emission power, coupling efficiency and radiation frequency left room to be improved.

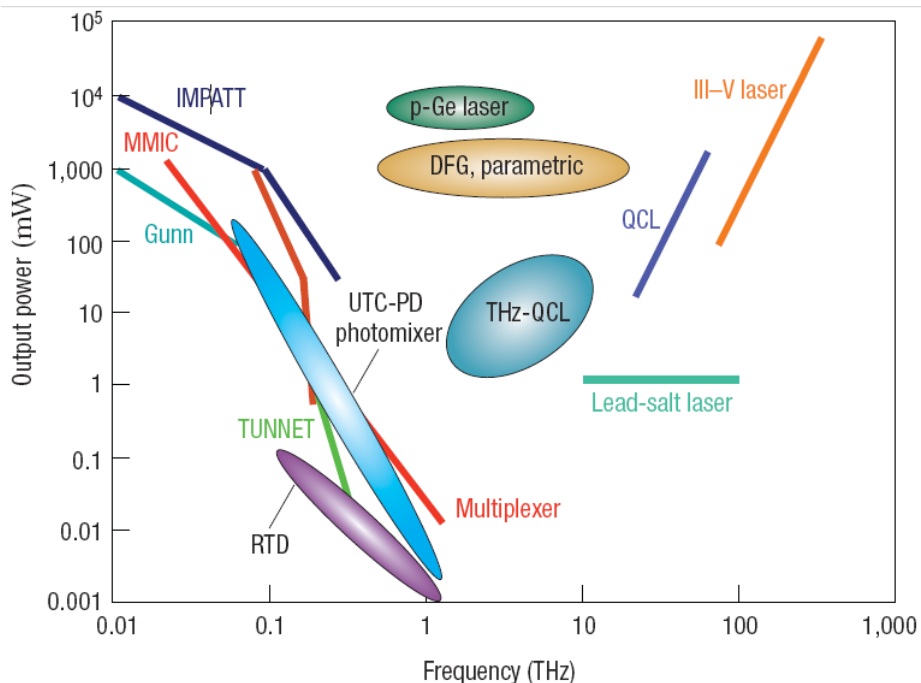


Figure 1-4: Emission power versus frequency [Tonouchi2007]

With slight modifications, the sources can be used in the detection mode. For example, in the THz time domain spectroscopy (THz-TDS) configuration, the photoconductive antennas are used both as the generation and detection components for THz pulse.

In the following paragraph, we mainly discuss on the detection and propagation of THz which are the two central themes of my thesis.

1.3 Terahertz detectors

The function of a detector is to convert incident THz radiation into measurable parameters. These physical parameters can be as temperature variation, resistance change, current flow or voltage drop. In coherent detection, both the THz amplitude and phase are recorded. One example is the determination of the complex permittivity of a material in the THz-TDS system. For the incoherent detection, only the amplitude information is recorded. Infrared detectors are

generally classified into two categories: thermal detectors and photodetectors [Rogalski2010]. Thermal detectors absorber the radiation energy by changing its temperature, while for photodetectors, the radiation is absorbed within the material by interaction with free electrons or electrons bounded to lattice (or impurity) atoms. The photodetectors has high signal to noise ratio and fast response time.

1.3.1 Detector figures of merit

To evaluate the performances of a detector, the most general and useful parameters are operation frequency and temperature, response time, responsivity and noise equivalent power (NEP).

1.3.1.1 Responsivity

The responsivity is the ratio of the RMS (root mean square) value between the output electrical signal and incident THz radiation power P. Its unit is V/W or A/W, depending on whether the output signal is voltage drop (V) or current flow (I). High responsivity contributes to large sensitivity.

$$R_{V/W} = \frac{V}{P}, \text{ or } R_{A/W} = \frac{I}{P} \quad (1-2)$$

1.3.1.2 Noise equivalent power (NEP)

The noise equivalent power (NEP) is the incident signal power which generates an electrical output equal to the detector noise output, saying the signal to noise ratio (SNR) is 1. When the reference bandwidth is assumed to be 1 Hz, the NEP has the unit W/Hz^{1/2}. In the expression (1-3), v_n and i_n are the noise voltage and current spectral density respectively.

$$NEP = \frac{v_n}{R_{V/W}}, \text{ or } = \frac{i_n}{R_{A/W}} \quad (1-3)$$

1.3.2 THz detection methods

One possible classification of THz detector is similar to microwave detectors: direct and heterodyne detections.

1.3.2.1 Direct detection

Table 1-1 lists the performances of THz direct detectors. Their functional mechanisms will be discussed respectively.

Table 1-1: Performances of THz direct detectors

Detector	f (THz)	Responsivity	Response(s)	NEP(W/Hz ^{1/2})	Ref.
Golay cell	0.02 - 20	10000 V/W	25.10 ⁻³	10 ⁻⁸ (300K)	Commercial (Microtech)
Pyroelectric (LiTaO ₃ crystal)	0.02 - 3	1000 V/W	10 ⁻³ -10 ⁻²	10 ⁻⁹ (300K)	Commercial (Microtech)
Silicon bolometer	0.15 - 20	-	10 ⁻³	10 ⁻¹³ (4.2K)	Commercial (IR Labs)
HEB	0.62	-	10 ⁻⁹	10 ⁻¹⁹ (0.36K)	[Karasik2011]
PC sampling (LT-GaAs)	0.375 (3dB bandwidth)	0.1 A/W	1.2.10 ⁻¹²	-	[Chen1991]
EO sampling (GaP and ZnTe)	3.6 and 37 (3dB bandwidth)	-	-	-	[Wu1997-1] [Wu1997-2]
AlGaN/GaN HFET (Gate length = 150 nm)	0.2 - 2.5	0.2 V/W at 0.2 THz	-	5.10 ⁻⁹ at 0.2 and 0.7 THz (300 K)	[Fatimy2006]
AlGaAs/GaAs DQW FET (Grating period = 4μm)	0.57 - 0.66	0.89 mV/W	7.10 ⁻⁷	6.10 ⁻⁶ (25 K)	[Peralta2002]
AlGaAs/GaAs FET (Gate length = 250 nm)	0.3	11 V/W	-	13.3.10 ⁻⁹ (300 K)	[Blin2012]
Si MOSFET (Length = 130 nm)	0.27 - 1.05	5000 V/W at 0.3 THz	-	10 ⁻¹² at 0.3 THz (300K)	[Schuster2011]
Schottky diode (Zero bias)	0.1 (0.9)	4000 (400) V/W	10 ⁻⁹	1.5.10 ⁻¹² at 0.15 THz and 20.10 ⁻¹² at 0.8 THz (300 K)	[Hesler2007]

I Thermal detectors

A Golay cell

Golay cell [Golay1947] is an opto-acoustic detector. When absorbing THz radiation, the gas is heated and the resulting pressure causes the deformation of a membrane. An optical reflectivity measurement detects the membrane deformation. If there are mechanical disturbs, the sensitivity and response will be degraded. A commercial Golay cell works below 20 THz and the response time and NEP values are tens of ms and 10⁻⁸ W/Hz^{1/2}, respectively. No cooling system is needed.

B Bolometer

Bolometer [Richards1994] operates on the principle that temperature change due to THz radiation absorption produces a variation of material resistance. When passing bias current through the detector, the output voltage will be monitored. To achieve high sensitivity, a material with small thermal capacity and large temperature coefficient (the resistance change factor per degree of temperature change) is needed, and cooled at liquid helium temperature. Several types exist: metal bolometers, thermostats and semiconductor bolometers. The commercial silicon bolometer has a response time in ms range and NEP value of 10⁻¹³ W/Hz^{1/2} in a wide frequency

band [0.15-20] THz. The high NEP value is achieved at the expense of liquid helium cooling at 4.2 K.

C Pyroelectric detector

When a pyroelectric crystal undergoes a temperature variation, surface charge appears due to the change of its spontaneous electrical polarization. Charge number change can produce current flow. This means that pyroelectric detector is sensitive to the variation of incident THz power. Large pyroelectric coefficient (the change in the spontaneous polarization vector with temperature) and low thermal conductivity are attractive crystal properties for the improvement of sensitivity. The common crystal materials are LiTaO₃ (Lithium tantalate), SBN (Strontium barium niobate) and DTGS (Deuterated triglycine sulfate) [Aggarwal2010]. It has lower responsivity than Golay cell but owns fast response (10^{-3} - 10^{-2} s) and small NEP value (10^{-9} W/Hz^{1/2}) at room temperature.

An advantage of thermal detectors is that they can respond to incident radiation in a broad spectrum range. However, they suffer from low response time, bulky volume or usually required cooling system, compared with the photon detectors.

II Photon detectors

A Photoconductor (PC) sampling

When an ultrafast optical pulse excites on a micron scale dipole antenna in a semiconductor, a rapid change of conductivity is produced. The current flow proportional to the amplitude of incident THz field can be recorded in function of the time. In the THz-TDS schema (Figure 1-2), PC sampling method is utilized to coherently detect the THz pulse. The antenna dimension design and carrier lifetime in the semiconductor affects the detection efficiency. Lifetime of 1 ps or less, which is short compared to $T = 1/f$ (f is incident THz wave frequency), is required. Commonly used semiconductor materials are LT-GaAs (low temperature grown gallium arsenide) [Zheng2003] and ion implanted SOS (silicon on sapphire) [Pfeifer1994]. The PC detector based on LT-GaAs was demonstrated to have a 1.2 ps response time with a 3dB bandwidth of 375 GHz [Chen1991].

B Electrooptic (EO) crystals sampling

When optical laser beam passes through a nonlinear crystal, a DC or low frequency polarization arises in the optical rectification process. A change of polarization appears from the incident THz electric field according to the linear electrooptic effect (Pockels' effect). THz electric field is measured linearly by the induced phase modulation of the femtosecond optical pulse [Wu1995]. High linear electrooptic coefficient of a crystal will enhance detection sensitivity. The reported nonlinear materials include LiNbO₃ (lithium niobate), GaAs, InP (indium phosphore), DAST (4-dimethylamino-N-methyl-4-stilbazolium tosylate) and metals [Dexheimer2008]. A 37 THz bandwidth was obtained using ZnTe [Wu1997-2].

C Nonlinear rectification

For tunable continuous THz wave detection, 2D plasmon located in semiconductor devices was investigated since the end of last century. Two dimensional (2D) plasmon in the silicon inversion

layer was observed more than thirty years ago [Allen1977]. The detection process by the plasmon waves origins from the rectification of THz current in the transistor channel induced by the incident THz field. This was initiated by the pioneering work of Dyakonov and Shur [Dyakonov1993]. After the theoretical demonstration of the non-linear properties of 2D plasmons in FET [Dyakonov1996-1], a lot of contributions have been devoted experimentally to the detection of THz radiation as well as emission [Knap2002-1, Popov2005, Muravjov2010]. A large concentration of electrons with high mobility is the main properties for heterojunctions based transistors, such as AlGaAs/GaAs, AlGaN/GaN, InAlN/GaN, SiGe/Si/SiGe, and GaInP/GaAs. The advantages of the plasma wave detector include: frequency tunability, fast temporal response, small size, easy to use in array and room temperature operation. A high value of $NEP = 5 \times 10^{-9} \text{ W/Hz}^{1/2}$ at 200 GHz and 700 GHz was reported at room temperature in a AlGaN/GaN HEMT [Fatimy2006].

However, the transistor based detection suffers from low coupling with THz wave. How to couple effectively the incident THz radiation with 2D plasmon is the key issue to increase the detection sensitivity. This will be studied in detail and discussed in Chapter 2.

Other detection mechanism under development includes quantum dot single electron transistor [Komiyama2000], which is capable of detecting single photon at very low temperature (100 mK).

1.3.2.2 Heterodyne detection

Schottky diode is used either in direct detection or as nonlinear element in heterodyne mixer in 4-300 K. It has strong nonlinear properties of current-voltage and capacity-voltage. The local oscillator signal with large and stable power is provided by a gas laser. The output signal, with the intermediate frequency proportional to the frequency difference between continuous wave THz radiation and local source signal, drops into the microwave range where it can be amplified and analyzed easily. Its amplitude is proportional to THz field. At THz frequency, planar Schottky diode is preferred for integration with other components on GaAs [Siegel1999], InP or semiconductor heterojunctions. The most important parameter of a heterodyne is the mixer noise temperature, which indicates the noise contributions from the mixer. Cryogenic temperature can improve the noise performance, or reducing the noise temperature. Schottky diode mixer is the most sensitive detector in THz range at room temperature because of the large local source power, but it has the disadvantages like: both local and incident beams should be coincident and polarized in the same direction, difficulty of utilizing in arrays.

Other heterodyne detectors receiving great attention in the astronomy community are SIS (superconductor-insulator-superconductor) tunneling junction mixer [Tucker1985] and HEB (hot electron bolometer) mixer [McGrath1995]. They are competitive at millimeter wavelength and require cryogenic cooling.

The noise equivalent temperature of the three types of detectors in double sideband operation (DSB) is shown in Figure 1-5 from 0.3-5 THz. Among them, SIS mixer is the best around 1 THz.

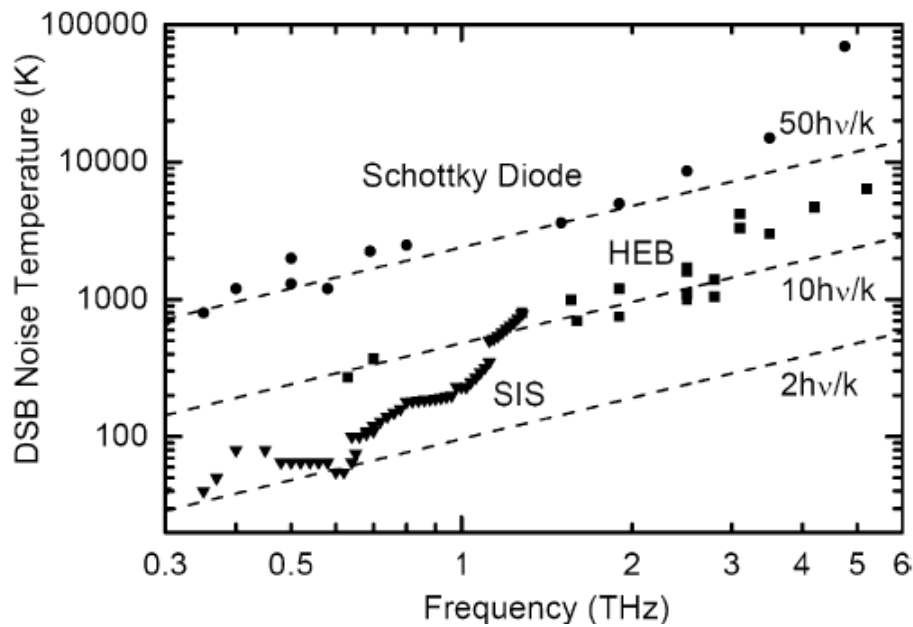


Figure 1-5: Noise temperature of heterodyne THz detectors [Hübers2008]

1.4 Terahertz waveguide

Concerning THz propagation, low loss and dispersion single mode waveguide structures and related emitting and receiving antennas are desirable for short distance transmission and also for the integration with detectors and sources based on semiconductor technology.

Among existing structures, THz waveguides can be generally divided into two classes. One confines THz radiation generated in free space or dielectric, the other is the on-chip waveguide in which THz field is confined near a surface, such as air/dielectric and metal/dielectric interfaces.

1.4.1 Free space and dielectric waveguide

The circular [McGowan1999] or rectangular [Gallot2000] metal waveguide filled with air is frequently used in the quasi-optical techniques to couple freely propagating THz pulses. The key issue is to strongly couple the linearly polarized incident THz focused beam with the dominant waveguide mode. This type of waveguide finds application in THz-TDS system for measuring absorption coefficient. Their performances of low attenuation surpass over the planar waveguides, such as microstrip and coplanar waveguides, but the large dispersion hinders their application in communications due to great phase delay. Dielectric waveguides fabricated with sapphire and high density polyethylene (HDPE) and polyethylene (PE) have achieved less than 1 Np/cm in THz range [Jamison2000, Mendis2000, Chen2006].

To further reduce the dispersion, parallel plate copper waveguide which supports single TEM mode is shown to own undistorted, low loss (below 0.1 Np/cm at 1 THz) propagation [Mendis2001]. Then, the transmission of THz pulse on stainless steel bare metal was demonstrated [Wang2004], although the efficient coupling between EM wave and single metal waveguide is difficult. This was improved by the two wire waveguide, which offers both low loss and good coupling to most photoconductive (PC) antennas [Pahlevaninezhad2010]. Table 1-2 lists typical performances of the non planar THz waveguide. Although they have attractive

attenuation and dispersion properties, the difficulties in fabrication and circuit integration will limit their applications. This can be overcome by the planar type waveguide.

Table 1-2: Performances of THz free space and dielectric waveguide (1 Np = 8.686 dB)

Waveguide	Dimensions	Materials	f (THz)	α (Np/cm)	Dispersion	References
Circular	Diameter = 240 μm Length = 24 mm	Stainless steel	0.8 - 3.5	< 1	1 - 20 ps	[McGowan1999]
Rectangular	250 $\mu\text{m} \times$ 125 μm Length = 25 mm	Brass	0.65 - 3.5	-	1 - 13 ps	[Gallot2000]
Parallel Plate	Gap = 108 μm Length = 24.4 mm	Copper	0.1 - 4	< 0.3	Almost zero	[Mendis2001]
Single Wire	Diameter = 0.9 mm	Stainless steel	0.25 - 0.75	< 0.03	Almost zero	[Wang2004]
Two Wire	Diameter = 0.2 - 1 mm Center distance = 0.2 - 3.5 mm	Gold	1	0.005 - 0.06	Almost zero	[Pahlevaninezhad 2010]
Dielectric waveguide (wire)	Diameter = 150, 250 and 325 μm Length = 7.3, 7.8 and 8.3 mm	Sapphire	< 2.5	< 6	0.6 - 13	[Jamison2000]
Dielectric waveguide (wire)	Diameter = 200 μm Length = 6, 13 and 17.5 cm	PE	0.31 - 0.35	< 0.01	-	[Chen2006]
Dielectric waveguide (strip)	150 $\mu\text{m} \times$ 2 cm Length = 20 mm	HDPE	0.1 - 3.5	< 1	1 - 40	[Mendis2000]

1.4.2 Planar on-chip waveguide

The printed transmission line is widely used because of many advantages, such as their compactness, easy and economical for fabrication, convenient for integration and connection in circuits. The characteristic parameters can be adjusted simply by the dimensions of metal width, the gap width between metals and the substrate thickness or permittivity. However, loss and dispersion prove to be the major obstacles.

Different types of waveguides applied in microwave community have been exhaustively studied both numerically and experimentally. Figure 1-6 shows the planar waveguides, including coplanar waveguide (CPW), microstrip, slotline, coplanar strip (CPS), Goubau line and stripline.

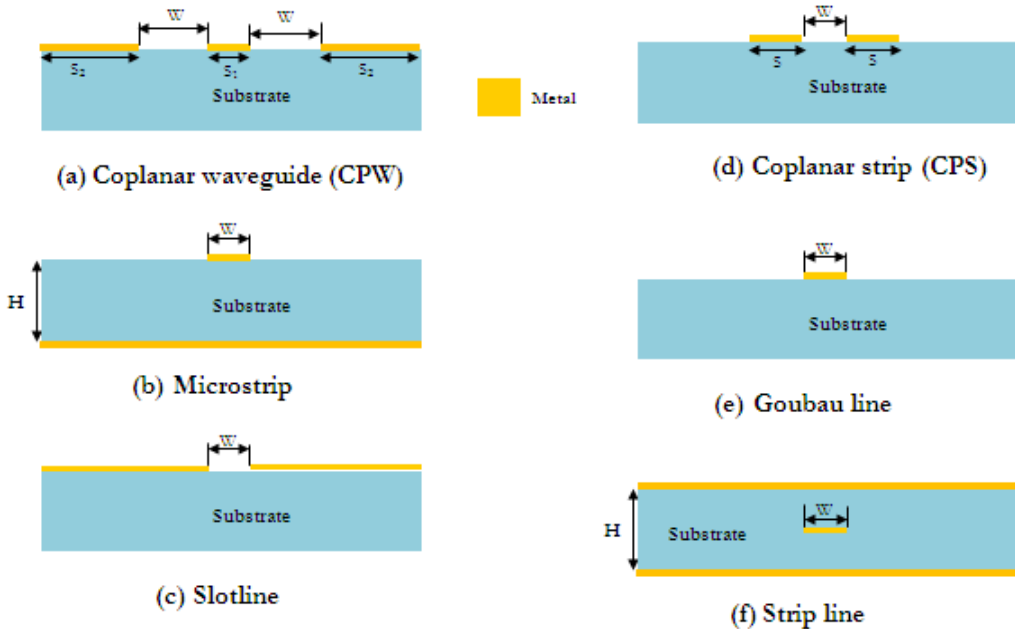


Figure 1-6: Standard planar waveguides

When the frequency is raised into THz region, the radiation loss will increase rapidly, which deteriorates the transmission performance [Gupta1996]. For instance in CPW and CPS, Grischkowsky [Grischkowsky1987] demonstrated experimentally that the radiation loss will dominates in the total losses when the frequency is over 200 GHz for line dimensions in several tens of micrometers. Rutledge [Rutledge1983] derived a cubic frequency dependency of attenuation loss under quasi static approximations. He explained the radiation loss of the transmission line mode as the electromagnetic shock wave into the substrate when its thickness is infinite or as the leakage into the surface waves in finite substrate, provided that the phase velocity of the transmission line mode is higher than that of the substrate wave. The attenuation amplitude depends critically on the discrepancy of phase velocities. Phatak [Phatak1990] and Frankel [Frankel1991] have modified the radiation loss of CPW and CPS using non quasi static effect (frequency dependent effective permittivity). This analytic formula was verified by the EO sampling measurement results until 1 THz on thick semiconductor substrate. While for other types of lines, the radiation loss is often neglected or cannot be predicted by present analytic theory. The present PhD work aimed to study numerically and systematically the radiation loss as well as other types of losses in dielectric and conductors by the variation of substrate permittivity, waveguide dimensions and configurations.

Table 1-3: Performances of THz planar waveguide

Waveguide	Dimension	Material	f (THz)	α (dB/mm)	Dispersion	References
Slotline	Gap = 270 μm , Conductor thickness = 300 nm, Metal width = 20 mm	Si wafer (with slit), Ti/Au	0.1 - 1	0.006 - 0.05	Almost zero	[Wächter2007]
Slotline (Simulation)	Gap = 20 μm Conductor thickness = 100 nm Metal width = 240 μm	GaAs substrate Au	1	20.7	-	[Pahlevaninezhad2011]
	Gap = 10 μm , Conductor thickness = 100 nm Metal width = 245 μm	Homogeneous GaAs Au		1.7	Zero	
	Gap = 10 μm , Conductor thickness = 100 nm Metal width = 245 μm	Periodic Si/SiO ₂ layered substrate Au		2.6	-	
CPW	Substrate thickness = 500 μm Metal thickness = 400 nm (50/350)	GaAs substrate Ti/Au	0 - 1	0 - 13	$\epsilon_{eff} = 7-7.7$	[Frankel1991]
	Gap = 15 μm Central metal = 20 μm Substrate thickness = 620 μm Metal thickness = 1.2 μm	GaAs substrate Au	0 - 0.22	0 - 2.25	-	[Lok2008]
	Gap = 10 μm Central metal = 10 μm Ground metal = 30 μm Substrate thickness = 8/270 μm Metal thickness = 2 μm	SiO ₂ /Si substrate	0 - 0.11	0 - 1.2	$\epsilon_{eff} = 3.7$ at 60 GHz	[Shi2009]
CPW (Simulation)	Gap = 5 μm Central metal = 16 μm BCB = 25 μm Metal thickness = 0.8 μm	BCB/low resistivity Si substrate Al	0 - 0.9	0 - 4	$\epsilon_{eff} = 2 - 1.75$	[Heiliger1997]

CPS	Substrate thickness = 430 μm Metal thickness = 400 nm	Sapphire substrate Al	0 - 1	0 - 18.2	$\epsilon_{eff} = 5.8 - 7.8$	[Frankel1991]
	Strip width = 20 μm Gap = 20 μm Membrane thickness = 700/300/400 nm	GaAs substrate and membrane ($\text{SiO}_2/\text{Si}_3\text{N}_4/\text{SiO}_2$) Al	0.025 - 0.6 and 0.025 - 1	0.9 - 11.3 and 0.5 - 0.9	$V_p/c = 0.38 - 0.355$ and 0.9	[Cheng1994]
	Strip width = 20 μm Gap = 20 μm Metal thickness = 5/200 nm	Polymer substrate PAX or ZEON, quartz and sapphire Ti/Au	0 - 1.7, 1.0 and 0.6	0 - 4.3, 6.9 and 8.7	$n_{eff} = 1.25, 1.75 - 1.85$ and 2.3 - 2.5	[Kadoya2008]
Microstrip	Metal width = 8 μm BCB thickness = 1.7 and 5.4 μm Metal thickness = 0.8 μm	BCB/low resistivity Si substrate Al	0 - 1	0 - 10 and 0 - 4	$\epsilon_{eff} = 2.7 - 2.4$ and 2.5 - 2.0	[Heiliger1997]
	Metal width = 8 μm SiO_2 thickness = 0.8 μm Metal thickness = 0.8 μm	SiO_2 /low resistivity Si substrate Al	0 - 1	0 - 23	$\epsilon_{eff} = 4.9 - 4.3$	
	Metal width = 20 μm Film thickness = 10 - 20 μm Metal thickness = 5/200 nm	Polyimide film TORAY Ti/Au	0 - 1.2	0 - 8.7	$n_{eff} = 1.6$	[Kadoya2008]
Planar Goubau line	Metal width = 5 μm Meal thickness = 300 nm (50/250)	Quartz substrate Ti/Au	0.14 - 0.22	2.8 - 4	-	[Akalin2006]

Table 1-3 lists the attenuation and dispersion properties of planar waveguide in THz range. Compared with the non planar waveguides, they demonstrate more losses and dispersions. For example, the slotline (gap width = 20 μm) on GaAs substrate has an attenuation of 20.7 dB/mm at 1 THz [Pahlevaninezhad2011]. This kind of performance is not acceptable when using such a structure as transmission line in circuits and the amelioration should be found. These measured or simulated (slotline) results will be compared in the frame of this work. Detailed analysis will be conducted in Chapter 3 in order to evaluate the dispersion and losses of planar guiding structure in THz range. Preliminary measurement results will also be presented.

Chapter 2 Modeling and Measurement of Plasmon-Polariton for Resonant Terahertz Detection

2.1 Introduction

Conventional electronic devices are mainly limited by the small cutoff frequency in microwave range. Significant efforts are still being put into the ensemble of electronic devices in order to use them in THz frequency and to make them functional at room temperature. Plasmonic sources and detectors are based on the coupling between the plasma and THz radiation via specific coupling structures. A high coupling efficiency is researched. Plasma frequency in semiconductor material can be possibly controlled in THz range.

Now, two dimensional electron gas (2DEG) presents a growing interest in THz for the development of compact, tunable, room temperature operating and low cost detectors and sources [Knap2009]. The high electron concentration, the large electron mobility and mainly the complex dispersion relation of plasmons are the main advantages of 2DEG confined in a quantum well (QW) based on heterostructures. From the aspect of device optimization, it is critical to study the coupling between the two dimensional (2D) plasmon and the THz electromagnetic (EM) field, namely the properties of the plasmon-polariton (PP). The PP can be excited through a metal grating deposited on top of the heterostructures. The PP are characterized by resonance phenomena which occur on transmission, reflection or absorption spectra. The electron density below metal fingers can be controlled by a bias voltage applied on metallization and the PP resonance will be tuned both in frequency and in amplitude.

To study PP resonances, we have chosen four kinds of heterostructures: AlGaAs/GaAs, AlGaN/GaN, InAlN/GaN and SiGe/Si/SiGe. Band diagrams and electron transport properties of Si, Ge, SiGe, GaAs and GaN quantum well have been extensively studied in our group [Aniel1996, Aniel2000, Richard2004, Richard2005]. Simulations of PP in this article are based on the known material parameters. Among the typical heterostructures, AlGaAs/GaAs has smaller lattice mismatch, while the modulation doping is indispensable to achieve high electron density. SiGe/Si material in the IV-IV group, owns its main advantages over the III-V group materials due to that it is compatible with the cheap and mature silicon technology [Paul2004]. High electron concentration and mobility have been achieved experimentally in modulation doped SiGe/Si heterostructures [Ismail1995]. Recently, GaN based structures attract more attention due to the large polarizations induced electron density without doping and find applications in grating gated field effect transistors (FET) [Muravjov2010, Popov2011, Wang2012].

Many numerical and analytical methods have been developed to study such corrugated heterostructure. Allen et al. [Allen1977] initially solved the problem of grating coupled transmission of light through 2D plasmon in silicon metal-oxide-semiconductor FET (MOSFET) by an analytical perturbative method. Zheng et al. [Zheng1990] generalized and improved the theory in regimes of high electron scattering time by a numerical non perturbative approach. Concerning complicated stratified system with perfect grating of finite thickness, Ager and Hughes [Ager1991] described a computational scattering matrix technique. This method was also applied to study 2D plasmon in AlGaAs/GaAs system [Tyson1994, Ager1992-1]. By considering the radiation capabilities of 2D plasmon through grating, Matov et al. [Matov1993] have

calculated numerically the complex plasmon frequency in a heterostructure, where the grating was treated as planar perfect strips. In a later article, Popov et al. [Popov2008-1] extended the EM theory with finite conductivity metal for THz emission and amplification in FET arrays and Muravjov et al. [Muravjov2010] demonstrated this approach for THz detection in a AlGaN/GaN HEMT. All of these work ignored the thickness of the QW and the ohmic loss in the actual grating of finite thickness. Wendler et al. [Wendler1999, Wendler2005] analyzed the spectrum of quasi 2D plasmon in AlGaAs/GaAs with lossy 3D grating by means of the transfer matrix method. The periodic grating issue was solved by the equivalent coupled wave method (CWM) and modal expansion method (MEM). For the purpose of resonance tunability, Ager and Hughes [Ager1992-2] studied the plasmon frequency in a modulated grating coupled 2DEG system based on scattering matrix method. Matov et al. [Matov2002] observed a dipole like resonant peak in a strongly modulated 2DEG system with semi-transparent NiCr grating.

Until now, direct comparisons of dispersion and absorption properties of quasi 2D plasmon in different structures coupled by the three dimensional (3D) lossy grating under the same numerical method have not yet been reported. In this work, we compare and synthesize the coupling effect between incident THz wave and 2D plasmons in four typical heterostructures (AlGaN/GaN, SiGe/Si/SiGe, AlGaAs/GaAs and InAlN/GaN) based on reported practical structure parameters in order to find out the best material for technical realization of THz detection. We used CWM for homogeneous and inhomogeneous 2DEG systems. For this latter case, the CWM was slightly modified. We demonstrate for the first time, that the commercial code ANSOFT HFSS based on finite element method (FEM) can solve the sophisticated problem of periodic screened heterostructures. For modulated 2DEG, the non uniform 2DEG charge distribution below and between metal fingers is considered for the structure AlGaAs/GaAs without and with bias voltage. For GaN based materials, the non uniform effect is not obvious without biasing, so the homogeneous 2DEG model is sufficient. In modulated AlGaAs/GaAs structure, three kinds of 2DEG concentration profiles (piecewise, linear and parabolic) have been used and compared to calculate the absorption spectrum. A strongly modulated 2DEG in AlGaAs/GaAs leads to a distinct PP resonance but its position cannot be predicted by the dipole like formula as in [Matov2002] due to the screening effect of metal.

This chapter is scheduled as follows: Some generalities will be discussed in the first section about 3D plasma and quasi-2D plasmon in heterostructures. Numerical method for analyzing the spectrum response of 2D plasmon to THz radiation in a grating assisted heterostructure are presented in section 2.3 by HFSS and CWM. Comparisons have been made between the two approaches. Section 2.4 focuses on the optimization of THz absorption in homogeneous 2DEG system through a parametric study (grating period, metal width, electron density, barrier thickness and temperature) in frequency range [0-5] THz by HFSS. The roles of the finite thicknesses of lossy metal grating and 2DEG layer on observed absorption are also emphasized. Section 2.5 is about the measurement setup and results. Section 2.6 mainly concentrates on the tunability of PP resonances in a modulated 2DEG system. The effect of metallic bias on the tunability of absorption spectrum is evaluated using the slightly modified CWM code.

2.2 Plasma in semiconductor

2.2.1 3D plasma in bulk semiconductor

In a metal, plasma is neutral and consists in a large amount of positively charged ions and negatively charged electrons. The heavy ions are assumed to be at rest, while the electrons move relatively to the ions. The plasma also exists in a doped semiconductor material, where the electrons (holes) move in the presence of positive donor (negative acceptor) ions. In the semiconductors, the density of electrons or holes can be controlled by the doping level.

The interaction of incident electric field with the free electrons in a metal is described by the movement equation of electrons [Ashcroft1976],

$$\frac{d\vec{p}}{dt} = \frac{-\vec{p}}{\tau} - e\vec{E}, \quad \vec{p} = m\vec{v} \quad (2-1)$$

where e and m are the unit charge value and mass of electrons. \vec{v} and \vec{p} are the velocity and momentum. τ is the mean free time between ionic collisions.

If the excitation monochromatic wave takes the form $E(t) = E_0 e^{-j\omega t}$, the Maxwell equations in the metal can be written as,

$$\nabla \times \vec{H} = \vec{J} + \epsilon_0 \frac{\partial \vec{E}}{\partial t}, \quad \vec{J} = \sigma \vec{E} \quad (2-2)$$

The frequency dependent conductivity and relative permittivity of metals are

$$\sigma = \frac{ne^2\tau}{m(1-j\omega\tau)} \quad \text{and} \quad \epsilon = 1 + \frac{j\sigma}{\omega\epsilon_0} \quad (2-3)$$

where n is the electron concentration per unit volume (cm^{-3}). If the mean free time is much larger than the period of excitation signal ($\omega\tau \gg 1$), the dielectric function has only the real part,

$$\epsilon = 1 - \frac{\omega_p^2}{\omega^2}, \quad \omega_p = \sqrt{\frac{ne^2}{m\epsilon_0}} \quad (2-4)$$

where ω_p is the 3D plasma frequency in a metal, which is proportional to the square root of electron density n . A typical electron density $n = 5.86 \times 10^{22} \text{ cm}^{-3}$ in gold corresponds to the plasma frequency $f_p = \omega_p/(2\pi) = 2175 \text{ THz}$. The plasma frequency does not depend on the wavevector of the incident field.

For the plasma in the bulk n-type semiconductor material, the above procedures can also be applied. One should replace the mass of free electrons by the effective mass of electrons in semiconductor, and take the material permittivity ϵ_s in the calculation. Plasmon, or the quantum

of plasma oscillation, is the phenomena of the collective oscillation of carriers at the plasma frequency.

Plasma also exists in low dimensional electron systems, where the motion of electron is limited in one (quantum wells), two (quantum wires) and even three dimensions (quantum dots). In low dimensional electron system, the plasmon frequency depends on the wavevector. Exact calculation of the dielectric function requires sophisticated quantum mechanisms, including electron correlation in many body problems [Pines1952]. Under certain approximations, good analytic formulas of permittivity can be obtained and introduced in calculation.

2.2.2 Heterojunctions and two dimensional electron gas 2DEG

2DEG has been intensively studied in the n-type inversion layer of metal-SiO₂/Si structure when a voltage bias is applied to the gate metal [Stern1967] and observed experimentally at the surface of liquid helium [Grimes1976]. Apart from the inversion layer, 2DEG also can be found in the heterostructures and the associated plasma frequency can be located or tuned in THz frequency by modifying the electron concentration through the bias voltage on overlying conductors for example. Electron concentration and mobility are the main characteristic parameters of 2DEG for thermalized carriers plasmon. With the development of semiconductor epitaxial growth technology, large carrier concentration has been measured at the interface of heterojunctions. In addition, δ -doping can be used during the growth process, and then very high electron mobility can be obtained even for small distance between the QW and the surface (20-25 nm).

2.2.2.1 About heterojunctions

The heterojunctions are divided into three types according to the relative alignment of conduction band (CB) bottom and valence band (VB) top of the two semiconductors, as shown in Figure 2-1. The type I is the most common alignment referred to as the straddled alignment, for instance, the most exhaustively studied heterostructure AlGaAs/GaAs, InAlN/GaN and AlGaN/GaN. For type II, or the staggered gap, the steps of the VB and CB are in the same direction. Strained Si/SiGe and GaInAs/GaAsSb are among this material group. The third type is the most extreme case, broken gap. InAs/GaSb is in this material system.

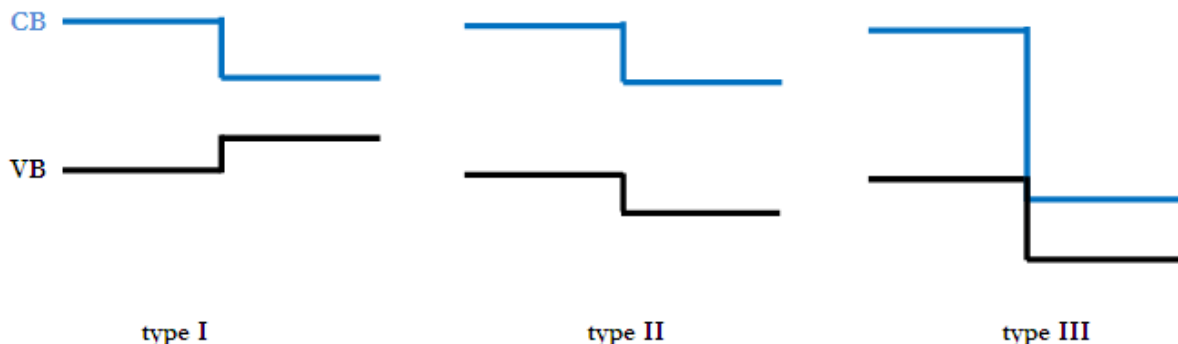


Figure 2-1: The three types of heterojunctions: type I (straddling gap), type II (staggered gap) and type III (broken gap)

For the application requiring high speed integrated circuit, devices based on 2DEG system are expected to operate at high voltage, high power and high temperature [Ozgur2005].

requirements on 2DEG are to have large carrier concentration N_s (m^{-2}) and high electron mobility μ_{2DEG} (cm^2/Vs). The carrier density is obtained by solving the Schrödinger equation coupled with the Poisson equation. Accurate band structure can be calculated by ab initio methods or via semi empirical approach (k.p, tight binding, and pseudo-potential). The conduction band discontinuity is of great interest for us because only the electron system is considered in this work. We have calculated the conduction band profile in the frame of the effective mass approximation (EMA) and of the envelope function [Tan1990]. Figure 2-2 illustrates the type I heterojunctions AlGaN/GaN. The conduction band offset is the reason for the formation of 2DEG layer. Compared with AlGaAs/GaAs structure, nitride based material has a large band offset ΔE_c , partly due to its large band gap, and mainly due to the high spontaneous and piezoelectric polarizations. Therefore, for the AlGaN/GaN heterojunctions, the polarization induced charge has to be contained in the Poisson equation.

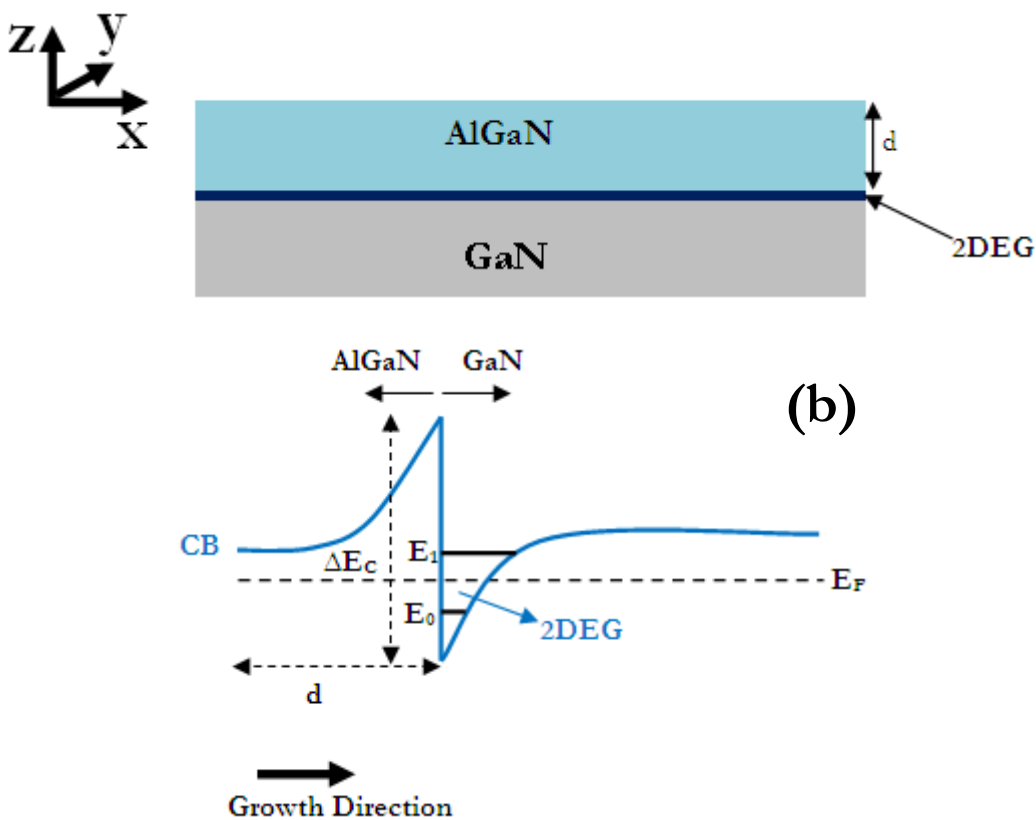


Figure 2-2: AlGaN/GaN heterojunctions (a) and the conduction band diagram (b)

In the following, we discuss the conduction band modeling method for GaN based heterostructure. However, it also applies for AlGaAs/GaAs if the polarizations are not taken into account. Calculation of the band diagram of strained SiGe/Si/SiGe structure is introduced briefly in section 2.2.2.4, where more rigorous theory is required.

2.2.2.2 Electron concentration

The Schrödinger equation and Poisson equation have been solved numerically to calculate the 2DEG density. The polarizations (both spontaneous and piezoelectric) induced charges are taken into account. Following the growth direction (for example along the z direction) of the

heterostructure as in the Figure 2-2, the electron wavevector is quantified and in the interface plane, the motion is considered as quasi free. For example in GaN, a triangular quantum well is formed at the side of smaller bandgap semiconductor. The confined electron layer thickness or the single well width is usually in the order of 10 nm and not above 100 nm. First of all, the conduction band of electrons confined in one dimension in AlGaN/GaN is modeled.

I Conduction band modeling

In the framework of EMA, one dimensional Schrödinger equation is written as,

$$-\frac{\hbar^2}{2} \frac{d}{dz} \left(\frac{1}{m^*(z)} \frac{d}{dz} \right) \psi(z) + V(z)\psi(z) = E\psi(z) \quad (2-5)$$

where \hbar is the Planck's constant divided by 2π , $m^*(z)$ is the position dependent effective mass of electron, $\psi(z)$ is the electron envelop wave function, $V(z)$ is the potential energy seen by the electron, and E is the electron energy.

For wurtzite semiconductor such as GaN, the polarization $P(z)$ must be included in the displacement field $D(z)$.

The Poisson equation is given as,

$$\frac{d}{dz} \left[-\epsilon_s(z) \epsilon_0 \frac{d\phi(z)}{dz} + P(z) \right] = e \left[p(z) - n(z) + N_D^+(z) - N_A^-(z) \right] \quad (2-6)$$

Where n (p) is the electron (hole) charge concentration (m^{-3}), and N_D^+ (N_A^-) is the ionized donor (acceptor) volume density.

The polarization P of the barrier AlGaN layer or the substrate GaN is the sum of two parts: the spontaneous polarization P_{SP} in the equilibrium, and the piezoelectric polarization P_{PE} .

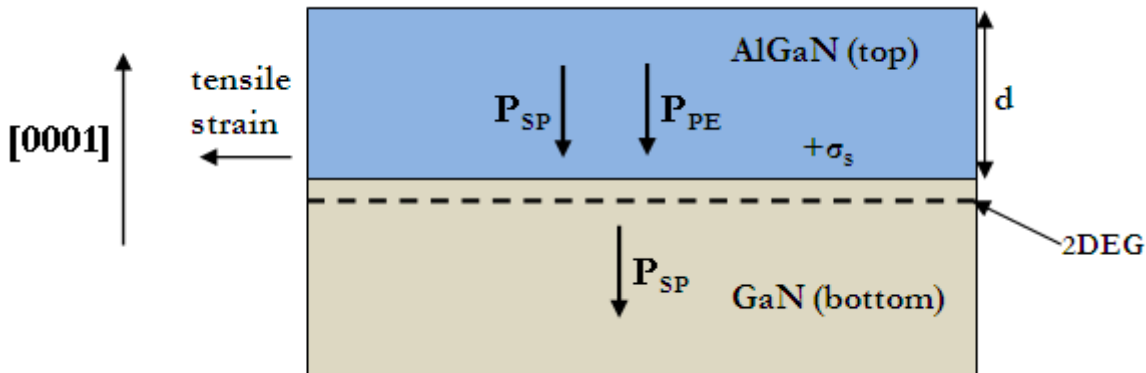


Figure 2-3: Polarization bound surface charge and 2DEG in pseudomorphic heterojunction with Ga-face wurtzite polarity

Due to the polarization discontinuity at the interface a charge density is induced. As shown in Figure 2-3, the polarization induced charge is positive at the interface AlGaN/GaN, for a Ga-face GaN layer [Ambacher1999].

The polarization induce surface charge density σ_s ,

$$\sigma_s = P(AlGaN) - P(GaN) \quad (2-7)$$

The spontaneous polarization of GaN is -0.029 C/m^2 [Bernardini1997]. For a relaxed $Al_xGa_{1-x}N$ layer the spontaneous polarization is a function of Al mole fraction x [Ambacher2000],

$$P_{SP}(Al_xGa_{1-x}N) = -0.052x - 0.029 \text{ C/m}^2 \quad (2-8)$$

The piezoelectric polarization for a biaxial tensile strained $Al_xGa_{1-x}N$ layer is,

$$P_{PE}(Al_xGa_{1-x}N) = 2 \times (r(x) - 1) \times \frac{a_0(x) - a(GaN)}{a_0(x)} \times (e_{31}(x) - e_{33}(x)) \frac{C_{13}(x)}{C_{33}(x)} \quad (2-9)$$

Where $r(x)$ is the barrier relaxation degree, a_0 is the equilibrium values of the lattice parameter, e_{31} and e_{33} are the piezoelectric constant, C_{13} and C_{33} are the elastic constants.

For barrier thickness around $d = 30 \text{ nm}$, the relaxation degree of AlGaN on GaN layer is approximately [Angerer1997],

$$r(x) = \begin{cases} 0, & 0 \leq x < 0.38 \\ 3.5x - 1.33, & 0.38 \leq x \leq 0.67, \text{ for } d \approx 30\text{nm} \\ 1, & 0.67 < x < 1 \end{cases} \quad (2-10)$$

The other x dependent parameters (a_0 , e_{31} , e_{33} , C_{13} and C_{33}) can be calculated in the frame of a linear interpolation of the two binary AlN and GaN. The spontaneous and piezoelectric parameters of III-Nitride binary are summarized in Table 2-1.

The electron concentration $n(z)$ is calculated as follow

$$n(z) = \sum_{k=1}^m \psi_k(z) \psi_k^*(z) n_k \quad (2-11)$$

Assuming Fermi-Dirac statistics, the electron occupation in the subband k is given by,

$$n_k = \frac{m *}{\pi \hbar^2} \int_{E_k}^{\infty} \frac{1}{1 + e^{(E-E_F)/k_B T}} dE = \frac{m * k_B T}{\pi \hbar^2} \ln[1 + e^{(E_F-E_k)/k_B T}] \quad (2-12)$$

E_F is the system Fermi level, k_B is the Boltzmann constant, and T is the temperature in Kelvin.

The procedure of the self consistent calculation of equation (2-5) to (2-12) can be found in [Tan1990].

Table 2-1: Spontaneous and piezoelectric parameters of III-Nitride wurtzite binary materials

Parameters	AlN	GaN	InN	References
a_0 (Å)	3.112	3.189	3.54	
c_0 (Å)	4.982	5.185	5.705	Lattice constant [Ambacher1998]
E_g (eV)	6.2	3.4	1.9	Energy gap at 300 K
ϵ_r	8.5	9.7	15.3	Relative static dielectric constant
m_e	0.48	0.22	0.11	Effective electron mass in unit of m_0
c_{13} (GPa)	108	103	92	
c_{33} (GPa)	373	405	224	Elastic constant [Wright1997]
e_{31} (C/m ²)	-0.60	-0.49	-0.57	
e_{33} (C/m ²)	1.46	0.73	0.97	Piezoelectric constant [Bernardini1997]
P_{sp} (C/m ²)	-0.081	-0.029	-0.032	Spontaneous polarization [Bernardini1997]

As the barrier layer is not infinite, polarization induced negative charge can also appear at the interface air/barrier layer. For the application of heterojunctions based devices, a metal electrode is deposited on the top of the barrier layer to form the Schottky contact. The polarization induced charge at the top of the barrier layer (AlGaN) will be compensated either by charged surface states for a surface air/AlGaN, or by the carriers in the metal for the contact metal/AlGaN. In both cases, a potential barrier height is formed in reference to the Fermi level. The electron density will be modified more or less depending on the value of barrier height.

For AlGaAs/GaAs heterojunctions, the total polarization is negligible.

II Numerical results

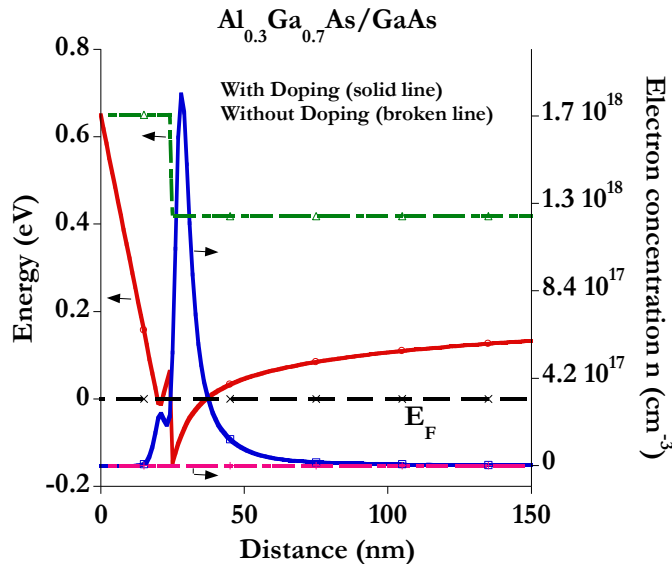


Figure 2-4: Conduction band profile and electron concentration for pseudomorphic heterojunctions $\text{Al}_{0.3} \text{Ga}_{0.7} \text{As}/\text{GaAs}$ with (solid line) and without (broken line) modulation doping. The donor concentration is $N_D = 2 \times 10^{19} \text{ cm}^{-3}$

Here, we use the free available code based on finite difference method which has been developed by G.Snider [Snider1990, <http://www.nd.edu/~gsnider/>] to calculate numerically the electron band diagram and electron density.

Figure 2-4 shows the conduction band and electron wave function distribution for $\text{Al}_{0.3} \text{Ga}_{0.7} \text{As}/\text{GaAs}$ heterojunctions. The barrier layer thickness AlGaAs is 25 nm. When the modulated doping technology is used, the conduction band is bended below the Fermi level at the interface AlGaAs/GaAs, and a 2DEG sheet concentration of $N_s = 1.65 \times 10^{12} \text{ cm}^{-2}$ is achieved, where the doping density $N_D = 2 \times 10^{19} \text{ cm}^{-3}$ is in a 2 nm thick layer at a distance of 3 nm from the GaAs surface. For the application of this specific heterojunctions, the doping is indispensable.

The influences of the total polarizations (spontaneous and piezoelectric) on the band profile and carrier density are displayed in Figure 2-5 for $\text{Al}_{0.25} \text{Ga}_{0.75} \text{N}/\text{GaN}$ heterojunctions without and with modulation doping. Here the doping density is $N_D = 10^{19} \text{ cm}^{-3}$, and the doping layer thickness and location is the same as in AlGaAs/GaAs. Without doping, no 2DEG is formed if no polarization (both spontaneous and piezoelectric) is considered, however, a high 2DEG concentration $N_s = 1.21 \times 10^{13} \text{ cm}^{-2}$ is obtained when the polarization is included. The large polarizations induced charges contribute to the high electron confinement at AlGaN/GaN interface. If the barrier AlGaN is doped, the corresponding 2DEG concentration is $N_s = 1.36 \times 10^{13} \text{ cm}^{-2}$ and $5.82 \times 10^{11} \text{ cm}^{-2}$ for the polarization and non polarization cases, respectively. The modulation doping increases slightly the carrier density. 2DEG concentration of undoped AlGaN/GaN is usually larger than that of doped AlGaAs/GaAs heterojunctions. This is the most attractive advantage of III-Nitride materials. Moreover, in the application of HEMT structure, the doping in AlGaN barrier will deteriorate the device performance: higher pinch off voltage, large gate leakage current and noise [Rizzi2002]. The undoped nitride HEMT structure is preferred for the ease of fabrication. Of course, the higher electron concentration is always appreciated for efficient coupling with incident THz in the detection applications (section 2.3).

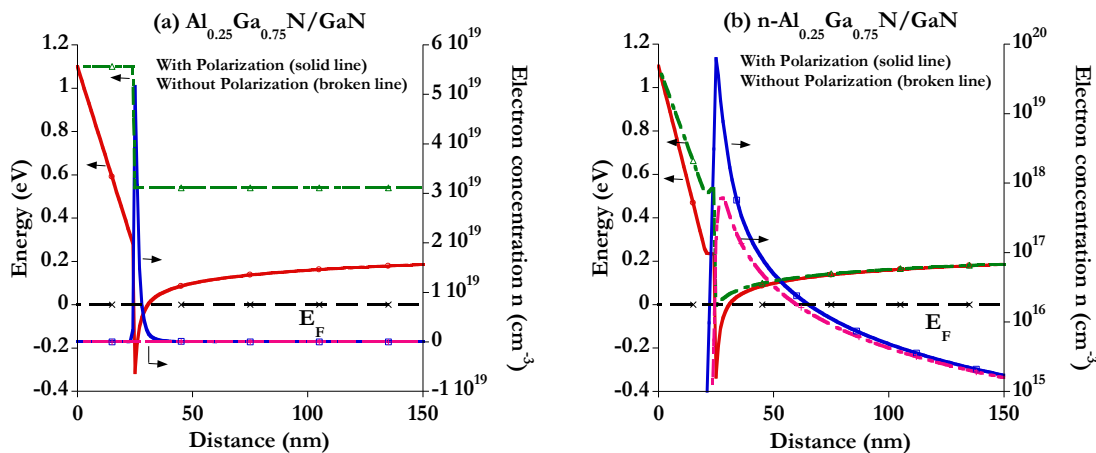


Figure 2-5: Conduction band profile and electron concentration for pseudomorphic heterojunctions $\text{Al}_{0.25} \text{Ga}_{0.75} \text{N}/\text{GaN}$ without (a) and with modulation doping (b). The donor concentration is 10^{19} cm^{-3} . In each plot, the polarization effect is compared (solid line stands for the case with polarizations, broken line for the case without polarizations)

At last, for the influence of temperature in the expression (2-12), it should be mentioned that the 2DEG density is almost not dependent on the temperature, but this is not the case for the electron mobility, as we will see in section 2.2.2.3.

2.2.2.3 Electron mobility

Another distinct advantage for a modulated doped 2DEG system is the high electron mobility, which can be much higher than the doped bulk semiconductors. Scattering mechanisms control the mobility. If different scattering effects μ_i are assumed to be independent with each other, the effective mobility μ_{2DEG} can be determined by Matthiessen's rule,

$$\frac{1}{\mu_{2DEG}} = \sum_i \frac{1}{\mu_i} \quad (2-13)$$

Electrons in a low dimensional electron system scatter from crystal lattice, defects, interface roughness, alloy, dislocations and other charges. These scattering mechanisms will be overviewed briefly in the following part. Detailed discussions can be found in the referred publications in each case.

I Remote donors scattering

The background impurities, or the residual ionized impurities in the substrate bulk material where the 2DEG layer is located is usually small for an undoped substrate, however, the scattering with remote impurities in the doped barrier is significant if the spacer layer (the undoped barrier layer between 2DEG and doped layer) is thin (3-5 nm). For the AlGaAs/GaAs heterojunctions, the electron scattering is negligible when the spacer is larger than 15 nm at an electron concentration $N_s = 10^{12} \text{ cm}^{-2}$ [Manasreh2005].

II Interface roughness scattering

The interface roughness between the barrier layer and the substrate influences the electron transport along the interface. The fluctuation of material thickness at the interface induces the electron scattering. This type of scattering can dominate at low temperatures [Masaki1989].

III Electron-electron scattering

The interaction of electron-electron can be divided into two components: short range and long range due to the fact that the electron gas exhibits both collective and individual particle behaviors. The long range interaction gives rise to the plasma oscillation, or the collective oscillation of electron gas, and manifest over distances greater than the characteristic screening length of the system. For short range electron-electron scattering, the electron gas behaves more as a collection of individual charged particles. This scattering is supposed to be elastic for low energy carriers [Brennan1999].

It has been pointed out that the electron-electron short range scattering has the same order of magnitude of mobility obtained for remote impurity and surface roughness scatterings for a typical AlGaAs/GaAs heterostructure with $N_s = 10^{12} \text{ cm}^{-2}$.

IV Phonon scattering

Phonon is caused by the atom vibrations around equilibrium positions in the crystal lattice. In face centered cubic semiconductor there are 6 phonon branches and 9 for wurtzite semiconductor. In polar semiconductor, the coupling is done both through deformation potential and piezoelectric coupling. In QW not only the electrons but also the acoustic phonons are confined leading to differences between 2D and 3D (bulk) transport properties. In most cases, 2D carrier mobility associated with phonons is higher than in bulk.

V Dislocation scattering

The defects in the substrate and the lattice mismatch between the barrier and substrate material have the potential to affect the electron transport and the 2DEG mobility.

The record 2DEG mobility is $51700 \text{ cm}^2/\text{Vs}$ at 13 K with line dislocation density $N_{\text{disl}} = 10^8 \text{ cm}^{-2}$ and $N_s = 2.23 \times 10^{12} \text{ cm}^{-2}$, which is much higher than the electron mobility $100 \text{ cm}^2/\text{Vs}$ in a 3D bulk GaN at 13 K with a carrier density $n = 10^{18} \text{ cm}^{-3}$ [Jena2000-1]. The dislocation scattering can be reduced by novel method of epitaxy to decrease the dislocation density in the growth process, such as the lateral epitaxy overgrowth (LEO) [Kato1991].

VI Dipole scattering

For AlGaN/GaN structure, the dipole will be formed in the barrier alloy AlGaN. Every Al or Ga plane has dipoles in each primitive cell, and the dipole moment at Al sites are higher than that at the Ga sites owing to the higher spontaneous polarization and piezoelectric constants in AlN than in GaN. The fluctuations of a perfect periodic structure in the AlGaN alloy will produce a random distribution of microscopic dipoles in AlN and GaN regions, and causing the scattering of electrons in 2DEG. The mobility limited by dipole scattering was studied theoretically by Jena et al. [Jena2000-2]. The dipole scattering mobility increases as the Al mole fraction x from 0 to 1 without modulation doping. At low temperatures, the mobility is in the range $2-4 \times 10^5 \text{ cm}^2/\text{Vs}$ for x in the range 0.1-0.4. By growing periodically either purely Al or Ga layers to overcome the random nature of the alloy, digital alloy growth method is suggested to reduce the dipole scattering, although it suffers from interdiffusion of atoms in the growth process [Jena2000-2].

VII Numerical results

As an example, the mobilities due to different scattering mechanisms and the total mobility are shown from 1 K to 300 K in Figure 2-6 for $\text{Al}_{0.15}\text{Ga}_{0.85}\text{N}/\text{GaN}$ modulation doped heterojunctions without spacer. Donor concentration is 10^{18} cm^{-3} in AlGaN corresponds to a 2DEG density of $1.59 \times 10^{12} \text{ cm}^{-2}$. The residual ionized impurities in GaN are: $4 \times 10^{15} \text{ cm}^{-3}$. The temperature independent scatterings due to dislocation, dipole and surface roughness are not included in the calculation. At low temperatures, the mobility is mainly limited by the remote donors, alloy disorder and residual impurity. From 10 K, the acoustic phonon scattering becomes important through the deformation potential and piezoelectric effects. At temperatures above 200 K, the mobility is limited nearly only by the optical phonon scattering and drops quickly with the temperature. The saturation mobility is about $2.7 \times 10^7 \text{ cm}^2/\text{Vs}$.

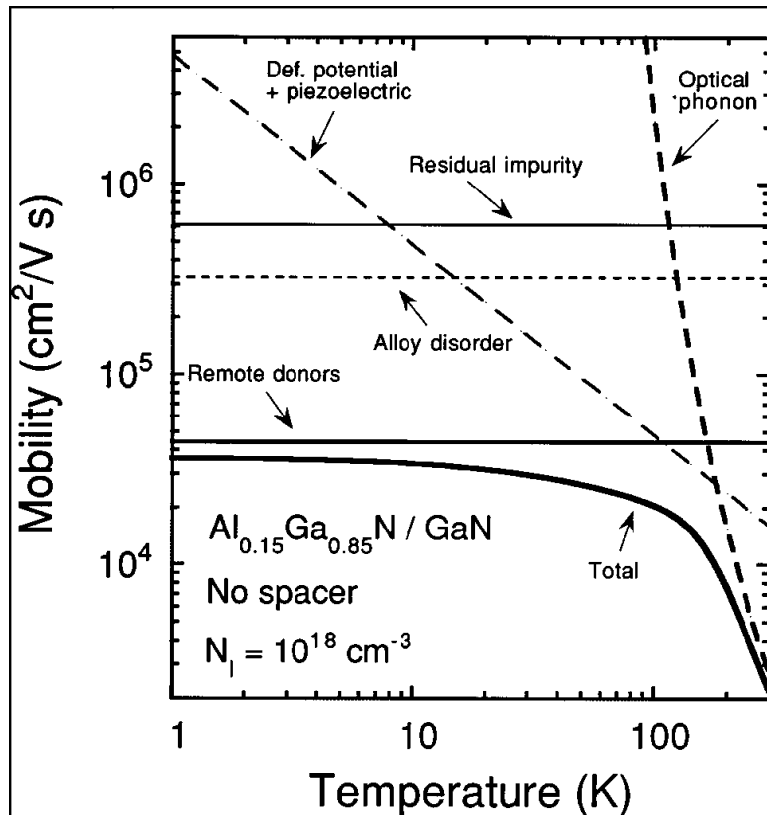


Figure 2-6: Calculated temperature dependence of the mobility of electrons in a $\text{Al}_{0.15}\text{Ga}_{0.85}\text{N}/\text{GaN}$ modulation doped heterojunctions. The residual ionized impurity concentration in this calculation is $4 \times 10^{15} \text{ cm}^{-3}$ and the doping level 10^{18} cm^{-3} corresponds to a electron gas density of $1.59 \times 10^{12} \text{ cm}^{-2}$. [Hsu1997]

To improve electron mobility, besides the above mentioned lateral epitaxy overgrowth method to decrease the dislocation scattering and the digital alloy growth technique to alleviate the dipole scattering in the barrier, there are other ways to reduce others scattering mechanism by ameliorate the substrate and the barrier materials. The alloy disorder scattering can be eliminated by inserting a thin layer of AlN into the AlGaN/GaN structure [Smorchkova2001], or by reducing the remote doping concentration. The remote donor scattering is reduced when increasing the spacer layer. High substrate purity helps to lower the residual impurity scattering.

2.2.2.4 SiGe/Si/SiGe heterostructure

A biaxial tensile strained Si layer grown on relaxed SiGe or virtual SiGe substrate produces a quantum well for electrons (2DEG). The biaxial stress can be divided into hydrostatic stress and uniaxial stress. The uniaxial stress causes the splitting of six-fold degenerated Δ valleys of the conduction band into two-fold and four-fold degenerate valleys, where the lowest valleys are the two-fold D valley along the 100 direction leading to a QW. Calculations of electron density and modeling of electron mobility in SiGe/Si/SiGe are beyond the scope of this work and have already been done in the team. Calculations based on 30 bands k.p can be found in references [Aniel2000, Richard2004].

Modulation doping has been also transferred to Si/SiGe system [People1984]. The main low temperature electron scattering mechanisms in modulation doped Si/SiGe are ionized impurity

scattering from the doped barrier layer, residual impurities scattering in the channel, surface roughness scattering [Stern1992]. High temperature mobility is mainly limited by the optical phonon scattering. The improvement of epitaxy growth conditions have greatly improved the electron mobility, combining with SiGe buffer layer [Schäffler1992]. A high electron mobility of $8 \times 10^5 \text{ cm}^2/\text{Vs}$ has been obtained at 15 K [Yutani1997, Sugii1998]. The large carrier density and mobility in strained Si/SiGe heterostructure have considerably exceeded the peak values in silicon inversion layer [Kukushkin1988] and further make it comparable with its III-V counterpart, for example, in the MODFET [Lee2005] and CMOS [Oh2012] applications.

Based on the descriptions of 2DEG properties (concentration and mobility), the interaction of the 2DEG with incident wave will be studied in the following section for THz detection. Firstly, the dispersion relation of 2D Plasmons-Polaritons is calculated both analytically and numerically. Then the spectrum is obtained numerically.

2.3 Dispersion and spectrum of Plasmon-Polariton (PP)

The heterostructures studied in the frame of this work constitute a multi-layers homogeneous system if the 2DEG concentration is constant in the interface plane x-y. If metal electrodes are deposited on top of the structure to control the electron concentrations, this will be considered as a non homogenous material layer. The interaction of an incident (I) THz radiation with 2DEG system is represented by the spectrum of transmission (T), reflection (R), or absorption (A), as shown in Figure 2-7 for example for the simplified AlGaN/GaN single heterojunctions. At the frequency of incident wave, if the coupling between THz radiation and 2D plasmon happens, a transmission minimum and an absorption maximum will appear at that frequency in the spectra. The absolute strengths of transmitted and absorbed signals are proportional to the incident wave intensity. Hence both the amplitude and frequency of the incident wave can be possibly predicted by the spectra. The remaining question is how to make this coupling occur.

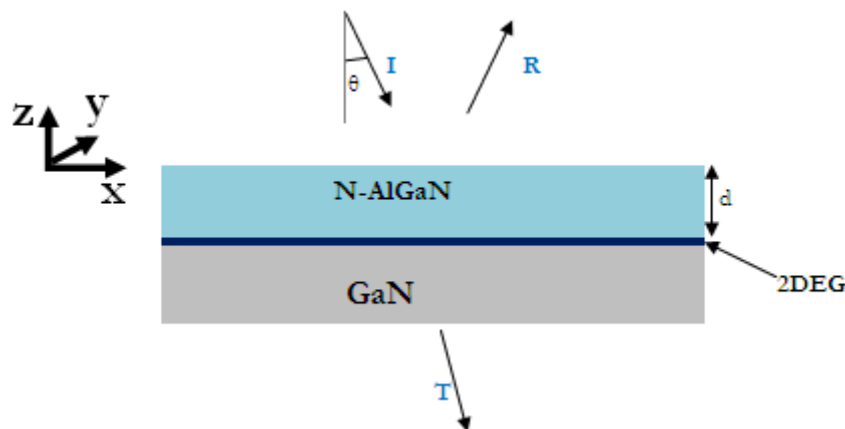


Figure 2-7: Spectrum analysis for a multi-layers system containing 2DEG layer

The notation “plasmon-polariton (PP)” represents the interaction of photons (Boson) and electrons (Fermions). We lead a spectrum analysis to study the PP dispersion in grating covered heterostructures. In this section, the dispersion discrepancy between 2D plasmon embedded in an infinite dielectric and PP at the interface of a heterostructure is emphasized by numerical

methods (CWM and HFSS). Although the spectrum calculation is discussed on nitride based material, modeling has also been applied to other structures following the same method.

2.3.1 Dispersion of 2D plasmon

In order to achieve the coupling between THz wave (photons) and plasma wave (plasmon), velocity phase condition has to be satisfied. Namely, at a certain frequency, the THz wave and plasmon should have the same wavevector. In long wavelength limit ($k < \sqrt{2\pi N_s}$), the dispersion of 2D plasmon in an infinite homogeneous dielectric (permittivity ϵ_s) is derived from the following relation [Stern1967],

$$k^2 = \frac{\epsilon_s \omega^2}{c^2} + \left(\frac{2\epsilon_s \epsilon_0 m * \omega^2}{N_s e^2} \right)^2, f = \frac{\omega}{2\pi} \quad (2-14)$$

Where k is the plasmon wavevector and ω is the plasmon frequency. Depending on the incident angle, the THz wave dispersion is $f = \frac{1}{2\pi} \frac{c}{\sin \theta} k$. Figure 2-8 plots the dispersions of 2D plasmon buried in GaN ($\epsilon_s = 9.7$, $N_s = 1.7 \times 10^{16} \text{ m}^{-2}$) and the light line, where the incident angle is assumed to be $\theta = 90^\circ$ to reach the maximum in-plane wavevector component. At 1 THz, the plasmon wavevector is about $4 \times 10^5 \text{ m}^{-1}$ (this value is larger at lower N_s), while the maximum incident wavevector is about $2 \times 10^4 \text{ m}^{-1}$, which is one order lower than the plasmon wavevector. Therefore, the 2D plasmon is not radiative and cannot couple directly with THz radiation. That is why coupling components for THz detection are needed.

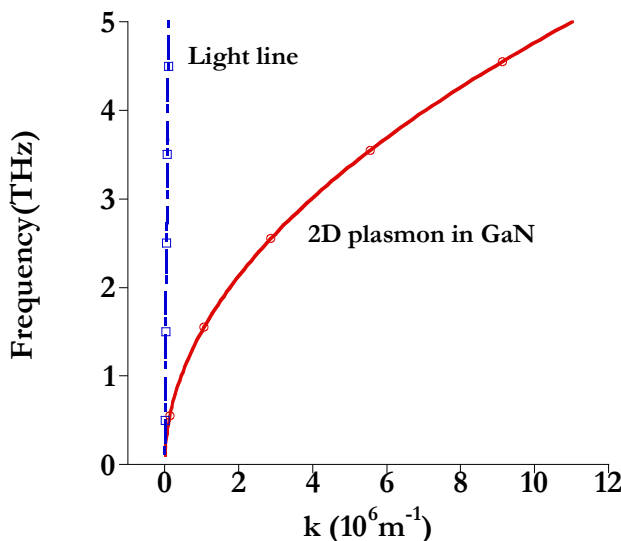


Figure 2-8: Dispersion of 2D plasmon buried in GaN and light line

2.3.2 Grating assisted coupling

To compensate the wavevector mismatch between incident wave and 2D plasmon, grating couplers are necessary. The metallic grating is schematized in Figure 2-9. The metal strips are

located on top of the barrier layer of the heterojunctions. They are uniform in y direction and periodic in x direction. L is the period and W is the metal strip width. The ratio W/L is usually called the filling factor in the air/metal periodic configuration. Incident electric field is polarized in the incident plane x - z . According to the electromagnetic theory of grating [Petit1980], the wavevector of the scattered waves (both reflected and transmitted waves) along the periodic direction x depends on the grating period (L) and the scattering order (n) :

$$k_{xn} = k_x + G_n = k_x + \frac{2\pi n}{L}, n = 0, \pm 1, \pm 2, \dots$$

, while the y component of the incident wavevector is

conserved as the y component of the incident wave in the multi-layers system. $k_x = \sin \theta_0 \omega / c$ and $k_z = \cos \theta_0 \omega / c$ are the x and z components of the incident wavevector. G_n is the reciprocal lattice vector. If the period of grating L is chosen in the micrometer range, then the in-plane wave vector k_{xn} will be in the order of 10^6 m^{-1} , making the coupling with 2D plasmon possible according to the 2D plasmon dispersion in Figure 2-8.

The dispersion of the entire layered system is described by the plasmon-polariton, which differs from both the dispersion of the incident THz wave and the dispersion of 2D plasmons buried in infinite dielectric. At these discrete resonant frequencies determined by the actual PP dispersion through the discrete in-plane wavevector, the collective oscillation of electrons (plasma waves) is pronounced and the corresponding interactions with EM waves are intense. If this oscillation is not damped by electron scattering, it will be expressed in the absorption spectrum of EM wave passing through the structure, which can be measured and detected in conventional spectroscopic transmission setup. However, no explicit formula exists for the dispersion of PP. It should be solved numerically with the existence of metal grating ($0 < W/L < 1$). Concerning the different models of both the grating and 2DEG layer (finite and zero layer thickness), the dispersions will be calculated in each case accordingly.

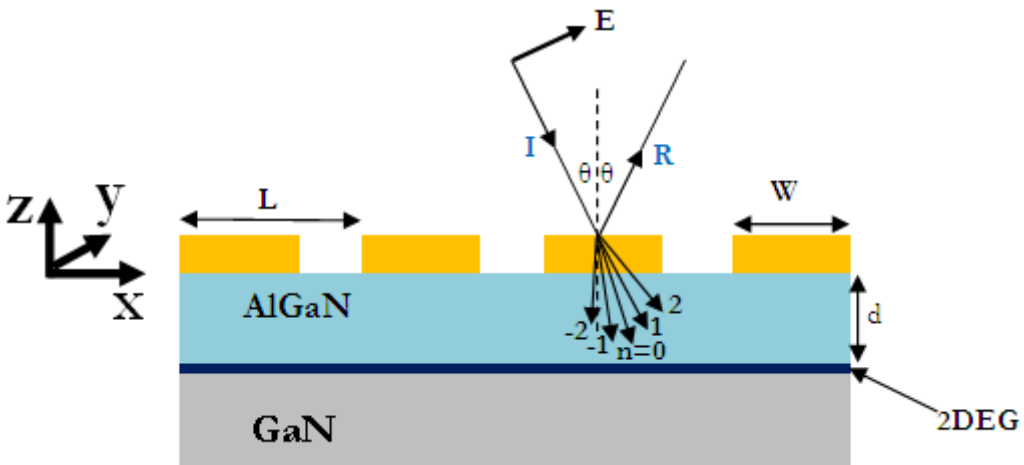


Figure 2-9: Grating coupler on top of the heterojunction AlGaN/GaN

2.3.3 Modeling of PP spectrum

The analysis of the layer with grating coupler can be conducted with either integral or differential method [Loewen1997]. Different profile and thickness of the grating have been treated with the modal expansion method [Li1993]. The electromagnetic field in the air gap and in the metal

finger are expanded with the product of a periodic part and a phase part e^{jkx} (x is periodic direction) according to the Floquet-Bloch theory [Sun1997]. Continuous boundary conditions (tangential components of E and H) at the lateral interface plane $y-z$ between metal and air are used to link the field amplitudes in each region, and an eigenvalue equation is produced accordingly to calculate the wavevector along the z direction.

A root finding program must be employed to find the complex eigenvalues and eigenfunctions for fields in the periodic material layer. Another approach is the coupled wave method (CWM) [Granet1996]. As described in [Petit1980], this method is considered as the conformal mapping in differential method, expanding the field components in the quasi-Fourier series (Rayleigh expansions) and the permittivity of the whole layer in Fourier series. In this way, the problem of corrugated surface is converted into the planar surface. The two methods (modal expansion method and CWM) have been compared and give the same spectroscopic results to a high precision in an anisotropic multi-layers system [Wendler2005], where the permittivity of metals is modeled as the 3D frequency dependent Drude dielectric constant. In this work, the CWM is adopted for the ease of numerical implantation in Matlab program. And the results will be compared with the commercially available software HFSS.

According to the nature of grating (3D with finite thickness or 2D with zero thickness), different calculation formula are adopted to conduct the spectrum analysis.

2.3.3.1 CWM analysis of PP with 3D grating

The metallic rectangular grating with finite thickness t in the z direction is shown in Figure 2-10. The metal occupies in the region $nL < x < nL+W$, and the gaps $nL+W < x < (n+1)L$ are filled with air, where n are integers. The metal dielectric constant is assumed to be isotropic $\epsilon_1(\omega) = \epsilon_{xx}(\omega) = \epsilon_{yy}(\omega) = \epsilon_{zz}(\omega)$ and frequency dependent.

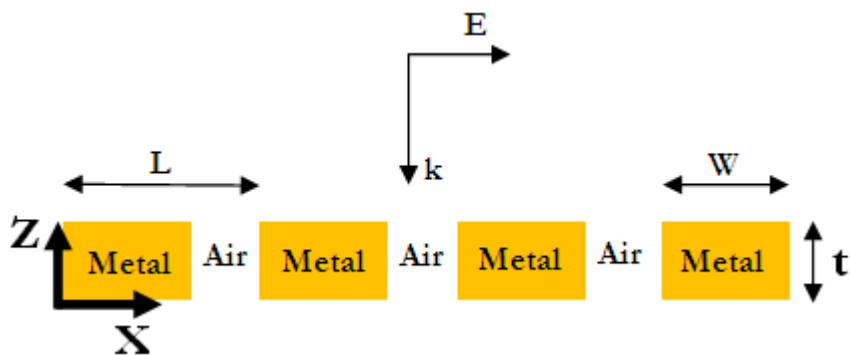


Figure 2-10: Periodic grating with finite thickness t

For TM polarization field at normal incidence, the y component of magnetic field H is expressed as the quasi-Fourier series (Rayleigh expansions),

$$\begin{aligned}
 H_y(x; z | \omega) &= \sqrt{\frac{\epsilon_0}{\mu_0}} \sum_{n=-\infty}^{+\infty} \exp(jk_{xn}x) H_{yn}(z | \omega) \\
 &= \sqrt{\frac{\epsilon_0}{\mu_0}} \sum_{n=-\infty}^{+\infty} \exp(jk_{xn}x) [A_n \exp(-jk_{zn}z) + B_n \exp(jk_{zn}z)]
 \end{aligned} \tag{2-15}$$

Where A_n and B_n are the incident (-z direction) and reflected (z direction) field amplitude, respectively. The x component of incident wave vector $k_x = 0$.

The electric field components in this layer ($0 < z < t$) are calculated automatically as,

$$\begin{aligned}
 E_x(x; z | \omega) &= \sum_{n=-\infty}^{+\infty} \exp(jk_{xn}x) E_{xn}(z | \omega) = \frac{-j}{\omega \epsilon_0 \epsilon_{xx}(x | \omega)} \frac{\partial H_y(x; z | \omega)}{\partial z} \\
 E_z(x; z | \omega) &= \sum_{n=-\infty}^{+\infty} \exp(jk_{xn}x) E_{zn}(z | \omega) = \frac{j}{\omega \epsilon_0 \epsilon_{zz}(x | \omega)} \frac{\partial H_y(x; z | \omega)}{\partial x}
 \end{aligned} \tag{2-16}$$

The dielectric constant in the form of Fourier series

$$\begin{aligned}
 \epsilon_{xx}(x | \omega) &= \sum_{n=-\infty}^{+\infty} \epsilon_n(\omega) \exp(j \frac{2\pi n}{L} x) \\
 \epsilon_n(\omega) &= \frac{1}{L} \int_0^L \epsilon_{xx}(x | \omega) \exp(-j \frac{2\pi n}{L} x) dx
 \end{aligned} \tag{2-17}$$

For the specific problem here, the metal is rectangular in the cross section x-z. The frequency domain Fourier component $\epsilon_n(\omega)$ has its explicit expressions. The permittivity in function of the position x can be expressed as:

$$\epsilon(x | \omega) = \begin{cases} \epsilon_1(\omega), & nL < x < nL + W, \text{ for metal} \\ 1, & nL + W < x < (n+1)L, \text{ for air} \end{cases} \tag{2-18}$$

With its Fourier component:

$$\epsilon_n(\omega) = \begin{cases} 1 + \frac{W}{L} (\epsilon_1(\omega) - 1) & n = 0 \\ \left(\epsilon_1(\omega) - 1 \right) \frac{1 - \exp(-j \frac{2\pi n}{L} W)}{j 2\pi n} & n \neq 0 \end{cases} \tag{2-19}$$

Similar expressions for the reciprocal of the permittivity,

$$\begin{aligned}
 \left(\frac{1}{\epsilon_{xx}} \right)(x | \omega) &= \sum_{n=-\infty}^{+\infty} \left(\frac{1}{\epsilon} \right)_n (\omega) \exp(j \frac{2\pi n}{L} x) \\
 \left(\frac{1}{\epsilon} \right)_n (\omega) &= \frac{1}{L} \int_0^L \left(\frac{1}{\epsilon_{xx}} \right)(x | \omega) \exp(-j \frac{2\pi n}{L} x) dx
 \end{aligned} \tag{2-20}$$

The second order wave function for H_y is,

$$H_y(x; z | \omega) = \frac{1}{j\omega\mu_0} \left(\frac{\partial E_x(x; z | \omega)}{\partial z} - \frac{\partial E_z(x; z | \omega)}{\partial x} \right) \quad (2-21)$$

In numerical calculation, the sum expressions should be truncated to a value of n_{max} , which stands for the maximum order of scattering waves included in the entire system. After substituting $E_{xn}(z | \omega)$ and $E_{zn}(z | \omega)$ in the function (2-21), and following the Fourier factorization described in [Li1996] to get better numerical convergence, we have to calculate an eigenvalue problem to solve the z-component of the wavevector in the grating region,

$$-k_z^2 C_n = \left\langle \frac{1}{\epsilon} \right\rangle^{-1} \left(diag(k_{xn}) \langle \epsilon \rangle^{-1} diag(k_{xn}) - \frac{\omega^2}{c^2} diag(I) \right) C_n \quad (2-22)$$

Where $\langle M \rangle$ stands for the $(2n_{max}+1) \times (2n_{max}+1)$ matrix with its (p,q) entry $M_{p,q}$ given by the Fourier component of dielectric or the reciprocal of dielectric. $diag(k_{xn})$ is a diagonal matrix with the non zero element k_{xn} , $diag(I)$ is the $(2n_{max}+1) \times (2n_{max}+1)$ unit matrix and the eigenfunction C_n is a column vector. The $2n_{max}+1$ eigenvalues $k_z l$ ($l = 1, 2, \dots, 2n_{max}+1$) and the corresponding vectors C_{nl} finally will appear in the EM field expression,

$$\begin{aligned} H_y(x; z | \omega) &= \sqrt{\frac{\epsilon_0}{\mu_0}} \sum_{n=-\infty}^{+\infty} \exp(jk_{xn}x) H_{yn}(z | \omega) \\ &= \sqrt{\frac{\epsilon_0}{\mu_0}} \sum_l \sum_n \exp(jk_{xn}x) C_{nl} [A_l \exp(-jk_{zn}(z - z_l)) + B_l \exp(jk_{zn}(z - z_l))] \end{aligned} \quad (2-23)$$

Once the EM distribution and wave vector are calculated in the grating layer, the spectrum of the transmission, reflection, and absorption spectrum of the whole system responding to incident THz wave can be obtained by the standard transfer matrix method developed for a multi-layers system and easily implanted in matrix form by a computer program [Wendler1999].

Since the other materials are homogenous, there are no variation of permittivity in x and y directions, and the z component of wave vector in these layers are given directly according to the wave equation,

$$k_{zn} = \sqrt{\frac{\epsilon_{xx}(\omega)}{\epsilon_{zz}(\omega)} (\epsilon_{zz}(\omega) \frac{\omega^2}{c^2} - k_{xn}^2)} \quad (2-24)$$

In our simulation, $n_{max} \geq 20$ in the grating layer is sufficient to achieve a better convergence criteria ($\max(\Delta T) < 10^{-6}$). The field amplitudes A_n and B_n in each material layer are linked by the boundary conditions (continuity of E_x and H_y at the surface and interfaces). By applying suitable initial excitations, the spectrum are given by the corresponding field amplitudes of the $n=0$ order wave in the semi-infinite air ($z > t$) and substrate GaN (see Figure 2-9).

$$T = \frac{|A_{n=0}^{\text{substrate}}|}{\sqrt{\epsilon_s} |A_{n=0}^{\text{air}}|}, R = \frac{|B_{n=0}^{\text{air}}|}{|A_{n=0}^{\text{air}}|}, A = 1 - T - R \quad (2-25)$$

Now the only unknown parameter in the calculation is the model of 2DEG. Two models are classified according to its thickness value.

I Quasi-2D plasmon

When the 2DEG layer has a finite and small thickness as in actual heterostructures, the CWM method is employed to investigate the dispersion and spectrum based on an anisotropic 2DEG permittivity and the results will be compared with the software HFSS based on FEM.

A CWM method

To include the 2DEG layer with a typical thickness of about 10 nm in the calculation, one needs the dielectric model of 2DEG in THz range. As illustrated previously, the motion of electrons in the plane x-y perpendicular to the growth axis is quasi free, so the Drude type permittivity model for free electrons in the metal (section 2.2.1) can be modified and implanted as the 2DEG model with finite thickness. Assuming the majority electrons are confined at the lowest state E_0 (Figure 2-2) and the smallest intersubband separation ($E_1 - E_0$) is larger than the submillimeter wave or THz excitation energy at 300 K, the intersubband transitions will not be considered in the motion of electrons in z direction. The properties of 2DEG in the z direction conserve those of the materials where QW locates. The frequency dependent permittivity of 2DEG is expressed by a local diagonal tensor [Wendler1999],

$$\epsilon = \begin{pmatrix} \epsilon_{xx} & 0 & 0 \\ 0 & \epsilon_{yy} & 0 \\ 0 & 0 & \epsilon_{zz} \end{pmatrix} \quad (2-26)$$

With the non-zero diagonal components,

$$\epsilon_{xx}(x|\omega) = \epsilon_{yy}(x|\omega) = \epsilon_s + \frac{j\sigma_{3D}(x|\omega)}{\omega\epsilon_0} \quad (2-27)$$

$$\epsilon_{zz} = \epsilon_s$$

And the three dimensional conductivity in S/m,

$$\sigma_{3D}(x|\omega) = \frac{N_s(x)e^2\tau}{m * d_{2DEG}(1 - j\omega\tau)} \quad (2-28)$$

Where ϵ_s is the static relative permittivity of the substrate (GaN in Figure 2-9). d_{2DEG} is the 2DEG layer thickness, or QW width. $N_s(x)$ is the electron sheet density distribution in the x direction. For a homogeneous 2DEG concentration, we have $N_s(x) = N_s$, where N_s is calculated by the self consistent Schrödinger-Poisson solutions described in section 2.2.2. $\tau = \mu_{2DEG}m^*/e$ is the phenomenological relaxation time and μ_{2DEG} is the electron mobility.

B FEM Method

The coupled wave method (CWM) integrated in the transfer matrix approach is a numerical model well suited for the periodic grating problems in the multi-layers system. Other methods are also available, such as the commercial code ANSOFT HFSS (www.ansoft.com) based on finite element method (FEM) in the frequency domain and CST Microwave Studio (www.cst.com) using finite integration technique (FIT) in the time domain. These commercial software are user friendly and versatile and address a large amount of physical problems. Many kind of boundary conditions are available..

Figure 2-11 illustrates the 3D model simulated in HFSS for an infinite heterostructure with periodic metallic grating on top of the barrier layer. With the specific Master/Slave boundary conditions around the peripheral four surfaces and Floquet excitation ports (Port 1 and 2 on top and at the bottom surfaces), only one of the multiple periods of structure (unit cell) needs to be modeled and one has to assign the material attributes to 3D models in the whole structure: 3D conductivity for the metal, and the relative permittivity and dielectric loss tangent (nonzero for 2DEG and zero for the barrier and substrate in this work) for the other volume layers. The whole configuration is infinite in the x-y plane (periodic in x and infinite in y direction) and the excitation signal is TM polarized plane wave with variable incident angle. This is consistent with the boundary conditions and the properties of the excitation wave assumed in the CWM. The spectra are calculated through the standard scattering parameters S, which are equivalent to the expression (2-25).

$$T = (S_{21})^2, R = (S_{11})^2, A = 1 - R - T \quad (2-29)$$

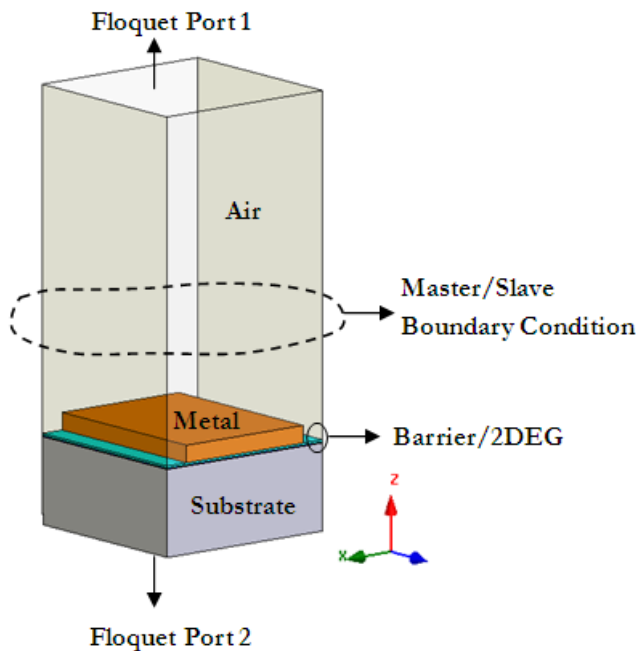


Figure 2-11: HFSS model for a heterostructure with periodic metallic grating

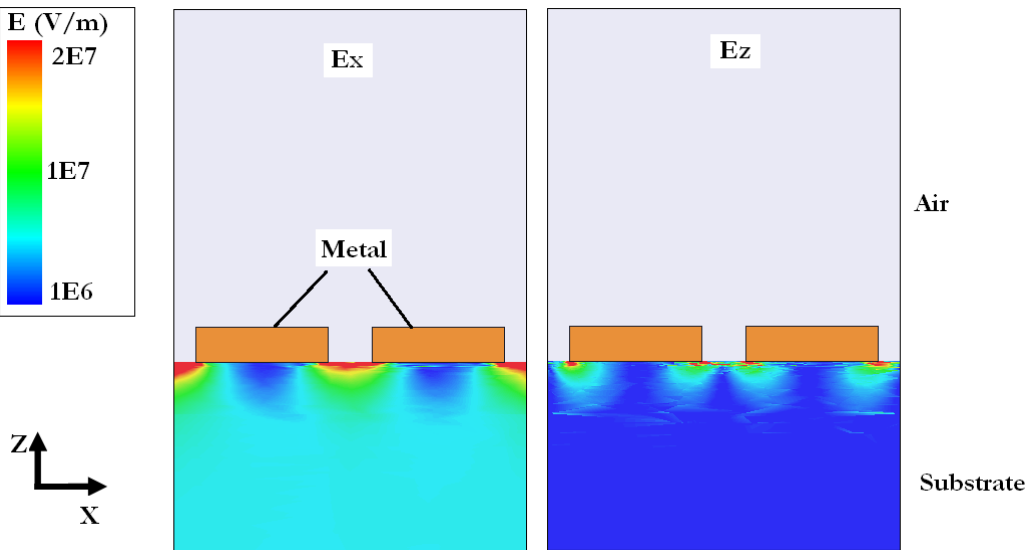


Figure 2-12: HFSS simulated distribution of electric field E_x and E_z in the vicinity of metal grating, $f = 1 \text{ THz}$, $L = 1 \mu\text{m}$, $W/L = 0.75$, TM polarization and normal incidence

HFSS has allowed to clarify the evanescent nature of the scattered waves, which express as the resonances in the spectra. In Figure 2-12, the distribution of the E_x and E_z components of the scattering waves in HFSS is shown to locate in the vicinity of the periodic grating and decay rapidly from the interface. The normally incident wave is TM polarized at 1 THz. The dimensions of grating are $L = 1 \mu\text{m}$ and $W = 0.75 \mu\text{m}$. The effective electric field component possibly interacting (E_x) with longitudinal plasma wave is strengthened in the gap region between grating finger, particular at the interface air/substrate. Below the metal center, electric field is weak because the conductor thickness ($t = 200 \text{ nm}$) is much higher than the Au skin depth (79.5 nm, $\sigma_{\text{Au}} = 4.1 \times 10^7 \text{ S/m}$) at 1 THz and little field can penetrate through the metal. Far away from the interface, only the propagating wave ($n = 0$) exists, which has E_x but no E_z component. The evanescent waves ($n > 0$) have both E_x and E_z , and the penetration depth of these waves into the substrate can be clearly demonstrated by the right figure. Therefore, the 2DEG layer should be close to the grating in order to couple efficiently with these evanescent fields.

C Screened and unscreened quasi-2D plasmon

In the domain, one used to distinguish two special cases of quasi-2D plasmon [Shur2003, Popov2010] for theoretical investigation. One is the unscreened plasmon ($W/L = 0$), where the top material is air. The other is the screened plasmon ($W/L = 1$), where the top material is metal. For the two types of plasmon, explicit, simple and useful dispersion relations of PP will be derived under certain assumptions. They can be considered as the limit cases for a normal grating structure discussed above with $0 < W/L < 1$ and their dispersions provide qualitative guidance for the behavior of PP dispersion with grating. However, the screened and unscreened plasmon can hardly be observed experimentally without grating coupler.

For each case, the composition of the layered structure will be clarified and followed by a rigorous EM analysis. Analytic expressions of PP dispersion are derived and their simplified forms under assumptions are discussed.



Figure 2-13: Screened and unscreened multi-layers structure with finite thickness 2DEG

The finite 2DEG layer ($d_{2\text{DEG}}$) is sandwiched between the barrier AlGaN and the semi-infinite substrate GaN. On top of the barrier, a semi-infinite thick air ($W/L = 0$) or metal ($W/L = 1$) is modeled. The multi-layer structure in the calculation is shown in Figure 2-13.

The procedure of numerical calculation without grating is as follows: Firstly, the EM field in each layer (finite and semi-infinite) is expressed based on the permittivity models inserted into the Maxwell equations. Then the field amplitudes in two adjacent layers are linked by the boundary conditions at the interface (the tangential components of electric and magnetic fields are continuous). Finally, the dispersion relation of the whole system is equivalent to the non trivial solution of an eigenvalue equation, assuming no incident field from the top material 1. The spectrum information is obtained by the ratio of Poynting power flux in the semi-infinite bottom and top layers.

The electric field polarization in each material is assumed to be TM type: $\vec{E} = (E_x, 0, E_z), \vec{H} = (0, H_y, 0)$. The electric field can be obtained by the magnetic component

$$E_x = \frac{-j}{\omega\epsilon_0\epsilon_{xx}} \frac{\partial H_y}{\partial z} \quad \text{and} \quad E_z = \frac{j}{\omega\epsilon_0\epsilon_{zz}} \frac{\partial H_y}{\partial x} \quad (2-30)$$

Where the material is supposed to be anisotropic. For isotropic material, $\epsilon = \epsilon_{xx} = \epsilon_{yy} = \epsilon_{zz}$.

From the Maxwell equations, the EM components in layer 1 (semi-infinite air or metal) are

$$\begin{cases} H_{y,1} = H_1 \exp[j(kx - \omega t) - \alpha_1 z] \\ E_{x,1} = \frac{j\alpha_1}{\omega\epsilon_0\epsilon_1} H_1 \exp[j(kx - \omega t) - \alpha_1 z] \\ E_{z,1} = \frac{-k}{\omega\epsilon_0\epsilon_1} H_1 \exp[j(kx - \omega t) - \alpha_1 z] & \text{for } z > d + d_{2DEG} \\ \alpha_1 = \sqrt{k^2 - \epsilon_1 \frac{\omega^2}{c^2}} \end{cases} \quad (2-31)$$

where k is the wavevector in the x direction, α_1 is the attenuation constant in semi-infinite material 1, which is positive to ensure that the wave is decaying in the $+z$ direction. No wave propagates in the $-z$ direction due to the semi-infinite material. For layers with finite thickness, propagating constants are not zero in both $+z$ and $-z$ directions. The field in layer 2 (AlGaN) and layer 3 (QW) are given as,

$$\begin{cases} H_{y,2} = (H_2 \exp(\alpha_2 z) + H'_2 \exp(-\alpha_2 z)) \exp[j(kx - \omega t)] \\ E_{x,2} = \frac{-j\alpha_2}{\omega\epsilon_0\epsilon_2} (H_2 \exp(\alpha_2 z) - H'_2 \exp(-\alpha_2 z)) \exp[j(kx - \omega t)] \\ E_{z,2} = \frac{-k}{\omega\epsilon_0\epsilon_2} (H_2 \exp(\alpha_2 z) + H'_2 \exp(-\alpha_2 z)) \exp[j(kx - \omega t)] & \text{for } d_{2DEG} < z < d + d_{2DEG}, \\ \alpha_2 = \sqrt{k^2 - \epsilon_2 \frac{\omega^2}{c^2}} \end{cases} \quad (2-32)$$

and

$$\begin{cases} H_{y,3} = (H_3 \exp(\alpha_3 z) + H'_3 \exp(-\alpha_3 z)) \exp[j(kx - \omega t)] \\ E_{x,3} = \frac{-j\alpha_3}{\omega\epsilon_0\epsilon_{xx}} (H_3 \exp(\alpha_3 z) - H'_3 \exp(-\alpha_3 z)) \exp[j(kx - \omega t)] \\ E_{z,3} = \frac{-k}{\omega\epsilon_0\epsilon_{zz}} (H_3 \exp(\alpha_3 z) + H'_3 \exp(-\alpha_3 z)) \exp[j(kx - \omega t)] & \text{for } 0 < z < d_{2DEG}. \\ \alpha_3 = \sqrt{\left(k^2 - \epsilon_{zz} \frac{\omega^2}{c^2} \right) \frac{\epsilon_{xx}}{\epsilon_{zz}}} \end{cases} \quad (2-33)$$

Where α_2 and α_3 are the attenuation constants in the barrier and QW layers, respectively. For 2DEG layer, the anisotropic permittivity model is used. All other layers are assumed to be isotropic. The field in the layer 4 (semi-infinite substrate GaN) should decay in the $-z$ direction.

$$\begin{cases} H_{y,4} = H_4 \exp[j(kx - \omega t) + \alpha_4 z] \\ E_{x,4} = \frac{j\alpha_4}{\omega\epsilon_0\epsilon_4} H_4 \exp[j(kx - \omega t) + \alpha_4 z] \\ E_{z,4} = \frac{-k}{\omega\epsilon_0\epsilon_4} H_4 \exp[j(kx - \omega t) + \alpha_4 z] \\ \alpha_4 = \sqrt{k^2 - \epsilon_4 \frac{\omega^2}{c^2}} \end{cases} \quad \text{for } z < 0. \quad (2-34)$$

In the above expressions, H_i and H'_i ($i = 1, 2, 3$ and 4) are unknown magnetic field amplitude determined by the initial conditions. At the interfaces $z = 0$, $z = d_{2DEG}$ and $z = d + d_{2DEG}$, the continuous boundary conditions are used. After a complex algebra and matrix manipulation, the dispersion relation of PP is finally expressed through an eigenvalue equation,

$$0 = \left(\frac{\alpha_1 + \alpha_2}{\epsilon_1} \right) \left(\frac{\alpha_2 + \alpha_3}{\epsilon_2} \right) \left(\frac{\alpha_3 + \alpha_4}{\epsilon_{xx}} \right) e^{\alpha_2 d + \alpha_3 d_{2DEG}} + \left(\frac{\alpha_2 - \alpha_1}{\epsilon_2} \right) \left(\frac{\alpha_3 - \alpha_2}{\epsilon_{xx}} \right) \left(\frac{\alpha_3 + \alpha_4}{\epsilon_4} \right) e^{-\alpha_2 d + \alpha_3 d_{2DEG}} + \left(\frac{\alpha_2 - \alpha_1}{\epsilon_2} \right) \left(\frac{\alpha_2 + \alpha_3}{\epsilon_2} \right) \left(\frac{\alpha_4 - \alpha_3}{\epsilon_4} \right) e^{-\alpha_2 d - \alpha_3 d_{2DEG}} + \left(\frac{\alpha_1 + \alpha_2}{\epsilon_1} \right) \left(\frac{\alpha_3 - \alpha_2}{\epsilon_{xx}} \right) \left(\frac{\alpha_4 - \alpha_3}{\epsilon_4} \right) e^{\alpha_2 d - \alpha_3 d_{2DEG}} \quad (2-35)$$

Until now, no approximations are made in deriving expression (2-35). The material permittivity can be either constant or frequency dependent. More layers can be added in the calculation following the same procedures, and the dispersion expression will become more complex. No explicit relation between the wavevector k and the frequency ω is obtained, so the dispersion relation should be solved numerically (only the real part of the frequency and the wavevector is calculated for all the dispersion curves in this work).

Based on the above expression, if the material 1 is metal, for instance, a gold layer, which corresponds to $W/L = 1$. If the material 1 is air, $\epsilon_1 = \epsilon_0$, which corresponds to $W/L = 0$ in Figure 2-9. The frequency dependent complex Drude type permittivity model can be used for metals including the damping term [Ordal1983],

$$\epsilon_1(\omega) = 1 - \frac{\omega_p^2}{\omega(\omega + j\omega_\tau)} \quad (2-36)$$

Where $\omega_\tau = \frac{1}{\tau} = 40.71 \text{ rad/s}$ is the damping frequency. τ is the electron lifetime. $\omega_p = \sqrt{\frac{ne^2}{m\epsilon_0}}$ is the plasma frequency in metal as defined in section 2.2.1. For gold, we have $\omega_{p,gold} = 1.37 \times 10^4 \text{ rad/s}$ at a free electron concentration $n = 5.86 \times 10^{28} \text{ m}^{-3}$.

Since the dispersion of PP (expression (2-35)) for a thin layer of 2DEG is still complex, some approximations will be made to simplify the equation and give explicit results.

II 2D plasmon

If the 2DEG layer thickness is much smaller than the plasmon wavevector ($k \times d_{2DEG} \ll 1$), its thickness could be ignored in EM modeling [Theis1978]. Exact 2D plasmon will be produced.

A CWM method

If $d_{2DEG} = 0$, the motion of electrons will become exactly 2D at the interface. One arrives at the simplified model of 2DEG by the sheet frequency dependent Drude type conductivity in Siemens (S) [Muravjov2010],

$$\sigma_{2D}(\omega) = \frac{N_s e^2 \tau}{m^*(1 - j\omega\tau)} \quad (2-37)$$

In this case, at the interface between the barrier and the substrate layer, the tangential component of H is no longer continuous, so the boundary conditions are modified as (see Figure 2-14),

$$\begin{cases} E_{x,2}|_{z=0} - E_{x,4}|_{z=0} = 0 \\ H_{y,2}|_{z=0} - H_{y,4}|_{z=0} = -\sigma_{2D}(\omega) E_{x,4}|_{z=0} \end{cases} \quad (2-38)$$

Then the spectrum analysis of the structure is similar to the calculation with finite 2DEG layer thickness, except for the above different boundary conditions. The detailed numerical formula will not be reproduced here, and at the last part, the 2D PP dispersion will be compared with that of the quasi-2D PP. It should be pointed out that HFSS is not able to model 2D frequency dependent complex sheet conductivity like (2-37).

B Screened and unscreened 2D plasmon

As shown in Figure 2-14, the layer 3 is now replaced by a plane at $z=0$, where 2DEG locates. Electromagnetic analysis of the structure is similar to the calculation with finite 2DEG layer thickness (quasi-2D), except that at the interface $z = 0$, the tangential magnetic field H_y is no longer continuous due to the existence of conduction electron interface. The tangential electric field E_x is still continuous.

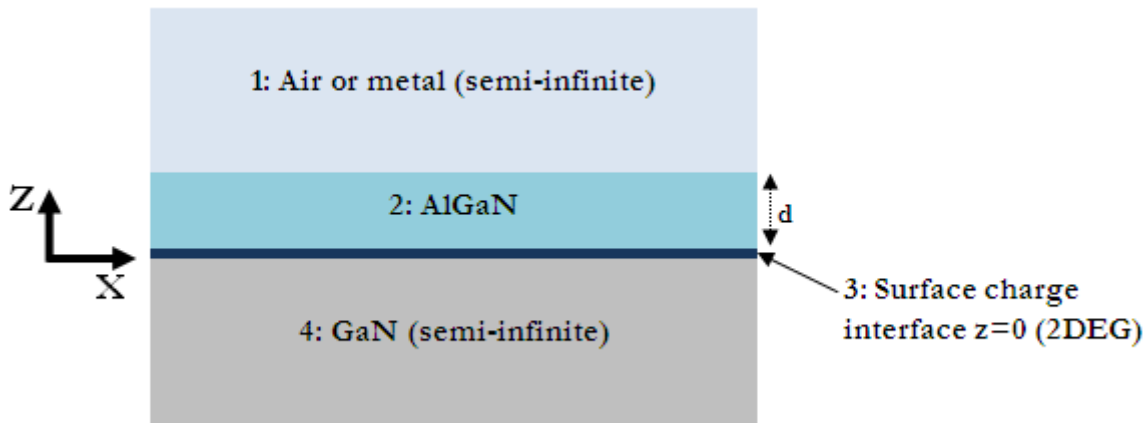


Figure 2-14: Screened and unscreened multi-layers structure with zero thickness 2DEG

The dispersion relation of exact 2D PP can be calculated by solving an eigenvalue equation, and ultimately is given explicitly as [Nakayama1974],

$$\frac{\left(\frac{\epsilon_1}{\alpha_1} + \frac{\epsilon_2}{\alpha_2}\right)\left(\frac{\epsilon_4}{\alpha_4} + \frac{\epsilon_2}{\alpha_2} - \frac{\sigma_{2D}}{j\omega\epsilon_0}\right)}{\left(\frac{\epsilon_1}{\alpha_1} - \frac{\epsilon_2}{\alpha_2}\right)\left(\frac{\epsilon_4}{\alpha_4} - \frac{\epsilon_2}{\alpha_2} - \frac{\sigma_{2D}}{j\omega\epsilon_0}\right)} = e^{-2\alpha_2 d} \quad (2-39)$$

The expression (2-39) is still so complex that it is difficult to tell the dependency of the frequency ω on the plasma wavevector k . Two assumptions are often used for deriving further explicit dispersion equations. Fortunately, both the two conditions are satisfied for normal grating dimensions (L, W) and 2DEG properties (N_s, μ_{2DEG}).

- (1) The plasmon wavevector k is much larger than the propagating wavevector in the bulk barrier and substrate materials. This is true as we have shown in Figure 2-14, because the static dielectric constant $\epsilon_{2,4}$ for the semiconductors studied here is around 10. Then one has $k \gg \sqrt{\epsilon_{2,4}}\omega/c$, or equivalently $\alpha_2 \approx \alpha_4 \approx k$ as in equation (2-32) and (2-34).
- (2) The phenomenological electron scattering time τ is larger than $1/\omega$ (ω is the frequency of incident wave). For high mobility 2DEG layer at low temperatures, the scattering time τ is around 10^{-12} s or even larger. At $f = 1$ THz, the value of $1/\omega$ is about 0.16×10^{12} s. For larger frequencies, the assumption is more reasonable. In fact, $\omega\tau > 1$ is also the condition for 2DEG responding resonantly to the THz radiation [Lü1998]. Within this approximation ($\omega\tau \gg 1$), the 2DEG sheet conductivity is purely imaginary, $\sigma(\omega) \approx \frac{je^2 N_s}{m^* \omega}$ as in equation (2-37).

For unscreened plasmon, $\epsilon_1 = 1$. The inequality $|\epsilon_1/\alpha_1| \ll |\epsilon_2/\alpha_2|$ holds, and the factor $(\frac{\epsilon_1}{\alpha_1} + \frac{\epsilon_2}{\alpha_2})/(\frac{\epsilon_1}{\alpha_1} - \frac{\epsilon_2}{\alpha_2})$ is close to -1. The dispersion relation for unscreened 2D PP is written as [Okisu1986],

$$\omega = \sqrt{\frac{e^2 N_s k}{m^* \epsilon_0} \frac{1}{\epsilon_4 + \epsilon_2 \tanh(kd)}} \quad (2-40)$$

Where ϵ_2 and ϵ_4 are the permittivity of the barrier AlGaN and the substrate GaN, respectively.

For screened plasmon, the amplitude of ϵ_1 at THz frequency is large according to the expression (2-36). The inequality $|\epsilon_1/\alpha_1| \gg |\epsilon_2/\alpha_2|$ holds at THz frequency range, and the factor $(\frac{\epsilon_1}{\alpha_1} + \frac{\epsilon_2}{\alpha_2})/(\frac{\epsilon_1}{\alpha_1} - \frac{\epsilon_2}{\alpha_2})$ is close to 1. The dispersion relation for the screened 2D PP is written as [Eguiluz1975, Meissner1976],

$$\omega = \sqrt{\frac{e^2 N_s k}{m^* \epsilon_0} \frac{1}{\epsilon_4 + \epsilon_2 \coth(kd)}} \quad (2-41)$$

For $0 < kd < \pi$, $\coth(kd)$ can be expanded into the Laurent series,

$$\coth(kd) = \frac{1}{kd} + \frac{kd}{3} - \frac{(kd)^3}{45} + \frac{2(kd)^5}{945} + \dots = \frac{1}{kd} + \sum_{n=1}^{\infty} \frac{2^{2n} B_{2n} (kd)^{2n-1}}{(2n)!} \quad (2-42)$$

Where B_n is the nth Bernoulli number.

If a further approximation $kd \ll 1$ is valid (the barrier thickness is much smaller than the 2D plasmon wavelength), then $\coth(kd) \approx \frac{1}{kd}$, therefore, the screened 2D PP dispersion is reduced to [Zheng1990],

$$\omega = sk = \sqrt{\frac{e^2 N_s d}{m^* \epsilon_2 \epsilon_0}} k \quad (2-43)$$

Where $s = \sqrt{\frac{e^2 N_s d}{m^* \epsilon_2 \epsilon_0}}$ is the plasma phase velocity. In this limit case, the plasmon frequency is proportional to the plasmon wavevector. For a typical AlGaN/GaN heterostructure, $s = 2.1 \times 10^6$ m/s with a concentration $N_s = 1.2 \times 10^{17}$ m⁻².

2.3.3.2 CWM analysis of PP with 2D grating

Metal grating are used only as the coupling element. The effects of metal thickness on the coupling efficiency are expected to be as small as possible. The incident wavelength should be larger than the thickness of the metallization and the width of QW. Thus, the problem can be ideally considered to be the coupled response of the planar grating conductor and the 2DEG sheet surface [Zheng1990]. When the metal thickness is comparable to the grating period [Zheng1991], it begins to influence the transmission spectrum.

In the 2D grating case, the magnetic component H_y is not continuous at the interface between the upper semi-infinite air and the barrier layer AlGaN. The sheet conductivity (in Siemens) is periodic along the x direction. The conductivity follows the frequency dependent Drude type $\sigma_i(\omega)$ for metals, and is null in the air region.

$$\begin{aligned} \sigma(x | \omega) &= \sum_{n=-\infty}^{+\infty} \sigma_n(\omega) \exp(j \frac{2\pi n}{L} x) \\ \sigma_n(\omega) &= \frac{1}{L} \int_0^L \sigma(x | \omega) \exp(-j \frac{2\pi n}{L} x) dx = \begin{cases} \frac{W}{L} \sigma_1(\omega) & n = 0 \\ \sigma_1(\omega) \frac{1 - \exp(-j \frac{2\pi n}{L} W)}{j 2\pi n} & n \neq 0 \end{cases} \end{aligned} \quad (2-44)$$

At the interface $z=0$ between air and the barrier layer, the boundary conditions have

$$\begin{cases} H_y^{(air)}(x; z=0 | \omega) - H_y^{(barrier)}(x; z=0 | \omega) = -J_x(x; z=0 | \omega) \\ E_x^{(air)}(x; z=0 | \omega) - E_x^{(barrier)}(x; z=0 | \omega) = 0 \end{cases} \quad (2-45)$$

Where the surface current is given by

$$J_x(x; z=0 | \omega) = \sum_{n=-\infty}^{+\infty} \sigma_n(\omega) \exp(j \frac{2\pi n}{d} x) E_x(x; z=0 | \omega) \quad (2-46)$$

These expressions relate the field amplitudes in each layer. The transfer matrix method described above for 3D grating can be also applied for the spectroscopic calculation with zero metal thickness (2D grating). The spectrum results will be presented in the following section.

2.3.4 Results and discussions

In this part, numerical dispersion and spectrum results of AlGaN/GaN heterostructures calculated in the frame of models described above are shown. Firstly, the comparisons will be made between CWM and FEM assuming 3D grating and quasi-2D plasmon. Then the simulated dispersion of PP by CWM is compared to the theoretical dispersion of 2D plasmon in infinite GaN and the approximate formula of totally screened and unscreened 2D plasmon. Both similarities and discrepancies are presented and discussed.

2.3.4.1 Comparison between CWM and FEM

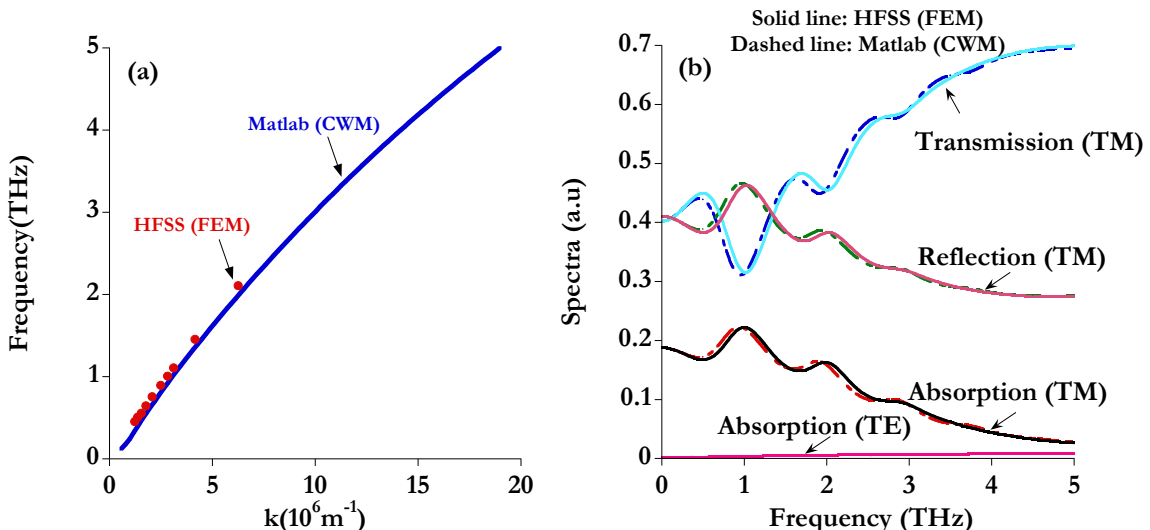


Figure 2-15: Comparisons of HFSS (FEM) and CWM calculated dispersions of (a) plasmon-polariton and (b) spectra ($L = 2.2 \mu\text{m}$, $k = 2.86 \cdot 10^6 \text{ m}^{-1}$, TM and TE polarizations) for AlGaN/GaN heterostructure at 300K, $N_s = 1.2 \times 10^{17} \text{ m}^{-2}$, $W/L = 0.75$, and $d = 25 \text{ nm}$

The PP dispersions with metallic grating are obtained by tracing the resonant frequency in the spectrum in function of the wavevector k (or the grating period L). In Figure 2-15, the comparisons of the PP dispersions (a) and spectra (b) have been made between HFSS (FEM) and CWM for AlGaN/GaN heterostructure at 300K with the electron sheet density $N_s = 1.2 \times 10^{17}$

m^2 . The 2DEG layer thickness is $d_{\text{2DEG}} = 12 \text{ nm}$. The electron mobility is $\mu_{\text{2DEG}} = 0.2 \text{ m}^2/\text{Vs}$ at 300 K. Metal grating are assumed to be gold with a conductivity $\sigma_{\text{Au}} = 4.1 \times 10^7 \text{ S/m}$. Its geometrical dimensions are: period $L = 2.2 \mu\text{m}$, metal filling factor $W/L = 0.75$ and metal thickness $t = 200 \text{ nm}$. The choice of the values of these parameters will be justified in section 2.4.

The incident wave is TEM type from the air region and its electric field can be polarized either in TE (electric field in y direction) or in TM (electric field in x direction) when the incident angle $\theta = 0^\circ$ (normal incidence). The frequency range is from 0 to 5 THz. All layers are assumed to extend infinitely in the x-y plane. The substrate GaN is assumed to be infinitely thick. Both the barrier and the substrate layers are modeled as the static dielectric constant without loss tangent (imaginary part is null). Figure 2-15 (a) shows the PP dispersions with the two methods by varying the grating period L and recording the first resonant frequency f_1 at normal excitation of a TM polarized wave, where the wavevector $k = 2\pi/L$.

The good agreement of dispersions validates the correctness of the CWM, and the consistency will be further proved by the spectra information. Figure 2-15 (b) demonstrates that, at TM polarizations, there are resonances peaks or valleys at the same positions on the three spectra: transmission, reflection and absorption. The coupling between incident THz radiation and 2D plasmon takes place at these resonant frequencies ($f_1 \approx 1 \text{ THz}$, $f_2 \approx 2 \text{ THz}$ and $f_3 \approx 3 \text{ THz}$). The resonant amplitudes reflect the coupling efficiency. The discrete resonant frequencies are selected by the different wavevector in x direction $k_{xn} = 2\pi n/L$ of the scattered wave. While for TE polarization, no absorption peaks appear due to the zero electric components in x direction. The small nonzero absorption is caused only by the conduction loss in the metal grating. In order to carried out the coupling, the incident electric field should be directed perpendicularly to the metal strips, and its wavevector is modulated by the periodic grating.

There is no doubt that the calculation with HFSS owns benefit of intuitive visual representation, especially for the EM field illustration. However, CWM has some advantages over FEM in HFSS: easy parametric variation, fast convergence and simulation time (this is why only several discrete points by HFSS are shown in Figure 2-15 (a)), convenient modeling for the inhomogeneous 2DEG distribution which will be illustrated in section 2.6. Last but not least, CWM is able to model 2D plasmon with frequency dependent sheet conductivity, while this cannot be treated by HFSS. Since both the two methods give the same dispersions and spectra results for the same structure under study, we will not distingue the results calculated by FEM or CWM, except for the non uniform 2DEG with gradual distribution functions in section 2.6.

2.3.4.2 Dispersion of Plasmon-Polariton

Now we concentrate on the influences of the finite thickness of 2DEG layer on the PP dispersion relations obtained by CWM. The results calculated by HFSS for 3D grating and quasi-2D plasmon validate the CWM results as demonstrated above. The dispersions for screened ($W/L = 1$) and unscreened PP ($W/L = 0$) in expression (2-39) are solved by a complex root finding program based on the Newton-Raphson algorithm [Ben1966]. They are compared with the dispersion of PP with grating ($W/L = 0.75$).

Figure 2-16 shows the complete dispersion curves for 2D plasmon in homogeneous GaN and dispersion of PP in AlGaN/GaN heterostructure, where 2DEG layer thickness has a finite

thickness (anisotropic permittivity) or no thickness (sheet conductivity). Three regions can be defined on top of the barrier AlGaN: a screened zone (continuous layer with infinitely thick metals), an unscreened zone (open surface with infinitely thick air) or a partially screened zone (filling factor $W/L = 0.75$ for example). The dispersion of a unscreened PP is close to the dispersion of 2D plasmon in infinite GaN, but it is difficult to observe experimentally the unscreened PP dispersion.

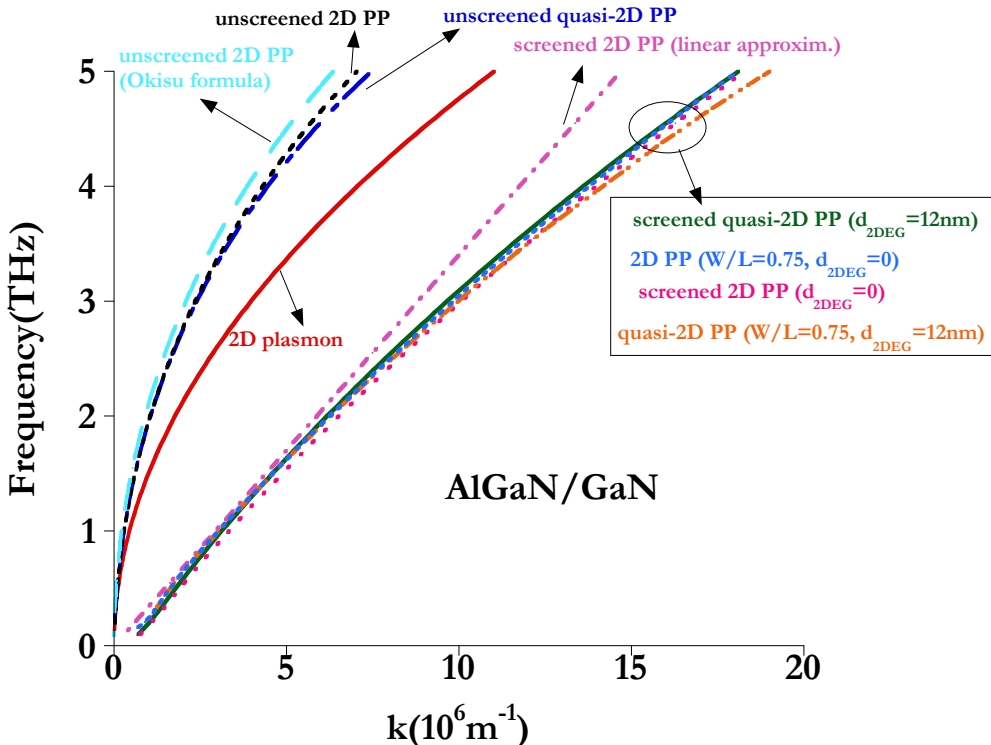


Figure 2-16: Dispersions of PP for screened ($W/L = 1$), unscreened ($W/L = 0$) and partially screened ($W/L = 0.75$) heterostructure AlGaN/GaN with 12nm thickness (quasi-2D) and zero thickness (2D) 2DEG layer. $N_s = 1.2 \times 10^{17} \text{ m}^{-2}$, $L = 2.2 \mu\text{m}$, and $d = 25 \text{ nm}$. Dispersion of 2D plasmon in infinite GaN dielectric is plotted for reference (expression (2-14), $N_s = 1.2 \times 10^{17} \text{ m}^{-2}$)

The approximations of zero thickness 2DEG and the Okisu formula (2-40) also give the similar results in the plasmon wavevector range k , because the following assumptions to derive the expression (2-40) are valid in the simulations: $k \times d_{2\text{DEG}} \ll 1$, $k \gg \sqrt{\epsilon_{\text{AlGaN},\text{GaN}}} \omega/c$, $\omega\tau \gg 1$, and $|\epsilon_0/\alpha_0| \ll |\epsilon_{\text{AlGaN}}/\alpha_{\text{AlGaN}}|$, where α is the attenuation constant as defined in (2-32) and (2-34).

On the other hand, we turn to the lower part in this figure. The screened PP frequency ω is proportional to k at low wavevector ($\omega \propto k$) and proportional to \sqrt{k} at high wavevector ($\omega \propto \sqrt{k}$) (lowest four curves in Figure 2-16) where the 3D metal thickness is $t = 200 \text{ nm}$ and the metal conductivity is $4.1 \times 10^7 \text{ S/m}$. Again, the screened PP dispersions with $d_{2\text{DEG}} = 0$ (screened 2D PP) and $d_{2\text{DEG}} = 12 \text{ nm}$ (screened quasi-2D PP) do not make remarkable differences because the product $k \times d_{2\text{DEG}}$ is well below 1 using the grating with micrometer periodicity. Grating-assisted PP at $W/L = 0.75$ shows similar results as the totally screened PP, demonstrating the plasmons between the metal fingers do not play an important role as the

plasmons below the metals in this case. The linear approximation formula fails to predict the dispersion in high wavevector region because of the relation $k \times d \ll 1$ is no longer valid, where $d = 25$ nm is the thickness of AlGaN.

Finally, it should be pointed out that the PP dispersions with 2D grating ($t = 0$) are as the same as those of 3D grating with finite metal thickness at $W/L = 0.75$, no matter whether the quasi-2D or 2D plasmons is modeled. These results are not shown for the clarity of the Figure 2-16. Similar PP dispersion relations have been experimentally observed for the emission spectrum in AlGaAs/GaAs heterojunctions with metal grating [Hirakawa1995]. Although only the results of AlGaN/GaN are shown, the same conclusions also apply to other heterostructures under study.

2.3.5 Conclusions

In summary, the general numerical method of spectrum analysis of grating assisted 2D plasmon in heterostructures has been presented in detail. Both zero and nonzero thicknesses of grating and 2DEG layer are considered. Spectra calculated by HFSS and CWM show the same results, validating the accuracy of CWM developed during this work. Dispersion of PP differs from that of 2D plasmon embedded in an infinite substrate. Theoretical simplified formula can give correct PP dispersion if the conditions of plasma wavelength is satisfied: $k \times d_{\text{2DEG}} \ll 1$ and $k \times d \ll 1$.

2.4 Optimization of resonant THz detection of PP in the heterojunctions III-V and IV-IV

Based on the anisotropic permittivity model of 2DEG layer, a parametric study of the influences of geometrical dimensions and material properties on the resonances (frequencies and amplitudes) in the absorption spectra have been done to find the optimal structure showing strongest resonances at room and cryogenic temperatures. Although the parametric study is mainly realized in HFSS by default, CWM also gives the same results.

2.4.1 Parameters of the studied structures

The heterostructures under study are III-V group (type I: AlGaN/GaN, InAlN/GaN and AlGaAs/GaAs) and IV-IV group (type II: SiGe/Si/SiGe). In the latter structure, the Si QW layer is a biaxially strained Si layer on relaxed SiGe buffer. The electric field of incident wave is TM polarized, which is prerequisite for the coupling of PP as demonstrated in Figure 2-15. The substrate materials GaN, GaAs or SiGe are modeled as semi-infinite semiconductors without losses (the loss tangents are null). If the parameters in the simulations are not mentioned explicitly, their values are by default : the 2DEG layer thickness is $d_{\text{2DEG}} = 12$ nm, incident angle $\theta = 0^\circ$, metal thickness $t = 200$ nm, metal conductivity $\sigma_{\text{Au}} = 4.1 \times 10^7$ S/m. Table 2-2 lists the nominal heterostructure parameters taken from the following publications [Aniel1996, Aniel2000, Richard2004, Richard2005, Paul2004, Dyakonov1996-2, Poisson2006, Poisson2010, Ismail1995, Takakuwa1986, Fischer1984, Nelson1993]. The choice of L will be explained in section 2.4.3. At present, we assume that the 2DEG distribution over one period of the grating is uniform ($N(x) = N_s$), and the non homogeneous case will be discussed in section 2.6.

Table 2-2: Simulation parameters for the four nominal heterostructures

Material	m^*/m_0	$N_s (10^{16} m^{-2})$	L (μm)	W/L	$\theta (\circ)$	d (nm)	$\mu_{2\text{DEG}} (\text{m}^2/\text{Vs})$	
							300 K	77 K
AlGaN/GaN	0.22	12	2.2	0.75	0	25	0.2	1.0
InAlN/GaN	0.22	12	1.55	0.75	0	10	0.11	0.33
SiGe/Si/SiGe	0.19	5	1.3	0.75	0	25	0.3	3.2
AlGaAs/GaAs	0.063	1	1.0	0.75	0	25	0.8	5

2.4.2 Absorption of PP

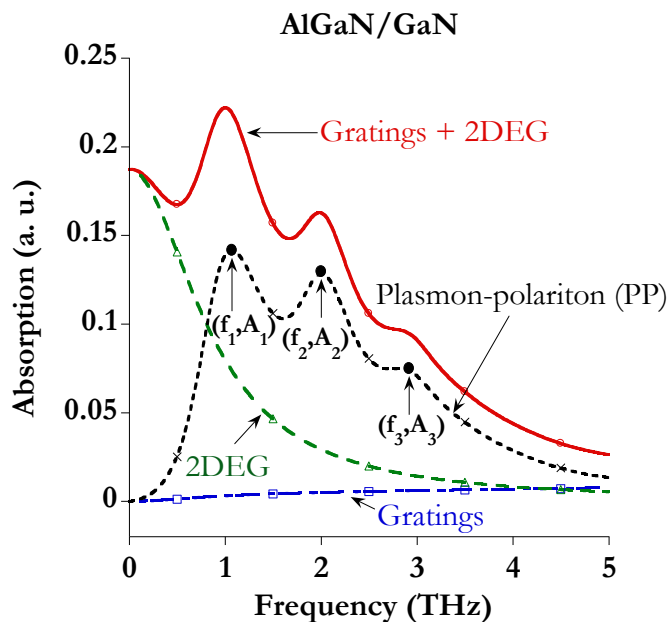


Figure 2-17: Separated different types of absorptions in the nominal heterostructure AlGaN/GaN at room temperature with $W/L = 0.75$ by HFSS

The absorption spectrum for the multi-layers system with lossy metallic grating and 2DEG can be decomposed into independent three parts: the Drude background absorption due to 2DEG without grating, the absorption due to conduction loss in the grating and the resonant absorption due to the PP coupling. The latter is used as a key parameter to evaluate the coupling efficiency. There are not any losses in the bulk barrier and substrate materials. Figure 2-17 shows the different absorption spectrum in material AlGaN/GaN with $W/L = 0.75$ at 300 K. The conduction loss in this case is negligible and the Drude type absorption dominates at low frequencies. The PP absorption begins as zero at DC frequency and it will terminate as zero at very large frequency. As we can see, there are at least three resonant peaks in the frequency range from 0 to 5 THz. The frequency positions and the amplitudes of the PP absorption peaks are noted as f_1 , f_2 , f_3 and A_1 , A_2 , A_3 , respectively. f_n are different order plasma frequency corresponding to different plasmon wavevector k_{xn} . A_n reflects the coupling amplitude of

scattered wave k_{xn} with 2D plasmons. For the following analysis, only the first three peaks (if exist) will be compared in different materials until 5 THz.

Various parametric studies have been lead to optimize the PP resonances. We analyzed the following influences: the period L of the metallic grating, the incident angle θ between 0° and 89° , the metal thickness t and the metal (gold) conductivity σ_{Au} , the temperature (300 K and 77 K), the electron surface concentration N_s , the barrier thickness d, or the distance between the grating and the 2DEG layer, and the filling factor W/L at 0.25, 0.5, 0.6 and 0.9. In each section, only one parameter is varied, and the values of the other parameters are listed by default in the Table 2-2.

2.4.3 Tunability of the resonant frequency versus the grating period

For the ease of comparison of the absorption amplitudes A_n between different materials, the first peak position f_1 is fixed at 1THz, and the other two resonant frequencies will slightly derivate from 2 THz and 3 THz due to the non linear PP dispersion behavior at high frequency as already seen in Figure 2-17.

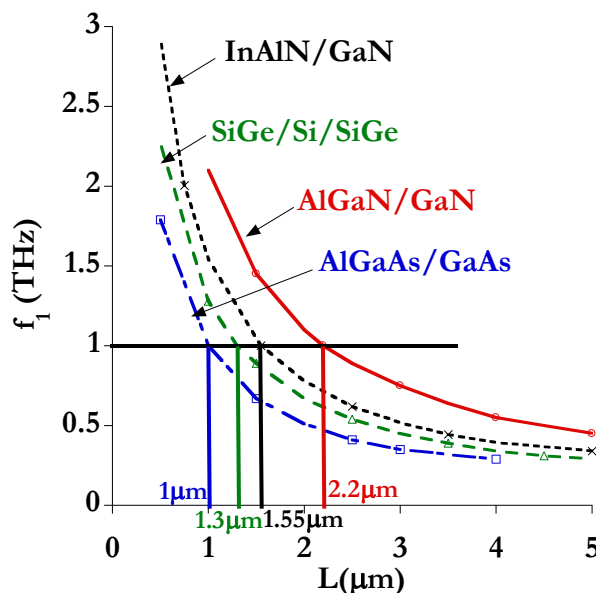


Figure 2-18: Tunability of the grating period L on the first resonant peak f_1 for the four heterostructures at 300 K and W/L = 0.75

The PP dispersion frequency is approximately proportional to the square root of the in-plane wave vector k_{xn} for plasmon without surface metallization [Okisu1986], and is proportional to k_{xn} for plasmon overlaid by continuous metals [Egiziluz1975]. Figure 2-18 plots f_1 in function of the period L for the four nominal materials at 300K with W/L = 0.75. The approximated relation holds [Muravjov2010, Hirakawa1995]: $f_1 \sim 1/L$ at this high filling factor.

Of course, the high order resonances at f_2 (or f_3) can also been tuned by L via high order scattered wavevector $k_{xn} = kx + 2\pi n/L$ ($n = 2$ or 3). At most cases, the first peak at f_1 is the most pronounced and is easily distinguished and recorded in the spectrum. The resonant frequency can be tuned in THz range [0.3-3] THz by the period L in micrometers [0.5-5] μm . If $f_1 = 1$ THz, the corresponding grating period of the four investigated structures are listed in Table 2-2. For III-V

nitride based materials, L is higher, because of their larger carrier concentrations which tend to make the resonant frequency higher.

However, two limit cases about the value of the period L should be distinguished and discussed:

(1) When L is extremely small ($\leq 0.5 \mu\text{m}$), the evanescent electric fields will be more confined at the vicinity the metal/barrier interface and the attenuation depth of the scattering wave becomes short. The amplitude of EM field reaching the 2DEG layer is not sufficient to interact with it and correspondingly the coupling becomes inefficient because the attenuation depth is equivalent or even larger than the barrier thickness d. For example, if $L = 0.1 \mu\text{m}$, the wave vector of the first evanescent wave ($n = 1$) in the direction x is $k_{x1} = 2\pi/L = 2\pi \times 10^7 \text{ m}^{-1}$. In the direction y, the materials are homogeneous which gives $k_{y1} = 0$. The component k_{z1} depends on k_{x1} and it is equal to $\sqrt{\epsilon_b \omega^2 / c^2 - k_{x1}^2} \approx jk_{x1} \text{ m}^{-1}$, where ϵ_b is the dielectric constant in the barrier. Thus, the field attenuation depth perpendicular to the interface is $D_1 = |k_{z1}|^{-1} = 16 \text{ nm}$. It is smaller or comparable to the barrier thickness $d = 10 \text{ nm}$ (InAlN/GaN) or 25 nm for the three other materials. For high order evanescent waves ($n > 1$), the attenuation depths ($D_n = |k_{zn}|^{-1}$) are even smaller and the observation of the PP resonances is difficult.

(2) When L is much large ($\geq 5 \mu\text{m}$), no resonant phenomena on the spectrum will appear. The reason is linked to a resonant detection condition given by $\omega\tau \gg 1$. This relation is no longer satisfied at small frequency ω . For AlGaN/GaN at 300 K, if $L = 5 \mu\text{m}$, the PP frequency is $f_1 = 0.34 \text{ THz}$, and the electron momentum relaxation time $\tau = 2.5 \times 10^{-13} \text{ s}$, giving the factor $\omega\tau = 0.5$. In this case, the detection becomes non resonant with little sensitivity [Knap2002-2].

2.4.4 Influence of incident angle θ

In Figure 2-19, the original absorption spectra (including contributions from Drude absorption and grating loss) with different incident angles ($\theta = 0^\circ - 89^\circ$) are displayed for the structure AlGaN/GaN (thickness = 3 μm). With the increase of incident angle (measured in reference to the surface normal), the PP resonances become weak. The peak's frequency does not increase greatly due to the fact that the incident maximum wavevector in x direction $\omega\sin\theta/c$ is well below $2\pi/L$. Normal incidence wave ($\theta = 0^\circ$) has the maximum electric field component E_x which is essential for the interaction with longitudinal 2D plasmon in the interface plane. For all the other simulations, the wave is assumed to be the normal incidence because the maximum PP resonances are obtained at this angle. Other materials give the same results.

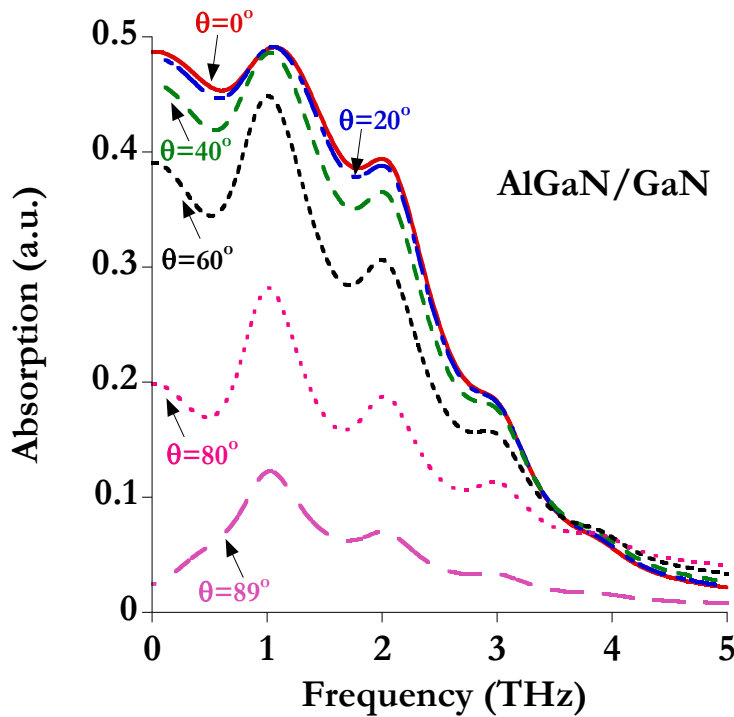


Figure 2-19: Original absorption of the heterostructure AlGaN/GaN (3 μ m) at room temperature with different incident wave angles by HFSS

2.4.5 Influence of the metal thickness, the conductivity and the QW width

Figure 2-20 shows the original absorptions when the metal thickness (a) and the gold conductivity (b) vary. The thickness range is $t = [0.1-2]$ μ m and the conductivity σ_{Au} is between 5×10^6 and 4.1×10^7 S/m. This study was only performed for AlGaN/GaN at room temperature with normal incident waves. Thick and low conductivity metals bring more conduction loss in the absorptions, but these influences are not evident, particularly at those resonances in comparison with other losses, such as the Drude background absorption.

Here we emphasize the influences of the thicknesses of lossy grating and 2DEG layer on the absorptions in Figure 2-21, where the original absorptions of nominal AlGaN/GaN structure calculated by CWM at different values of t and d_{2DEG} . Figure 2-21(a) plots only the conduction losses without 2DEG ($N_s = 0$). As the grating thickness t increases, the absorption rises accordingly due to larger ohmic losses in the metal. If t is comparable to grating period L , the contribution of the conductor attenuation to the total absorption is no longer negligible, especially at high frequency. 3D grating with finite conductivity should be used in the calculation. Of course, small metal conductivity (5×10^6 S/m) causes the increase of conduction losses at high frequency which may become a dominant factor in absorption. Figure 2-21 (b) shows the original absorptions for exact 2D plasmon ($d_{2DEG} = 0$, $\sigma_{2D}(\omega) = \frac{N_s e^2 \tau}{m^*(1 - j\omega\tau)}$ as in [Muravjov2010])

and quasi-2D plasmon ($d_{2DEG} = 12$ nm). The absorption amplitudes are nearly not affected by the thickness of the thin 2DEG layer, however, the resonant positions for quasi-2D plasmon move to slightly higher frequencies. The small frequency variation cannot be distinguished in present spectral experiments.

As we are only interested in the PP absorptions, the conduction loss in metals will finally be subtracted from the total absorption spectrum (Figure 2-17) and the influences of metal thickness and conductivity are excluded in PP resonances. $t = 200 \text{ nm}$, $\sigma_{\text{Au}} = 4.1 \times 10^7 \text{ S/m}$, and $d_{\text{2DEG}} = 12 \text{ nm}$ are used as the default thickness and conductivity of metal for the optimization of PP resonances.

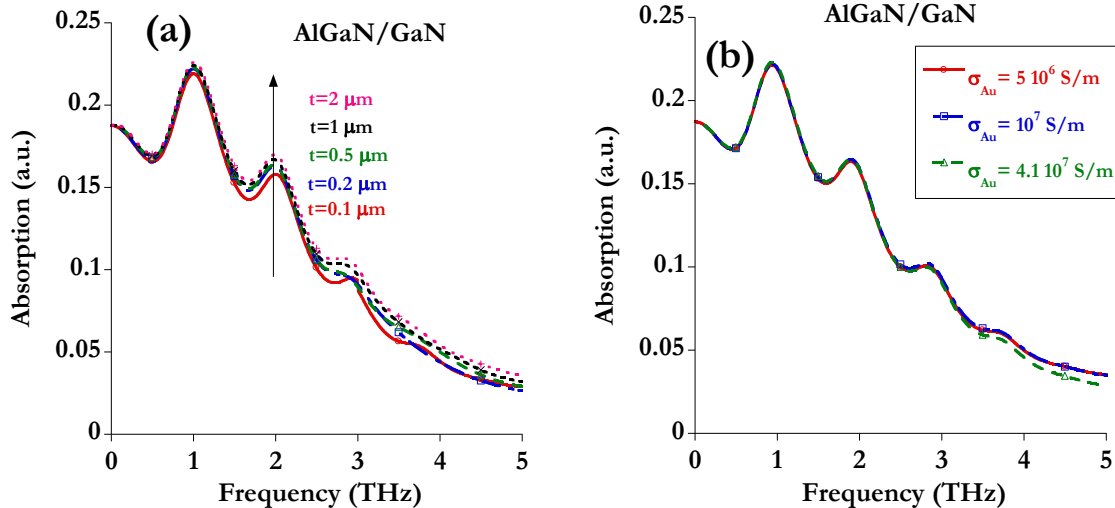


Figure 2-20: Original absorption of the heterostructure AlGaN/GaN at room temperature with different metal thicknesses (a) and conductivities (b) by HFSS

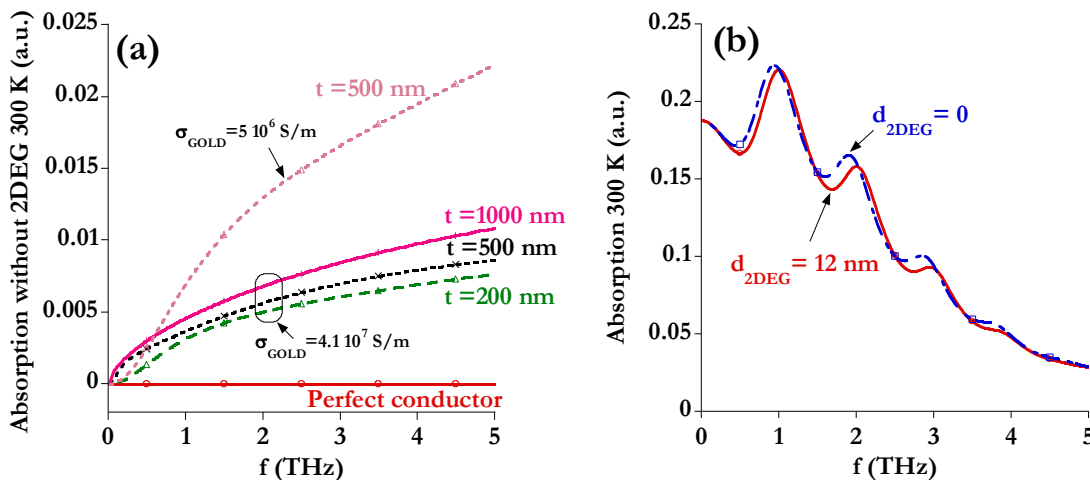


Figure 2-21: Original absorption spectrum of the nominal AlGaN/GaN structure calculated by CWM at 300 K, where $L = 2.2 \mu\text{m}$, $W/L = 0.75$ and $N_s = 1.2 \times 10^{17} \text{ m}^{-2}$. (a) Conduction losses due to finite conductivity of grating ($\sigma_{\text{Au}} = 4.1 \times 10^7$ and $5 \times 10^6 \text{ S/m}$) at different grating thicknesses. No 2DEG layer exists. The case with perfect grating is plotted for reference. (b) Absorptions at different 2DEG layer thicknesses. Grating parameters: $t = 200 \text{ nm}$, $\sigma_{\text{Au}} = 4.1 \times 10^7 \text{ S/m}$

2.4.6 Influence of temperatures on the PP resonances

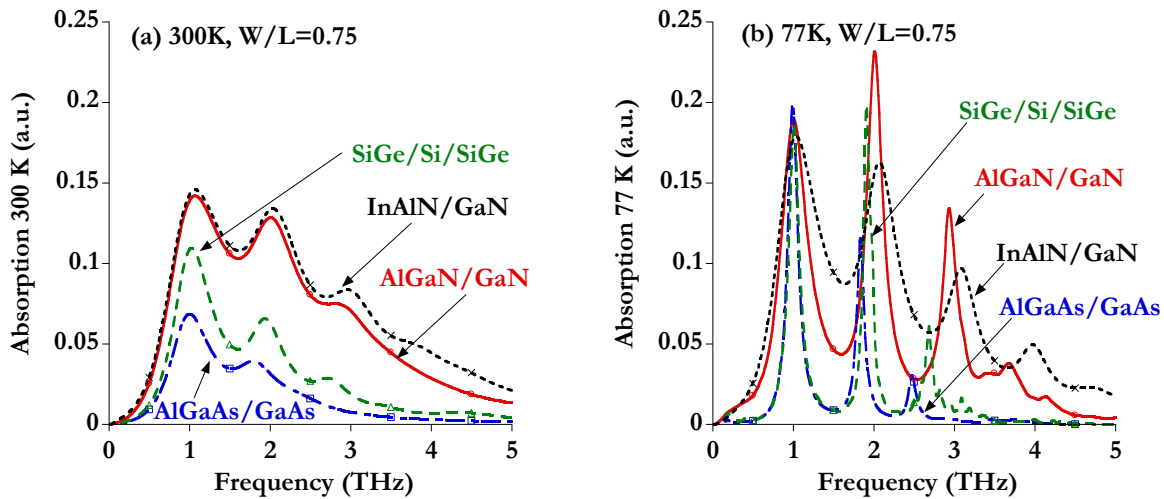


Figure 2-22: PP absorption spectrum of the four nominal structures with $W/L = 0.75$ at (a) 300 K and (b) 77 K

As discussed in section 2.2.2.3, the 2DEG mobility μ_{2DEG} decreases as the temperature increases due to the different scattering mechanisms while the electron concentration N_s is nearly constant from 1 K to 300 K. Figure 2-22 shows the PP absorption spectrums for the four materials at cryogenic (77 K) and room temperatures. At low temperature, the resonant peaks are narrow and high. This is attributed to the reduced Drude type absorption by 2DEG at low temperature, as shown in Figure 2-23. At the resonances (f_n), the absorption in material SiGe/Si/SiGe and AlGaAs/GaAs drops rapidly due to the large increase of electron lifetime τ at 77 K. For InAlN/GaN, the PP absorption in Figure 2-22 (b) is not enhanced greatly from 300 K to 77 K, because the Drude absorption is slightly reduced (Figure 2-23), in other words, the increase of 2DEG mobility (from 0.11 to 0.33 m^2/Vs) is not as considerable as in other materials . We can deduce that a strong coupling effect can occur when the electron lifetime τ between adjacent two scatterings becomes longer. Similar temperature dependant absorptions have been shown in a short gate FET structure [Popov2005]. The resonant frequencies do not change greatly because the approximation $\omega\tau > 1$ is valid for both temperatures. At 300 K, the nominal material based on nitride have the maximum absorption peaks whatever the order of the resonance (f_n). InAlN/GaN appears as the optimal one due its large electron concentration and its small barrier thickness (compared with AlGaN/GaN). However, AlGaAs/GaAs and SiGe/Si/SiGe present also interesting performances notably at low temperature due to their large increase of electron relaxation time related to the mobility used in the simulations.

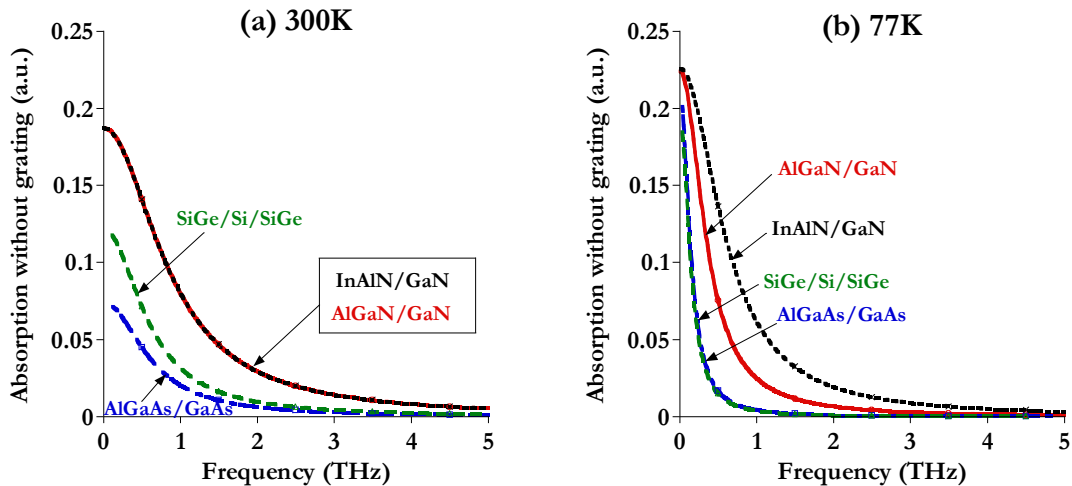


Figure 2-23: Absorption spectrum of the four nominal structures without grating at (a) 300 K and (b) 77 K

At certain conditions, the higher order PP absorption amplitude (A_n ($n > 1$)) may becomes higher than the fundamental one (A_1). Figure 2-22 (b) demonstrates for AlGaN/GaN and SiGe/Si/SiGe materials at 77 K and $W/L = 0.75$: $A_2 > A_1$. There are two reasons to explain this effect.

Firstly, as the metal filling factor W/L increases, the in-plane electric field component (E_x) of scattered waves with different orders will be improved, particularly for higher order wave ($n > 1$). It is the E_x component that interacts effectively with the 2D plasmon. Figure 2-24 shows the normalized E_x components of the first three order waves versus W/L (0.25-0.9) at the QW plane (25 nm from the interface) in AlGaN/GaN structure at 300 K and $L = 2.2 \mu\text{m}$. The calculation is finished by CWM. Structure SiGe/Si/SiGe has similar results. E_x of the higher order waves ($n = 2$ and 3) increases more rapidly than that of the first order ($n = 1$). As $W/L > 0.6$, E_x at $n = 2$ and 3 becomes comparable and even stronger than E_x ($n = 1$) at their corresponded resonant frequency f_n . This will possibly make the higher order PP resonances more intensive at high values of W/L .

Secondly, a large value of the factor $\omega_n \tau$ can be reached at higher order frequencies (f_n). This is to say that, the possibility of electron scattering with the semiconductor lattice atoms is reduced. Therefore, the Drude absorption decreases at high n , as clearly seen in Figure 2-23. Furthermore, E_x filed of different waves at low temperature can also be raised in reference to their values at 300 K. Figure 2-24 (d) shows E_x of the second order ($n = 2$) wave at 77 K. Compared with Figure 2-24 (b), the enhancement of E_x is evident at 77 K. The other waves ($n = 1$ and 3) have similar results.

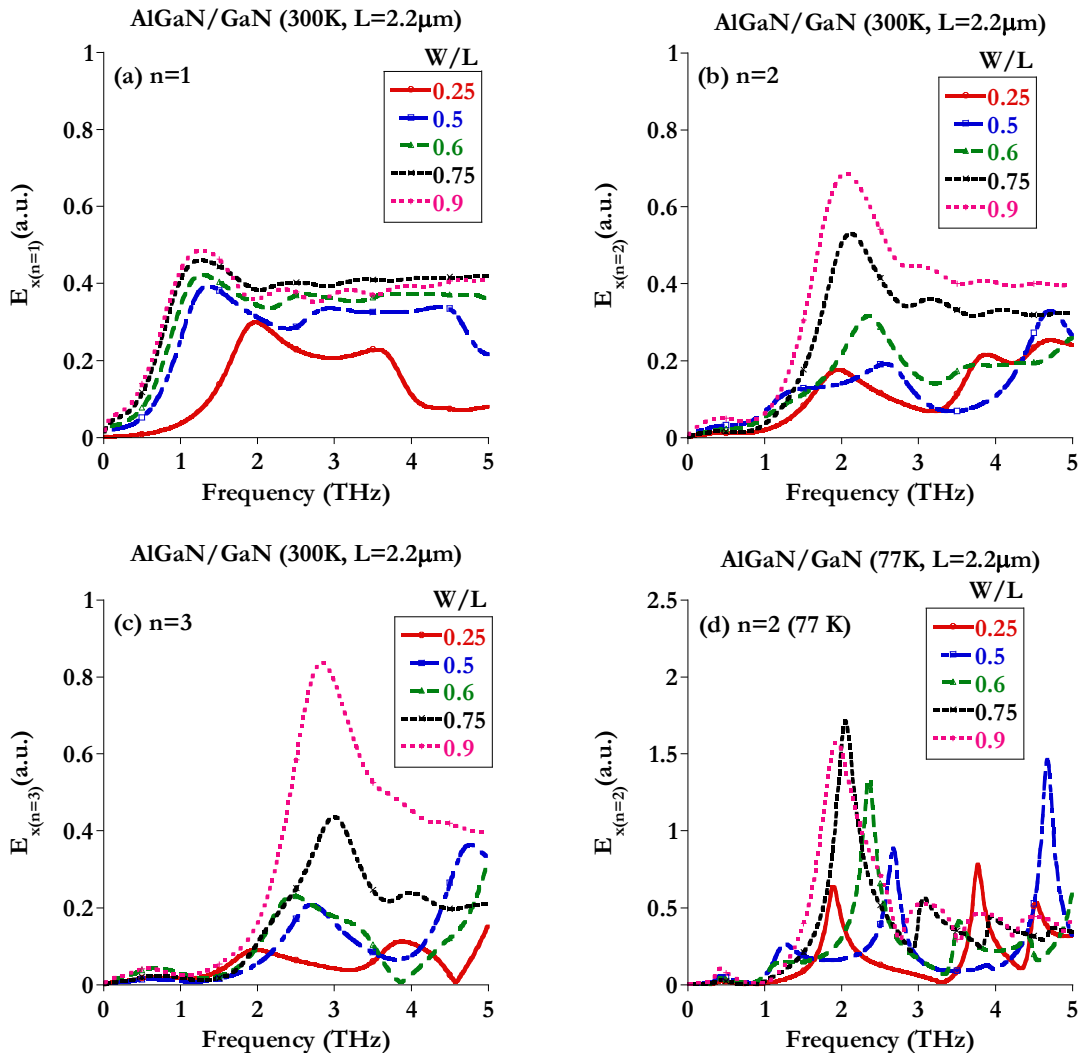


Figure 2-24: Amplitude of electric field E_x of different scattered waves versus W/L (0.25-0.9) at the plane of 2DEG layer (a distance of 25 nm from the surface) in AlGaN/GaN structure. (a) $n = 1$, (b) $n = 2$, (c) $n = 3$ at 300 K, and (d) $n = 2$ at 77 K. They were calculated by CWM. $L = 2.2 \mu\text{m}$

To further illustrate the stronger excitation of PP resonances by high order waves, Figure 2-25 plots the PP absorption of the four materials with metal filling factor (0.6 and 0.9) around the nominal value (0.75 in Figure 2-22). At $W/L = 0.6$, the amplitudes of higher order PP are always lower than the fundamental PP amplitude ($n = 1$) at both room and cryogenic temperature, because the higher order field E_x are not strong enough. At $W/L = 0.9$, GaN based materials show higher order PP resonances ($A_2 > A_1$) at room temperature (Figure 2-25 (c)). At 77 K in Figure 2-25 (d), all materials except AlGaAs/GaAs have stronger higher order PP resonances: $A_{2,3 \text{ and } 4} > A_1$ for AlGaN/GaN, $A_{2 \text{ and } 3} > A_1$ for InAlN/GaN and $A_2 > A_1$ for SiGe/Si/SiGe. In AlGaAs/GaAs, A_2 is slightly lower than A_1 . To achieve $A_2 > A_1$ in AlGaAs/GaAs, increasing W/L or decreasing the temperature is possible solution.

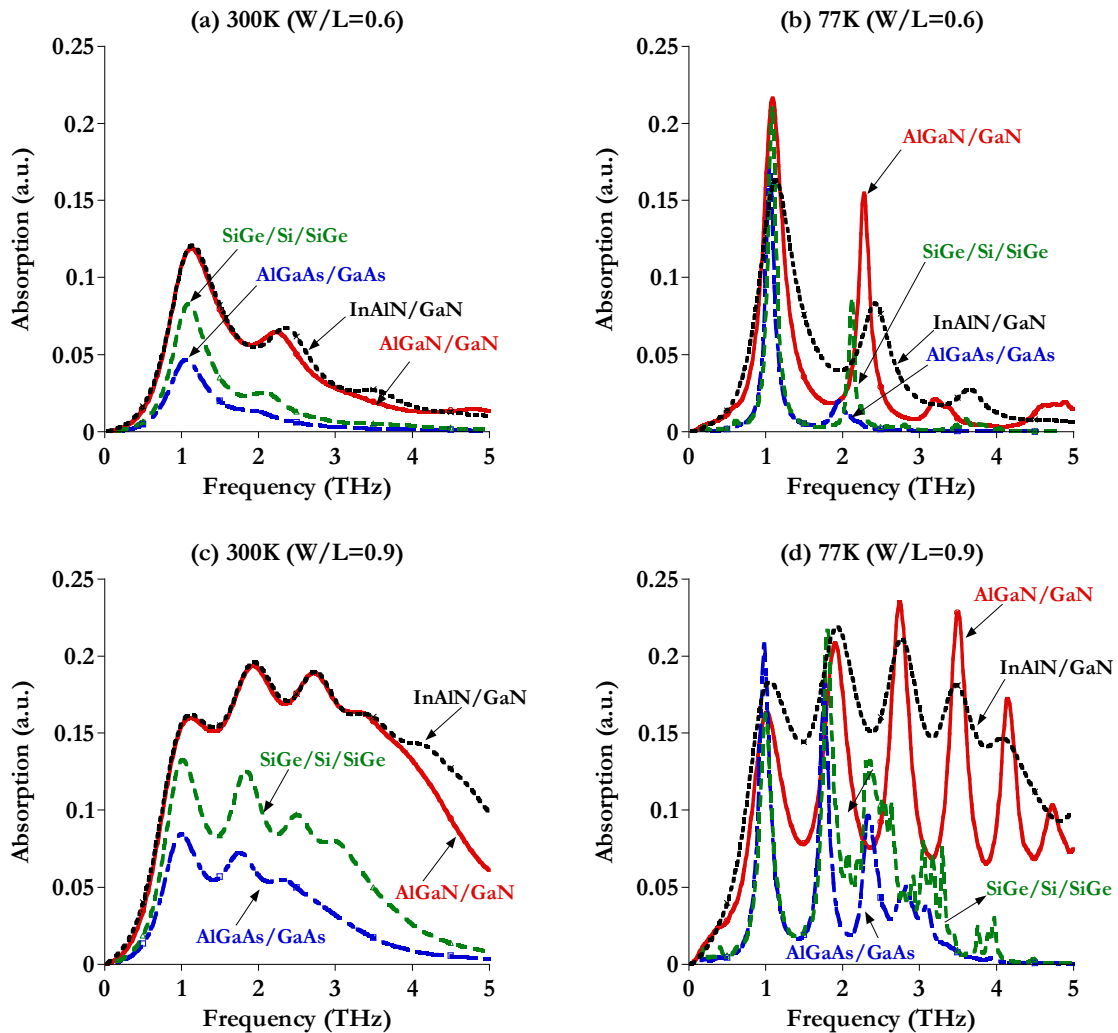


Figure 2-25: PP absorption spectrum of the four structures. (a) 300 K, W/L = 0.6, (b) 77 K, W/L = 0.6, (c) 300 K, W/L = 0.9, and (d) 77 K, W/L = 0.9

To conclude the discussion, high filling factor and low temperature are helpful to excite strongly the higher order PP resonances (A_n , $n > 1$). This can push further the maximum frequency in the THz resonant detection. Based on the material parameters used in the simulation, stronger higher order PP resonances are possible: AlGaN/GaN (W/L ≥ 0.9 at 300 K and W/L ≥ 0.75 at 77 K), AlGaAs/GaAs (W/L > 0.9 at 77 K), SiGe/Si/SiGe (W/L ≥ 0.75 at 77 K), and InAlN/GaN (W/L ≥ 0.9 at 300 K and 77 K).

2.4.7 Influences of the electron concentration and the geometric parameters on PP resonances at 300 K

The influences of carrier concentration N_s , barrier thickness d and filling factor W/L on the frequency and amplitude at room temperature are displayed from Figure 2-26 to Figure 2-29, respectively. For each material, PP resonances with five discrete values around the nominal parameters are considered in a reasonable range for technological realization, as listed in Table 2-3. The 2DEG anisotropic permittivity model (2-26) is assumed to be valid for different carrier concentrations in this parametric study. Similar studies of the influences of N_s , d , and W/L have been reported in AlGaAs/GaAs structure ignoring the finite width of QW [Tyson1994,

Ager1992-1, Mikhailov1998]. Here we concentrate on the comparative analysis between materials based on practical device parameters.

Table 2-3: Simulated range of N_s , d and W/L based on the four nominal structures

Material	$N_s (10^{16} \text{ m}^{-2})$	$d (\text{nm})$	W/L
AlGaN/GaN	1, 5, 8, 12 and 20	10, 25, 50, 100 and 200	0.25, 0.5, 0.6, 0.75 and 0.9
InAlN/GaN			
SiGe/Si/SiGe	0.5, 1, 3, 5 and 6	10, 25, 50, 80 and 100	
AlGaAs/GaAs	0.1, 0.5, 0.8, 1 and 1.5		

2.4.7.1 Influence of N_s

As shown in Figure 2-16, at high filling factor $W/L = 0.75$, the screened PP dispersion formula (2-41) can predict correctly that f is proportional to the square root of N_s . Figure 2-26 (a) shows the observed resonant frequency (f_1 , f_2 and f_3) in function of the electron density. This tendency of square root relation is well observed in all the resonant peaks. Concerning the resonance peaks A_1 , A_2 and A_3 (Figure 2-26 (b)), high electron concentration produces strong absorption due to the increased number of electrons per unit area participating in the interaction with the scattered waves. For device application, N_s is varied by applying voltage on the metal fingers. The dependency of the resonant frequency on the carrier concentration and the absorption spectrum with different bias voltage have also been reported in other publications [Mikhailov1998, Theis1978].

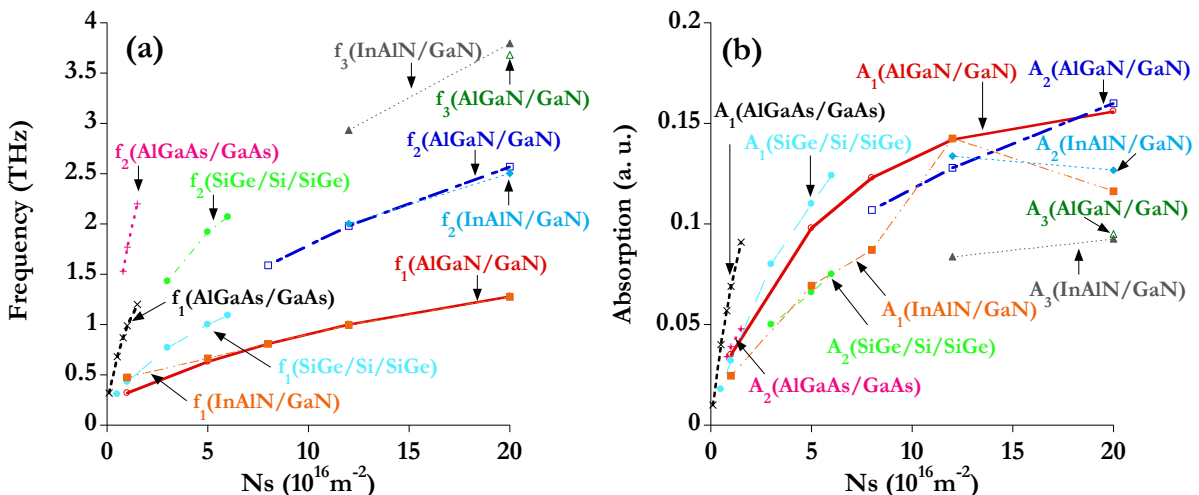


Figure 2-26: Influences of carrier surface concentration N_s on PP absorption spectrum of the four nominal structures at 300 K with $W/L = 0.75$. (a) resonant frequency and (b) absorption amplitude

2.4.7.2 Influence of the distance d

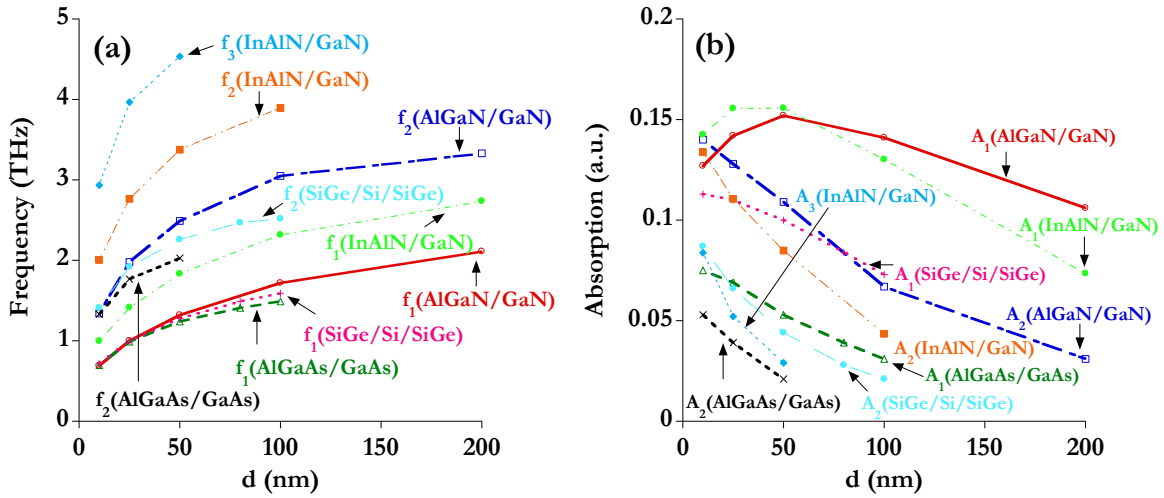


Figure 2-27: Influences of barrier thickness d on PP absorption spectrum of the four nominal structures at 300 K with $W/L = 0.75$. (a) resonant frequency and (b) absorption amplitude

According to the dispersion relation of screened PP (2-41), the resonant frequency depends on the barrier thickness d following the relation of screened PP:

$$f = \frac{1}{2\pi} \sqrt{\frac{e^2 N_s k}{m^* \epsilon_0}} \frac{1}{\epsilon_s + \epsilon_b \coth(kd)} = \begin{cases} \frac{1}{2\pi} \sqrt{\frac{e^2 N_s d}{m^* \epsilon_b \epsilon_0}} k & \text{for } kd \ll 1 \\ \frac{1}{2\pi} \sqrt{\frac{e^2 N_s k}{m^* (\epsilon_s + \epsilon_b) \epsilon_0}} & \text{for } kd \gg 1 \end{cases} \quad (2-47)$$

As seen in Figure 2-27 (a), a square root relation at small d and a quasi constant behavior at large d appear. Figure 2-27 (b) represents the evolution of the amplitude of each PP peak versus d . The resonant amplitude decreases when d is beyond 50 nm because of the evanescent nature of the scattering wave at the vicinity of metal grating.

An optimal distance corresponded to maximum PP absorption exists around 50 nm for AlGaN/GaN and 25 nm for InAlN/GaN if we look only the first peak A_1 in Figure 2-27 (b). For the other two materials, the optimal distance does not appear with the variation of d in [10-100] nm.

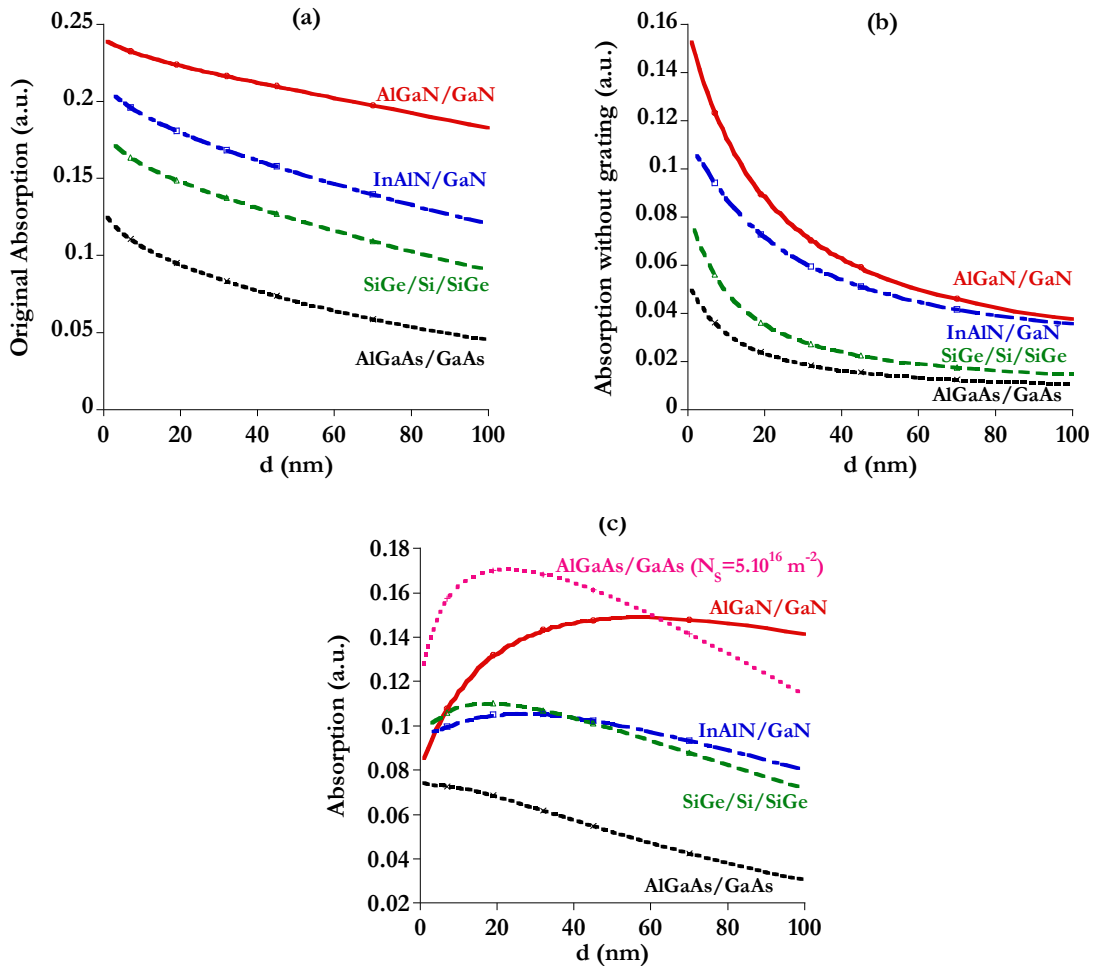


Figure 2-28: (a) *Original absorption with 2DEG and grating*, (b) *Absorption without grating*, and (c) *PP absorption (A_1) of the four nominal structures versus barrier thickness d (1-100 nm) at the first resonant frequency (f_1) at 300 K with $W/L = 0.75$. A_1 for AlGaAs/GaAs at $N_s = 5.10^{16} \text{ m}^{-2}$ is superimposed in (c) for comparison*

In order to find the origin of this optimal distance, the total absorption with grating and 2DEG (can be measured directly in the experiment), Drude type absorption without grating, and PP absorption (A_1) at the first resonance of the four nominal materials are plotted versus d (1-100 nm) at room temperature in Figure 2-28. The absorption due to metal grating is omitted (< 0.005). The total absorption in Figure 2-28 (a) increases monotonically as the barrier becomes thinner. This is mainly attributed to the great enhancement of Drude absorption in 2DEG layer at low frequency f_1 ($< 1 \text{ THz}$) when d is decreased below 50 nm as shown in Figure 2-28 (b). Strictly speaking, the absorption in Figure 2-28 (b) is caused by the imaginary part of 2DEG permittivity, which increases with the growth of electron concentration N_s and with the decrease of frequency (small d). Indeed, the large N_s in GaN based structures have more absorptions over other two materials with relatively low N_s . When the absorption in Figure 2-28 (a) is subtracted by the Drude absorption in Figure 2-28 (b), the resulting PP absorption in Figure 2-28 (c) drops from the following specific distances as d is reduced from 100 nm to 1 nm : 44 nm (AlGaN/GaN), 25 nm (InAlN/GaN), 19 nm (SiGe/Si/SiGe). The absorption for AlGaAs/GaAs does not decline until $d = 1 \text{ nm}$.

The other direct explanation of the optimal distance can be possibly described in the following quantitative manner. At these optimal distances, the factor $\omega\tau$ is 1.98 (AlGaN/GaN), 1.2 (InAlN/GaN) and 1.85 (SiGe/Si/SiGe). As d is further decreased, $\omega\tau$ falls rapidly to be lower than 1. The possibility of scattering of electrons by the background semiconductor lattice increases, resulting in the strong damping of plasma oscillation, particularly at high electron concentration. While for AlGaAs/GaAs structure with the lowest N_s (10^{16} m^{-2}) among the four materials, the electron scattering does not begin to attenuate the PP absorption even at $d = 1 \text{ nm}$ ($\omega\tau = 0.79$). If N_s is increased to 5.10^{16} m^{-2} in AlGaAs/GaAs structure, an optimal distance ($d = 20 \text{ nm}$) also appears as shown in Figure 2-28 (c).

It should be noted that the results in Figure 2-28 (c) cannot be measured directly in the experiment. Normally, the absorptions in Figure 2-28 (a) are characterized and they monotonically depend on the barrier thickness (d). Moreover, when d is reduced below 10 nm, the technological realization becomes difficult.

2.4.7.3 Influence of the filling factor W/L

In this section we first study the influence of the ratio W/L which varies between 0.25 and 0.9 for the four nominal materials. The period L is fixed.

As shown in Figure 2-16, at the same plasmon wavevector k , the unscreened ($W/L = 0$) PP resonant frequency is always greater than the screened one ($W/L = 1$). As the value W/L increases from 0.25 to 0.9, the PP frequency decreases monotonically in Figure 2-29 (a). From $W/L = 0.6$, the PP frequency is nearly equal to the totally screened case, indicating that screened plasmon becomes dominant in the resonant absorption at these high W/L values. At low filling factor ($W/L < 0.5$), the observed PP frequency raises and approaches the unscreened case. So we can assume that the effect of the unscreened plasmon becomes important at $W/L < 0.5$. In Figure 2-29 (b), the absorption amplitudes increase drastically with W due to the enhancement of scattered field component E_x .

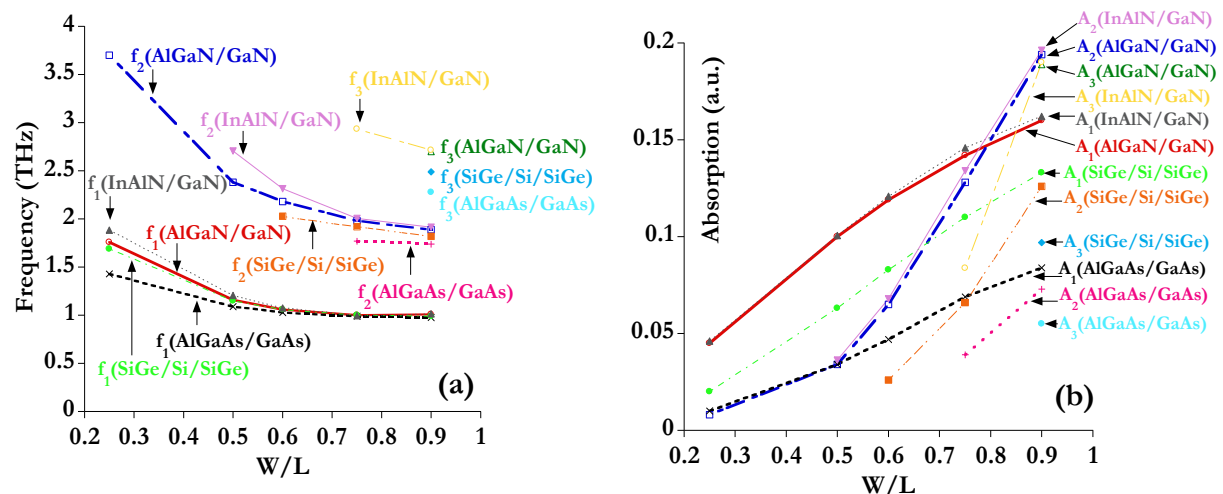


Figure 2-29: Influences of filling factor W/L (0.25-0.9) on PP absorption spectrum of the four nominal structures at 300 K. (a) resonant frequency and (b) absorption amplitude

Figure 2-30 shows the distribution of the electric field E_x in the vicinity of grating at different filling factor from 0.25 to 0.95, where L is fixed at 1 μm . With the decrease of gap width, the amplitude of the evanescent field component E_x becomes intense at the interface air/substrate and it extends deeper into the substrate, making the coupling with the underlying 2D plasmons stronger. And the PP absorption is strengthened [Allen1977, Theis1978].

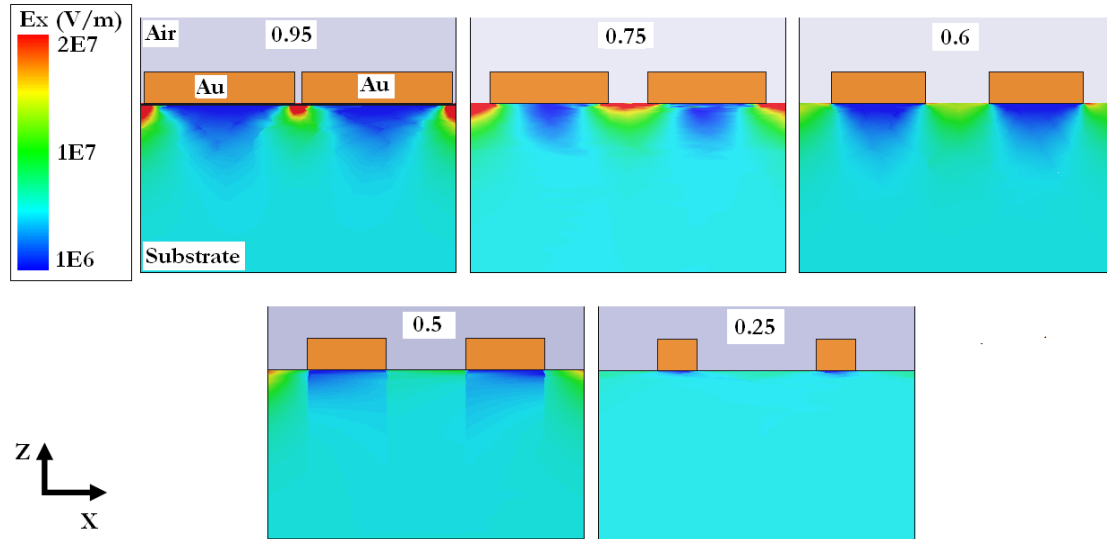


Figure 2-30: Electric field E_x distribution in the vicinity of metal grating at 1 THz by HFSS. $L = 1 \mu\text{m}$ and $W/L = 0.25-0.95$

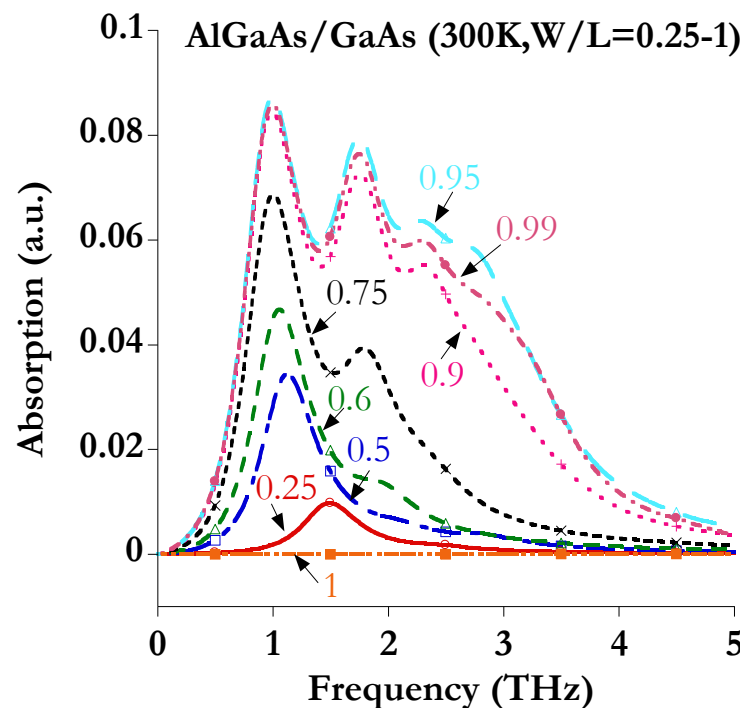


Figure 2-31: Influences of filling factor W/L (0.25-1) on PP absorption spectrum of nominal structure AlGaAs/GaAs at 300 K

However, the absorption amplitude does not increase monotonically when W/L approaches 1 in the simulation. Figure 2-31 shows the PP absorption spectrum for AlGaAs/GaAs nominal structure versus W/L from 0.25 to 1 at room temperature. A maximum absorption locates at $W/L = 0.95$. Beyond $W/L = 0.95$, the absorption amplitudes begin to decrease. At this limit condition, the normal scattering theory will lose its correctness. The extremely narrow gap will not be seen by the incident THz wave and the grating is approximately considered to be a continuous conductor layer. If its thickness is larger than the metal skin depth at the frequency of the incident field, little power will be transmitted through the metal and the corresponded absorption of the system will be nearly zero. Moreover, in the limit case where the gap width $W_G = L-W$ is smaller than 50 nm, some technological difficulties in the sample realization by lithography may be generated. For the limit case of the totally screened plasmon ($W/L = 1$), the absorption is zero.

2.4.8 Conclusions

- (1) Materials based on III-nitride are the optimal structures for resonant THz detection, especially InAlN/GaN. This is mainly due to their higher carrier concentrations induced by large spontaneous and piezoelectric polarizations which eliminate the need of doping in the barrier semiconductor.
- (2) In order to realize a strong excitation of 2D PP, a high carrier concentration, a small barrier thickness, a large filling factor and a low temperature are appreciated. However, very thin barrier can lead to low PP absorption amplitude due to the increase of Drude absorption. Lower temperature can improve the resolution of resonant peaks due to the increase of electron scattering time and evanescent field, and high temperature has the potential to drive the detection into non resonant type (without noticeable resonant peaks).
- (3) For PP frequency, a thick barrier layer and a large carrier density tend to increases the resonant frequencies, while wide metal finger will make the frequency drop when the period L is not varied. The temperature does not greatly influence the resonant frequency.
- (4) The period of grating L in micrometer can modulate significantly the frequency of absorption peaks in THz range. To achieve the frequency tunability when L has been designed after the sample was fabricated, the voltage bias on metal fingers will be applied and their functions will be discussed in the section of inhomogeneous 2DEG modeling.

After the numerical investigation of THz detection with 2D PP in different heterostructures, the spectrum will be measured and compared with the calculated result for a heterostructure based on III-nitride.

2.5 Measurement of the transmission spectrum of PP in AlGaN/GaN by FTIR

In this section, a sample AlGaN/GaN on the substrate sapphire with deposited periodic metal grating has been prepared and measured by FTIR (Fourier transform infrared spectroscopy) at cryogenic and room temperatures. The simulated and experimental transmission spectra are compared at different filling factors W/L from 0.25 to 0.75.

2.5.1 Sample fabrication

The heterostructure $\text{Al}_{0.25}\text{Ga}_{0.75}\text{N}/\text{GaN}$ is grown on a 330 μm thick substrate of sapphire. The thickness of AlGaN and GaN is 25 nm and 3 μm , respectively. The measured average electron sheet concentration $N_s = 8 \times 10^{12} \text{ cm}^{-2}$. Periodic Au gratings were carried out with the electron beam lithography at LPN (Laboratoire de Photonique et de Nanostructures). Its thickness $t = 200 \text{ nm}$ and the period $L = 2.2 \mu\text{m}$. The ratio W/L has been chosen to be 0.25, 0.5, 0.6 and 0.75. Figure 2-32 shows the microscopic image of the sample surface, where the gaps between metal strips can be clearly identified.

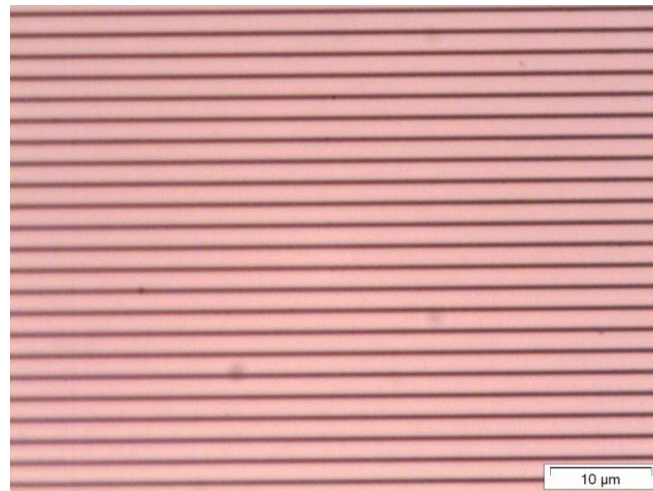


Figure 2-32: Microscopic image of the Au gratings on top of the sample AlGaN/GaN, $L = 2.2 \mu\text{m}$, $W/L = 0.75$

2.5.2 Introductin to FTIR

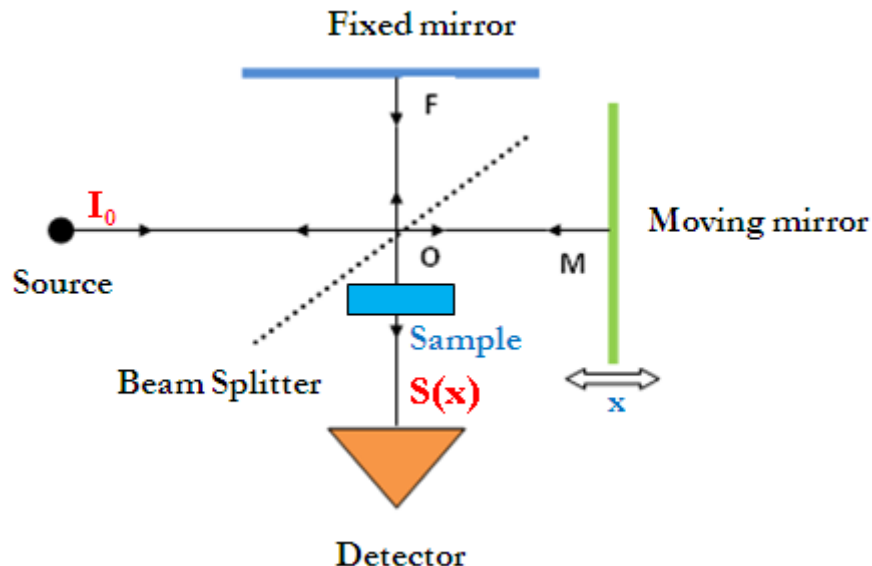


Figure 2-33: Schema of the standard FTIR setup

Figure 2-33 shows the simplified quasi-optic FTIR measurement setup. The broadband beam from the mercury lamp is directed to the beam splitter (central point O), where one half of the

signal power is reflected to a fixed mirror (F) and the other part transmits the beam splitter and travels to a moving mirror (M). The position of the moving mirror is denoted as x. When x is scanned, the phase delay or retardation length between the two beams is achieved. The two parts recombine at the beam splitter and pass through the sample under test. The amplitude of the position dependent signal S(x) (transmitted or reflected beam) is detected by a thermal detector, with its output voltage or current proportional to the incident power in a certain frequency band. The upper part of the configuration (without the sample and the detector) is a typical Michelson interferometer [Griffiths2007].

The detected intensity signal is modulated by the position of the mobile mirror,

$$I(x) = \int_0^{+\infty} \frac{I(k)}{2} (1 + \cos(2\pi kx)) dk = \frac{I_0}{2} + \frac{S(x)}{2} \quad (2-48)$$

Where $k = 1/\lambda$ is the wavenumber, $x = 2(OM - OF)$ is the retardation distance, and $I_0 = \int_0^{+\infty} I(k) dk$ is the incident intensity from the source. The frequency domain counterpart of the interferogram signal S(x) is I(k),

$$S(x) = \int_0^{+\infty} I(k) \cos(2\pi kx) dk = \int_{-\infty}^{+\infty} \frac{I(k)}{2} \exp(i2\pi kx) dk \quad (2-49)$$

They constitute a pair of Fourier transform and FFT (fast Fourier transform) algorithm available for computer operations. As the interferogram is measured, all frequencies are being measured simultaneously. The transmission and reflection spectra are obtained by the frequency function I(k) normalized to that detected without samples.

The main advantages of FTIR are the high speed (all frequencies are measured simultaneously), improved sensitivity by fast scans of the mobile mirrors and reduced noise by signal averaging, simple mechanical configuration, the self calibrating by the internal HeNe laser, fine frequency resolution, and large bandwidth of THz signal. However, comparing with the THz-TDS system in transmission and reflection mode for studying the material properties (for example, the complex refractive index $n(\omega) = n'(\omega) - jk(\omega)$), FTIR suffers from many disadvantages:

- weak source signal peak optical intensity: FTIR uses the continuous wave (CW) non coherent broadband blackbody radiator, rather than the coherent narrow pulse sources (typically 1-2 ps duration) as in THz-TDS configuration. FTIR source intensity is several orders of magnitude smaller than the high brightness source in THz-TDS [Beard2001].
- lacks of direct phase information: FTIR only measures the field intensity and the absorption index $k(\omega)$, in contrast, both parts of the complex refractive index $n(\omega)$ can be obtained directly by the measured amplitude and phase of the transmitted field in TDS. Although the refractive index $n'(\omega)$ is related to $k(\omega)$ by Kramers-Kronig relations [Griffiths2007] for FTIR experiment, the calculation is not straightforward and there are many potential sources of error [Naftaly2007].

- small signal noise ratio (SNR): Due to the coherent pump-probe detection schema, THz-TDS system has much higher SNR in power than that for FTIR [Leahy2009].

Since only the PP absorption spectrum is of interests for THz detection, the FTIR experiment applies for the present investigation. General agreement of the material absorption feature between FTIR and THz-TDS has been demonstrated [Huang2004].

2.5.3 Transmission spectrum excited by TM polarized FIR laser beam

The transmission spectrum for the sample AlGaN/GaN is measured and compared with the simulation results from 0.6 THz to 1.7 THz. Numerical treatment is utilized to eliminate the Fabry-Pérot resonances in the spectrum caused by the thick substrate. One disadvantage is that the frequency resolution of the spectrum will be increased.

2.5.3.1 Experiment setup

The FTIR measurement for the sample AlGaN/GaN is conducted with Bruker IFS 66v/s system, which is shown in Figure 2-34. It operates in vacuum environment to reduce the strong atmosphere absorption and acoustic perturbation. A mercury lamp is used as the FIR blackbody source. The 50 μm Mylar beam splitter works at the frequency range [0.3 -1.7] THz. Silicon-diamond composite bolometer cooled at 4.2 K is the detector to achieve higher sensitivity in rapid scan mode comparing with the DTGS-PE type. The beam is collimated focused onto the sample surface with a diameter around 4 mm. The TM polarized wave incents at an angle of 11°. The sample is mounted on a copper support in a cryostat cooled at liquid nitrogen (78 K) and liquid helium (10 K) temperatures for cryogenic measurements.

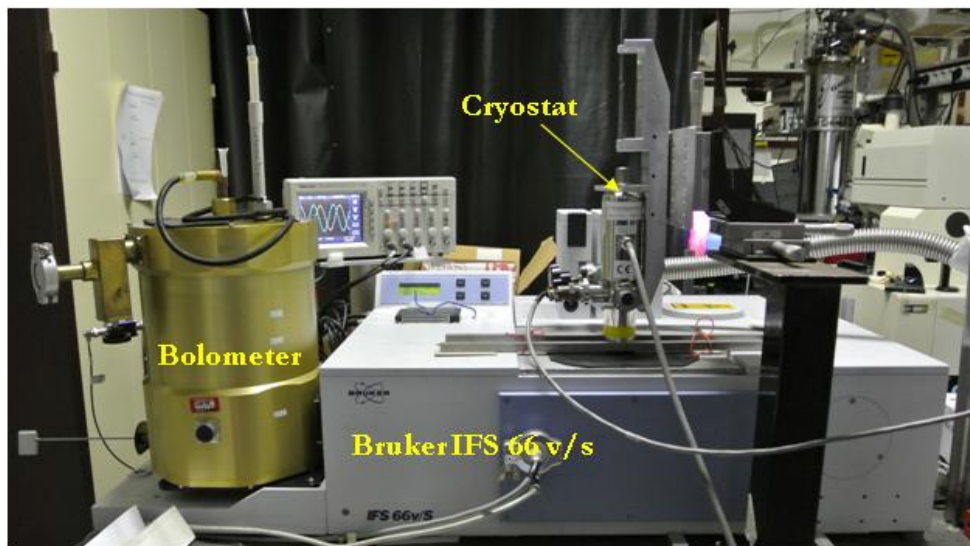


Figure 2-34: Experimental setup of the FTIR measurement with a bolometer detector

2.5.3.2 Elimination of Fabry-Pérot resonances

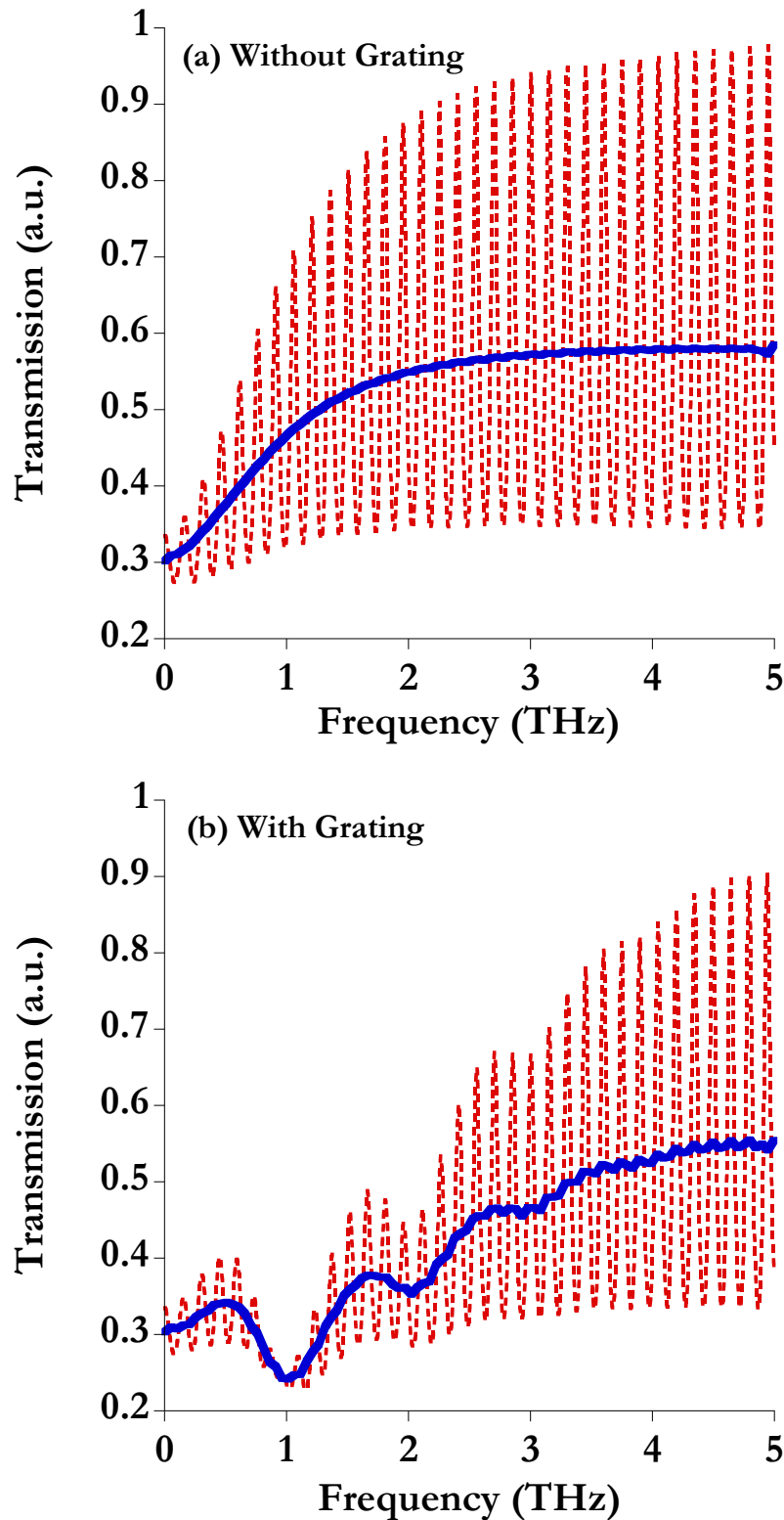


Figure 2-35: CWM simulated transmission spectrum for AlGaN (25 nm)/GaN (3 μm)/Sapphire (330 μm) at 300 K: (a) without grating, $N_s = 1.2 \times 10^{17} \text{ m}^2$, (b) with grating, $L = 2.2 \mu\text{m}$, and $W/L = 0.75$. Dotted red curve: original spectrum, solid blue curve: averaged spectrum without Fabry-Pérot resonances

In order to eliminate the Fabry-Pérot resonances due to the thick sapphire substrate (330 μm), the original transmission spectrum is averaged within a frequency interval of the Fabry-Pérot resonances Δf , resulting in the increase of resolution from 7.5 GHz (0.25 cm^{-1}) to around 0.146 THz, as calculated by the expression (2-50).

$$\Delta f = \frac{c}{2\sqrt{\epsilon_r h}} = 0.146 \text{ THz} \quad (2-50)$$

Where $\epsilon_r = 9.7$ and $h = 330 \mu\text{m}$ are the relative dielectric constant and thickness of the sapphire layer. Figure 2-35 shows the simulated original (dotted red curve) and averaged (solid blue curve) transmission spectra based on CWM for the structure AlGaN (25 nm)/GaN (3 μm)/Sapphire (330 μm) without and with metal grating. With the average method, the influence of the thick sapphire layer is minimized and the spectrum looks more like as the previous discussed cases AlGaN (25 nm)/GaN (semi-infinite). For the spectrum with metal grating, the three PP resonances ($f_1 = 1 \text{ THz}$, $f_2 = 2 \text{ THz}$ and $f_3 = 3 \text{ THz}$) appear in the background spectrum with Fabry-Pérot resonances. Moreover, for the analysis of experimental FTIR data, the transmitted signal with the presence of metallic grating is usually normalized by that without grating to obtain the relative transmission [Muravjov2010]. The measured relative transmission spectrum will be compared with the simulated one based on the Drude model of 2DEG in the following part.

2.5.3.3 Comparison of transmission spectrum between simulation and measurement

Figure 2-36 shows the simulated and measured relative transmission spectra from 0.6 to 1.7 THz at different temperatures (300 K, 78 K, and 10 K) with $W/L = 0.6$. At low frequencies below 0.6 THz, the Signal Noise Ratio (SNR) is small, resulting in poor spectrum information. At frequencies high than 1.7 THz, both the two types of detectors (bolometer and DTGS-PE) do not work well. With the decrease of environment temperature, the first resonant peak due to PP coupling becomes more pronounced, but the resonant frequency does not vary greatly. This is consistent with the previous simulation results. Near the maximum edge of the measured band, the second PP resonance appears at 1.6 THz at 10 K due to the large electron mobility. At room temperature, the small absorption amplitude is caused mainly by low mobility of electrons as shown in Figure 2-6. Electron motilities in the fitted simulation spectrum are 0.1, 0.35 and 0.45 m^2/Vs as the temperature decreases. The discrepancy between the experimental and theoretical results is due to several possible effects: firstly, the transparent polymer windows of the cryostat are not considered in the modeling. The resonant amplitudes will be influenced more or less. Secondly, the resolution of the spectrum increases to 0.146 THz, while the frequency step is only 0.01 THz in the simulation. Finally, the assumed geometrical dimensions (L , W and d) and material properties (ϵ , N_s and $\mu_{2\text{DEG}}$) may differ from the sample. Moreover, in the simulation, GaN layer is semi-infinite and no sapphire is present. All bulk materials are assumed to be lossless (without loss tangent).

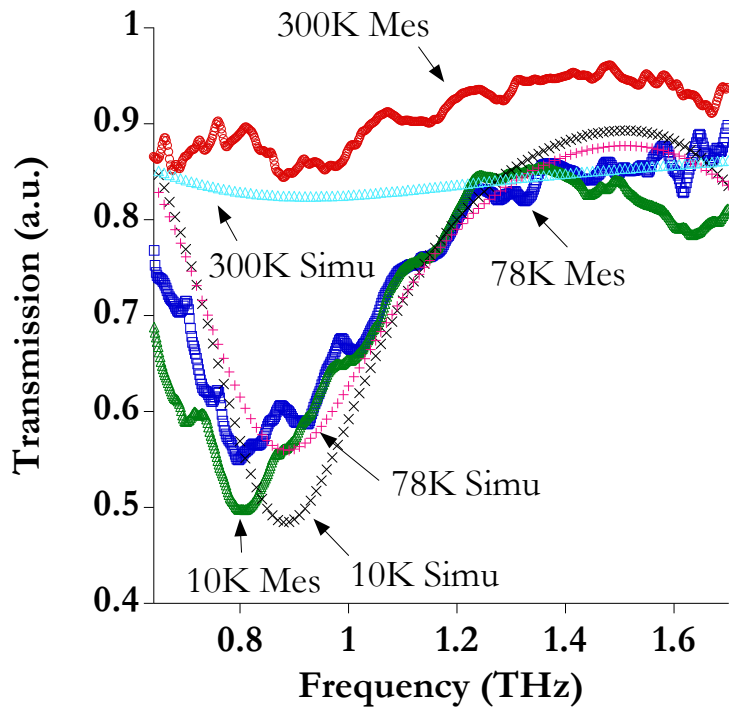


Figure 2-36: Measured transmission spectrum at different temperatures for $\text{Al}_{0.25}\text{Ga}_{0.75}\text{N}/\text{GaN}$ ($W/L = 0.6$, $N_s = 8 \cdot 10^{16} \text{ m}^{-2}$)

Figure 2-37 plots the experimental (a) and theoretical (b) relative transmission spectrum with different metal filling factor W/L (0.25, 0.5, 0.6 and 0.75) at 78 K. With the increase of the ratio W/L , the resonant frequency shifts to a smaller value and the absorption amplitudes becomes stronger, indicating a large coupling between incident THz radiation and plasmons in the heterostructure. At large W/L , the second resonance can also be seen. The unscreened plasmons display as a small resonance at around 1.35 THz in the spectrum with $W/L = 0.25$. The good agreement between the modeled and measured transmission spectrum validates the function and efficiency of the metal grating on top of the structure as the coupler. The assumed homogenous 2DEG distribution function $N_s(x) = N_s$ over one period of the grating seems reasonable for the AlGaN/GaN heterostructure.

Until now, we have considered the THz absorption in the homogeneous 2DEG system. After the sample is fabricated, a bias voltage could be applied on the metallization to tune the PP resonances. In this case, the distribution of electron becomes inhomogeneous in x direction and this is what we will discuss in the next section.

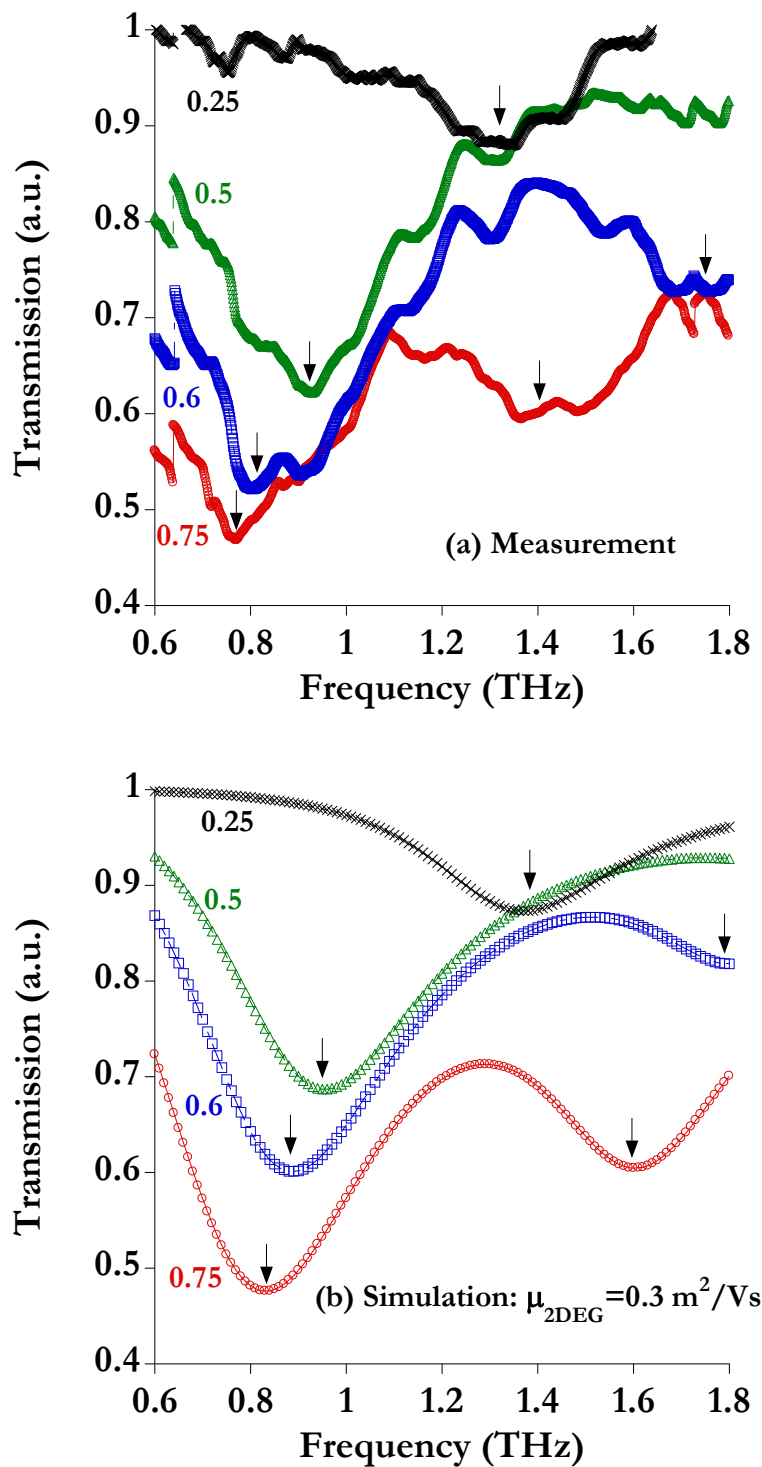


Figure 2-37: Transmission spectrum with different ratio W/L for $\text{Al}_{0.25}\text{Ga}_{0.75}\text{N}/\text{GaN}$ (78 K, $N_s = 8. 10^{16} \text{ m}^{-2}$), (a) measurement and (b) simulation with $\mu_{2\text{DEG}} = 0.3 \text{ m}^2/\text{Vs}$

2.6 Modeling of non homogeneous 2DEG

The modulated 2DEG has been investigated without [Matov1998] and with [Ager1992-2, Matov2002, Fateev2010] grating on AlGaAs/GaAs. The electron distribution is assumed to be piecewise constant or sinusoidal in theoretical modeling. Here we investigate the tunability of PP resonances through the biasing of the metallization over the AlGaAs/GaAs heterostructure. Three kinds of electron concentration profile (piecewise constant, linear and parabolic) along the axis perpendicular to the grating are compared. In high modulated condition, a distinct absorption peak is observed. Its position cannot be predicted correctly by existing formula with semitransparent NiCr grating [Matov2002] or without grating [Popov2003]. The screening effect of Au grating in our simulation causes the shift of resonant frequency.

In addition, in most publications dealing with the PP resonances with metal grating, the carrier concentration is considered to be constant with the position in the x direction if no bias is applied. Due to the differences between barrier height at the interfaces metal/semiconductor and Fermi levels pinning at air/semiconductor, the electron density will vary within one period.

2.6.1 Non homogeneous electron concentration

The electron density distribution in 2DEG layer with and without metals on top of the structure can be calculated numerically (section 2.2.2), provided that the surface potentials are known. In Figure 2-38, the carrier concentration below and between the metals are denoted as N_1 and N_2 . At the adjacent region of screened and unscreened 2DEG, a transition region t_1 exists due to the abrupt variation of electron density. Firstly, a simple step function with abrupt change of concentration at the position x corresponding to the lateral edges will be discussed, and then two other types of distribution functions will also be studied to approximate the real gradual concentration variation: linear and parabolic curves in function of the position x .

2.6.1.1 Electron concentration in the screened and unscreened parts over one period of grating

Table 2-4 lists the calculated N_1 , N_2 and t_1 (Figure 2-38) for the first three types of heterostructures at 300 K. ϕ_B is the Schottky barrier height (Au/Ti), ϕ_s is the surface Fermi level without metal. The potential values are referenced to reported experimental data, as for AlGaAs [Zhang1999] and GaN based materials [Hache1993, Yu1993-1]. Concerning the surface Fermi level of the SiGe/oxide interface no measurements data are available at the present. For the two hetero structures based on group III-nitride layers, the Fermi level pinning does not vary greatly in the two regions then the approximation of a homogeneous 2DEG distribution ($N_1 \approx N_2$) is reasonable.

Due to the relatively large variations between N_1 and N_2 in AlGaAs/GaAs heterostructure, only this structure will be considered for the non homogeneous 2DEG modeling with the home made program based on the CWM. In order to achieve the electron density in the order of 10^{16} m^{-2} , the barrier AlGaAs layer of 25 nm thickness is delta-doped ($\text{Al}_{0.3}\text{Ga}_{0.7}\text{As}$ (20 nm, NID)/ $\text{Al}_{0.3}\text{Ga}_{0.7}\text{As}$ (2 nm, $N_D = 2 \times 10^{19} \text{ cm}^{-3}$)/ $\text{Al}_{0.3}\text{Ga}_{0.7}\text{As}/\text{GaAs}$ (3 nm, NID)/GaAs (NID)). NID stands for non intentionally doping. For nitride based heterojunctions, the doping is not necessary in the barrier.

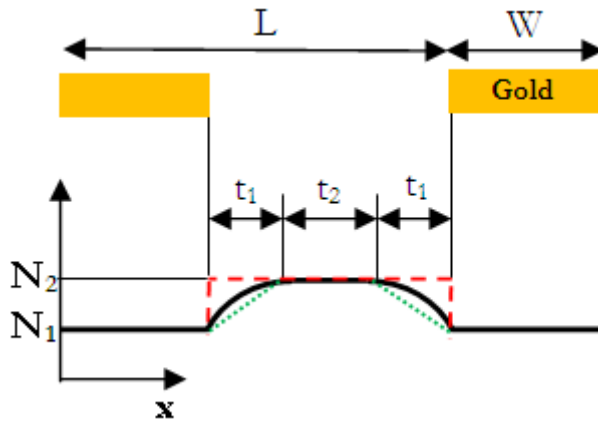


Figure 2-38: Non homogeneous distribution of electron concentration

Table 2-4: Calculated concentration at 300 K by a self consistent 1D Poisson- Schrödinger solver

Material	d (nm)	ϕ_B (eV)	ϕ_s (eV)	N_1 (10^{16} m^{-2})	N_2 (10^{16} m^{-2})	t_1 (nm)
Al _{0.25} Ga _{0.75} N/GaN	25	0.9	1.1	12.4	12.1	20
In _{0.18} Al _{0.82} N/GaN	10	0.85	0.9	12.0	11.7	10
Al _{0.3} Ga _{0.7} As/GaAs	25	0.85	0.65	1.28	1.65	20
SiGe/Si/SiGe						No experimental data available on the strained SiGe/oxide interface

2.6.1.2 Absorptions with non homogeneous 2DEG models

The periodic dielectric properties of 2DEG with alternating electron concentration N_1 and N_2 can be treated in a similar way as the metal grating (alternating Air/Metal), which has been addressed in section 2.3.3. According to the anisotropic permittivity of 2DEG layer, the components ϵ_{xx} (ϵ_{yy}) depends on the position through the electron concentration and ϵ_{xx} is still assumed to be the static dielectric constant. For the application in the non uniform 2DEG, one just has to replace ϵ_{xx} in the program dealing with isotropic problem of grating by the constant value ϵ_s and expand ϵ_{xx} (ϵ_{yy}) in Fourier series. For the step distribution function, both the program based on CWM and the code HFSS based on FEM apply, however, the latter is not suitable for the modeling of the other two types of distribution functions. Hence, only the CWM is employed to investigate the dispersion and spectrum of heterostructures with linear and parabolic 2DEG distribution functions at the transition part t_1 .

To evaluate the validity and the accuracy of the program, the absorption spectrum are compared with those obtained by HFSS based on FEM, taking the structure AlGaN/GaN at 300 K as an example with a step 2DEG density distribution function, which is shown in Figure 2-39. N_1 is fixed and N_2 is taken arbitrarily around N_1 . The two methods agree well, showing the capability of the CWM to deal with the periodic and non uniform 2DEG problems.

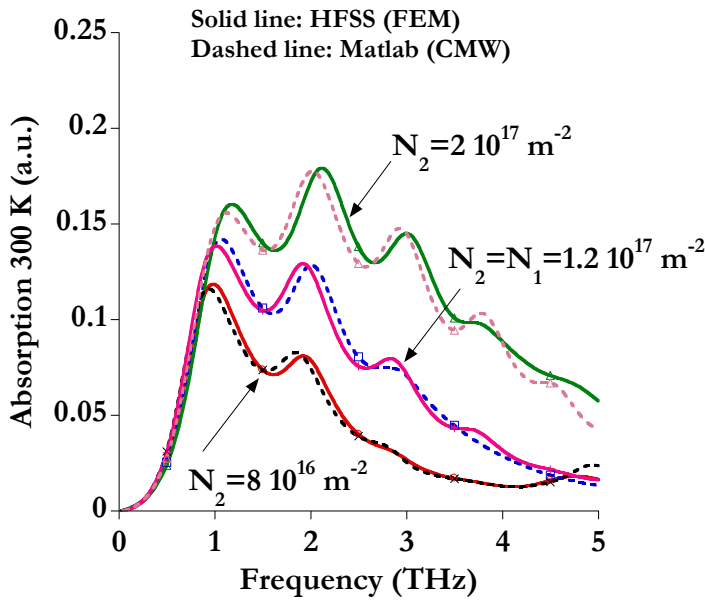


Figure 2-39: Comparison of the two numerical methods: Absorption spectrum of the nominal AlGaN/GaN structure with different concentration N_2 at 300 K, where $W/L = 0.75$, $N_1 = 1.2 \times 10^{17} \text{ m}^{-2}$ (solid line: HFSS (FEM), $\Delta S=0.005$. broken line: Matlab (CMW), $n_{\max}=20$)

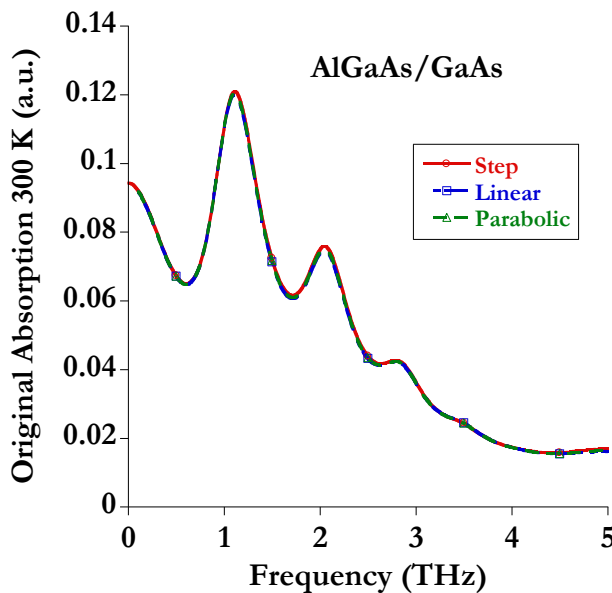


Figure 2-40: Comparison of the absorption spectrum with the three types of 2DEG density distribution functions (step, linear and parabolic) for AlGaAs/GaAs at 300 K, where $N_1 = 1.28 \times 10^{16} \text{ m}^{-2}$, $N_2 = 1.65 \times 10^{16} \text{ m}^{-2}$, $t_1 = 20 \text{ nm}$, $L = 1 \mu\text{m}$ and $W = 0.75 \mu\text{m}$

Since it is only necessary to consider the large difference between N_1 and N_2 in AlGaAs/GaAs structure, the following calculation with CWM is focused on this material. In Figure 2-40, the three types of 2DEG distribution functions are compared for the AlGaAs/GaAs structure at room temperature. The sheet density $N_1 = 1.28 \times 10^{16} \text{ m}^{-2}$. The non zero absorption at low frequencies is attributed to the Drude absorption background, where the metal grating do not exist. The three models show exactly the same spectrum, and this is due to the connection region

width t_1 (12 nm) which occupies a very weak portion in the whole gap region with the width $W_G = L - W$ (250 nm in minimum). For the structure AlGaAs/GaAs, we used the step function model.

2.6.2 Variation of electron concentration N_1 below biased metals

Both the frequency and amplitude of the PP resonances strongly depend on the electron density, as it has been discussed in the homogenous 2DEG case. By applying a bias V_G on the metal, the effective Schottky barrier height becomes $\phi_B - V_G \times e$ and the density N_1 (see Figure 2-38) will be altered accordingly. Positive V_G can decrease the barrier height and the corresponding N_1 will be increased. For negative V_G , the influence on N_1 is in the opposite direction. The tunability of the resonance frequency in the absorption spectrum can be possibly achieved by varying the applied bias, as it will be shown by the modeling (Figure 2-42).

Table 2-5: Electron sheet concentration N_1 in the screened region with applied voltage V_G (V) for AlGaAs/GaAs structure, where $N_2 = 1.65 \times 10^{16} \text{ m}^{-2}$

V_G (V)	N_1 (m^{-2})
0.4	1.72×10^{16}
0.2	1.65×10^{16}
0	1.28×10^{16}
-0.5	0.71×10^{16}
-0.8	0.12×10^{16}

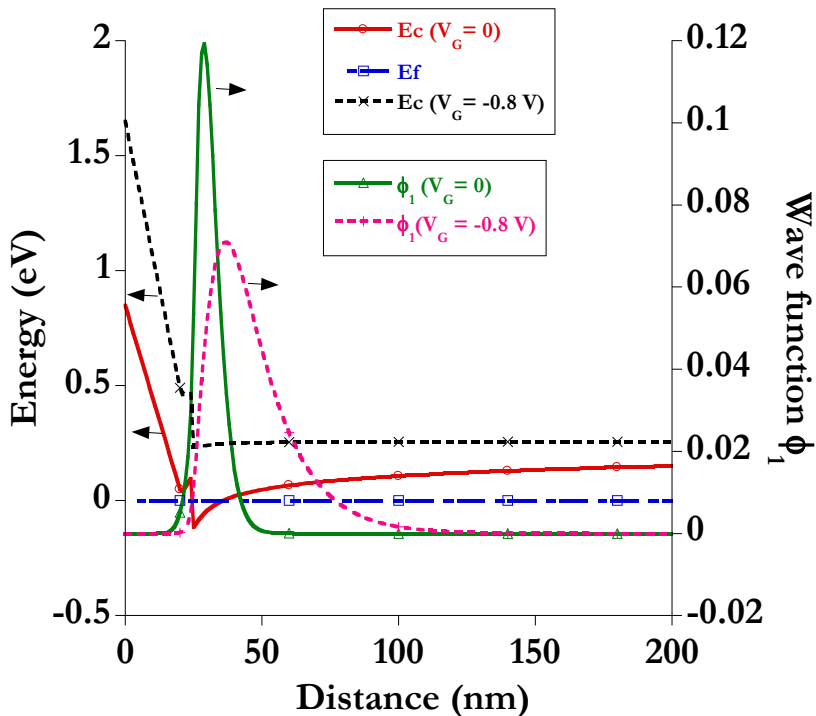


Figure 2-41: Calculated wave function and energy bands in AlGaAs/GaAs for the two cases: $V_G = 0$ and $V_G = -0.8 \text{ V}$

The calculated wave function and energy bands corresponding to the first electron eigenstate are displayed in Figure 2-41 and sheet carrier concentration N_1 is listed in Table 2-5 with different applied voltages, where $N_2 = 1.65 \times 10^{16} \text{ m}^{-2}$ is assumed to be not influenced. As demonstrated in the part 2.2.2.2, here we also use the code developed by G.Snider [Snider1990] with suitable applied barrier height at the surface. $V_G = 0.2 \text{ V}$ gives a homogeneous 2DEG ($N_1 = N_2$) and the values around 0.2 V will alter slightly N_1 . Large negative V_G can greatly reduce N_1 . At $V_G = -0.8 \text{ V}$, the electron conduction band is lifted above the system Fermi level and a small wave function peak locates around the interface AlGaAs/GaAs. In this condition, N_1 is smaller than ten percent of N_2 , indicating most of electrons below the metal strips are pushed out of the region.

Now we turn to the influences of “gate” biasing on the absorption spectrum. The electron concentration N_2 in the unscreened region is kept constant and N_1 in the screened region is varied between $0.12 \times 10^{16} \text{ m}^{-2}$ and $1.65 \times 10^{16} \text{ m}^{-2}$. The influence of N_1 on the absorption spectrum of the AlGaAs/GaAs structure at room temperature is shown in Figure 2-42 with two typical metal filling factors $W/L = 0.75$ (a) and 0.5 (b). For $W/L = 0.25$, the absorptions at the resonance peaks are weak.

Several observations can be made:

- (1) In comparison with the concentration N_2 , a slightly higher (lower) N_1 will shift the resonant peaks to high (low) frequencies. This is because the PP resonant frequency increases monotonically with the carrier density. The resonant amplitude has a higher value than that with the homogeneous 2DEG concentration $N_1 = N_2 = 1.65 \times 10^{16} \text{ m}^{-2}$. The step distributed 2DEG is not equivalent to a homogeneous 2DEG with an average concentration $N_{\text{avg}} = N_1 \times W/L + N_2 \times (L-W)/L$, because plasmon overlaid by metallic conductor and open air follow different dispersions [Nakayama1974] and absorption mechanisms [Fateev2010].
- (2) When the 2DEG is mostly overlaid by metals ($W/L = 0.75$) as in Figure 2-42 (a), the absorption amplitudes are reduced by decreasing N_1 . At $N_1 = 0.12 \times 10^{16} \text{ m}^{-2}$ ($N_1 \ll N_2$), the absorption (at 0.4 THz) becomes not discernible due to the extremely small N_1 . Moreover, a new resonance peak with a substantial amplitude appears and dominates at a higher frequency (2.3 THz). As the metal strip width W decreases as shown in Figure 2-42 (b), two resonance peaks appear and the dominant peak shifts to low frequency (1.7 THz). The second peak exists at 5.05 THz but it is not shown in Figure 2-42 (a) because it is beyond the maximum frequency of 5 THz in the simulation. Obviously, the dominant peak position depends on the gap width $W_G (= L-W)$. We attribute this phenomenon as the onset of microcavities in the region W_G where the unscreened plasmon begins to play the most important role in the absorption spectrum. Further explications will be shown in next section on the strong modulated 2DEG ($N_1 \approx 0$). Finally, the resonant amplitude has a higher value than that with the homogeneous 2DEG concentration $N_1 = N_2 = 1.65 \times 10^{16} \text{ m}^{-2}$, showing that the plasmon in open surface region can be more efficient to couple with the incident THz signal [Popov2008-2].
- (3) As the metal width W decreases, all the absorption amplitudes decrease and the resonant peaks of the screened plasmon move to a slightly larger values as discussed in section 2.4.7.3 for the influence of W/L on the resonant frequency, while the shift of the unscreened plasmon resonant position is in an opposite direction.

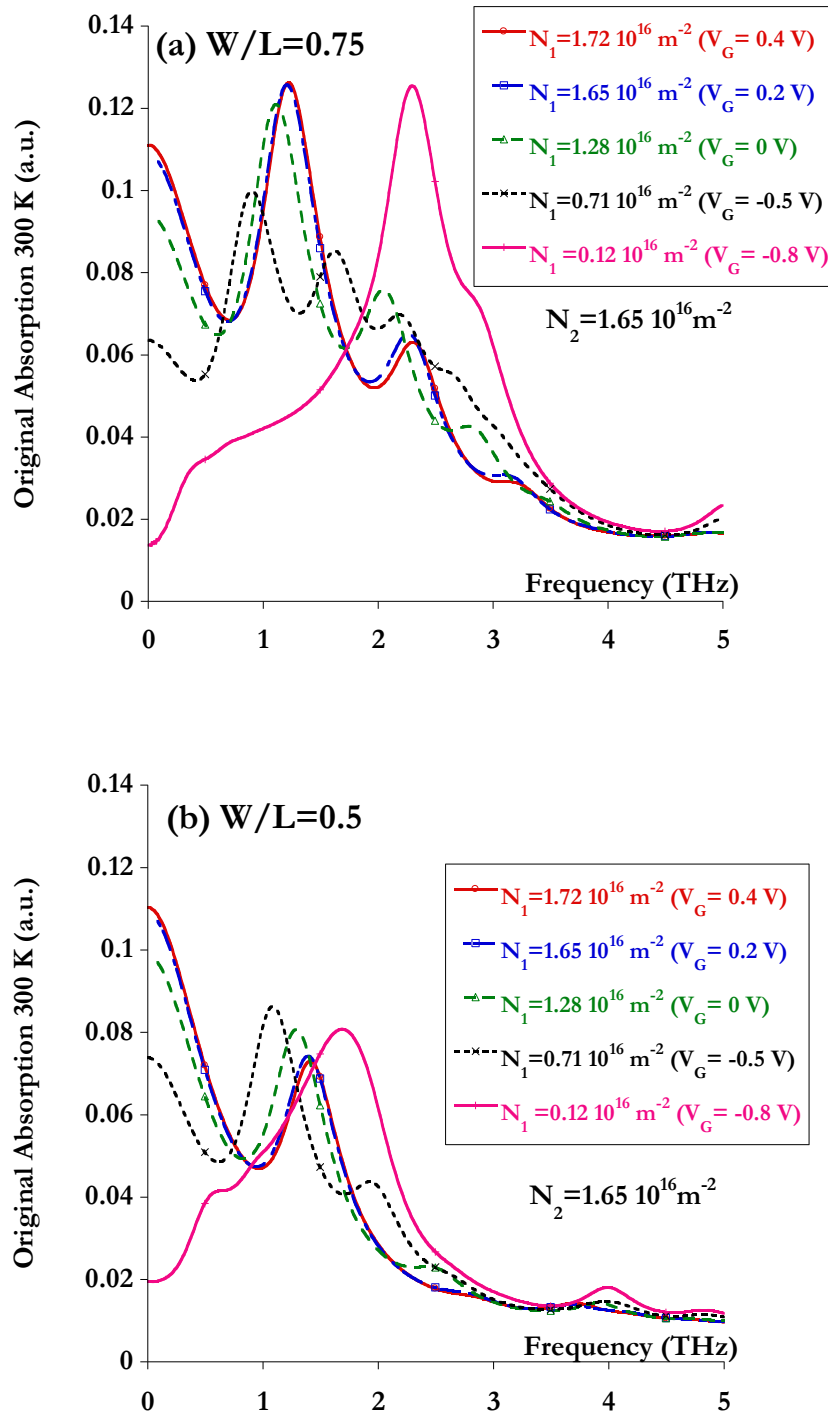


Figure 2-42: Absorption spectrum of the AlGaAs/GaAs structure with different 2DEG concentration N_1 at 300 K, where the metal width (a) $W = 0.75 \mu\text{m}$ and (b) $W = 0.5 \mu\text{m}$. The step function model is used with the parameters $N_2 = 1.65 \times 10^{16} \text{ m}^{-2}$ and $L = 1 \mu\text{m}$

2.6.3 Strongly modulated 2DEG

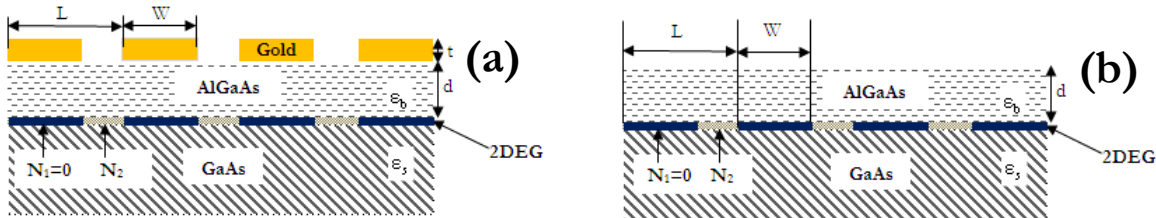


Figure 2-43: Schema of strongly modulated 2DEG in AlGaAs/GaAs structure: (a) with metallic grating, and (b) without metallic grating

Here the strongly modulated 2DEG system in AlGaAs/GaAs ($N_1 = 0$, $N_2 = 1.65 \times 10^{16} \text{ m}^{-2}$) will be studied both with and without grating coupler by CWM, as shown in Figure 2-43 (a) and (b), respectively. Figure 2-44 plots their original absorption spectra at 300 K with $W/L = 0.75$ ($L = 1 \mu\text{m}$). Compared with the curve with grating, where only one dominant resonant peak at 2.3 THz is observed, the small vibrations in the curve ($N_1 = 0.12 \times 10^{16} \text{ m}^{-2}$ and $N_2 = 1.65 \times 10^{16} \text{ m}^{-2}$) in Figure 2-42 (a) are attributed to the screened plasmon below the metal fingers with nonzero electron concentration N_1 . For the curve without grating in Figure 2-43 (b), one dominant resonance also appears at 3.05 THz with a much weaker amplitude. Therefore, the grating is helpful to reinforce the absorption of plasmon in this strongly modulated system. The amplitude and frequency of this type of resonance will be traced in function of the metal width in next paragraph.

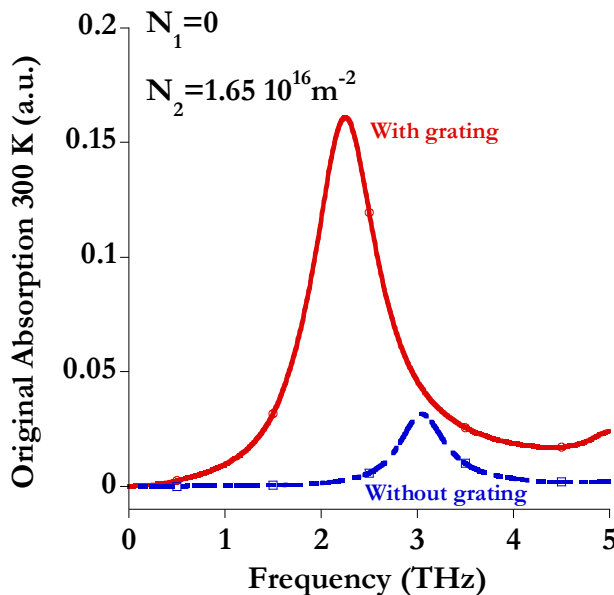


Figure 2-44: Original absorption spectrum of the strongly modulated AlGaAs/GaAs structure with and without metallic grating at 300 K. $N_1 = 0$, $N_2 = 1.65 \times 10^{16} \text{ m}^{-2}$, $L = 1 \mu\text{m}$, $W = 0.75 \mu\text{m}$ and $d = 25 \text{ nm}$

The references [Matov2002] and [Popov2003] demonstrated that there is a fundamental dipole like oscillation (antisymmetric electron density distribution at the opposing boundaries of electron strip) under the open surface part ($W_G = L - W$) when N_1 is zero. The dipole mode frequency in the classical one dimensional (1D) array of isolated electron channel with rectangular profile is evaluated by the formula,

$$f_{1D} = \frac{1}{2\pi} \sqrt{\frac{N_s e^2}{m^*(L-W)\epsilon_0 \bar{\epsilon}}} \quad (2-51)$$

Where $\bar{\epsilon}$ is the effective permittivity of the heterostructure including the dielectric screening effects of the layers of materials around 2DEG. The motion of electrons is classically confined (not quantum confinement) in the x direction. For the screened and unscreened structure, $\bar{\epsilon}$ has explicit approximate expressions [Ager1992-1] according to the expressions (2-41) and (2-40),

$$\bar{\epsilon} = \begin{cases} \frac{1}{2}(\epsilon_s + \epsilon_b \coth(kd)) & \text{screened} \\ \frac{1}{2}(\epsilon_s + \epsilon_b \tanh(kd)) & \text{unscreened} \end{cases} \quad (2-52)$$

Where ϵ_s and ϵ_b are the corresponded relative permittivity of the substrate GaAs and the barrier AlGaAs, d is the barrier thickness, and $k = \pi/W_G$ is the plasmon wavevector in this case.

In Figure 2-45, the frequency f_{1D} and amplitude A_{1D} of the principle resonance in the modulated AlGaAs/GaAs system are recorded versus the metal filling factor in [0.02-0.98]. Frequencies calculated by the analytic formula (2-51) are also superimposed for comparisons in Figure 2-45 (a). As the case of homogeneous 2DEG, the resonant frequency with grating is always below that without grating in the strongly modulated 2DEG. At $W/L \approx 0$, both of them begin at the same $f_{1D} \approx 0$. Because in this condition the 2DEG is almost homogeneous with electron density N_2 without grating coupler, no resonance will appear. The analytic formula using screened effective permittivity underestimates the observed resonant frequency with grating for $W/L < 0.9$, while the formula employing unscreened effective permittivity overestimates the resonant frequency without grating for $W/L < 0.6$. As W/L approaches 1, both the four curves converge at extremely high frequency due to the explosive growth of plasmon wavevector $k = \pi/W_G$ ($W_G \approx 0$). In this condition, the screened and unscreened effective permittivity are equal because $\coth(kd) = \tanh(kd)$ as $kd \gg 1$. It should be mentioned that when the 200 nm thick Au gratings are replaced by the semitransparent NiCr grating in [Matov2002, Mackens1984], it is approximately equivalent to the case of strongly modulated 2DEG without grating (open surface in Figure 2-43 (b)) because the semitransparent grating has nearly no screening effect. We can conclude that the Au metal grating strongly screens the plasmon in the open surface region even though the electron density below metal finger is nearly zero and the dominant peak position can be predicted to locate between the screened and unscreened dipole like resonance by expressions (2-51) and (2-52).

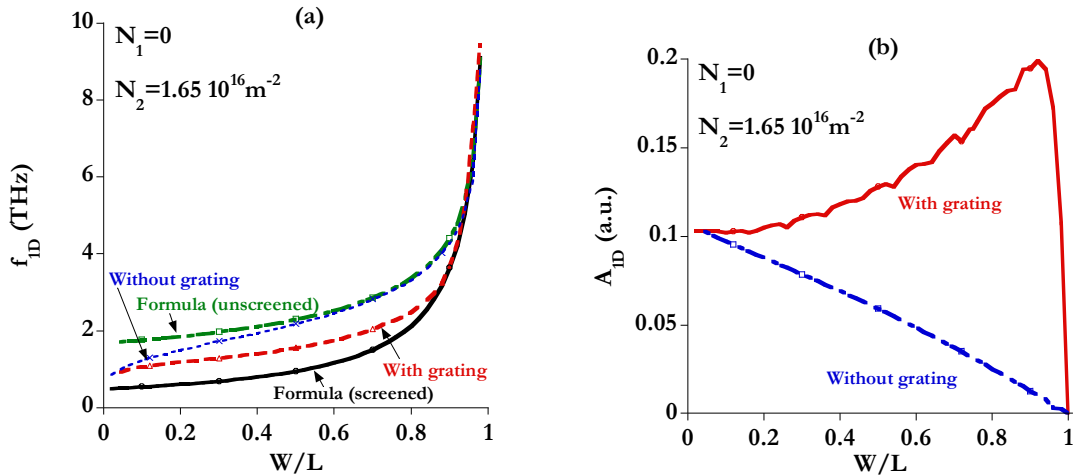


Figure 2-45: (a) Frequency and (b) amplitude of original absorption spectrum of the strongly modulated AlGaAs/GaAs structure versus the filling factor ($W/L = 0.02-0.98$) with and without metallic grating at 300 K. $N_1 = 0$, $N_2 = 1.65 \times 10^{16} m^{-2}$, $L = 1 \mu m$ and $d = 25 nm$. Simulated by CWM

Finally, we turn to the original absorption amplitude A_{ID} versus filling factor in Figure 2-45 (b). At $W/L \approx 0$, the grating in Figure 2-43 (a) can be considered to be not existent and it is equivalent to the case in Figure 2-43 (b) without grating. So the two curves converge to the same absorption at $W/L \approx 0$ (the nonzero absorption at 0.1 is due to the Drude background absorption of homogeneous 2DEG with concentration N_2). Then with the increase of W , the two types of amplitude behave in an inverse direction. A_{ID} with grating increases monotonically till $W/L = 0.93$ then decreases abruptly to zero. This is the same phenomena observed in the homogeneous 2DEG in AlGaAs/GaAs structure with grating (Figure 2-29 and Figure 2-31). For A_{ID} without grating, the absorption is mainly attributed to the Drude background type of 2DEG in the open face region. Naturally, it decreases monotonically to zero with reduction of the number of electrons in the 2DEG layer, or equivalently with the enlargement of W . We conclude that in the strongly modulated 2DEG system in AlGaAs/GaAs without grating, the self modulated 2DEG layer cannot replace the functions of metallic grating to scatter the incident THz wave and to make strong coupling between the evanescent waves and the plasmons. Metallic grating is still indispensable to achieve high absorptions in the strongly modulated case. The tunability of f_{ID} and A_{ID} can only be achieved by modifying metal width as the electron density N_2 is no longer allowed to alter. Furthermore, the technological realization of a modulated 2DEG system without grating is difficult.

2.6.4 Conclusions

Numerical method based on slightly modified CWM is used to study the spectrum response of an inhomogeneous 2DEG system. Two types of modulation are distinguished. The first is the natural modulation of electron concentration below and between metal fingers due to the difference between the barrier height at metal/semiconductor interface and Fermi level pinning at air/semiconductor interface. This is evident for 2DEG in AlGaAs/GaAs structure and is negligible in nitride based materials. The second type is the forced modulation by applying bias

voltage on metal fingers to alter electron concentration. The tunability of THz detection can be realized.

In the system of strongly modulated 2DEG in AlGaAs/GaAs, metal grating with relatively high filling factor helps to reinforce plasmon absorption in the quasi-1D array of electron strips. The tuning of absorption frequency and amplitude is not easy to realized once the sample is fabricated.

2.7 Conclusions of Chapter 2

To conclude this chapter,

2D plasmon in the heterostructures has been introduced. The calculation of the electron concentration is modelled when considering the polarization induced sheet charge. Different electron scattering mechanisms in the two dimensional system are discussed for the determination of electron mobility in function of the temperature. Numerical method of spectrum calculation for heterostructure with periodic metallic grating to realize the coupling between THz radiation and 2D plasmon has been derived in detail assuming TM polarized plane wave excitation from the air region on top of the grating. The dispersions of plasmon and plasmon polariton (PP) are displayed for three cases: screened plasmon ($W/L = 1$), unscreened plasmon ($W/L = 0$) and partially screened plasmon ($0 < W/L < 1$). Both the thicknesses of grating and 2DEG layer are considered and compared in the dispersions curves.

The effectiveness of the coupling between 2D plasmon and THz waves for several hetero structures such as AlGaN/GaN, InAlN/GaN, SiGe/Si/SiGe, AlGaAs/ GaAs has been calculated using HFSS software and home made model. The overall optimal hetero structure which has the maximum absorption due to the excitation of plasmon polariton has been proved to be the nitride based material. A large carrier concentration could be formed by the high spontaneous and piezoelectric polarizations without any doping layer. The other types of structures also have interesting performances at cryogenic temperatures because of the dramatic increase of the momentum relaxation time. Experimental and theoretical transmissions spectra agree very well in different temperatures and filing factors. Lower temperature and higher ratio W/L are appreciated for stronger PP resonances.

Then the incidence of a non uniform 2DEG concentration in the QW has been investigated. Three non uniform 2DEG profile models (piecewise constant, linear and parabolic) have been compared by the coupled wave method for the structure AlGaAs/GaAs. They are equivalent in this case because of the calculated small width t_1 of the transition region. The effect of the metallization voltage on the absorption spectrum reveals that the tunability of the resonant frequency by the bias voltage is also possible.

When the amplitude of applied negative voltage is sufficiently large to exclude the electron density below metals, the strongly modulated 2DEG will be formed. In this case, a dipole like resonance mode appears. Analyze of the frequency and amplitude of the resonance in function of the metal filling factor showed that both of them can be altered by the metal width.

Chapter 3 3D Electromagnetic Modeling and Measurements of Planar Waveguides in THz Frequency

3.1 Introduction

Planar waveguides are widely used in the microwave hybrid and monolithic integrated circuits (ICs) due to following advantages: (1) The waveguide characteristics (impedance, phase velocity, effective dielectric constant, etc.) can be easily controlled by the geometrical dimensions in a single plane. (2) The fabrication process can be realized by the standard technologies of photolithography, etching or lift-off process. (3) Parallel and serial combination of different structures may be conveniently accomplished without bringing great difficulties in the manufacture.

Among these waveguides, the structures exhaustively studied in millimeter wavelength range are stripline, microstrip line, coplanar waveguide (CPW), slotline and finline. Each type of line has its own advantages [Gupta1996]. Stripline has the unique feature of pure Transverse Electromagnetic (TEM) propagation (no dispersion) in the microwave frequency range. Its inconvenience comes from its geometry. Specific technological steps are needed notably in connection level with active or passive elements in the case of open planar circuits to be measured by a standard vector network analyzer. Microstrip line has been intensively studied and is well understood. This waveguide dominates in the microwave circuit with flexible adjustments, however via/holes are required to ground active devices which need complex technological steps and may degrade circuit performances at millimeter wave frequency. In reference to microstrip line [Pucel1981], CPW facilitates the connection with field effect transistor (FET), where the RF ground needs to be placed close to the device. Via/holes are not necessary. The major disadvantage of CPW is the unintentional excitation of parasitic slotline mode. The slotline shares some merits of CPW, but exhibits high dispersion behavior which makes it usually not applicable for broadband applications [Maloratsky2003]. Another type of transmission line, called Goubau line (G-line), was proposed firstly by Goubau in 1950 [Goubau1950] employing a lossy conductor with a cylindrical cross section coated by thin dielectric in free space. As the planar version of G-line compatible with semiconductor technology, planar Goubau line (PGL) with a rectangular cross section is preferred for its easy realization and integration.

However, as the frequency increases up to THz, both the losses and dispersions of these planar waveguides will differ from their properties in microwave range. So far, their propagation properties at THz frequency are not completely known and understood. In order to fill the gap, reevaluation of planar waveguides is necessary for short distance propagation as well as for the integration with the sources and detectors based on plasmonic semiconductor devices.

In this chapter, a 3D analysis of planar waveguides using ANSOFT HFSS® (<http://www.ansys.com/>) based on the frequency domain finite element method (FEM) and CST MWS® (<http://www.cst.com/>) based on finite integration technique has been conducted. Four kinds of waveguides have been studied: CPW with finite ground plane width (with and without backed conductor), microstrip, slotline and stripline on polymer or semiconductor

substrate. Many efforts have been put together to make a qualitative assessment of the dispersion and the losses in these different waveguides to optimize the THz transmission.

The CPW study enters in a continuity of the first analysis done in our group applied to the transmission of the THz pulse emitted from a InGaAs photoconductor (PC) switch on the InP substrate. Through this thesis, the CPW was investigated on a different substrate (a benzocyclobutene polymer). Simulations of slotline and stripline were also investigated in part by a master student during her internship in the team.

The influences of waveguide dimensions, metal conductivity and dielectric properties (low permittivity polymer and high permittivity semiconductor) on attenuations and dispersions are analyzed quantitatively by parametric studies performed numerically. After separated discussions for each transmission line, the four types of waveguides were compared to identify the best structure.

Finally, I have fabricated the waveguide CPW and microstrip on BCB in the clean room (CTU/MINERVE) at IEF. Preliminary experimental results of CPW with various widths and lengths will be presented in [340-500] GHz frequency range and compared with numerical simulations.

3.1.1 Electromagnetic modeling methods

The analysis approach of waveguide can be generally divided into two groups: quasi static and full wave methods. Quasi static method assumes the TEM mode propagation in the structure and it can be applied mainly at low frequency, where the conductor dimensions and dielectric thickness are much smaller than the wavelength in the dielectric substrate. This method can give analytical results of attenuations in a simple waveguide structure and provide qualitative reference for the designer at high frequency. To overcome the frequency limit of quasi static method, a more rigorous approach named full wave method was developed to consider the hybrid nature of mode in a waveguide and to calculate the complex propagation constant as a function of the frequency. According to the space or time discretization, different numerical methods appear: finite element method (FEM), finite integration technique (FIT), finite difference time domain (FDTD) method, etc. In this work, HFSS based on FEM and CST MWS based on FIT were employed to model all types of planar waveguides. The main analysis procedures for a waveguide structure can be briefly described following different steps as: 3D model development (conductors, dielectrics and surrounding air), material property attribution, boundary condition assignment, excitation signal setup (waveport), and EM analysis (meshing properties, convergence criteria and solution frequency).

3.1.2 Dispersions and losses of a waveguide

The figure of merit for any type of waveguide is the complex propagation constant $\gamma(\omega) = \alpha(\omega) + j\beta(\omega)$ where $\omega = 2\pi f$ is the angular frequency and j is the imaginary unit. The real part $\alpha(\omega)$ corresponds to attenuation losses per unit length and imaginary part $\beta(\omega) = 2\pi / \lambda_g$ (λ_g is the wavelength of guided mode) represents the phase constant in function of the frequency. The phase and group velocities can be obtained directly from $\beta(\omega)$. An ideal

transmission line has a TEM propagating mode with minimal attenuations. In HFSS, $\beta(\omega)$ and $\alpha(\omega)$ are calculated in different manners as discussed in the next sections.

3.1.2.1 Dispersions

The dispersions relation $\beta(\omega)$ represents the phase constant as a function of the frequency for all existing modes in a waveguide. It is extracted directly from HFSS from modeling with two waveport excitations. 2D waveport is designated to excite 2D or 3D models of waveguides. The modes excited in the waveguide are determined by the natural solutions of Maxwell's equations at a certain frequency in the 2D waveport area plane x-y (HFSS User's Guide, version 10, 2005),

$$\nabla \times \left(\frac{1}{\mu_r} \nabla \times \vec{E}(x, y) \right) - k_0^2 \epsilon_r \vec{E}(x, y) = 0 \quad (3-1)$$

Where ϵ_r and μ_r are the relative complex permittivity and permeability of the material, k_0 is the free space wave number. Each mode has a distinct $\vec{E}(x, y)$ pattern and a phase constant $\beta(\omega)$ if no degeneracy appears at the frequency ω .

Based on the dispersion relation $\beta(\omega)$, other parameters, namely the phase velocity V_p and the group velocity V_g can be defined as,

$$V_p = \frac{\omega}{\beta(\omega)}, V_g = \frac{d\omega}{d\beta(\omega)} \quad (3-2)$$

For TEM wave propagating in an homogeneous dielectric: $V_p = V_g = c / \sqrt{\epsilon_r}$. If there is dispersion (non TEM wave), both V_p and V_g will be dependent on frequency.

Another parameter frequently used in the planar waveguide is the effective dielectric constant for a certain mode. It is related to the phase constant $\beta(\omega)$ as,

$$\epsilon_{eff} = \left(\frac{\beta(\omega)c}{\omega} \right)^2 \quad (3-3)$$

For a mode propagating at the interface air/dielectric substrate, ϵ_{eff} is between 1 and ϵ_r . The ϵ_{eff} value reflects the relative level between field confinement in the dielectric and in the air regions. If ϵ_{eff} approaches ϵ_r , the most of the EM energy is concentrated in the dielectric substrate region. Various modes can propagate in the waveguide and thus with different ϵ_{eff} .

In regard to the four types of waveguide and as we know in microwave frequency, only the principle mode in a stripline (or tri-plate) surrounded by homogenous dielectric has its phase constant equal to the one of the dielectric substrate. The others lines are non TEM, because the

propagation takes place in two media simultaneously and components of the EM fields appears in the direction collinear to the wave vector. Moreover parasite or high order modes appear at certain frequencies (cutoff frequencies). Even in stripline high order modes appear at high frequency.

If parasite modes appear, the dominant mode may lose energy: Its phase velocity can become higher than the other modes, making possible the coupling between them and then an energy transfer. Among the unwanted modes there are the surface wave and the high order modes in the dielectric slab with finite thickness [Collin1960]. The surface waves can be possibly excited above the cutoff frequencies in planar waveguides owing the interface air/dielectric or metal/dielectric (Appendix A: Surface waves in a planar waveguide).

From the general point of view, when one mode M_1 has a phase velocity equal or higher than the other mode M_2 , a part of energy can be transferred from mode M_1 to mode M_2 . The frequency at which the two modes have the same phase velocity is defined as the critical frequency. For instance, in CPW structures, the critical frequencies between the CPW mode and the surface wave modes (Appendix A: Surface waves in a planar waveguide) are calculated with the approximation that the effective dielectric constant for CPW mode is the average value of 1 and ε_r [Collier1999],

$$f_{cri} = \sqrt{\frac{2}{\varepsilon_r - 1}} \frac{c}{\pi(2h)} \left(\arctan A + \frac{n\pi}{2} \right), n = 0, 1, 2, \dots \quad (3-4)$$

Where $A = \varepsilon_r$ for TM mode and $A = 1$ for TE mode. h is the thickness of dielectric. The formula is also valid for other waveguides if one assumes that the effective permittivity of the principle mode is $(1 + \varepsilon_r)/2$ and the surface waves exist. This formula can tell us approximately at which frequency, the coupling between modes becomes possible. Actual observed frequency may differ from the expression (3-4) due to the frequency dependent ε_r . The theoretical cutoff and critical frequencies of surface waves in CPW structure will be discussed in section 3.2.3.2 but they also apply in the other transmission lines.

3.1.2.2 Origin of losses

The total losses in a waveguide can be truncated as a linear combination of three kinds of loss:

$$\alpha_T = \alpha_R + \alpha_D + \alpha_C \quad (3-5)$$

Where α_R , α_D and α_C are the radiation, dielectric and conduction loss, respectively.

The radiation loss is often omitted in microwave circuit design, but they cannot be neglected at THz frequency. Different physical mechanism contributes to these attenuations. Following the expression (3-5), the three types of losses are independent and they can be investigated separately for each transmission line. To evaluate the losses in the 3D structure by HFSS, two waveports are used at the entrance and exit planes, and the scattering parameters (S parameters) are extracted between waveports. At each frequency, excitation signal is the type of sinusoid continuous wave

(CW). The attenuation α (positive, in dB) introduced by the waveguide is defined as the ratio of the transmitted power to the total power delivered to the device through S parameters,

$$\alpha = -10 \log \frac{|S_{21}|^2}{1 - |S_{11}|^2} \quad (3-6)$$

For a homogeneous line without impedance variation and transition, $|S_{11}| = 0$. This is true with waveport excitation of a uniform transmission line in HFSS. The excitation is directly done through a source perfectly match to the waveguide at each frequency. The loss can be then simplified and written as:

$$\alpha = -20 \log |S_{21}| \quad (3-7)$$

To separately study the origins of losses, the material properties of the substrate and the conductivity of the metal are manipulated according to the values in Table 3-1. For the radiation loss α_R , the metal is assumed to be quasi perfect (PEC) with an extremely large conductivity ($\sigma_{Au} = 10^{10}$ S/m) and the loss tangent in the dielectric is null. A finite metal conductivity ($\sigma_{Au} = 4.1.10^7$ S/m or 5.10^6 S/m for gold) is assigned to the conductor for the evaluation of the conduction loss α_C .

To estimate dielectric loss α_D , the loss tangent of substrate material is included and the metal is PEC. In our study a semiconductor or polymer substrate was used: indium phosphide (InP), or benzocyclobutene (BCB). For InP, the loss tangent is frequency dependent and its expression is $\tan \delta_{InP} = \sigma_{InP} / (\epsilon_{InP} \epsilon_0 \omega)$, where ϵ_0 is the permittivity in vacuum and $\sigma_{InP} = 2.4$ S/m is the conductivity of InP. We employed also benzocyclobutene (BCB) as polymer dielectric substrate. BCB film has attracted much attention in THz range due to its small permittivity (2.65 at 10 GHz) and low loss tangent (0.002 at 10 GHz). It is usually used as the dielectric on which the conductor lines are deposited to reduce the dielectric and radiation losses by pushing the propagation of high order surface wave modes at higher frequencies. The loss tangent for BCB is 0.007 by default in the simulation. The permittivity of InP and BCB are respectively $\epsilon_{InP} = 12.5$ and $\epsilon_{BCB} = 2.42$. The imaginary part of the permittivity accounts for the dielectric losses in the waveguides are listed in Table 3-1.

In the total losses α_T , both the contributions from the metal and the dielectric are included.

Table 3-1: Dielectric and conductor parameters for the losses calculation

Losses α	σ_{Au} (S/m)	σ_{InP} (S/m)	$(\tan \delta)_{BCB}$
α_R	10^{10}	0	0
$\alpha_R + \alpha_C$	$4.1.10^7$ or 5.10^6	0	0
$\alpha_R + \alpha_D$	10^{10}	2.4	0.007
$\alpha_T = \alpha_R + \alpha_D + \alpha_C$	$4.1.10^7$ or 5.10^6	2.4	0.007

Based on above strategies, the phase constant β and attenuation constant α will be analyzed separately for each waveguide versus frequency up to THz.

3.2 Harmonic analysis of CPW on BCB at THz frequency with HFSS

The conventional CPW was first proposed by C.P.Wen [Wen1969] in 1969. It consists in a central metal strip as signal line and two exterior strips with infinite width as ground planes on a semi-infinite substrate. In practical sense, as shown in Figure 3-1, both the side strip width S_2 and substrate thickness H are finite. S_1 is the central line width, W is the gap width between the central and ground plane, t is the metal thickness and L is the waveguide length in the propagation direction.

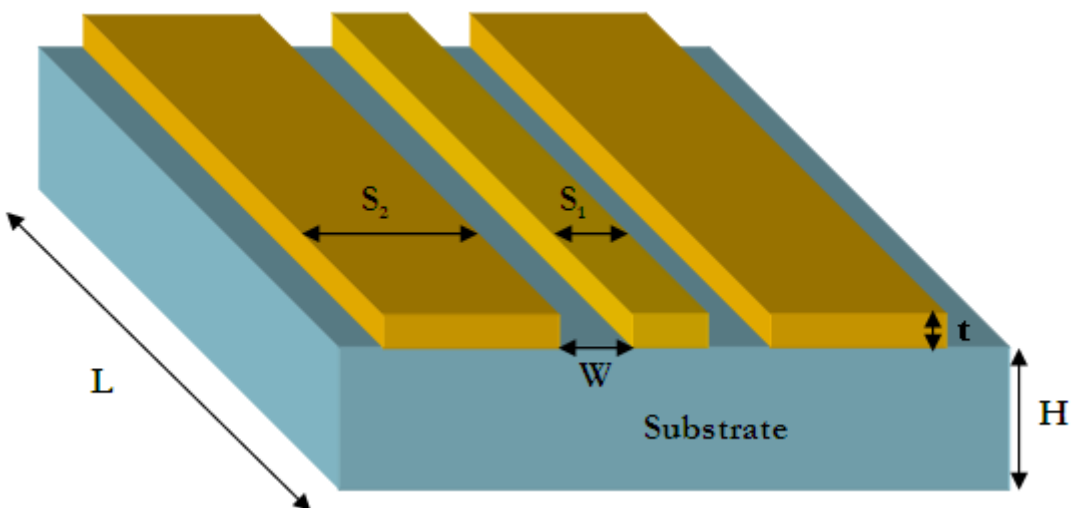


Figure 3-1: Schematic of a coplanar waveguide (CPW) on a dielectric substrate

Comparing with the other kinds of transmission lines, the most flexibility of CPW is to operate in shunt or series configurations. At a few GHz, two fundamental modes propagate in CPW: a symmetric CPW mode and an anti-symmetric slotline (SL) mode. For actual waveguides with substrate of finite thickness and ground planes with finite width, surface wave modes can occur at certain cutoff frequencies modifying the dispersion of the device. The SL mode is also parasitic. In Figure 3-2, the electromagnetic fields are presented for the two modes (CPW and SL modes). The CPW mode has its electric field distribution symmetric in reference to the middle plane of the central metal strip and most EM energy is confined at the two gaps regions between central line and outer ground planes. The parasitic SL mode has asymmetric field extensions, so this mode can be minimized by using the airbridges [Lee1999] or by maintaining the line symmetry to avoid its excitation [Jackson1986]. As air and dielectric substrate are semi-infinite (Appendix A: Surface waves in a planar waveguide), no surface waves exist in this conventional CPW.

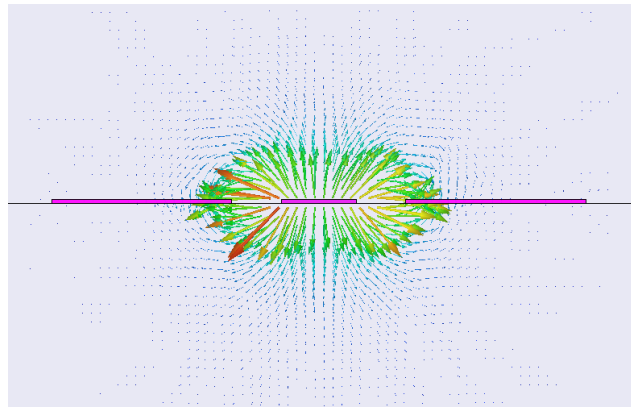
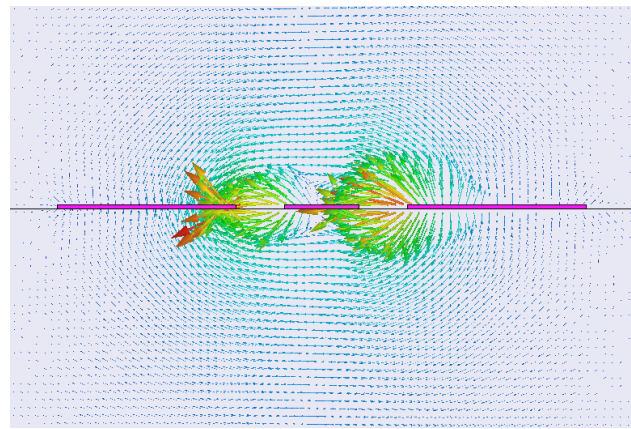
(a) *Symmetric CPW mode*(b) *Asymmetric Slotline mode*

Figure 3-2: Vector electric field distribution of the two principle modes in a conventional CPW structure, (a) Symmetric CPW mode and (b) Asymmetric slotline mode. The highlighted parts correspond to metals

Metallic air-bridges (ABs) connecting the two outer ground planes are usually added to enhance the symmetric mode propagation and to attenuate the slotline mode. We will discuss the role of the ABs in the section 3.2.2. Such CPW can be characterized by its dispersion, its losses but also by its impedance which both depend on its geometrical dimensions.

In addition to be air-bridged, the CPW can be backed with a metal layer which is deposited below the dielectric substrate. This latter allows electromagnetic isolation from components in adjacent layers in a multilayer circuit. For CPW with backed conductor, in addition to the two main modes (CPW and SL modes in Figure 3-3 (a) - (b)), another mode called "Microstrip mode" can be produced, as shown in Figure 3-3 (c). Most electric field is directed from the top metal layer to the underlying conductor, as in a microstrip line.

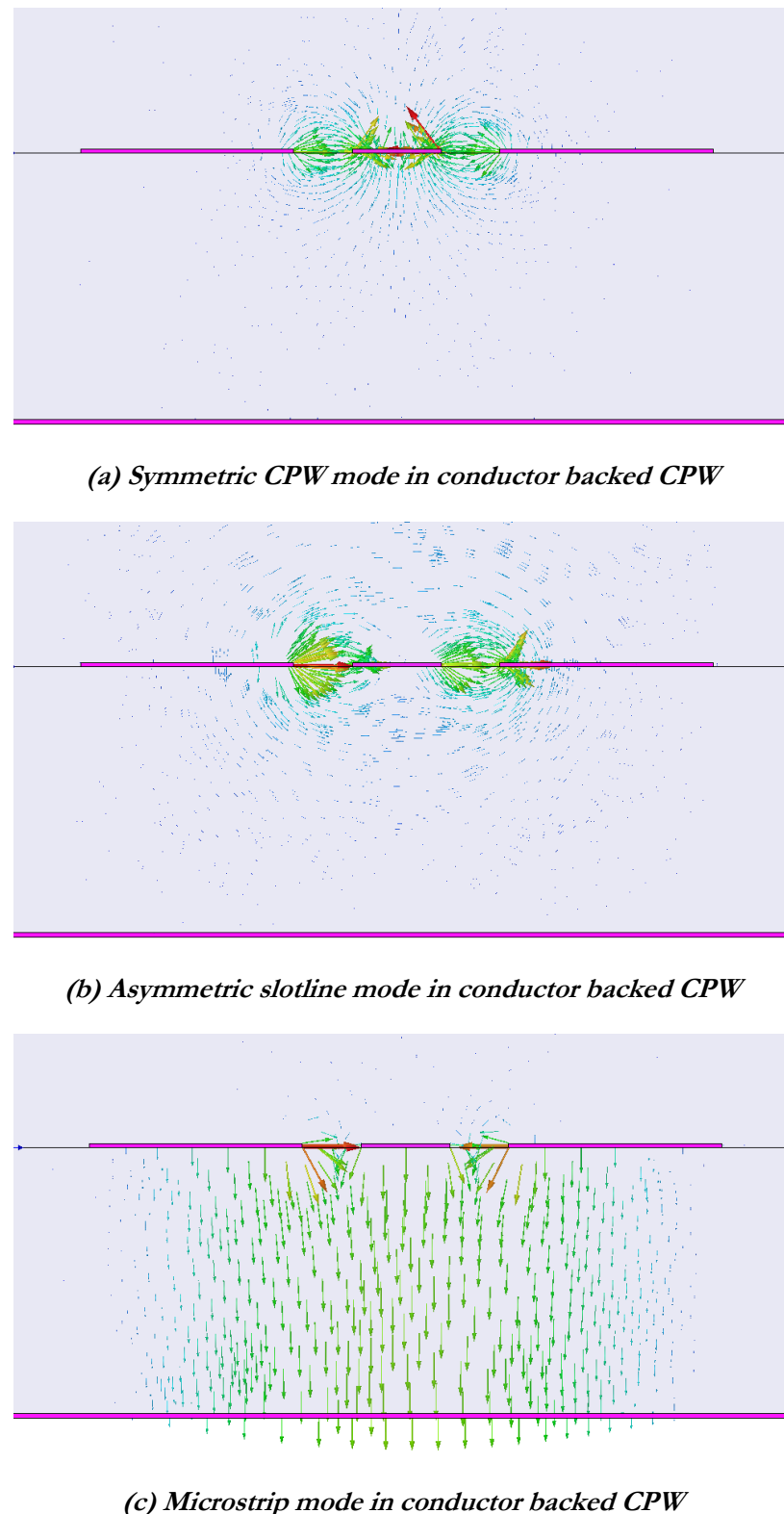


Figure 3-3: Vector electric field distribution of the three propagating modes in a conductor backed CPW (CB-CPW) structure: (a) CPW mode, (b) Slotline mode, and (c) Microstrip mode. The highlighted parts correspond to metals

In the next section we present the different CPW configurations studied.

3.2.1 Simulated CPW structures

Four configurations are proposed according to the presence or not of the ABs and backed conductor (BC) (Figure 3-4), where the underlined letters denotes the absence of component. The substrate thickness is fixed at 30 μm with the backed conductor (Figure 3-4 (c) and (d)) and assumed to be semi-infinite for the first two cases (Figure 3-4 (a) and (b)) by employing perfect match layer (PML) around the whole structure to simulate open air or infinite extension of materials. Figure 3-5 shows the 3D model in HFSS of the structure Figure 3-4 (d). Waveports are used for the excitation of the modes in CPW. The width of the waveport is chosen to be at least three times of the effective width W_{eff} ($= S_1 + 2W$) to avoid the fringing field coming from the central strip trace to waveport edge.

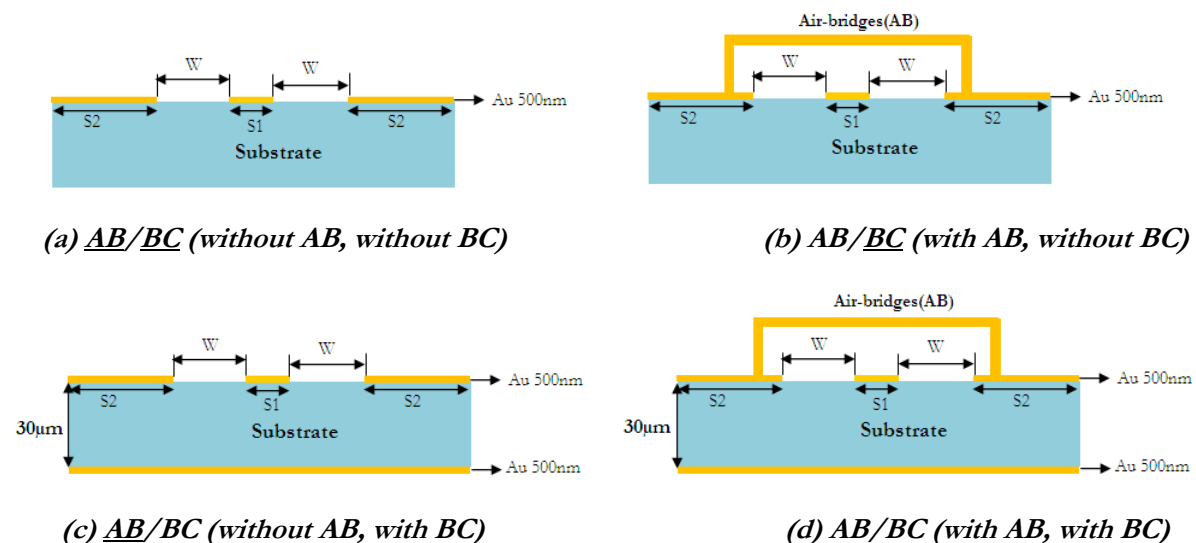


Figure 3-4: Four types of CPW configurations in the numerical simulation (BC: Baked Conductor)

A typical CPW structure contains a central strip and two metallic ground planes on a semiconductor dielectric substrate. The geometric parameters are chosen as follows: the central strip width ($S_1 = 10 \mu\text{m}$), ground plane width ($S_2 = 24 \mu\text{m}$) and the gap width ($W = 1.6, 6.6$ and $12 \mu\text{m}$). The characteristic impedance of an ideal CPW at low frequency decreases with substrate permittivity ϵ_r and is proportional to the ratio W/S_1 . CPW on InP with $W = 6.6 \mu\text{m}$ corresponds to the nominal structure used for PC switch applications studied in our group. Its characteristic impedance is 50Ω at 20 GHz and $W = 1.6$ (30Ω) and 12 (66Ω) μm are selected around $6.6 \mu\text{m}$ to study the geometrical influence. We kept the same dimensions for CPW on BCB substrate to perform comparisons. Thus the impedances will change and their values at 20 GHz are: 73 ($W = 1.6 \mu\text{m}$), 102 ($W = 6.6 \mu\text{m}$) and 123 ($W = 12 \mu\text{m}$) Ω . To achieve a characteristic impedance of 50Ω for CPW on BCB, the gap width W should be $0.4 \mu\text{m}$ ($S_1 = 10 \mu\text{m}$), making the technological realization difficult. This can be overcome by increasing S_1 . For instance, at $S_1 = 36 \mu\text{m}$, W will be $3 \mu\text{m}$ (50Ω CPW), which is well located within the fabrication limit. The 50Ω CPW on BCB will be characterized in the experiments at the end of this chapter.

The simulated line length is 1 mm with two ABs equally placed at a distance of 50 μm from the two ends. Their thickness, height and depth are 1, 3 and 7 μm , respectively, as shown in Figure 3-5 (b). The thickness of the strip lines and the backed conductor is 500 nm. The propagation

wavelengths $\lambda_g = 2\pi/\beta$ of the different modes and the losses are calculated in the frequency range [20 – 1000] GHz.

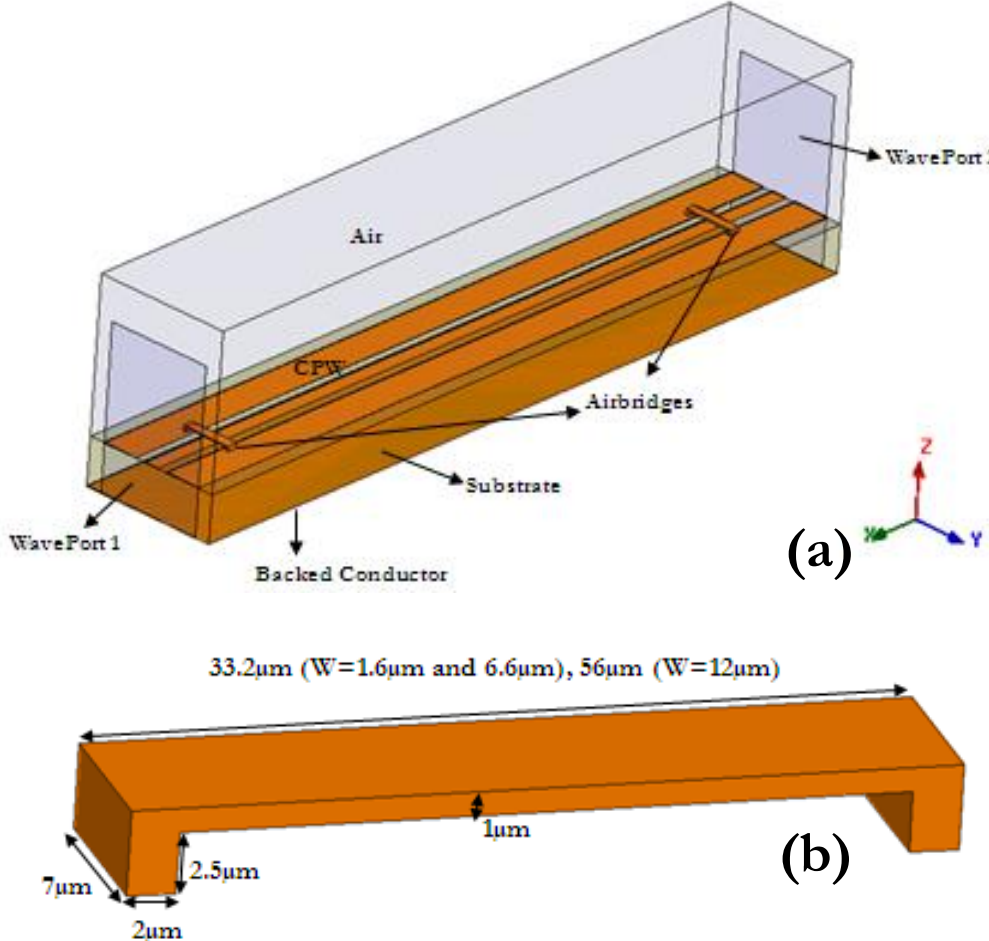


Figure 3-5: (a): HFSS 3D model of CPW with airbridges and backed conductor (Figure 3-4 (d)) and (b): Dimensions of the 3D airbridges (AB) in the simulation

In the following sections, we will firstly discuss the role of ABs on the dispersion and losses of CPW on semi-infinite substrate BCB. Then the performances of CPW with ABs on semi-infinite substrate InP and BCB are compared versus the gap width W. The function of backside metallization (BC) is relatively complex. Therefore, the analysis of BC is scheduled at the end of this CPW numerical study.

3.2.2 Role of the air-bridges (ABs) on effective permittivity and total losses

Airbridges are employed to attenuate the parasitic unwanted slotline mode in the standard CPW structure [Lee1999]. In this part, we look at the role of the air-bridges on the effective permittivity, the dispersion and the attenuation constant for the CPW on BCB substrate. For this study, the metal conductivity is chosen at $\sigma_{Au} = 5.10^6$ S/m in order to take into account the non perfect character of metallization in the fabrication process. AB (AB) represents the case with (without) airbridges in the simulation, while the other dimensions and dielectric properties are the same.

3.2.2.1 CPW without backed metallization

Figure 3-6 shows the effective permittivity of CPW mode for the three dimensions with and without ABs. As we can observe, ABs do not have an important impact on the propagation constant or the effective dielectric constant of the wanted CPW mode and of the parasitic slotline mode.

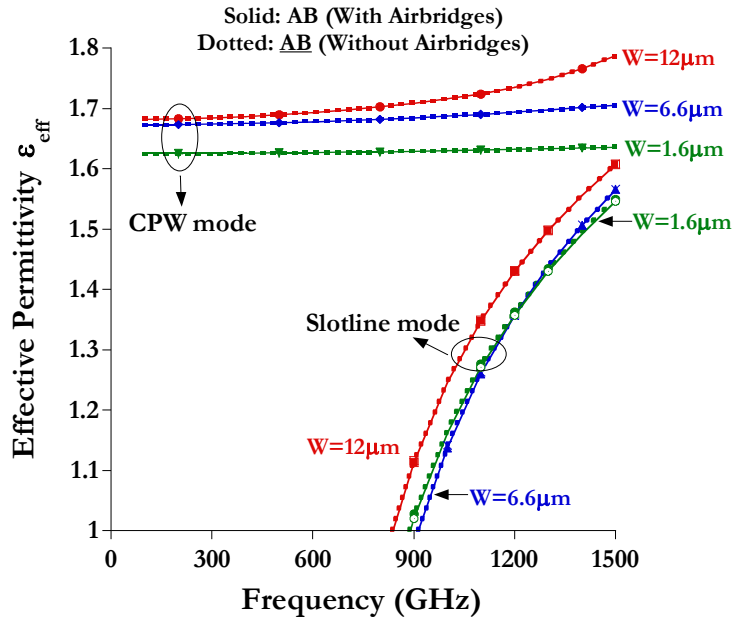


Figure 3-6: Influences of airbridges (AB) on the effective permittivity of the mode CPW and slotline for CPW on semi-infinite BCB

Next, we move to the aspect of total losses. In Figure 3-7 (a) with $W = 1.6 \mu\text{m}$, the presence of ABs drastically increases the attenuation constant of slotline mode at low frequency with a typical value of 20 dB at 600 GHz, even at 1.5 THz, an additional 10 dB value is obtained. The symmetric CPW mode shows no considerable differences. At the large gap $W = 12 \mu\text{m}$ (Figure 3-7 (c)), the loss increase of the slotline mode is also comparable with the case $W = 1.6 \mu\text{m}$. At the high frequency side, CPW with ABs shows a little more attenuation because the fringing field in the gaps will extend further into the air region and touch the ABs on top with the increase of gap width. An additional conduction loss existing in the ABs may contribute to the increase of total losses.

Although the case of CPW on InP is not shown here, it has been observed that ABs are also efficient to prevent the propagation of slotline mode, and at the same time have little impact on the CPW mode. Their influences on the phase and group velocities of CPW mode will be further discussed in section 3.2.3. In spite of all the advantages of ABs, the technical realization of the airbridges remains a challenging fabrication process.

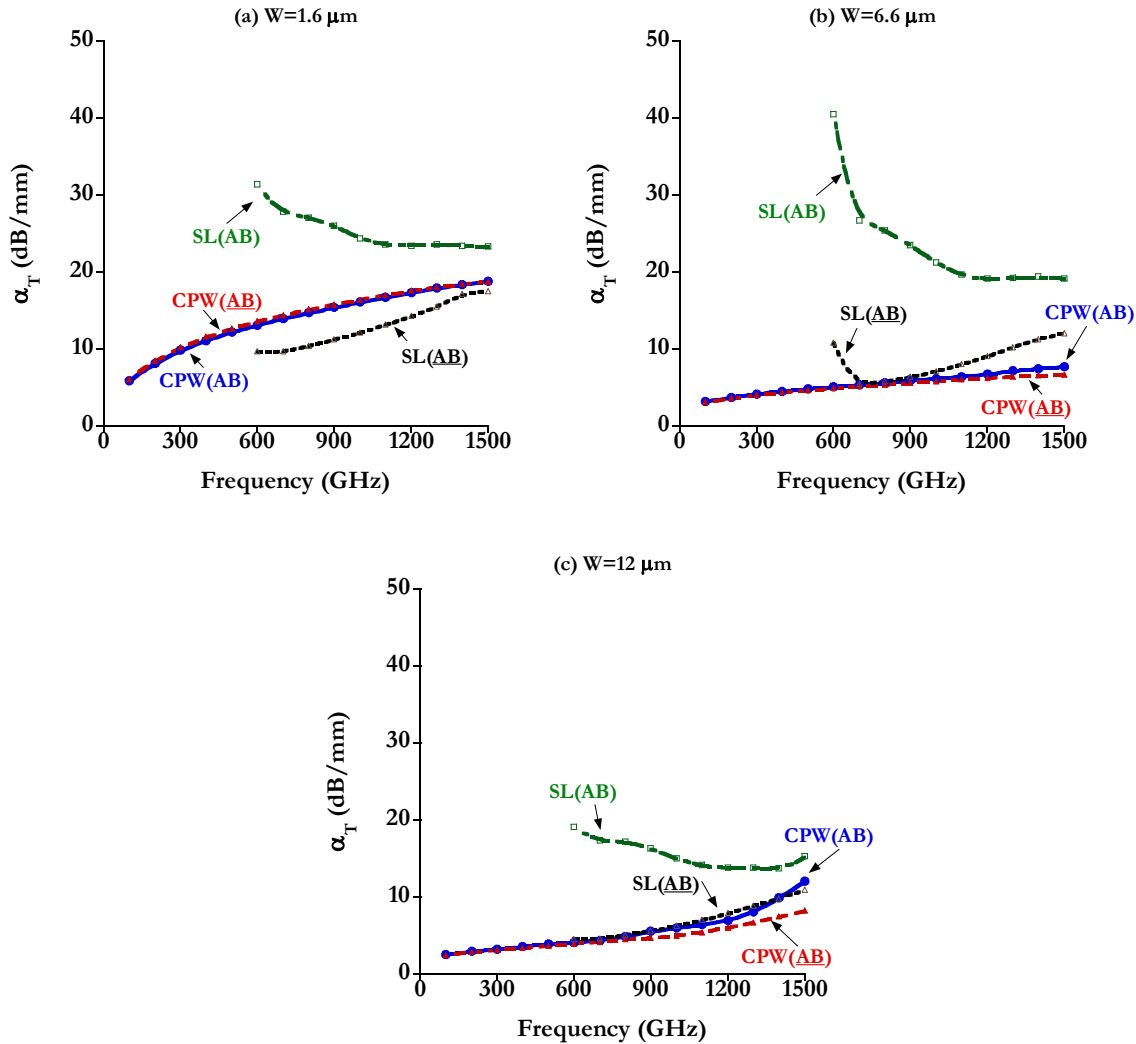


Figure 3-7: Influences of airbridges (AB) on the total attenuation of CPW mode and Slotline (SL) mode for CPW on semi-infinite BCB: (a) $W = 1.6\text{ }\mu\text{m}$, (b) $W = 6.6\text{ }\mu\text{m}$ and (c) $W = 12\text{ }\mu\text{m}$

3.2.2.2 CPW with backed metallization

In the conductor backed CPW, the effective permittivity of the three modes (CPW, Slotline and Microstrip) are plotted in Figure 3-8. Again, ABs have no impact on the dispersions of all the modes.

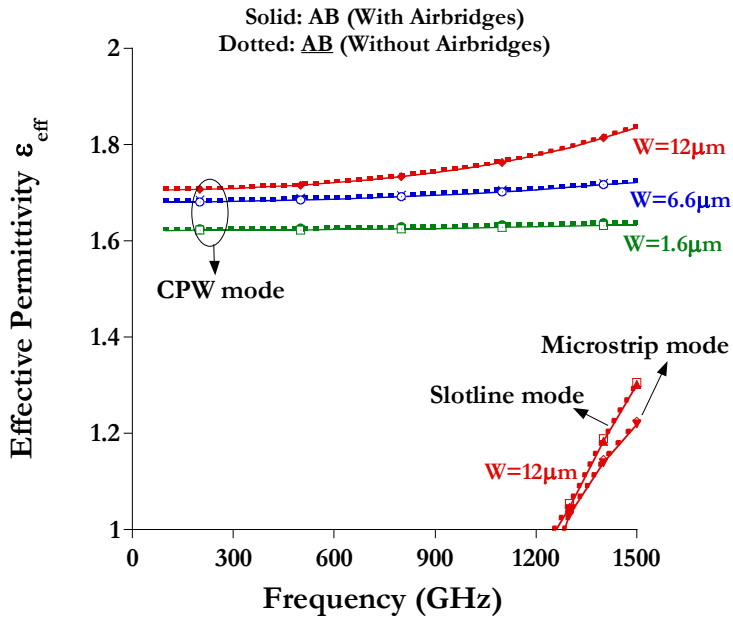
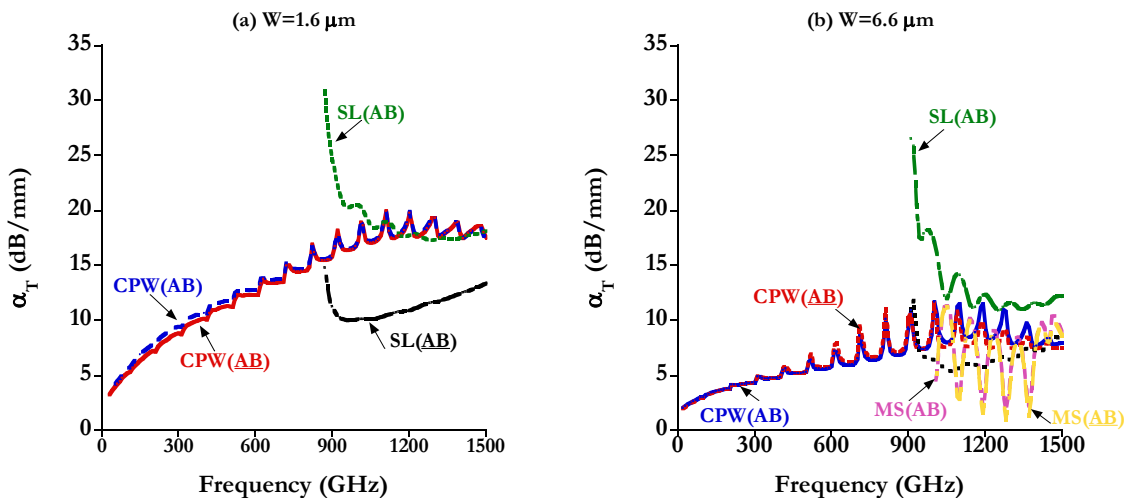


Figure 3-8: Influences of airbridges (AB) on the effective permittivity of the mode CPW, slotline and microstrip for CPW on 30 μm BCB with backed conductor at different W

Figure 3-9 shows the total losses for the three modes in conductor backed CPW, where BCB thickness is 30 μm . For the mode CPW and microstrip, their attenuations are not modified greatly by ABs at $W = 1.6$ and 6.6 μm . While at $W = 12 \mu\text{m}$, the conduction losses in ABs result in the noticeable increase of attenuation from 0.9 THz. For the mode slotline, ABs have also the ability to increase its propagation loss. An additional loss of 10 dB/mm at 1 THz and 5 dB/mm at 1.5 THz in reference to the case without ABs at $W = 1.6 \mu\text{m}$. This advantage becomes weak at large gap ($W = 12 \mu\text{m}$).

The fluctuations appearing in the losses are attributed to the formation of resonances due to the existence of metallic parallel plate in the structure, which will be discussed in section 3.2.4.2.



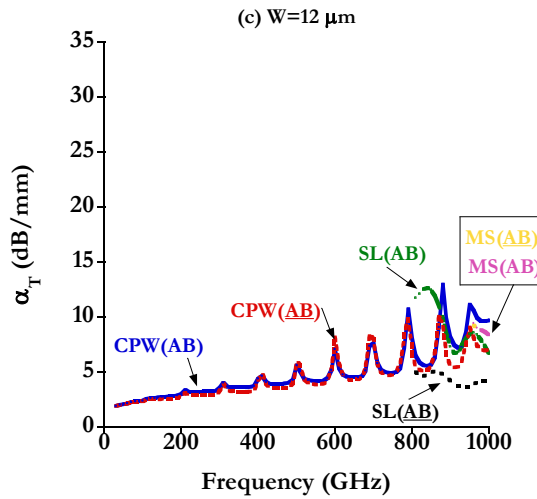


Figure 3-9: Influences of airbridges (AB) on the total attenuation of mode CPW, Slotline (SL) and Microstrip (MS) for CPW on 30 μm BCB with backed conductor: (a) W = 1.6 μm, (b) W = 6.6 μm and (c) W = 12 μm

We conclude that the ABs do not play an important role on the dispersion and losses of CPW mode with and without backed conductor for frequency below 1 THz. But they can reduce the effects played by the slotline mode in the signal propagation in CPW. It should be mentioned that the number, dimensions and positions of ABs in CPW structure may modify the roles presented above. In the following, we choose the CPW configuration with ABs to evaluate the influences of backed conductor on its dispersions with the variations of substrate and gap dimensions.

3.2.3 Modal dispersions, coupling effect, phase and group velocities

The dispersion curves of a waveguide offer the relationship between the propagation constant β and the excitation signal frequency for all the modes supported by the structure. Moreover, it also allows calculating the coupling coefficients between two different modes to numerically quantify their interactions. For example, the coupling between CPW mode and the other modes or waves (slot line mode, substrate wave and surface waves) may influences the radiation loss of CPW mode [Grischkowsky1987] based on the analysis of phase and group velocities.

3.2.3.1 AB-CPW without backed conductor

The Figure 3-10 plots the dispersions of both the two modes (CPW and Slotline modes) of CPW structure AB/BC (Figure 3-4 (b)) on the two types of dielectric BCB and InP. The loss and dispersion properties of CPW on the substrate InP comes from a previous work of our group [Grimault2012].

The straight lines TEM_{BCB} or TEM_{InP} represent the free propagating wave in the bulk substrates ($\beta = 2\pi f \sqrt{\epsilon_r} / c$) as the reference. The gap width is fixed at W = 6.6 μm. For CPW on BCB, the dispersion curve of the mode CPW does not intersect with other modes in all the frequency range up to 3 THz, indicating that low power leakage from CPW mode to Slotline mode.

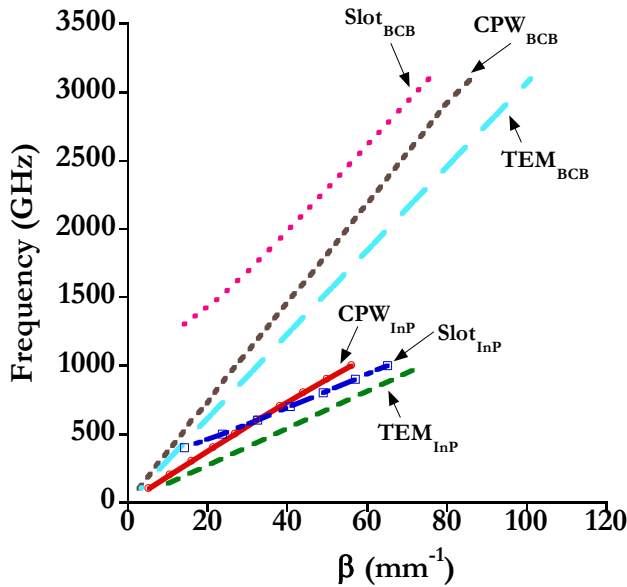


Figure 3-10: Comparison of dispersion curves for conventional CPW on semi-infinite substrate BCB and InP with airbridges ($S_1 = 10 \mu\text{m}$, $S_2 = 24 \mu\text{m}$, $W = 6.6 \mu\text{m}$)

When the frequency of the excitation signal is close to the critical frequency, mode coupling will become strong and we can evaluate numerically the coupling efficiency between two propagating waves in the structure with the calculation of a field overlap integral. According to the coupled mode theory [Haus1991], we can define a coupling coefficient whose expression is [Riaziat1990]:

$$C = \frac{0.5 \int (\vec{E}_1 \times \vec{H}_2 + \vec{E}_2 \times \vec{H}_1) \cdot d\vec{S}}{\sqrt{\|(\vec{E}_1 \times \vec{H}_1) \cdot d\vec{S}\| \|(\vec{E}_2 \times \vec{H}_2) \cdot d\vec{S}\|}} \quad (3-8)$$

Where $d\vec{S}$ is the normal surface vector in the propagation direction of transmission line, and subscripts 1 and 2 indicate the two interacting waves. A large value of C between 0 and 1 stands for great coupling effect.

Indeed, the calculated coupling coefficient is 0.0033 at 3 THz for CPW on BCB while for CPW on InP, the curve of the slot line mode crosses the CPW mode at 0.6 THz, predicting the onset of energy exchange between the two modes. The coupling coefficient is 0.2764 at 600 GHz. Because the phase velocity of CPW mode is always greater than the TEM wave in the substrate, the CPW is unconditionally leaky that leads to the radiation losses. The coupling coefficients between CPW mode and Slotline mode are listed in Table B-1 and Table B-2 for CPW without and with ABs, respectively in Appendix B: Coupling coefficients in CPW. Up to 1.5 THz, the coupling is still negligible and the functions of ABs on reducing the coupling effect are not obvious for CPW on BCB. However, as seen in previous sections, ABs can greatly attenuate the slotline mode.

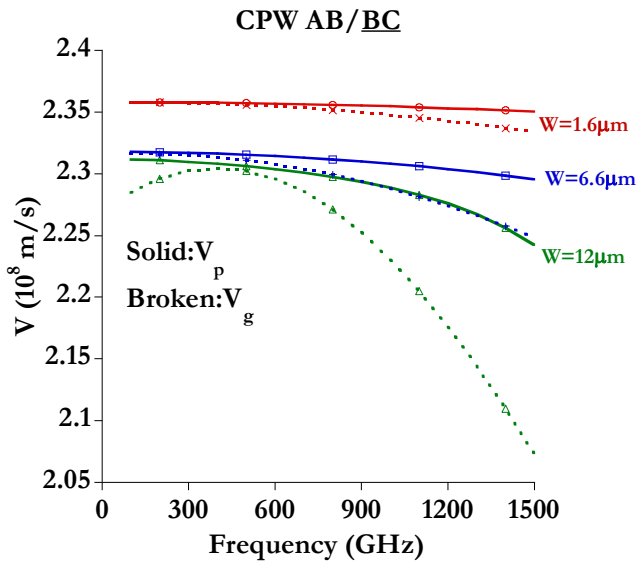


Figure 3-11: Phase (solid) and group (broken) velocities of CPW mode in conventional CPW on BCB substrate with ABs

Figure 3-11 presents the phase and group velocities of the CPW mode in conventional CPW structure. We conclude that CPW mode is more dispersive as the frequency or the gap width increases because the discrepancy between V_p and V_g becomes larger.

3.2.3.2 AB -CPW with backed conductor

In Figure 3-12, the dispersions curves of the three propagating modes in a conductor backed CPW ($W = 12 \mu\text{m}$) on BCB are shown. The cutoff frequency is 0.8 THz for slotline mode and 0.9 THz for microstrip mode due to the excitation scheme. Because their phase velocity is always greater than that of the CPW mode from DC frequency to 1.5 THz, less leakage from CPW mode to them is expected to occur. At 1.5 THz, the coupling coefficient is 0.0114 between CPW mode and slotline mode and 0.0003 between CPW mode and microstrip mode. Mode coupling is weak, so the radiation loss will be mainly due to the leakage into the substrate of the dominant CPW mode. The coupling coefficients between CPW mode, Slotline mode and microstrip mode are listed in Table B-3 and Table B-4 for CPW without and with ABs, respectively in Appendix B: Coupling coefficients in CPW. At the cutoff frequency of microstrip mode, the coupling coefficient with CPW mode is much higher than that between Slotline and CPW modes, showing microstrip mode is easier to couple with CPW mode due to their common symmetry of field distributions in the two gap regions (Figure 3-3 (a) and (c)). As in conventional CPW, the functions of ABs on reducing the coupling effect in conductor backed CPW is not obvious, but ABs can also greatly attenuate the slotline mode.

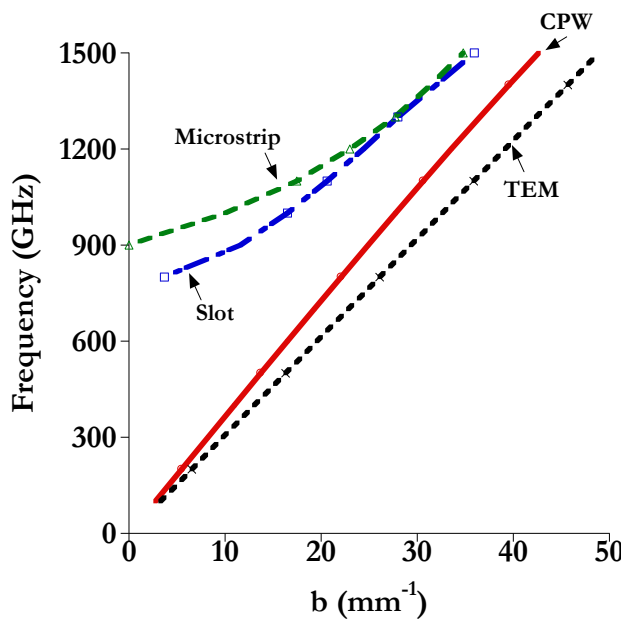


Figure 3-12: Dispersion curves of the three supported modes for conductor backed CPW on 30 μm BCB substrate with airbridges ($S_1 = 10 \mu\text{m}$, $S_2 = 24 \mu\text{m}$, $W = 12 \mu\text{m}$)

One may observe that the cutoff frequency of the slotline mode is not zero as predicted by microwave theory. This is due to the specific excitation method for CPW in the software HFSS with a waveport. The excitation of surface waves in dielectric waveguide is also prohibited.

Furthermore, even if the surface waves are excited in the conductor backed CPW, there influences on the CPW mode will not be broad in the considered frequency range. Table 3-2 summarizes the cutoff frequencies and the critical frequencies of the first four surface waves in CPW with backed conductor on the low permittivity BCB and high permittivity InP. Only TM odd and TE even modes appear. The first surface wave is TM_0 with zero cutoff frequency in theory and the critical frequency is located at 2.2 THz for CPW on BCB due to the small dielectric constant. The next mode is TE_1 with the cutoff frequency of 2.1 THz. For CPW on substrate with large permittivity, both the cutoff frequency and the critical frequency of the surface waves decrease. Fortunately, the critical frequencies of the first surface wave TM_0 are very high (2.2 THz for BCB and 1.0 THz for InP). Therefore the coupling effect between CPW mode and different surface wave modes are omitted in numerical calculations.

Table 3-2: The cutoff frequencies of surface waves in the structure air/conductor backed dielectric (thickens $h = 30 \mu\text{m}$, $\epsilon_{BCB} = 2.42$, $\epsilon_{InP} = 12.5$)

Surface wave	BCB		InP	
	Cutoff frequency (THz)	Critical frequency (THz)	Cutoff frequency (THz)	Critical frequency (THz)
TM_0	0	2.2	0	1.0
TE_1	2.1	4.5	0.7	1.6
TM_2	4.2	8.2	1.5	3.1
TE_3	6.3	10.4	2.2	3.6

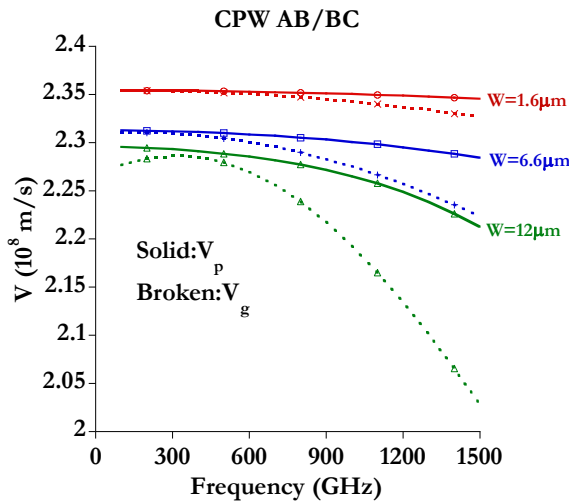


Figure 3-13: Phase (solid) and group (broken) velocities of CPW mode in conductor backed CPW on BCB substrate with (b) airbridges

In Figure 3-13 the phase and group velocities of the CPW mode in conductor backed CPW structure at the three W values are presented and compared. As in the conventional CPW, CPW mode is more dispersive at larger f (>500 GHz) and for larger W.

3.2.3.3 Comparison of effective permittivity between AB CPW with and without backed conductor

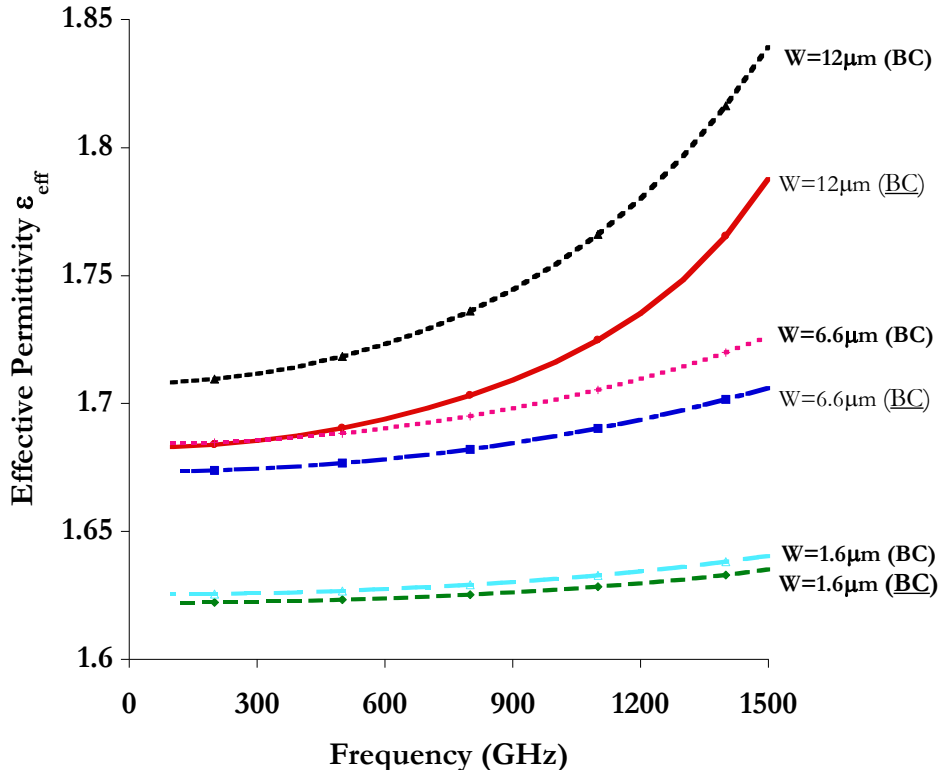


Figure 3-14: Effective dielectric constant of CPW mode on the substrate BCB with airbridges ($S_1 = 10 \mu\text{m}$, $S_2 = 24 \mu\text{m}$)

To evaluate directly the influences of backed conductor on the dispersion of the mode CPW, Figure 3-14 compares the effective permittivity at different gap width for CPW with (BC) and without (BC) backed conductor. The effective permittivity was calculated by equation (3-3).

Both the waveguide dimensions and the frequencies affect ϵ_{eff} . As seen in Figure 3-14, the effective permittivity increases with both the frequency and gap width due to more confinement of EM field in the dielectric side. At large W, the increase ϵ_{eff} is rapid. Hence CPW at greater W suffers from more dispersion. Additionally, the existence of backed conductor helps to enhance the penetration of field components in the dielectric for the three gap widths, therefore showing a relatively larger effective permittivity ϵ_{eff} than conventional CPW.

After examinations of these propagating modes in conventional and conductor backed CPW, the different contributions in the losses will be evaluated quantitatively.

3.2.4 Influence of the gap width on the losses

In this section, the effect of gap width on the losses of CPW on different substrate (BCB and InP) is investigated in order to find the optimal structure.

3.2.4.1 Losses of CPW without backed conductor

The CPW with ABs is firstly evaluated in the case without backed conductor.

I Radiation loss α_R

Radiation loss is often negligible in comparing with other attenuation components at microwave frequencies. This is not the case in THz range, according to Gupta et al., the radiation loss of an ideal CPW is proportional to the cube of the frequency [Gupta1996]. Two principal effects contribute to the radiation loss. The first is the energy transfer from guided wave into the substrate in the manner of a shock wave because the guide wave travels faster than the propagating TEM wave in the dielectric [Kasilingam1983]. This condition is always satisfied if the effective dielectric constant is below the dielectric permittivity when the guided wave propagates at the interface air/dielectric.

The second effect is due to the coupling between guided wave and other existing waves or modes as seen in the dispersion curves. A waveguide can support multi-modes propagation. Each mode has its distinct field distribution and the cutoff frequency. The coupled mode theory [Haus1991] predicts that when two waves have close phase velocities in a transmission structure, their phase constant $\beta(\omega)$ will be modified through a coupling coefficient, which is a function of the overlap field integral between the two modes in the plane perpendicular to the propagation direction. When coupling occurs, there will be energy exchange between them. Normally, the surface wave TE_0 (TM_0) with zero cutoff frequency and the high order waves in the structure air/dielectric slab [Collin1960] are the main radiation causes when they travel slower than the guide wave. The cutoff frequencies of high order surface waves depend on the dielectric thickness and permittivity. Besides surface waves, other parasitic modes also have the possibility to couple with the guided mode.

The surface waves are not excited in the structure and the coupling coefficient between CPW mode and the other parasite modes (Slotline mode and Microstrip mode) is quite small for CPW on BCB, the main contribution in the attenuation comes from the radiation of CPW mode into the substrate. CPW mode is unconditionally leaky. This phenomenon has been explained as the shock wave [Rutledge1983, Grischkowsky1987], and the CPW mode losses its energy at an angle of Ψ into the substrate. It is determined by the Cerenkov radiation condition [Jolley1958],

$$\cos \Psi = \frac{\beta_{CPW}}{\beta_s} = \frac{v_s}{v_{CPW}} = \frac{\sqrt{\epsilon_{eff}}}{\sqrt{\epsilon_r}} \quad (3-9)$$

Where v is the phase velocity, β is the propagation constant, S represents the dielectric substrate, CPW signifies the guided CPW mode. This angle reflects the mismatch between the two corresponding phase velocities. When $\epsilon_{eff} = \epsilon_r$, $\Psi = 0$, the energy emission into the substrate will be prohibited. Hence the radiation loss depends critically on this angle. Normally, ϵ_{eff} is a function of frequency and can be obtained by fitting the dispersion relation of experiment data.

The dependency of the radiation losses of an ideal CPW on the gap width and the frequency could be estimated based on non static approximation [Frankel1991]:

$$\alpha_R = 0.1661 \times \frac{(1 - \epsilon_{eff} / \epsilon_r)^2}{\sqrt{\epsilon_{eff} / \epsilon_r}} \frac{(S_1 + 2W)^2 \epsilon_r^{3/2}}{c^3 K(k) K'(k)} f^3 \text{ (dB/mm)} \quad (3-10)$$

Where K and K' are the first and second kinds of the complete elliptic integrals. $k = \frac{S_1}{S_1 + 2W}$ is

the geometric factor. The length and frequency are in SI units. The term $\frac{(1 - \epsilon_{eff} / \epsilon_r)^2}{\sqrt{\epsilon_{eff} / \epsilon_r}}$ depends

on the CPW dimensions W , the material permittivity ϵ_r and the radiation frequency, and

$\frac{(S_1 + 2W)^2}{c^3 K(k) K'(k)}$ is only a geometric dependent factor.

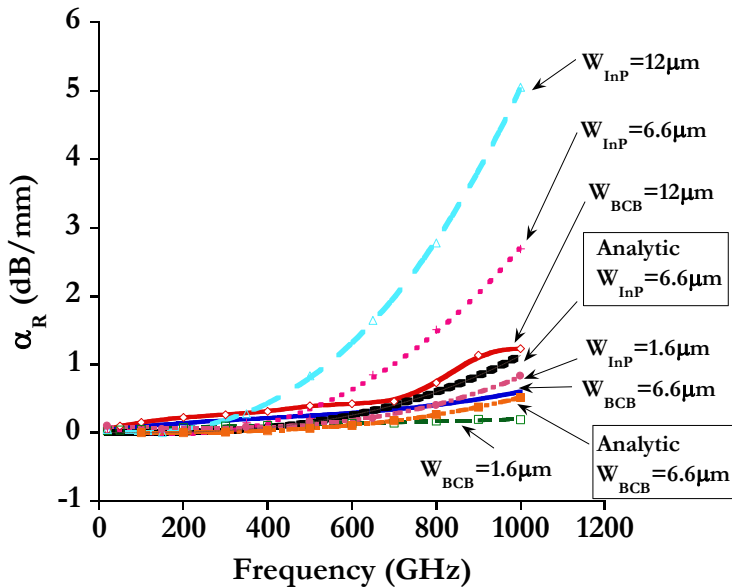


Figure 3-15: Comparison of radiation losses for the CPW configuration AB/BC on BCB and InP

Figure 3-15 plots the radiation losses versus frequency for CPW configuration with airbridges and without backed conductors on the two kinds of substrates. The analytic curve is calculated through equation (3-10) under the approximation: $\epsilon_{eff} = (1 + \epsilon_r)/2$. All the simulated discrete points are fitted by a polynomial curve with a maximum order of 3. For the frequency below 400 GHz, the dependency of α_R on the frequency is weak, while at high frequencies, a cubic relation $\propto f^3$ appears. The theoretical value with $W = 6.6 \mu\text{m}$ follows the increasing trend but underestimates the losses especially for CPW on InP, due to the static approximation and other losses terms or coupling effects not considered in the formula. The discrepancy probably also comes from that the width of the ground plane is $S_2 = 24 \mu\text{m}$ in the simulation, which exhibits a finite width far from the ideal case $S_2 = \infty$. A large gap width will make the electric line penetrate more into both the substrate and the air. This sensitivity could be seen from the relation $\alpha_R \propto (S_1 + 2W)^2$ in the expression (3-10) when ϵ_{eff} is assumed to be not frequency dependant. The radiation loss will increase drastically with W . It should be mentioned that the loss incensement is not relevant to the increase of effective permittivity with W as shown in Figure 3-14. In fact if the waveguide dimensions are fixed, a large effective permittivity will decrease the radiation loss, due to the reduction of the radiation angle Ψ in equation (3-9). The advantage of the BCB substrate over InP is the small permittivity ($\epsilon_{eff}/\epsilon_r$ for CPW on BCB is larger than that

of CPW on InP), leading to a weak factor $\frac{(1 - \epsilon_{eff}/\epsilon_r)^2}{\sqrt{\epsilon_{eff}/\epsilon_r}}$ and low losses in THz frequency range.

Another reason is that the coupling between CPW and slotline mode in CPW on InP is much higher than that for CPW on BCB as demonstrated in section 3.2.3.1. The radiation loss dominates at high frequencies when comparing with other types of losses discussed in the following.

II Conduction loss α_c

Conduction loss or ohmic loss is attributed to the finite conductivity σ ($4.1 \cdot 10^7$ S/m) of the metal strip. The complex surface impedance for a metal is expressed as [Keil1992],

$$Z_s = \frac{(1+j)}{\sigma\delta} \coth\left(\frac{(1+j)t}{\delta}\right) \quad (3-11)$$

Where $\delta = \frac{1}{\sqrt{\pi f \mu \sigma}}$ is the skin depth, μ is the permeability of metals and t is the conductor thickness.

The resistance R_s is the real part of Z_s . Large resistance increases the conduction loss when the metal dimensions are fixed. If the metal thickness is much larger than the skin depth, the surface resistance is approximately written as $R_s = 1 / (\sigma\delta)$. Then a large conductivity σ can reduce the resistance and the conduction loss.

The conduction loss is caused by the ohmic surface resistance when the metal thickness is larger than the skin depth. A square root dependency on the frequency is predicted by the analytic relation with wide ground planes with quasi-static approximation at microwave frequency [Gupta1996]:

$$\alpha_c = 4.88 \times 10^{-7} R_s \epsilon_{eff} Z_0 \frac{P'}{\pi W} \left(1 + \frac{S_1}{W}\right) \frac{1 + \frac{1.25t}{\pi S_1} + \frac{1.25}{\pi} \ln \frac{4\pi S_1}{t}}{\left(2 + \frac{S_1}{W} - \frac{1.25t}{\pi W} \left(1 + \ln \frac{4\pi S_1}{t}\right)\right)^2} \text{ (dB/mm)} \quad (3-12)$$

Where R_s is the real part of surface impedance of a conductor as in the expression (3-11),

$Z_0 = \frac{30\pi}{\sqrt{\epsilon_{eff}}} \frac{K'(k)}{K(k)}$ is the characteristic impedance of the CPW, t is the metal strip thickness and P'

is a geometry dependent parameter. As we can see, when the CPW dimensions are given, the conduction loss is proportional to the frequency dependent surface resistance from expression

(3-12): $\alpha_c \propto R_s \approx \frac{1}{\sigma\delta}$. The approximation is valid when the metal thickness is larger than the

skin depth. Given the metal conductivity $\sigma_{Au} = 4.1 \times 10^7$ S/m, the skin depth is $\delta = 178$ nm at 200 GHz and 79 nm at 1000 GHz. So the condition $t = 500$ nm $> \delta$ is satisfied in the above formula.

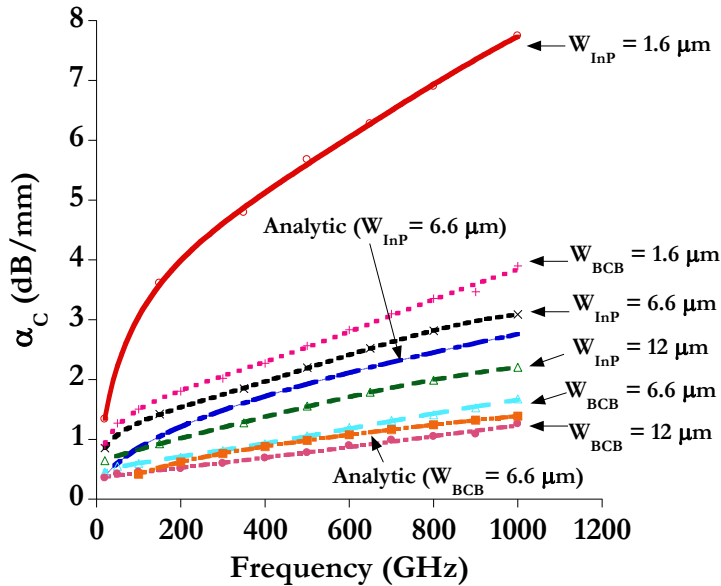


Figure 3-16: Comparison of conduction losses for the CPW configuration AB/BC on BCB and InP ($\sigma_{Au} = 4.1 \times 10^7 S/m$)

In Figure 3-16, conduction losses for CPW on BCB and InP are shown versus the frequency at different gap width. This analytic expression underestimates the conduction losses. As the gap width decreases, the current density is more confined at the surface of the central strip resulting in the increment of the ohm losses R_s . At the same W value, when comparing with CPW on InP, CPW on BCB also shows a better performance on reducing conduction losses because of its small effective permittivity ($\alpha_c \propto \epsilon_{eff} Z_0 \propto \sqrt{\epsilon_{eff}}$ as in equation (3-12)). This again validates the advantage of low permittivity BCB. The conduction loss is the main loss mechanism in CPW at low frequencies.

III Dielectric loss α_D

Dielectric loss arises from the imaginary part of the dielectric permittivity or equivalently, the loss tangent $\tan \delta$. It is defined as the ratio of the imaginary and real part in the permittivity as in the expression (3-13), where σ_d is the dielectric conductivity. Large value of $\tan \delta$ will make the dielectric loss increase.

$$\epsilon = \epsilon_r + j\epsilon_i = \epsilon_r + j \frac{\sigma_d}{\omega \epsilon_r \epsilon_0} = \epsilon_r (1 + j \tan \delta) \quad (3-13)$$

The non zero loss tangent $\tan \delta$ in the substrate is the source for dielectric losses. The approximation expression for substrate loss at low frequencies (f in Hz, c in m/s) is given by [Gupta1996]:

$$\alpha_D = 2.73 \times 10^{-2} \frac{\epsilon_r}{\epsilon_r - 1} \frac{\epsilon_{eff}^{-1}}{\sqrt{\epsilon_{eff}}} \frac{\tan \delta}{c} f \text{ (dB / mm)} \quad (3-14)$$

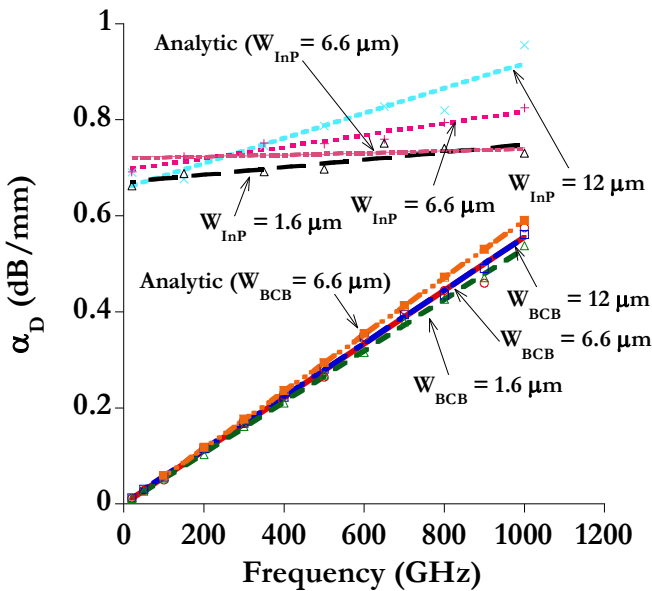


Figure 3-17: Comparison of dielectric losses for the CPW configuration AB/BC on BCB and InP

When the effective permittivity is assumed to be constant with frequency, the dependency of the losses on frequency comes only from the factor $f \tan \delta$. As shown in Figure 3-17, the calculated dielectric losses for CPW on InP and BCB have different characteristics on frequency, because the loss tangent is modeled in different manners on the two substrates: according to the calculation parameters in Table 3-1, for BCB, a constant value of loss tangent 0.007 is used bringing a quasi linear relation of dielectric losses on frequency f , however, for InP, the loss tangent $\tan \delta = \frac{\sigma_{InP}}{2\epsilon_0 \epsilon_r \pi f}$ is inversely proportional to frequency, yielding the dielectric losses are

nearly not relative to the excitation frequency f . The observed slight dielectric loss variation on frequency and on gap width comes from the frequency dependent effective permittivity due to the non TEM nature of CPW mode, and obviously, this influence is more sensitive for CPW on higher substrate dielectric (InP). The analytic approach again underestimates the losses at high frequencies for CPW on InP, while it predicts well with CPW on BCB. The dielectric losses are still smaller for CPW on BCB. It should be noted that α_D is much smaller than the two other types of losses at high frequencies [Grischkowsky1987].

For real dielectric material in the measurement, the loss tangent should depend more or less on the frequency. A more precise phenomenological loss tangent model of the polymer BCB (CYCLOTENE 4026-46 photosensitive resins from Dow Chemical Company) has been obtained by fitting the experimental FTIR transmission and reflection spectra of BCB films with theoretical values in THz range in our group [Perret2008]. Here we compare the dielectric losses of CPW on BCB with a reported loss tangent model ($\tan \delta = 0.0073 + 0.0017 \times f$ (in THz)) and with the constant value ($\tan \delta = 0.007$). Figure 3-18 shows the calculated dielectric loss on BCB with a gap width $W=12 \mu\text{m}$. The frequency dependent model produces more losses at high frequencies. The maximum increased dielectric loss is about 0.3 dB/mm at 1500 GHz. When comparing with other types of losses in a CPW structure, this additional loss is almost negligible.

By default, the model of constant loss tangent is sufficient to produce satisfactory results of dielectric loss.

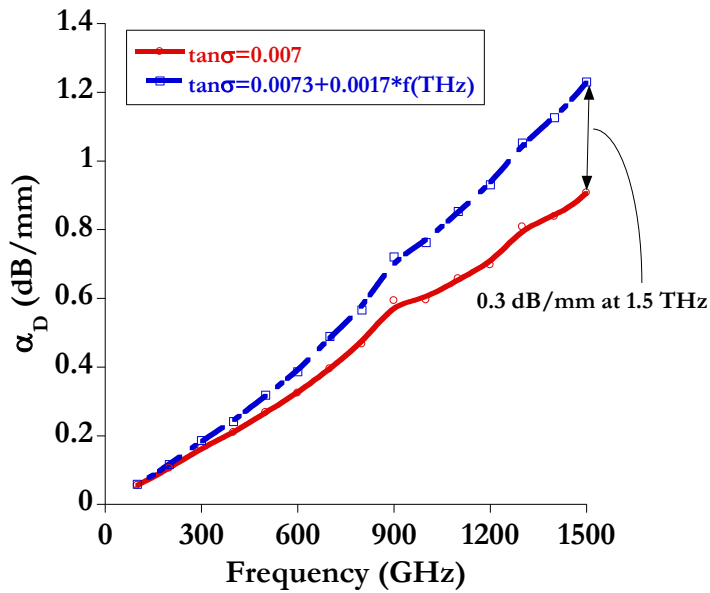


Figure 3-18: HFSS calculated dielectric losses for the mode CPW in configuration AB/BC on BCB with a constant and a frequency-dependant loss tangent $\tan\delta$ ($W = 12 \mu m$)

IV Total losses α_T

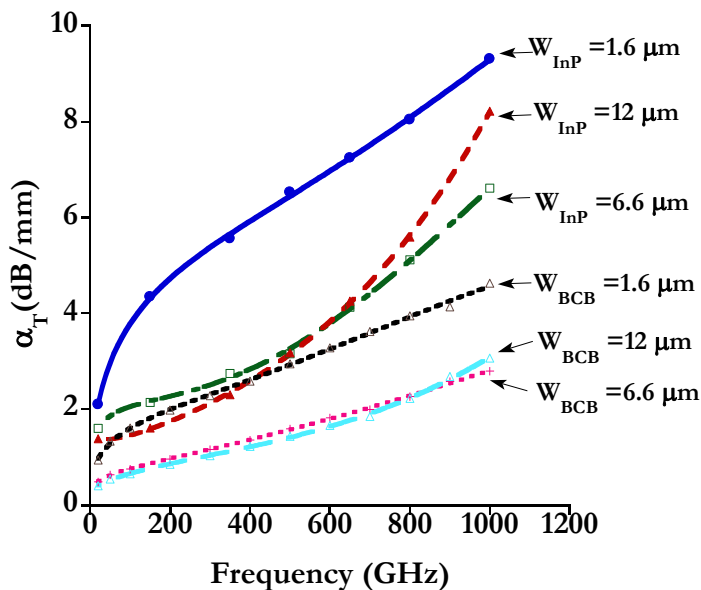


Figure 3-19: Comparison of total losses for the mode CPW in configuration AB/BC on BCB and InP

The total attenuation of the CPW mode is assumed to be the sum of all the above three types of losses ($\alpha_T = \alpha_R + \alpha_D + \alpha_C$). Figure 3-19 represents the calculated total losses for the mode CPW with different gap width W on the two types of substrates. The metal conductivity is $4.1 \times$

10^7 S/m and the BCB dielectric loss tangent is 0.007. As indicated in above sections, at high frequencies, the total losses are mainly consisted by the radiation losses, which have a cubic dependency on the frequency. However, it is governed by the conduction losses at low frequencies. With the same gap width and the same frequency, CPW on BCB always has better performances in THz transmissions. CPW with the smallest width $W = 1.6 \mu\text{m}$ suffers from the largest conduction loss. The overall optimal structure is the CPW with $W = 6.6 \mu\text{m}$ for both the two substrates, although the $W = 12 \mu\text{m}$ has the slightly lower losses below certain frequencies (800 GHz for BCB and 600 GHz for InP).

3.2.4.2 Losses of CPW with backed conductor

CPW with backside metallization is widely used in interconnect and packaging structure. The backed ground conductor may deteriorate the waveguide performance for single mode propagation. The most important consequence is the occurrence of resonances [Haydl2000, Heinrich2000] due to the parallel plate mode or the patch antenna mode consisted by the ground plane and the backside metallization. In the following section, CPW without ABs but with backed conductor will be studied.

I Radiation losses α_R

A Influence of W

Figure 3-20 shows the radiation losses of BC CPW and the CPW without backed conductor versus W . Resonant peaks occur in the radiation loss spectrum with backside metallization. At smaller W , these peaks are narrower. The resonances could be explained by the patch antenna theory, where the patch would be composed by the top ground plane ($S_2 \times L$) and the backed conductor. The resonance frequencies are predicted by the following expression [Heinrich2000],

$$f_{mn} = \frac{c}{2\pi\sqrt{\epsilon_r}} \sqrt{\left(\frac{m\pi}{S_2}\right)^2 + \left(\frac{n\pi}{L}\right)^2} \quad (3-15)$$

Where ϵ_r is the permittivity of dielectric confined between the plates. m and n are the half wave number in the width direction y and length direction x , respectively. They also represent the mode of resonances. $L = 1 \text{ mm}$ is the total length of waveguide.

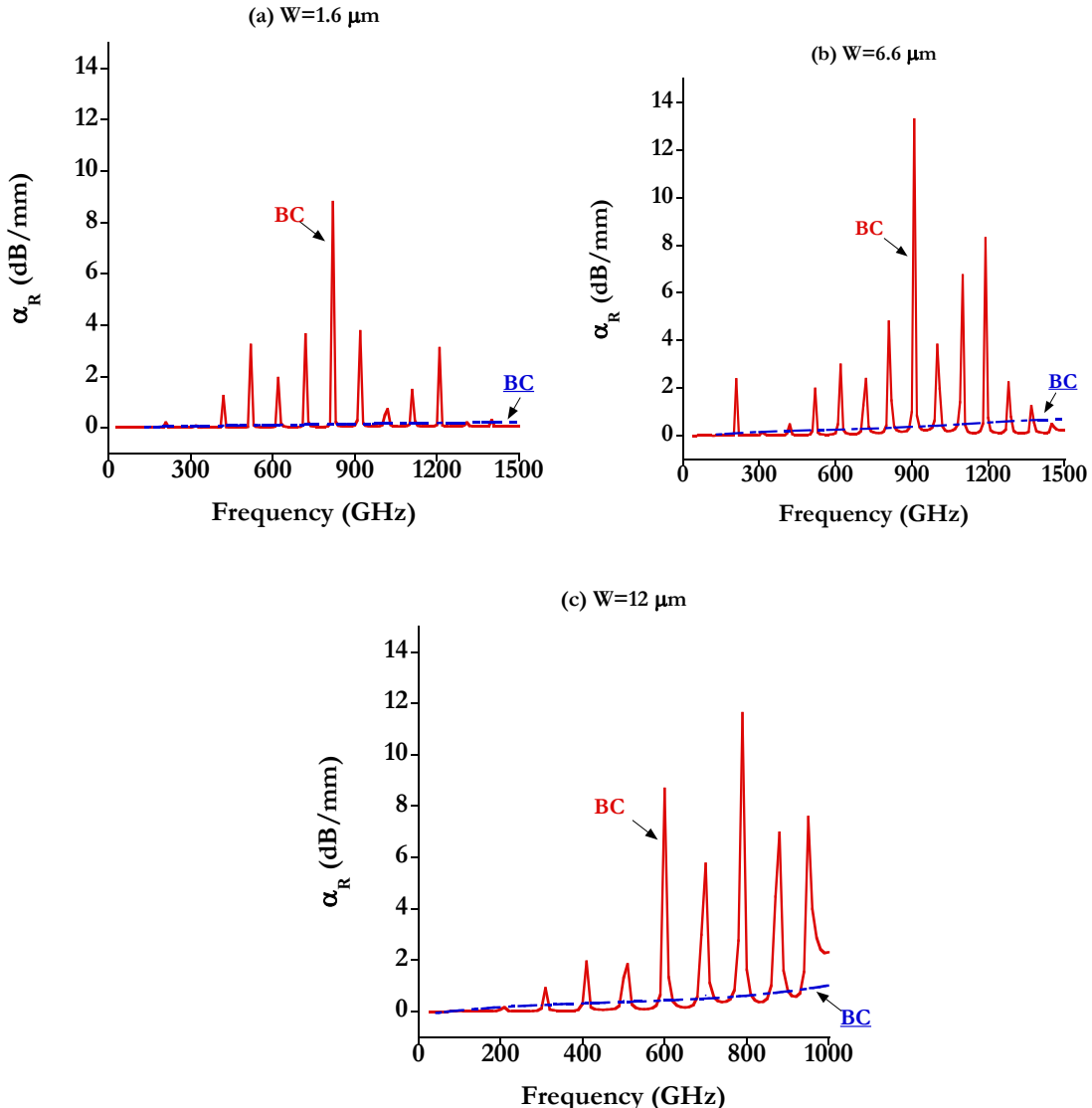


Figure 3-20: Influences of backed conductor (BC) on the radiation loss of the CPW mode for CPW on 30 μm BCB: (a) $W = 1.6 \mu\text{m}$, (b) $W = 6.6 \mu\text{m}$ and (c) $W = 12 \mu\text{m}$

The considered metal strip width are : $S_1 = 10 \mu\text{m}$ and $S_2 = 24 \mu\text{m}$. Due to the line length $L = 1 \text{ mm} \gg S_2$ (or W_{tot}), the first resonance frequency will be the f_{01} type. Moreover, f_{10} is 4.01 THz (using S_2 in the formula) or 1.17 THz (using W_{tot} in the formula) at $W = 12 \mu\text{m}$. The latter case is not likely to happen because the slot width is large enough and becomes comparable to the ground plane width. In this case, S_2 should be used instant of W_{tot} .

When the slot width W is much smaller than the ground plane width S_2 ($W \ll S_2$), the patch will be approximately composed by the total metal width $W_{\text{tot}} = 2W + 2S_2 + S_1$ and the two slots are neglected. The resonance frequencies are calculated with the same formula when replacing S_2 by W_{tot} . This is approximately true for $W = 1.6$ and $6.6 \mu\text{m}$.

Table 3-3 compares the simulated and theoretically obtained resonant frequencies of f_{0n} for conductor backed CPW. More than thirteen resonances have been observed in the HFSS simulation range from 10 GHz to 1500 GHz at a step of 10 GHz (the first several resonances are

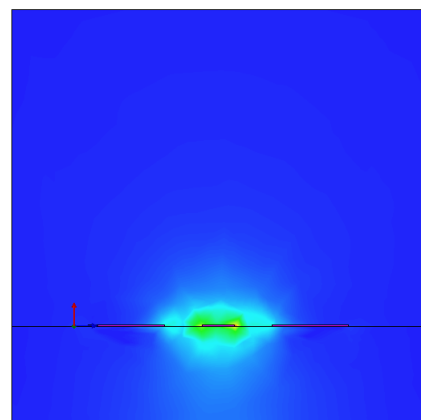
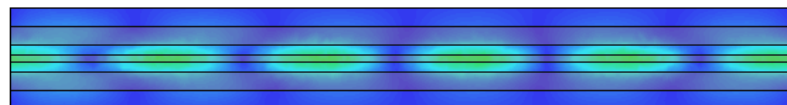
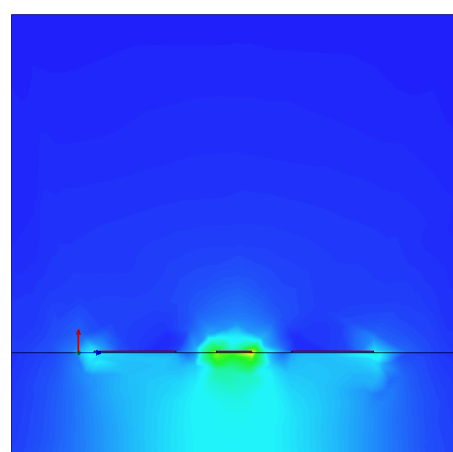
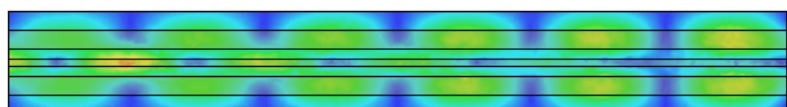
not visible because of their small amplitudes in Figure 3-20). These simulated frequency positions agree well with those predicted by theoretical formula (3-15) which are listed in the rightmost row. Furthermore, we see that dependence of the resonance frequency on the width W is not obvious, because the relation $L = 1 \text{ mm} \gg S_2$.

Table 3-3: Resonant frequencies (GHz) in HFSS simulations and f_{0n} calculated by theoretical formula (thickness $h = 30 \mu\text{m}$, $\epsilon_{BCB} = 2.42$) for the conductor backed CPW

CPW top metal strip $S_1 = 10 \mu\text{m}$ $S_2 = 24 \mu\text{m}$ $L = 1 \text{ mm}$				
n	$W = 1.6 \mu\text{m}$	$W = 6.6 \mu\text{m}$	$W = 12 \mu\text{m}$	Calculated f_{0n}
1	110	100	100	96
2	210	210	210	193
3	320	310	310	289
4	420	420	410	385
5	520	520	510	482
6	620	620	600	578
7	720	720	700	674
8	820	810	790	771
9	920	910	880	867
10	1020	1000	950	963
11	1110	1100	-	1060
12	1210	1190	-	1156
13	1310	1280	-	1253
14	1400	1370	-	1349

In order to understand the origin of these resonances, it is necessary to look at the electromagnetic field distributions in the dielectric at resonant and non-resonant frequencies. Figure 3-21 plots the electric field (E) distribution along the wave propagating direction for conductor backed CPW at slot width $W = 12 \mu\text{m}$. The cross section plane is chosen to be at the middle of BCB layer with a thickness of $30 \mu\text{m}$. At the non-resonance frequency 550 GHz (Figure 3-21 (a)), electric energy is mainly concentrated at the two slot regions and there are little electric field under the masse plane or directed to the backside metallization, showing the characteristics of the CPW mode. However, at the resonance frequency f_{06} (Figure 3-21 (b)) and f_{08} (Figure 3-21 (c)), electric field is no longer primarily confined as the non resonant case. Below the two outside ground planes regions, a considerable amount of electric energy is located, demonstrating the formation of parallel plate resonators. If we count the number of half waves in the whole guiding structure at resonant frequencies, they are $n = 6$ and 8 , corresponding well to the theoretically predicted values. The field variation along the width direction is less than a half

wavelength ($m = 0$). The intensive extensions of EM energy into the ground plane region and even the substrate region not covered by metals are the cause for the large radiation losses at resonant frequencies. It should be also pointed out that outside the resonant frequencies (see Figure 3-20), the radiation loss with backed conductor is actually slightly smaller than that without backed conductor. This could be clarified qualitatively by the dispersion curves in Figure 3-14, conductor backed CPW has larger effective permittivity, benefits a smaller radiation angle into the substrate. Indeed, the backside metallization has the tendency to attract electric lines from the central signal strip on top to form the quasi microstrip EM distributions. As we will see in the section about microstrip lines, the radiation loss of a microstrip mode is usually smaller than that in the CPW structure, when the strip width in a microstrip is equal to the central strip width in a CPW.

(a) $f = 550 \text{ GHz}$ (b) $f = 600 \text{ GHz} (f_{06})$

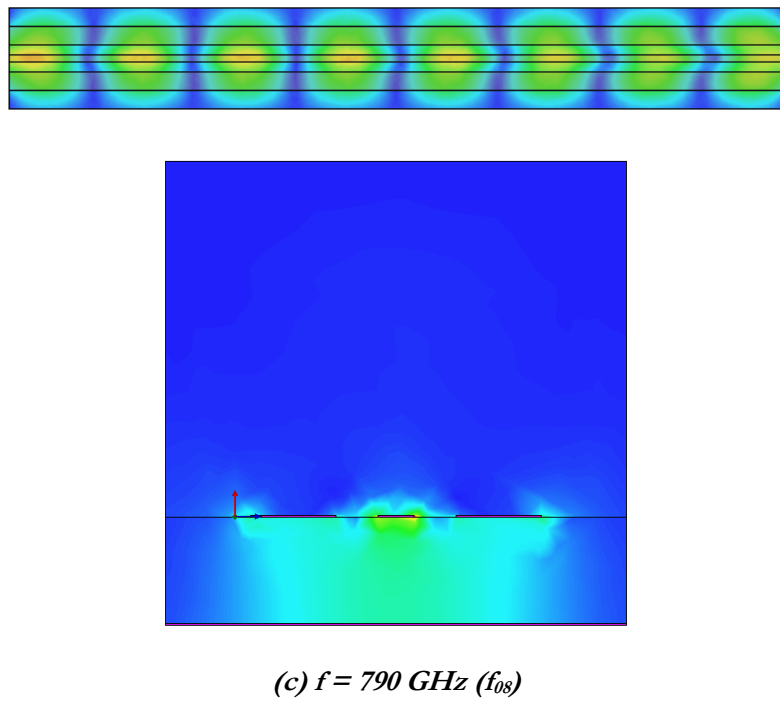
(c) $f = 790 \text{ GHz } (f_{08})$

Figure 3-21: Electric field distribution along BC CPW propagation direction at the center plane in dielectric BCB and at the profile plane (thickness $h = 30 \mu\text{m}$, gap width $W = 12 \mu\text{m}$): (a) $f = 550 \text{ GHz}$, (b) $f = 600 \text{ GHz } (f_{06})$ and (c) $f = 790 \text{ GHz } (f_{08})$

B Influence of L

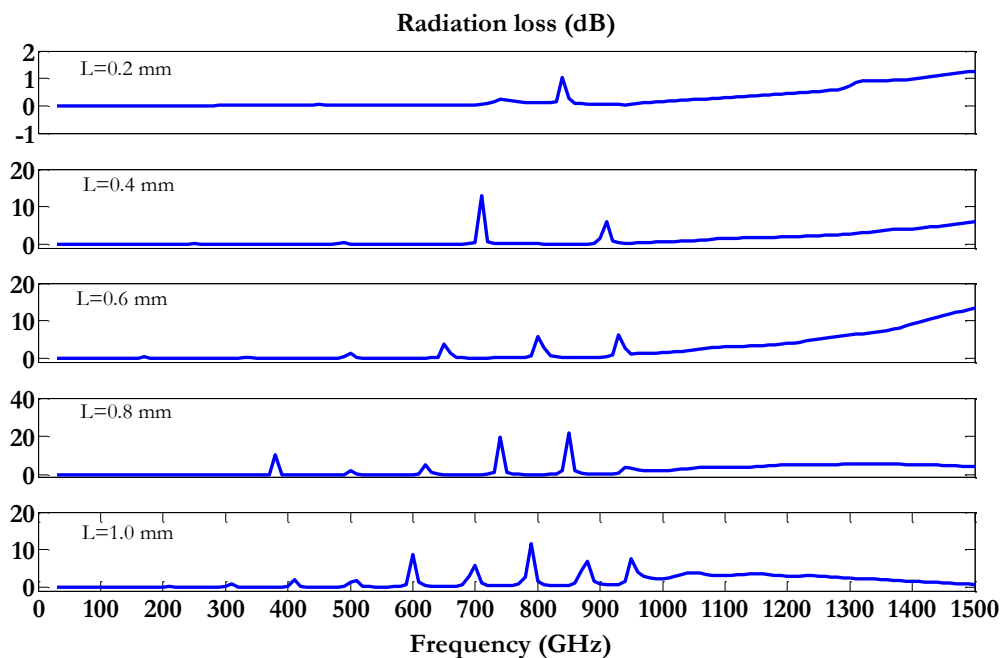


Figure 3-22: Radiation loss (dB) of the CPW mode versus the line length L (0.2 - 1 mm) for conductor backed CPW on 30 μm BCB

The radiation loss α_R (dB) in function of the line length L from 0.2 mm to 1 mm is shown in Figure 3-22 for $W = 12 \mu\text{m}$. With the increase of L, a large number of resonant peaks appear and the first peak shift to low frequency. Long waveguide deteriorates the transmission performances.

Besides L, other parameters (substrate permittivity, substrate thickness, ground plane width, etc.) can also modify the positions and amplitudes of these resonances. Special care should be taken for the design of long CPW line with backed conductor at THz range. From analytic formula (3-15), we can conclude that the resonances have a strong dependency on the simulated line length L.

Variation of loss tangent in the substrate and metal conductivity in metals cannot move the resonant peaks. Due to the existence of strong resonances at high frequencies, it is difficult to extract the dielectric and conduction losses in this wave propagating structure, especially around the resonant frequencies. The total losses will be compared with different gap widths in the conductor backed CPW.

II Conduction α_C , dielectric α_D and total losses α_T

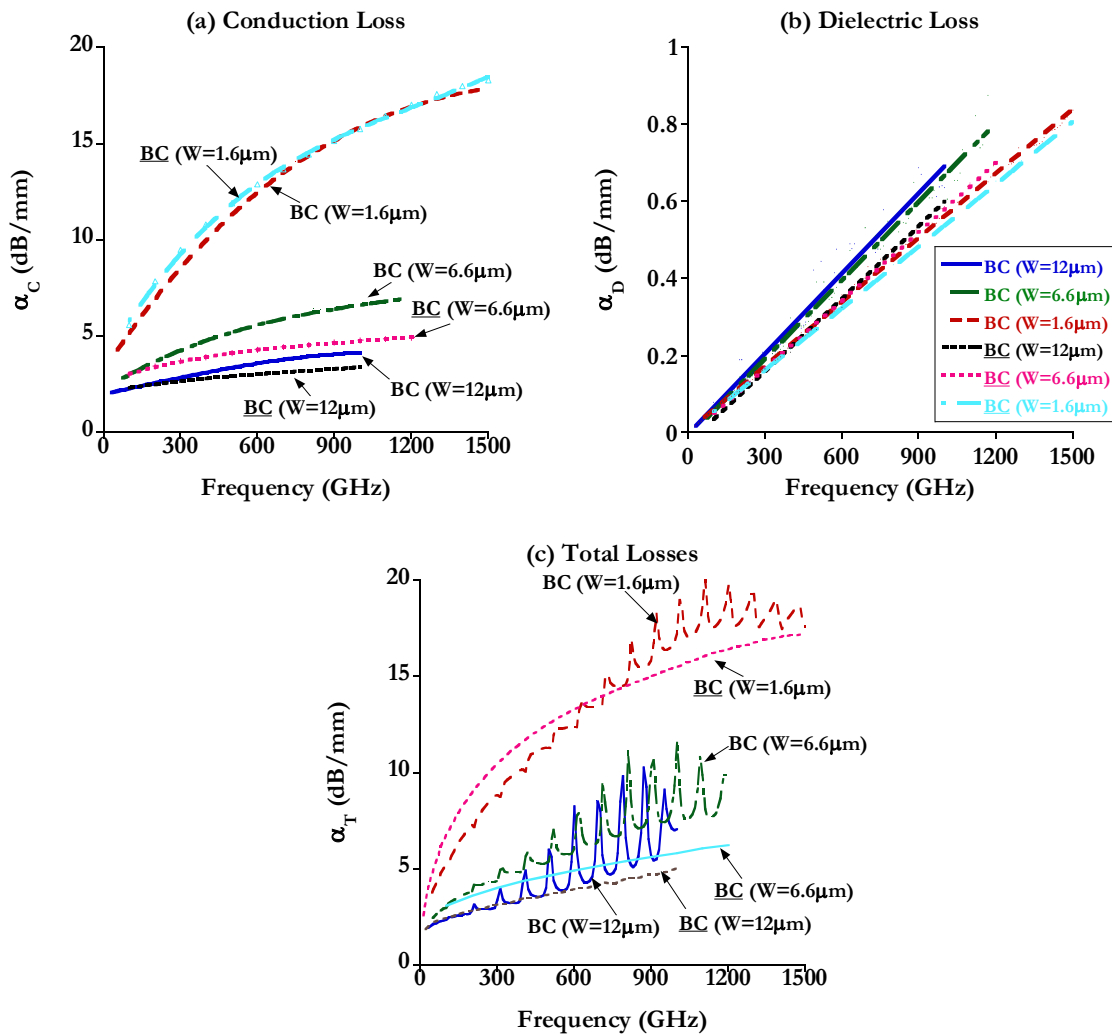


Figure 3-23: Influences of backed conductor (BC) on the total losses of the mode CPW for CPW on 30 μm BCB. (a) Conduction loss ($\sigma_{Au} = 5 \cdot 10^6 \text{ S/m}$), (b) Dielectric loss, and (c) Total losses ($\sigma_{Au} = 5 \cdot 10^6 \text{ S/m}$)

Figure 3-23 shows the conduction, dielectric and total losses in the three CPW structures, where BCB loss tangent is 0.007 and metal conductivity is 5×10^6 S/m for material loss parameters. At $W = 1.6 \mu\text{m}$, the effect of backed conductor on α_c and α_d is negligible. With the increase of W , the conductor backed CPW show more conduction and dielectric losses. For example, at 1 THz, α_c for CPW with (without) backed conductor are: 15.8 (14.1) at $W = 1.6 \mu\text{m}$, 6.7 (4.8) at $W = 6.6 \mu\text{m}$ and 4.1 (3.4) dB/mm at $W = 12 \mu\text{m}$. And the corresponding α_d are: 0.6 (0.54) at $W = 1.6 \mu\text{m}$, 0.62 (0.58) at $W = 6.6 \mu\text{m}$ and 0.63 (0.59) dB/mm at $W = 12 \mu\text{m}$. This is because the EM field penetrate through the dielectric and the consumption of EM energy in the backed conductor is improved. Both α_c and α_d increase, particularly at wide gap width.

The peaks of α_T for the conductor backed CPW in Figure 3-23 (c) come from the radiation α_R in Figure 3-20. The resonances are considerable from 700 GHz for $W = 1.6 \mu\text{m}$, 500 GHz for $W = 6.6 \mu\text{m}$ and 400 GHz for $W = 12 \mu\text{m}$. The operation frequency should be avoided from these frequencies. The conduction loss accounts for a large percentage in the total attenuation due to the high resistivity at $W = 1.6 \mu\text{m}$ (Figure 3-23 (a)). That is why the CPW mode with small slot width shows large attenuation constant.

Several methods have been proposed to eliminate one certain resonance at several GHz frequency, such as with via/holes placed at the maximum electric field positions along the outer and inner edges of the ground planes [Yu1993-2], or with different shapes of slots in the ground planes [Lo1993]. However, these methods are not an efficient way to exclude all the resonances at submillimeter wave and even THz frequencies. These via/holes also bring difficulties in the manufacturing process.

3.2.5 Conclusion

In this section on CPW, we have studied the parametric influences (three variable gap width W (1.6, 6.6 and 12 μm) and substrate permittivity (BCB and InP)) on the dispersions and the different types of losses in four CPW configurations. The radiation losses of the mode CPW dominate in the high frequency range and grow with wider gap. Some principal coupling effects account for the radiation loss, including CPW - Slotline, CPW - Microstrip, CPW - TM_0 and other high order surface wave modes, CPW mode radiation into substrate wave, etc. The conduction losses are important at low frequencies and lower at greater gap width due to the decreasing ohmic resistance at the metal surfaces. Comparing with the previous two types of losses, the dielectric losses are not significant and their dependency on frequency is decided by the model of loss tangent or material conductivity (α_d is frequency independent for CPW on InP and is proportional to frequency for CPW on BCB according to the parameters in Table 3-1). The impact of gap width on the dielectric losses is not obvious for both types of dielectric.

CPW on BCB benefits many advantages: low attenuation constants for all the types of losses, high cutoff and critical frequencies of the surface waves and small coupling coefficients between CPW mode and other parasitic modes.

The air-bridges (ABs) can attenuated the unwanted slotline mode by at least 10 dB at 1 THz for CPW on BCB, while the CPW mode is not much affected. The existence of backed conductor

(BC) at the backside of substrate will introduce resonance peaks at certain frequencies determined by the parallel plate resonance theory. Many parameters can impact on the resonant phenomena: waveguide length L , dielectric thickness h and permittivity ϵ_r . These should be carefully considered in the design of low loss conductor backed CPW at THz frequencies. When comparing the total losses for the mode CPW with different substrates and dimensions studied here, CPW on BCB at $W = 6.6 \mu\text{m}$ is the best coplanar waveguide.

The CPW on BCB seems to be a good candidate for low loss THz transmission. The other types of lines, like microstrip, Slotline and Stripline studies will be studied separately and compared at the end.

3.3 HFSS analysis of microstrip line on 30 μm BCB

Microstrip line is an open structure with the single conductor ribbon deposited on top of the finite dielectric layer and a single ground plane on the opposite side. Its characteristic impedance is adjustable by the strip dimensions and dielectric thickness, making the interconnections and modifications easy. In microwave frequency, quasi static analysis of the characteristic impedance and effective permittivity of microstrip line below X band (8 - 12 GHz) was studied by Wheeler [Wheeler1964] and Schneider [Schneider1969]. In the more rigorous full wave analysis, the propagating mode in a microstrip line was no longer purely TEM type. The dependency of characteristic impedance and effective permittivity on frequency was evaluated by integral equation method in the space domain [Denlinger1971] and Galerkin's method in the spectral domain [Itoh1973] up to 18 GHz. The coupling frequency between the quasi-TEM mode and the lowest surface wave mode was analyzed by Vendelin [Vendelin1970]. For quartz substrate with a thickness of 500 μm , this frequency is 100 GHz. By employing thin film and low permittivity substrate, the coupling frequency can be possibly improved beyond the maximum interested frequency. Concerning the attenuation in microstrip line, the conduction loss was calculated in closed form for thick (higher than four times the skin depth) [Pucel1968] and thin [Welch1966] metals. The dielectric loss does not depend on the line dimension and can be given in analytic expression [Welch1966]. The dispersion and losses properties of microstrip line have been applied in the transmission structure in microwave integrated circuit.

Recently, microstrip lines on BCB film find applications in THz-TDS system using a photoconductor (PC) sampling schema for the absorption spectra measurement of polycrystalline material [Byrne2008], THz evanescent field microscopy of dielectric materials [Cunningham2008], and the biosensors of DNA specimen [Kasai2009]. The common aspect in all the systems is to utilize the effect that the evanescent THz field extending above and propagating along the microstrip line penetrates and interacts with dielectric samples held in close proximity.

In this part, the dispersion and losses of microstrip line on BCB in THz frequency will be analyzed numerically, including the radiation loss, which is omitted in microwave. The non TEM nature of the microstrip propagating mode will be also stressed. Comparisons with analytical formula and available measurement results are also made.

3.3.1 Microstrip structure

The microstrip line is represented in Figure 3-24 with its main dimensional parameters (width W, conductor thickness t, dielectric thickness H and the line length L).

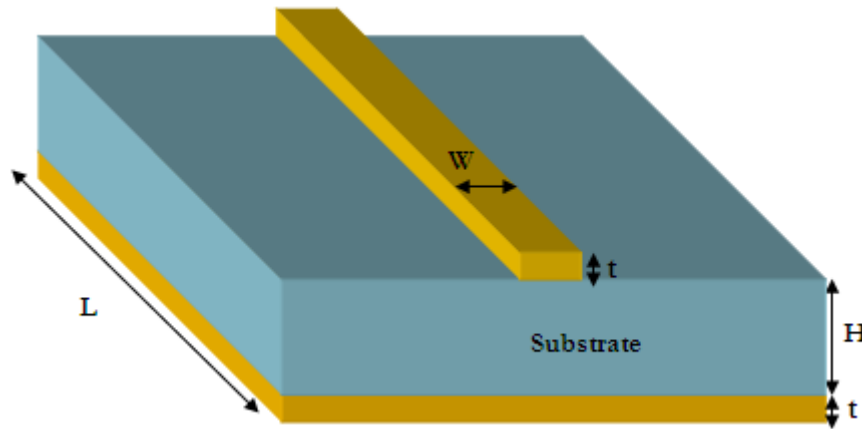


Figure 3-24: Microstrip line on a dielectric substrate of thickness H

The principal mode in a microstrip line is considered as quasi-TEM wave (small longitudinal EM components exist due to the interface air/dielectric) at low frequencies. The EM vector field distribution is shown in Figure 3-25. Electric field is mainly directed between the top strip and the bottom ground plane and the magnetic field encircles the top signal line.

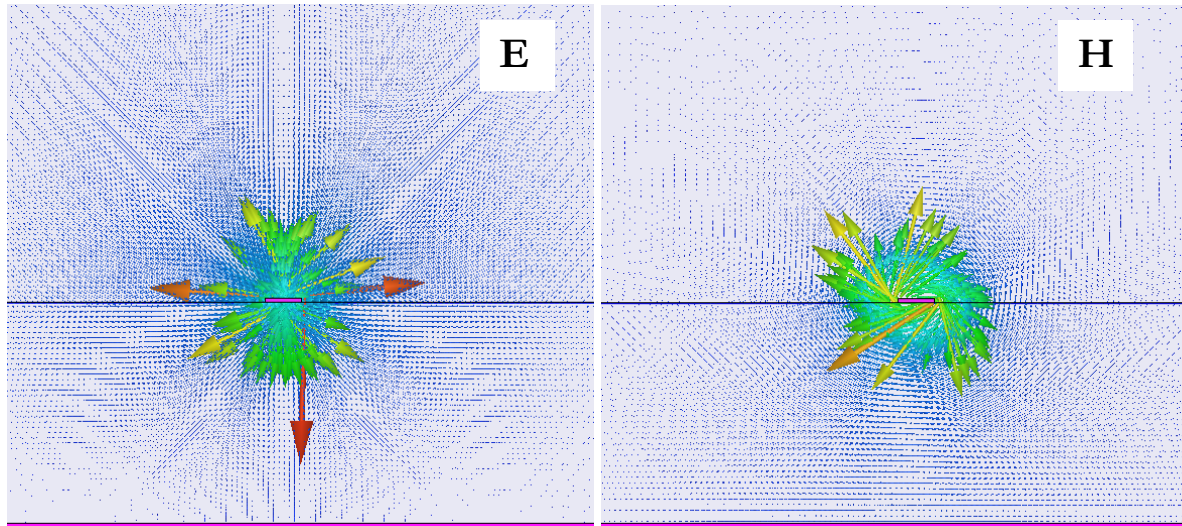


Figure 3-25: Electromagnetic vector field distribution in a microstrip line. Left: Electric field, Right: Magnetic field. The highlighted part represents metals

For conventional microstrip lines in microwave, a thick semiconductor wafer is employed as the substrate. The high thickness of substrate will push the cutoff frequency of surface waves into the interested band, around which the microstrip becomes dispersive [Roskos1991]. A better choice is to fabricate the buried ground plane microstrip line, where both the ground and signal

line are located on top of the wafer separated by a thin insulator layer. In our case, the ground plane is deposited directly on a silicon wafer and a 30 μm thick BCB is served as the dielectric.

The thick wafer layer is not included in the numerical model due to the isolation of conductor ground plane. The characteristic impedance can be adjusted through the ratio W/H. Large impedance can be achieved by increasing H or decreasing W [Gupta1996]. Despite of the low permittivity of BCB, an impedance of 50 Ohms can be easily realized within current technology limitations. In the parametric study using HFSS, the thickness of substrate BCB is H = 30 μm and metal thickness t = 500 nm. Characteristic impedance decreases with the growth of W and ϵ_r , but increases with H. At H = 30 μm , W should be 85 μm in order to have an impedance of 50 Ω for microstrip on BCB. Signal line width is varied at 5 μm (210 Ω), 10 μm (152 Ω), 20 μm (107 Ω) and 30 μm (93 Ω) in order to conduct a comparative and parametric study. Total length is L = 1 mm. The ground plane is assumed to be infinite in the horizontal plane.

3.3.2 Dispersions

As in Table 3-2, the surface waves do not couple significantly with the quasi-TEM microstrip mode in the simulated frequency range due to the small thickness and low permittivity of BCB. In the studied frequency range, the microstrip line is monomode and only the results of the main mode are reported in the next discussions.

Figure 3-26 plots the phase constant, effective dielectric constant, phase and group velocities of the dominant mode at the four widths of signal line. β is always smaller than the phase constant of TEM wave in BCB at each frequency, showing the dominant mode has a higher phase velocity. ϵ_{eff} increases monotonically with increasing frequency and line width W, because the fraction of microstrip mode energy in the dielectric is larger. The dependency of ϵ_{eff} on frequency introduces dispersion in the propagation of high speed electrical pulses [Yamashita1979] particularly at large strip width. ϵ_{eff} has been demonstrated to increase from 9.4 to 9.9 for microstrip on GaAs in [2 - 20] GHz [Finlay1988] and from 7 to 12 for microstrip on SiO₂ in [10 - 1000] GHz [Gondermann1993]. We see that at high frequencies, the static approximation of TEM mode in the microstrip line is no longer valid. Both the phase and group velocities decrease with the increase of the frequency and of the strip width. At frequency higher than 300 GHz, the bending of the curves of V_p and V_g in function of frequency is more pronounced. The dispersion properties can be well expressed by ϵ_{eff} , V_p and V_g . The discrepancy between V_p and V_g with wide strip is larger at high frequency, showing the microstrip mode becomes more dispersive. For example, at 1 THz, $|V_g - V_p| = 0.07 \times 10^8$ m/s for W = 5 μm and 0.11×10^8 m/s for W = 30 μm .

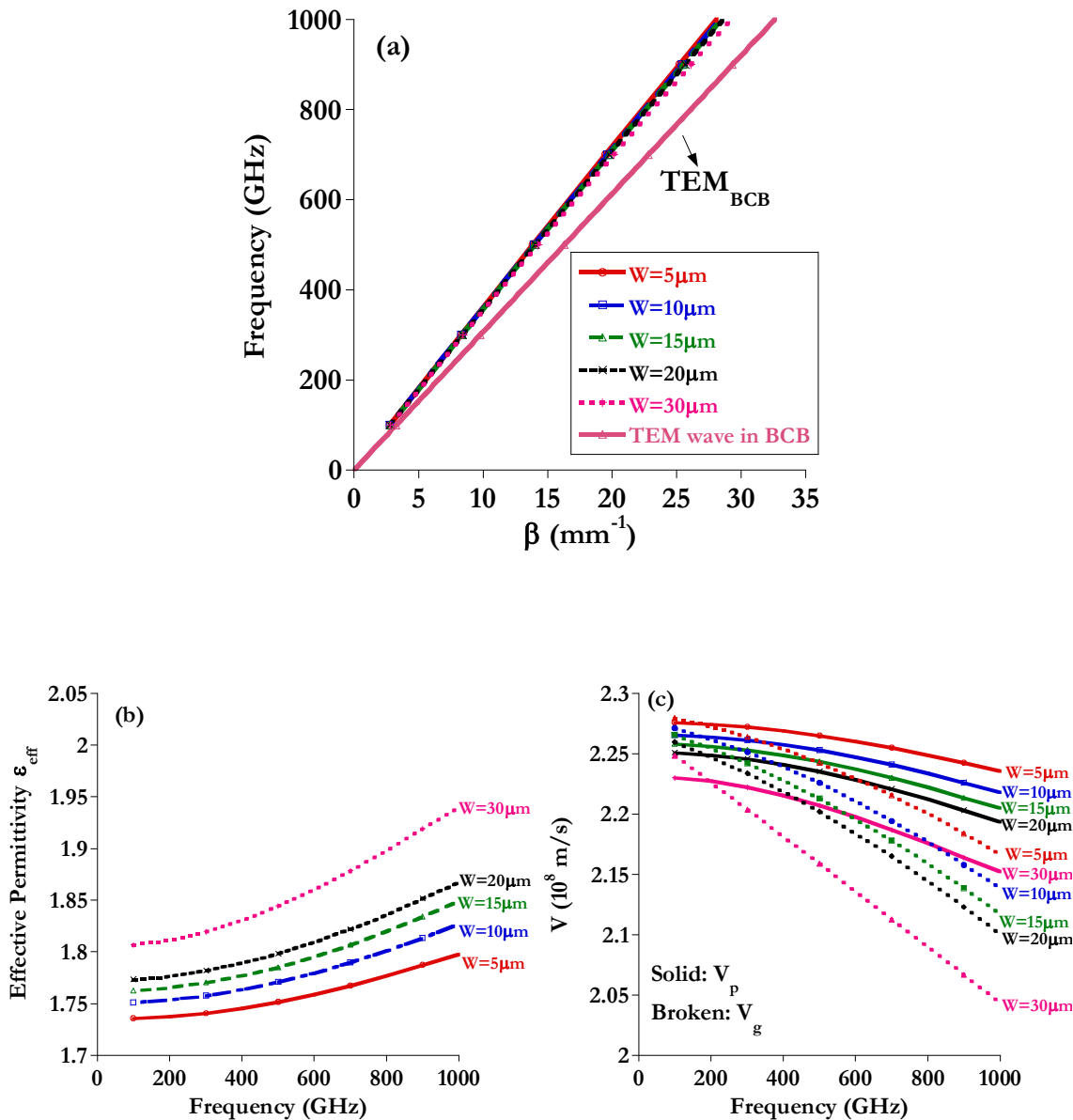


Figure 3-26: (a) Phase constant, (b) effective dielectric constant, and (c) phase and group velocities of microstrip line on 30 μm BCB, W is the signal trace width

3.3.3 Losses

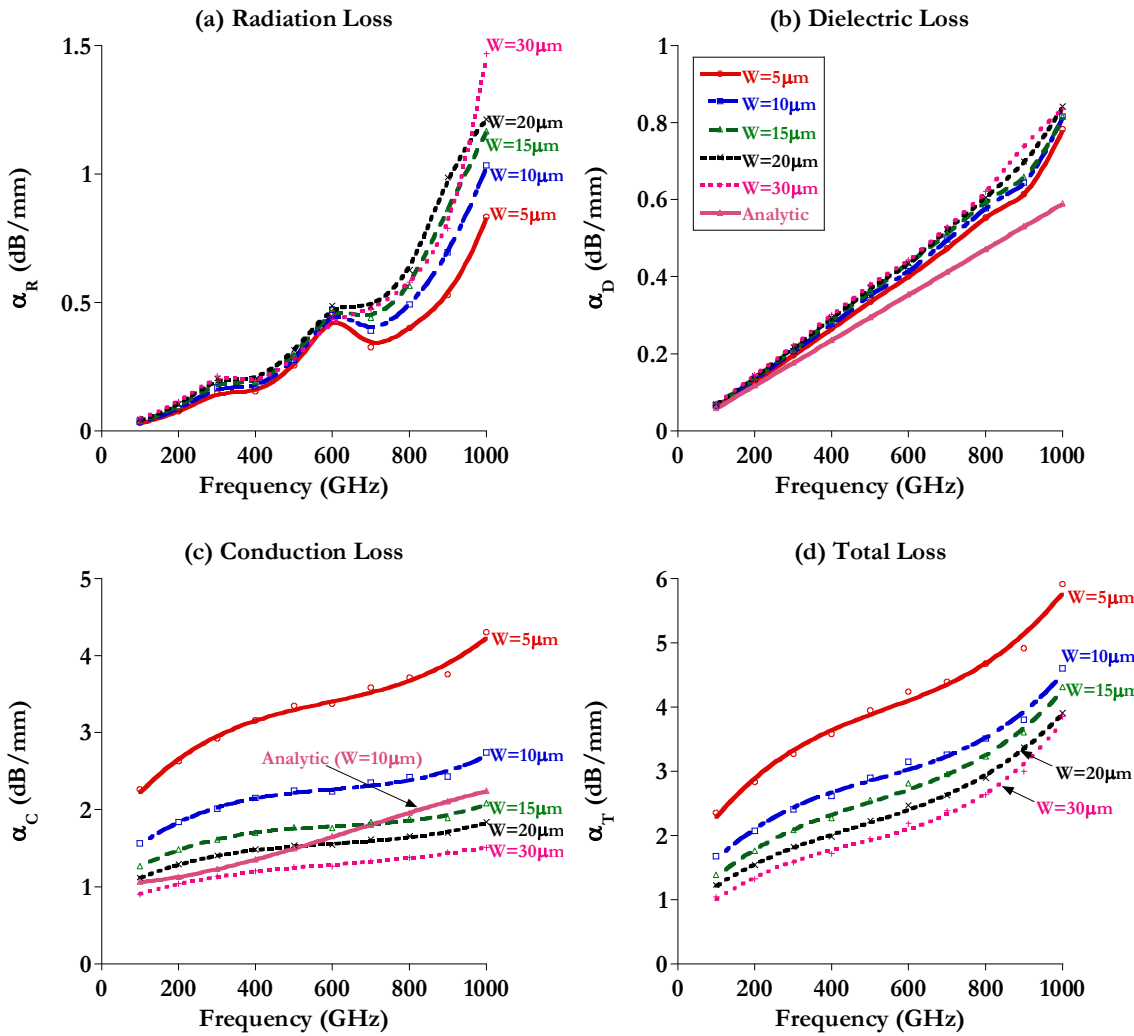


Figure 3-27: HFSS calculated losses of microstrip line on 30 μm BCB, (a) Radiation loss, (b) Dielectric loss, (c) Conduction loss and (d) Total losses

Figure 3-27 shows the losses in the five microstrip lines. They are summarized to follow the rules: all types of losses increase with frequency (the small oscillations in the radiation loss in Figure 3-27 (a) are explained in the text); with increasing W , the radiation loss increases, the conduction loss decreases and the dielectric loss is quasi constant. For $W < 30 \mu\text{m}$, radiation loss is comparable to the dielectric loss and the conduction loss is well above the other two types of losses assuming the metal conductivity $\sigma_{\text{Au}} = 5 \times 10^6 \text{ S/m}$: $\alpha_R \sim \alpha_D < \alpha_C$. Hence the total losses mainly follow the behavior of the conduction loss. This is different from CPW, where the radiation loss is dominant at high frequency. At $W = 30 \mu\text{m}$, the conduction loss is greatly reduced and it approaches the radiation loss at 1 THz.

3.3.3.1 Radiation loss

No parasitic modes and surface waves are excited in the microstrip line in the simulation with HFSS. The only possible power exit channel originates from the shock wave radiation from the

propagating microstrip mode into the substrate waves when the mismatch of phase velocity exists. When W increases, more fraction of EM energy of the principle mode is confined in the substrate between the signal strip and ground planes, making the coupling with substrate wave stronger. Figure 3-27 (a) concludes that the radiation effect is more intensive for a large metal width or large frequency (1.5 dB/mm at $f = 1$ THz and $W = 30 \mu\text{m}$). The small vibrations on α_R are attributed to the formation of possible parallel plate resonance between top and bottom conductors as introduced in the conductor backed CPW. The resonant positions are determined by the waveguide length due to $L \gg W$. For $L = 1$ mm, the resonant frequency is approximately predicted to be at the multiples of 100 GHz. Because the width of top conductor is not large enough ($W_{\text{tot}} > 60 \mu\text{m}$ in CPW), these resonances are not intensive.

3.3.3.2 Dielectric loss

Dielectric loss of CPW in the expression (3-14) applies also for microstrip line, because it is only related to the dielectric properties and there is no explicit dependency on metal dimensions. The loss tangent of BCB is assumed to be constant ($\tan \delta = 0.007$) in the simulation, so the dielectric loss is proportional to frequency. Analytic dielectric loss begins to underestimate the present calculated one from 500 GHz, while at low frequency they agree well. At 1 THz, the dielectric loss is about 0.8 dB/mm.

3.3.3.3 Conduction loss

Ohmic loss depends critically on metal width, excitation frequency and strip conductivity. Conduction loss scales roughly with \sqrt{f} [Heiliger1997] at low frequency, but no explicit expression for conduction loss exists at high frequency when considering the dispersion of the dominant mode. Even at low frequency, α_c is not negligible compared with other losses. Microstrip line with large metal width has small surface resistance in the signal strip, so the conduction loss will be weak (4.3 dB/mm for $W = 5 \mu\text{m}$ and 1.51 dB/mm for $W = 30 \mu\text{m}$ at 1 THz). Moreover, high conductivity metal always helps to decrease the surface resistance and the ohmic attenuation, as in the CPW case.

If the dispersion of the dominant mode is neglected, the close form conduction loss for microstrip was reported in [Pucel1968, Bahl1977] as,

$$\alpha_c (\text{dB / mm}) = \begin{cases} \frac{R_s}{Z_0 H} \frac{8.68 \times 10^{-3}}{2\pi} \left[1 - \left(\frac{W_{\text{eff}}}{4H} \right)^2 \right] \left[1 + \frac{H}{W_{\text{eff}}} + \frac{H}{\pi W_{\text{eff}}} \left(\ln \frac{4\pi W}{t} + \frac{t}{W} \right) \right] & \text{if } \frac{W}{H} \leq \frac{1}{2\pi} \\ \frac{R_s}{Z_0 H} \frac{8.68 \times 10^{-3}}{2\pi} \left[1 - \left(\frac{W_{\text{eff}}}{4H} \right)^2 \right] \left[1 + \frac{H}{W_{\text{eff}}} + \frac{H}{\pi W_{\text{eff}}} \left(\ln \frac{2H}{t} + \frac{t}{H} \right) \right] & \text{if } \frac{1}{2\pi} < \frac{W}{H} < 2 \\ \frac{R_s}{Z_0 H} \frac{8.68 \times 10^{-3}}{\left[\frac{W_{\text{eff}}}{H} + \frac{2}{\pi} \ln(5.44\pi) \left(\frac{W_{\text{eff}}}{2H} + 0.94 \right) \right]^2} \left[\frac{W_{\text{eff}}}{H} + \frac{W_{\text{eff}}}{\pi H \left(\frac{W_{\text{eff}}}{2H} + 0.94 \right)} \right] \left[1 + \frac{H}{W_{\text{eff}}} + \frac{H}{\pi W_{\text{eff}}} \left(\ln \frac{2H}{t} + \frac{t}{H} \right) \right] & \text{if } \frac{W}{H} \geq 2 \end{cases} \quad (3-16)$$

All the dimensions are expressed in meters. The effective metal width W_{eff} and microstrip characteristic impedance Z_0 are given respectively by,

$$W_{eff} = \begin{cases} W + \frac{1.25t}{\pi} (1 + \ln(\frac{4\pi W}{t})) & \text{if } \frac{W}{H} \leq \frac{1}{2\pi} \\ W + \frac{1.25t}{\pi} (1 + \ln(\frac{2H}{t})) & \text{if } \frac{W}{H} \geq \frac{1}{2\pi} \end{cases} \quad (3-17)$$

$$Z_0(\Omega) = \begin{cases} \frac{60}{\sqrt{\epsilon_{eff}}} \ln(\frac{8H}{W_{eff}} + 0.25 \frac{W_{eff}}{H}) & \text{if } \frac{W}{H} \leq 1 \\ \frac{120\pi}{\sqrt{\epsilon_{eff}} \frac{W_{eff}}{H} + 1.393 + 0.667 \ln(\frac{W_{eff}}{H} + 1.444)} & \text{if } \frac{W}{H} \geq 1 \end{cases} \quad (3-18)$$

and the effective permittivity ϵ_{eff} :

$$\epsilon_{eff} = \begin{cases} \frac{\epsilon_r + 1}{2} + \frac{\epsilon_r - 1}{2} [(1 + 12H/W)^{-1/2} + 0.04(1 - W/H)^2] - \frac{\epsilon_r - 1}{4.6} \frac{t/H}{\sqrt{W/H}} & \text{if } \frac{W}{H} \leq 1 \\ \frac{\epsilon_r + 1}{2} + \frac{\epsilon_r - 1}{2} (1 + 12H/W)^{-1/2} - \frac{\epsilon_r - 1}{4.6} \frac{t/H}{\sqrt{W/H}} & \text{if } \frac{W}{H} \geq 1 \end{cases} \quad (3-19)$$

As seen in Figure 3-27 (c), the theoretical values given by (3-16) at $W = 10 \mu\text{m}$ predict 60% - 80% of the conduction losses in [100 -1000] GHz calculated by HFSS.

3.3.3.4 Total losses

Concerning the total losses in Figure 3-27 (d), the best microstrip dimension having the minimum attenuation is $W = 30 \mu\text{m}$, where the attenuation is 3.8 dB/mm at 1 THz. The reported measured losses of microstrip (8 μm wide and 0.8 μm thick) on thin film BCB (1.7 μm and 5.4 μm) at 1 THz were 10 dB/mm and 4 dB/mm [Heiliger1997], respectively. Our results are 4.6 dB/mm at 1 THz for 10 μm wide strip on 30 μm thick BCB.

3.3.4 Conclusions

Microstrip has the advantages of low radiation loss at THz frequency range due to a good EM energy confinement in the substrate when compared with CPW structure.

In microstrip line on BCB substrate, only the dominant mode is included in the calculation. From frequency above 300 GHz, the line becomes dispersive. Concerning the attenuation, ohmic loss accounts for a major contribution, especially at small strip width. Radiation and dielectric losses are comparable. To improve line performance, a relatively larger strip width can be chosen to minimize the conduction loss without introducing great additional radiation loss. However, in the case of large strip width, it is possible to form parallel plate type resonances with large amplitudes and the received signal amplitude will be reduced accordingly.

3.4 CST MWS analysis of stripline

The stripline was invented by R. Barrett in 1950. It is well known that an ideal stripline supports the pure TEM mode as the fundamental mode, when it is uniformly filled with a homogeneous

dielectric material (Left in Figure 3-28). The characteristic impedance and conductor and dielectric losses of this symmetric shielded strip transmission line have been analyzed in closed form expressions [Cohn1955]. Non dispersion and low losses are the main attractive properties of this waveguide. The most application of stripline is found in feeding network of antennas, low dispersive delay lines for phased array and radar systems, multilayer circuits, low temperature co-fired ceramic (LTCC) technology [Jang2006], and feeding lines for stripline slot antennas [Marchais2006]. The principle disadvantages lie in the realizations of the buried strip structure and characterizations of stripline performances. The requirement of strong symmetry introduces difficulties in the design of circuit functions and the tuning becomes difficult. Any vertical asymmetry in the stripline structure could couple to waveguide modes bounded by the ground planes and the side walls [Rao1979, Burchett1993]. For experimental characterization, transitions usually employ the type of microstrip/stripline due to their structural similarity, including vertical transitions with via/holes [Kim1998, Leib2010] and planar transition [Machado2011].

Few work has been conducted on stripline in THz range. As we will see in this part, the radiation loss depend on the central strip width and the dielectric permittivity. Dispersion and attenuation of stripline in both homogeneous and inhomogeneous dielectric circumstances are calculated. For the former, influences of dielectric permittivity on the attenuation of dominant mode are pointed out.

3.4.1 Stripline structure

A stripline consists of a strip conductor centered between two parallel ground planes with two equal slabs of a dielectric separating the center conductor from the ground planes, as illustrated at the left of Figure 3-28. Structural parameters are strip width W , dielectric thickness H , and conductor thickness t . Its characteristic impedance decreases with W and dielectric permittivity ϵ_r , but increases with H [Maloratsky2003]. A 50Ω waveguide (at 20 GHz) can be achieved with $W = 25 \mu\text{m}$ and $H = 30 \mu\text{m}$ for stripline in BCB. In the parametric study, H is fixed at $30 \mu\text{m}$, and W will vary around $25 \mu\text{m}$ to achieve impedance variation as well as comparisons with other types of waveguide. $W = 5$ (30) μm corresponds to 120 (45) Ω .

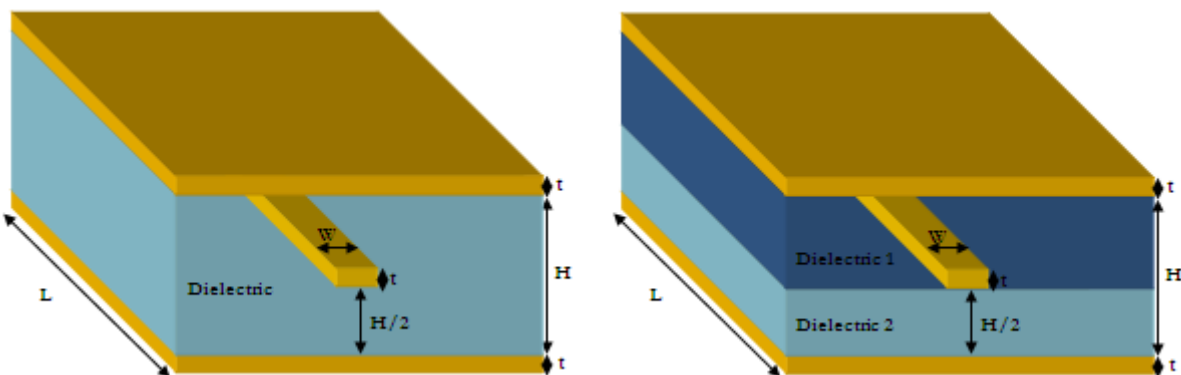


Figure 3-28: Schematic of the stripline surrounded by homogenous dielectric (left), and two layered dielectric with equal thickness (right)

In the multilayered circuit, two or more dielectric may exist between the top and bottom ground planes. The right plot in Figure 3-28 shows the nonuniform symmetric stripline ($H_2 = H/2$) with

two different dielectrics. As the two materials (dielectric 1 and 2) have the same thickness, the phase velocity of the stripline mode is always slower than or equal to the parallel plate mode. The power leaky from the dominant mode into the parallel plate mode is not allowed. However, when they have different thicknesses and the thinner dielectric has a smaller dielectric constant, power leakage from stripline mode to the parallel plate mode happens, because the effective permittivity of stripline mode is close to that of thin dielectric and the effective permittivity of the parallel plate mode is dominated by the thick dielectric [Das1991]. Moreover, when air gaps exist between the two dielectric slabs due to finite conductor thickness and fabrication faults, the dominant mode in the stripline with air gap will become leaky. This mode radiates into the TM_0 surface wave mode and other higher order modes of the background structure and results in undesirable crosstalk and spurious performance [Nghiem1992].

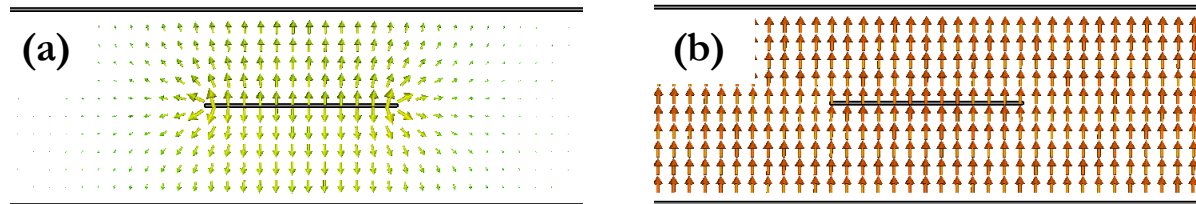


Figure 3-29: Electric vector field distributions of a stripline in homogeneous BCB. (a) Symmetric stripline mode, and (b) Asymmetric parallel plate mode

In the parametric simulation with CST MWS, the ground planes are considered to be extended infinitely in the lateral direction, so the PML boundary conditions are applied. Figure 3-29 demonstrates the field distributions of the two dominant modes (stripline mode and parallel plate mode) in the homogeneous dielectric of a stripline. As the CPW mode in the coplanar waveguide, E field of the stripline mode points symmetrically and radially around the central strip and H field circles around it. The parasitic parallel plate mode has its asymmetric electric field distribution both around and far away from the central strip. Following paragraph talks about the stripline mode in homogeneous dielectric (polymer BCB and semiconductor materials) and also in non homogeneous dielectric (superstrate (top) material: air, substrate (bottom) material: BCB).

3.4.2 Dispersions and losses

3.4.2.1 Homogeneous stripline

In the homogeneous stripline, the polymer BCB is used as dielectric material by default as in other types of waveguides for the ease of realization. Other kinds of dielectric, such as GaAs and Ge in semiconductor group, will be compared with BCB, although it is not possible to fabricate stripline with these semiconductors because present epitaxy technology is not applicable over metallization. The objective is to study and comprehend the influence of dielectric permittivity on the main mode in a homogeneous stripline.

I Stripline with polymer BCB substrate

As well known in microwave, the dominant stripline mode in a homogeneous stripline is purely TEM type and its effective permittivity is equal to the dielectric permittivity of the substrate, as shown in Figure 3-30. Its phase constant is exactly the same as that in the dielectric, so the phase

and group velocities always match those of BCB, so the radiation channel from the TEM dominant mode into the substrate as well as the coupling with the higher order modes is closed.

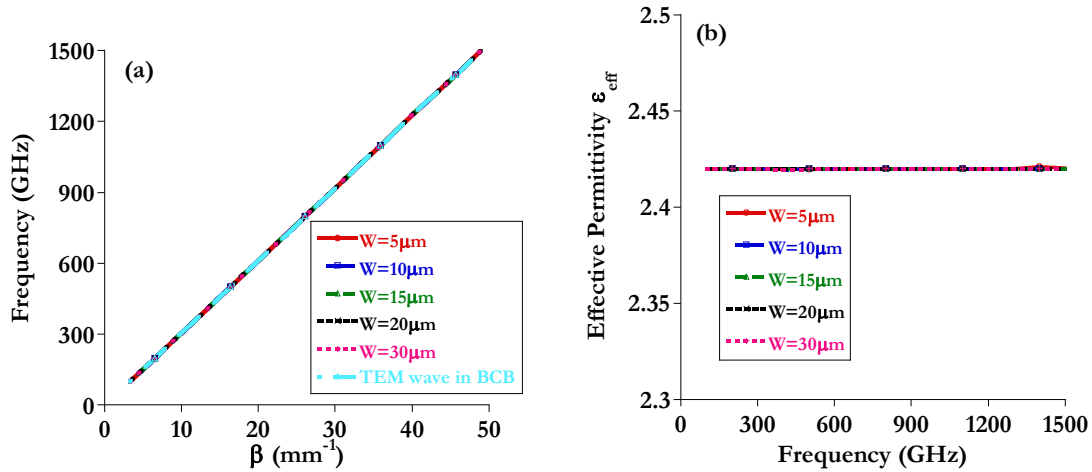


Figure 3-30: Phase constant (a) and effective dielectric constant (b) of stripline in homogeneous BCB, W is the central strip width

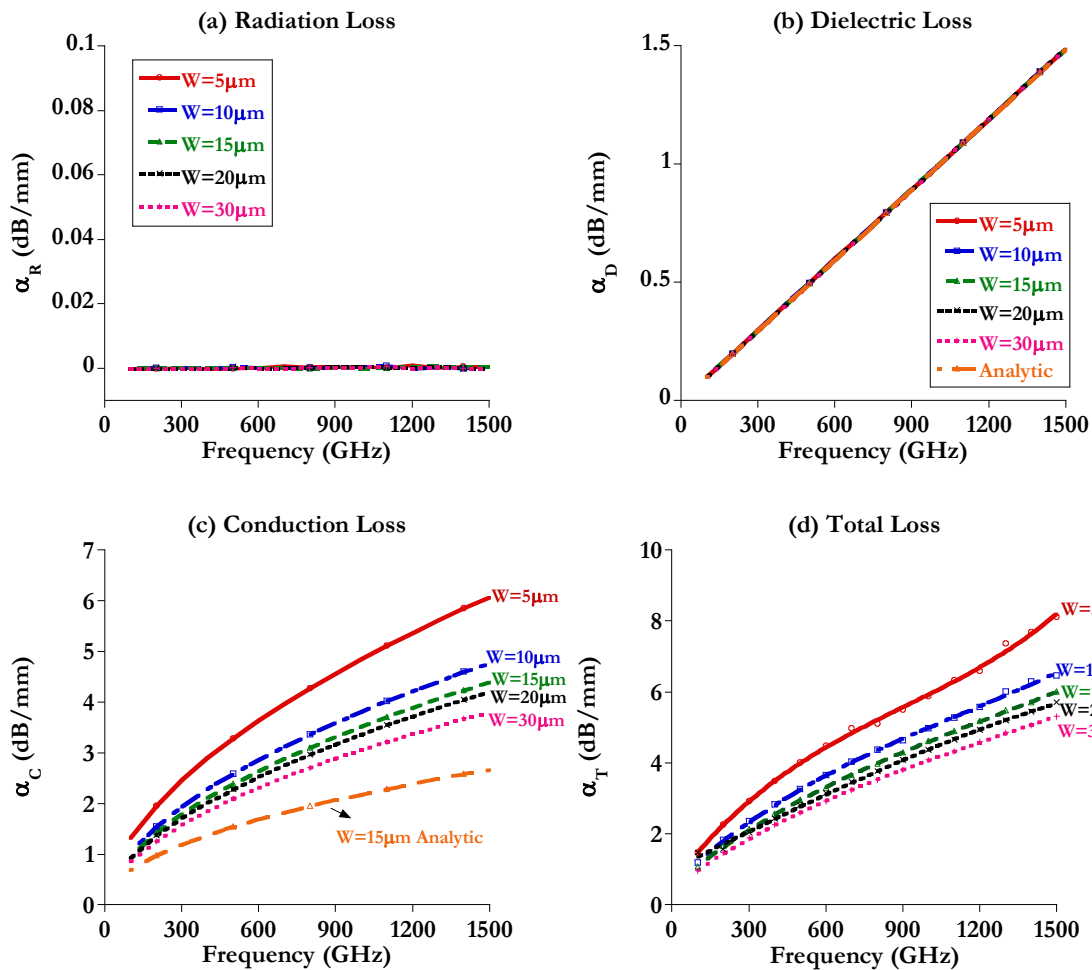


Figure 3-31: CST calculated losses of stripline in homogeneous 30 μm BCB, (a) Radiation loss, (b) Dielectric loss, (c) Conduction loss ($\sigma_{Au} = 5.10^6 \text{ S/m}$) and (d) Total losses ($\sigma_{Au} = 5.10^6 \text{ S/m}$)

As expected, the radiation loss in the stripline is 0.0001 dB/mm at 1.5 THz for $W = 30 \mu\text{m}$ in Figure 3-31 (a), which is well below the dielectric loss (1.49 dB/mm at 1.5 THz). Consequently, the total losses are approximately expressed by the sum of dielectric loss and conduction loss,

$$\alpha_T \approx \alpha_D + \alpha_C \quad (3-20)$$

Dielectric losses can be obtained through replacing $\epsilon_{eff} = \epsilon_r$ for the homogeneous stripline in the expression (3-14),

$$\alpha_D = 27.3 \times 10^{-3} \frac{\sqrt{\epsilon_r} \tan \delta}{c} f \text{ (dB / mm)} \quad (3-21)$$

Wheeler's formula for conduction losses [Wheeler1978, Maloratsky2003],

$$\alpha_C = \begin{cases} \frac{23.4 \times 10^{-6} R_s \epsilon_r Z_0}{30\pi(H \cdot t)} A \text{ (dB/mm)} & \text{for } \sqrt{\epsilon_r} Z_0 < 120\Omega \\ \frac{1.39 \times 10^{-3} R_s}{Z_0 H} B \text{ (dB/mm)} & \text{for } \sqrt{\epsilon_r} Z_0 > 120\Omega \end{cases} \quad (3-22)$$

Where A and B are geometry (t , H , and W) dependent factors, Z_0 is the characteristic impedance and R_s is the surface resistance for metal conductor.

The analytic formula underestimates the conductor losses in strips and ground planes in the simulated frequency range. For example, at $W = 15 \mu\text{m}$, the simulated conduction loss is 4.41 dB/mm instead of 2.67 dB/mm calculated by the analytic formula (3-22) at 1.5 THz. The dielectric loss can be perfectly estimated by the theory (3-21), because the stripline mode is TEM type and there are no assumptions in the expression (3-21). They both show the linear dependency on frequency. As seen in Figure 3-31, the conduction loss is the dominant source of attenuation in a stripline on BCB. The conduction loss at large metal width is low due to the weak metal resistivity in central strip, $W = 30 \mu\text{m}$ shows the least total losses (4.08 dB/mm at 1 THz and 5.32 dB/mm at 1.5 THz).

To evaluate the function of dielectric permittivity on stripline properties, an "**imaginary**" structure is proposed, where the low permittivity BCB is replaced by the semiconductor materials with high permittivity ($\epsilon_{GaAs} = 12.9$ and $\epsilon_{Ge} = 16$). It is obviously not possible to fabricate such waveguides.

II Stripline with semiconductors GaAs and Ge substrate

A complementary study is conducted to analyze the radiation losses of stripline based on the structure $W = 30 \mu\text{m}$ presenting the most radiation in the case of BCB.

Figure 3-32 shows the dispersion curves and radiation losses for stripline with a central strip of $30 \mu\text{m}$ width in homogeneous BCB, GaAs and Ge. As in the low permittivity BCB, both the two dominant modes (stripline mode and parallel plate mode) of stripline in high permittivity semiconductors have the same phase constant (or effective permittivity/phase velocity) as that in

the substrate. The TEM nature of the stripline mode is not altered with the variation of dielectric and no higher order modes appear up to 1.5 THz. That is why the radiation loss in function of the frequency is always nearly zero, no matter which type of dielectric (Figure 3-32 (b)). These are believed to be the unique properties of stripline.

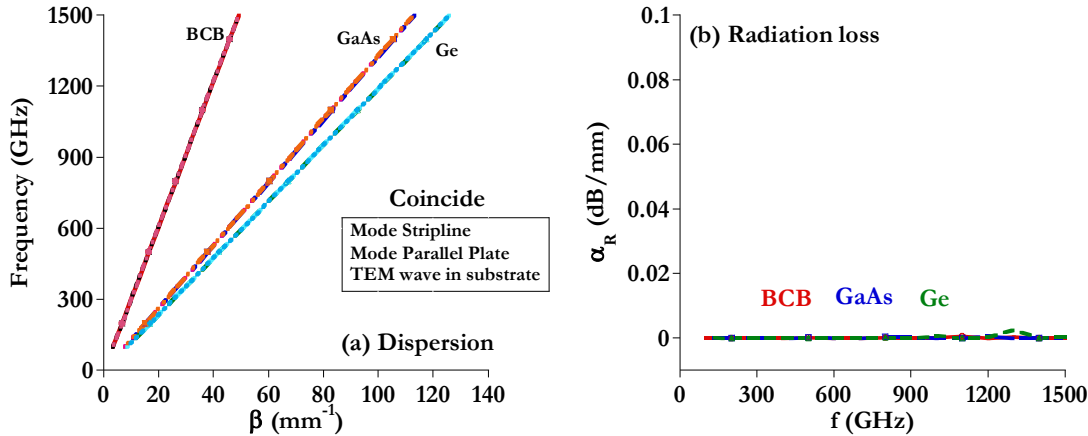


Figure 3-32: Dispersion (a) and radiation loss (b) of stripline ($W = 30 \mu\text{m}$) in homogeneous $30 \mu\text{m}$ BCB, GaAs and Ge

3.4.2.2 Inhomogeneous stripline

The last aspect we have investigated is about the stripline in non homogeneous dielectric. Only the radiation loss is calculated to comprehend the leaky nature of the dominant mode. The condition for the existence of TEM wave in the structure is destroyed due to the interface between adjacent different materials. Figure 3-33 compares the phase constant and radiation loss for stripline in non homogeneous $30 \mu\text{m}$ thick dielectric ($15 \mu\text{m}$ air as superstrate and $15 \mu\text{m}$ BCB as substrate) and for stripline in homogeneous $30 \mu\text{m}$ BCB. This structure can also be considered as a microstrip line with a conductor cover. Apparently, the phase velocity of the dominant mode of stripline in air/BCB is improved higher than that in homogeneous BCB. So the radiation loss into substrate increases. One also notices resonances at regular positions in Figure 3-33 (b) owing to the parallel plate modes formed between central strip and underlying metallization. Resonances with small amplitudes have also been observed in the spectrum of radiation loss in the studied microstrip lines.

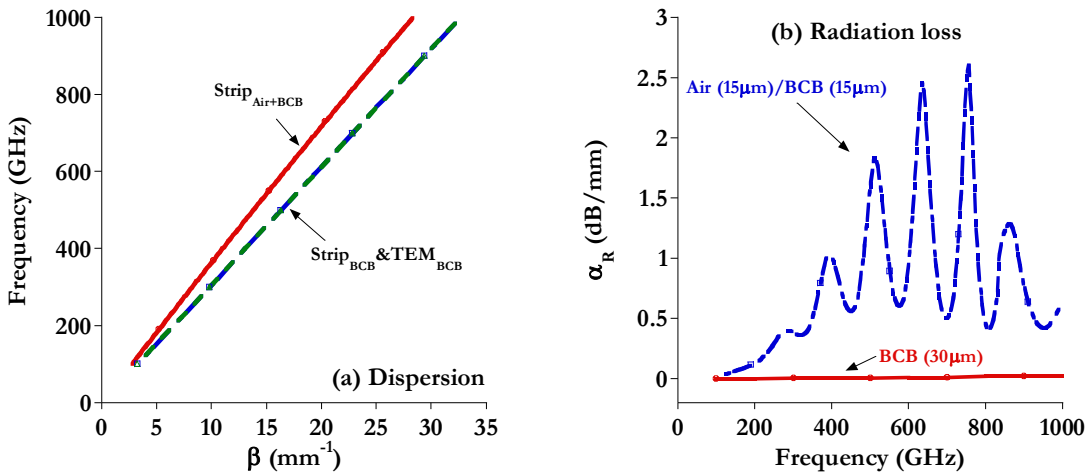


Figure 3-33: Dispersion (a) and radiation loss (b) of stripline ($W = 30 \mu\text{m}$) in non homogeneous $30 \mu\text{m}$ dielectric (15 μm air and 15 μm BCB)

3.4.3 Conclusions

The stripline with homogenous dielectric has a purely TEM mode in the frequency range [100-1500] GHz when the substrate is BCB. Thus, the radiation losses are negligible and the conduction loss contributes the most in the total losses. A waveguide with the largest strip width ($W=30 \mu\text{m}$) owns the least total attenuation (5.32 dB/mm at 1.5 THz).

Then the "imaginary" structure of stripline in semiconductor GaAs and Ge is proposed to study the impact of dielectric permittivity on radiation losses. The dispersion and losses of the stripline mode are still calculated to be zero when the dielectric permittivity increases.

The stripline with non homogeneous dielectric (Air/BCB) is multimode and it has dispersion and the radiation loss can be increased up to 2.5 dB/mm due to the presence of parallel plate resonances.

3.5 CST MWS analysis of slotline on substrate BCB

The slotline was first proposed by Cohn in 1968 [Cohn1968]. As shown in the left graph in Figure 3-34, a slotline consists of a narrow gap in a conductive metal coating on one side of a dielectric substrate, the other side of the substrate being bare. For the ideal case, the metal width is infinite ($S = \infty$). The characteristic impedance increases with slot width and is less sensitive to substrate height. It was given numerically by Cohn for gap width less than the substrate thickness, and by Knorr for wide slot [Knorr1975]. By curve fitting the results of Cohn, closed-form expressions of the impedance and effective permittivity of slotline on finite thickness substrate (dielectric constant is between 7 and 20) were obtained [Garg1976]. Kitazawa [Kitazawa1973] calculated the phase constant of the dominant mode and the first higher order mode for slotline with gap width 1 mm on a 1 mm thick substrate ($\epsilon_r = 9.6$) up to 40 GHz. The first higher order mode appeared at 20 GHz and had the phase constant smaller than that of the dominant mode. From the aspect of attenuation, the dielectric loss depends on the properties of substrate and follows the same expression as in CPW and microstrip lines. Rozzi [Rozzi1990] compared the dielectric and conduction losses for slotline on 635 μm thick alumina substrate until 30 GHz. The

conduction loss was always higher than the dielectric loss at different slot widths ($[0.1-1]$ mm), where the metal conductivity is $4.1 \cdot 10^7$ S/m and loss tangent of substrate is $2 \cdot 10^{-4}$ in the calculation. For conductor thickness in the range $[3-50]$ μm , the closed form expressions of the characteristic impedance, effective permittivity, dielectric and conduction losses of slotline on finite thickness substrate ($2.22 < \epsilon_r < 20$) were presented in [2-60] GHz [Majumdar2010].

Slotline has the following advantages: easy to fabricate, shunt mounting of elements without holes though the substrate, incorporation with microstrip lines for new types of circuits. Moreover, its gap configuration makes slotline quite compatible with THz PC switches [Grischkowsky1988]. The main disadvantage arises from its high dispersive behavior when the substrate is thick but not infinite, meaning that slotline is not usually applicable for broadband applications [Maloratsky2003]. For experimental evaluation of losses of slotline, the transitions like CPW-slotline [Ma1999] and microstrip-slotline [Schüppert1988] are the possible solutions.

In THz frequency, the transmission properties of slotline have not been studied completely. Particularly the dispersion and radiation loss of the dominant mode are not known. In next section, we will present the complex propagating constant of both conventional and conductor backed slotline on BCB substrate. The modeled results will be compared with existing numerical and experimental data.

3.5.1 Slotline structure

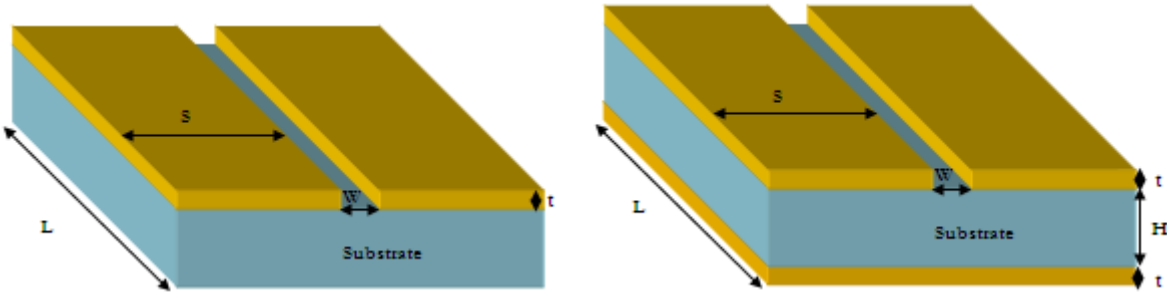


Figure 3-34: Schematic of a conventional slotline on a semi-infinite dielectric substrate (left), and a conductor backed slotline on a finite substrate (right)

The conventional slotline in the left of Figure 3-34 has two characteristic parameters: slot width W and metal thickness t . The substrate thickness is assumed to be infinite, so PML boundary conditions are applied at the bottom surface of substrate in CST MWS. Practical metal width is chosen to be much greater than the gap ($S \gg W$) to approximate an ideal slotline structure: $S = 240 \mu\text{m}$ and $W = [5-30] \mu\text{m}$. The characteristic impedance at 20 GHz can be varied from 95 ($W = 5 \mu\text{m}$) to 160Ω ($W = 30 \mu\text{m}$). Technically, it is difficult to realize a 50Ω slotline on BCB substrate ($W \ll 0.5 \mu\text{m}$) by traditional optical lithography. In this parametric study, the width of slotline is chosen around tens of micrometers as the reported slotline on high permittivity GaAs substrate ($W = 10-20 \mu\text{m}$) at 1 THz [Pahlevaninezhad2011].

However, as the conductor backed CPW, the conductor backed slotline (right in Figure 3-34) is also interesting, since the backside metallization ensures improved electrical isolation, good heat sinking and easy DC biasing. The potential drawback in the application : the leakage of power

into surface waves or into the dielectric region between the plates, unexpected or unwanted coupling to neighboring lines [Shigesawa1988].

The dispersions and attenuations of conventional and conductor backed slotline will be discussed separately. Comparisons will be made between them.

3.5.2 Modal dispersions and losses

3.5.2.1 Conventional slotline without backed conductor

For slotline on a semi-infinite substrate, the slotline mode is the propagating mode with nearly zero cutoff frequency.

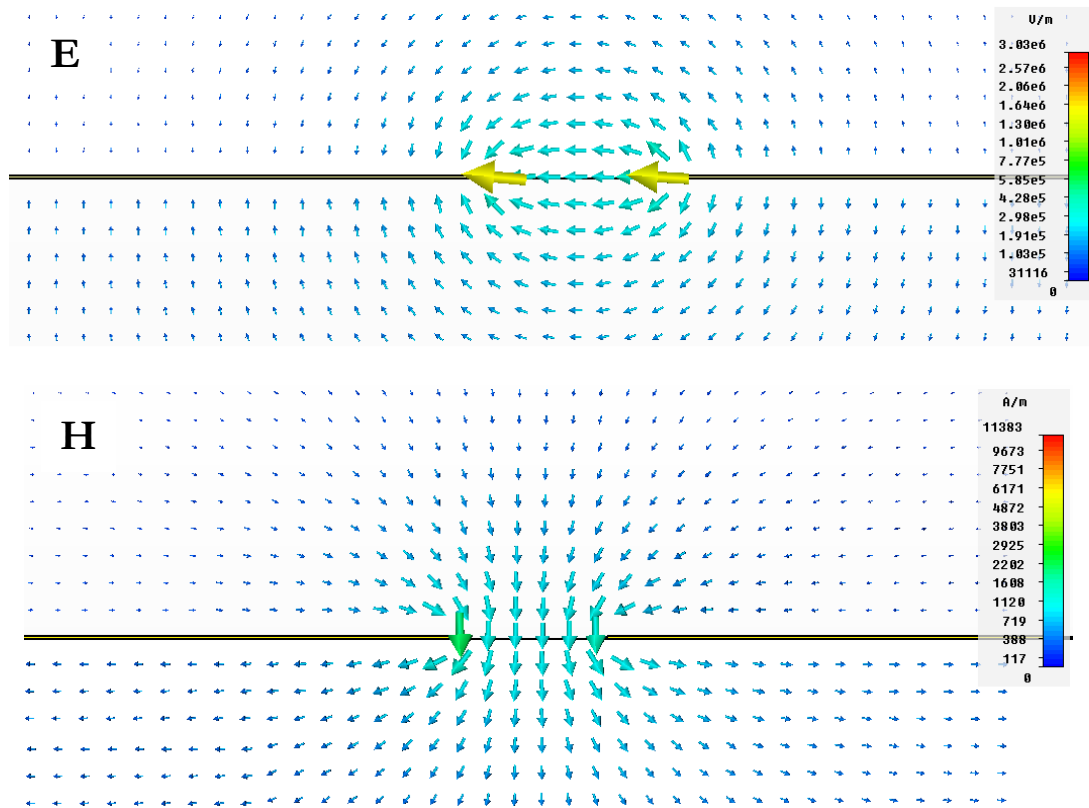


Figure 3-35: Electromagnetic vector field distribution of the dominant slotline mode in a conventional slotline. (a): Electric field and (b): Magnetic field

Figure 3-35 shows the EM fields distributions in a conventional slotline. E field vector is mainly directed from one plate to the other in the gap region, and H filed concentrates principally around the gap. In the following part, the dispersions and losses of conventional slotline at different slot width on substrate BCB are presented.

I Dispersions

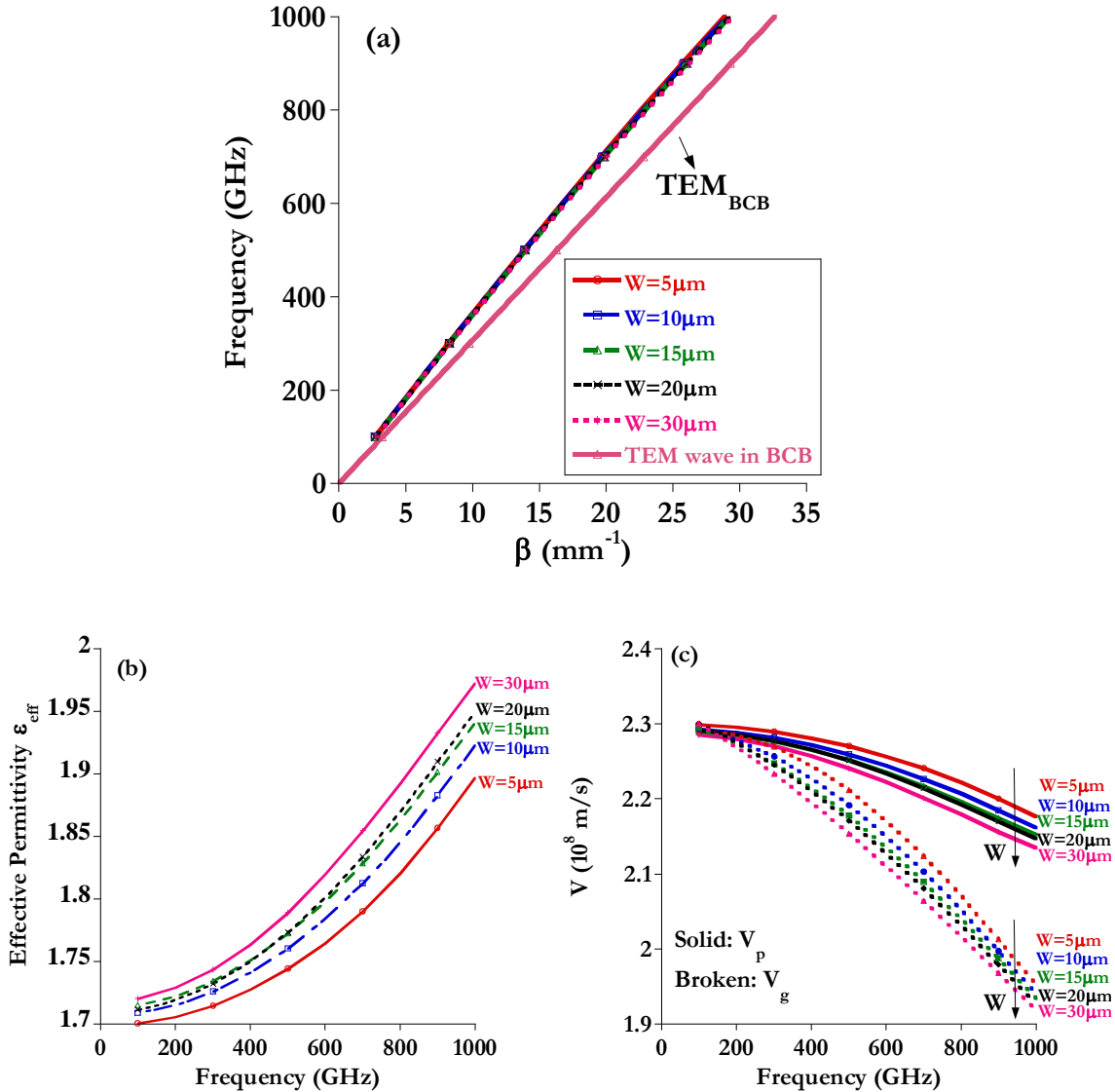


Figure 3-36: Phase constant (a), effective permittivity (b), phase and group velocities (c) of a slotline on semi-infinite BCB at different slot width W (5-30 μm)

In Figure 3-36, the phase constant, effective permittivity, phase and group velocities of the slotline mode (principle mode) in a slotline on semi-infinite BCB are plotted. In the simulated frequency range up to 1 THz, no higher order modes appear. Due to the low permittivity of substrate, the discrepancies of the phase constant among the five dimensions are not discernible. It is better to demonstrate the effective permittivity or phase velocities, shown in Figure 3-36 (b) and (c). As the phase velocity of the slotline mode is always greater than the TEM wave in substrate, the radiation of the main mode into the substrate happens unconditionally. And the energy transfer from the slotline mode to the high order mode is inhibited, if we assume only the dominant mode is propagated in the homogeneous slotline structure up to 1 THz. If multiple modes are present in the structure due to bends and discontinuities in the propagation direction, the coupling between the higher order mode and slotline mode becomes possible, resulting in

large radiation loss in slotline. In the design of slotline, the higher order modes should be avoided or pushed far from the interested frequency range.

The phase velocity decreases with frequency due to the growth of effective permittivity ($1 < \epsilon_{eff} < 2.42$). At a certain frequency, wide slot brings in larger effective permittivity. The increasing speed of effective permittivity versus frequency is higher than in other types of lines studied, demonstrating the slotline is more dispersive. Comparisons of the different waveguides in section 3.6 will again address this effect.

II Losses

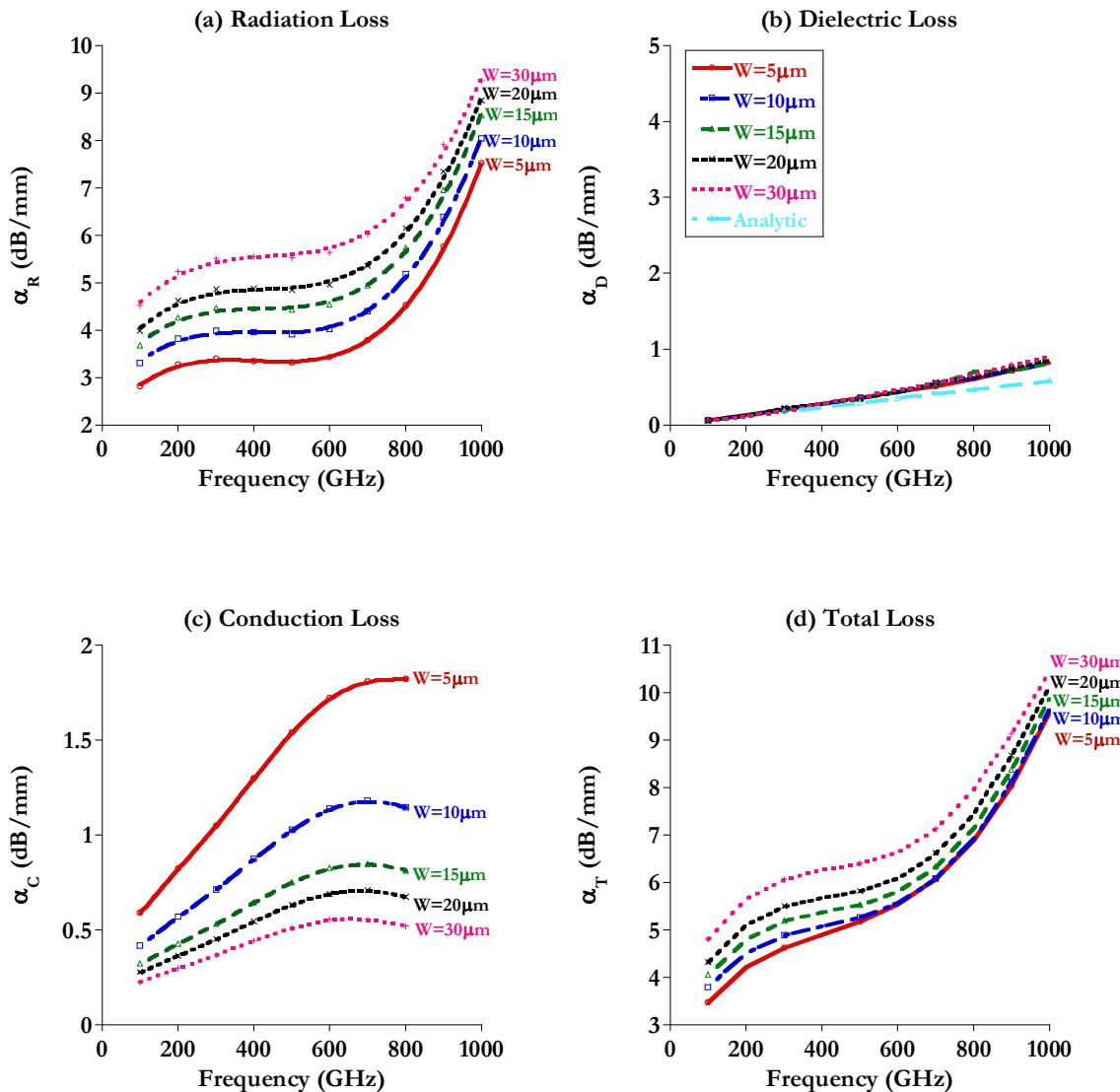


Figure 3-37: CST calculated losses of slotline on semi-infinite BCB, (a) Radiation loss, (b) Dielectric loss, (c) Conduction loss ($\sigma_{Au} = 5.10^6$ S/m) and (d) Total losses ($\sigma_{Au} = 5.10^6$ S/m)

We turn to the losses in Figure 3-37. α_R increases monotonically with slot width (9.2 dB/mm at 1 THz for W = 30 μm). As shown by the dispersion curves in Figure 3-36, this is because the radiation loss is mainly attributed to the energy loss into the substrate, and increases with the

level of phase mismatch between slotline mode and TEM wave in BCB. α_D always has a quasi linear dependency on frequency and the gap width does not have much impact on the losses in BCB. This suggests α_D is again linked to the nature of dielectric and is not sensible on dimensions of line deposited on top, as in CPW, microstrip and stripline. The analytic curve slightly underestimates the simulated α_D in CST. The conduction loss α_C is high at a small gap width, because the electric fields are more concentrated in the slot region, especially at the corners of two metal plates. This will result in great resistivity. The increase speed of α_C versus frequency is slower than that of α_R from 600 GHz. Even at frequencies below 600 GHz, α_C is always less than α_R . In the conventional slotline, α_R dominates in the total attenuation.

Among the five slotline, $W = 5 \mu\text{m}$ is the optimal one owning less total losses ($\alpha_T = 9.6 \text{ dB/mm}$ at 1 THz) due to its least radiation loss. From 500 GHz, slotline with $W = 10 \mu\text{m}$ shows equivalent total losses as $W = 5 \mu\text{m}$ because of its lower conduction loss. At 1 THz, slotline with $W = 20 \mu\text{m}$ has an attenuation of 10.1 dB/mm. For comparison, the simulated losses of slotline ($W = 20 \mu\text{m}$ and $t = 100 \text{ nm}$) on high permittivity substrate GaAs was about 20.7 dB/mm at 1 THz [Pahlevaninezhad2011]. This shows that the low permittivity substrate can reduce slotline losses.

As observed, the radiation loss in slotline is much higher than in other types of waveguides studied above. Several methods have been proposed to ameliorate the performances of conventional slotline. For slotline without backside metallization, shock wave radiation from the slotline mode into the substrate wave always exists. Modifications of the substrate properties, such as slotline in homogeneous medium, and slotline on a periodic layered substrate [Pahlevaninezhad2011], help to make the phase velocities of the propagating mode and substrate wave very close or even equal to each other.

The simulated results of slotline ($W = 10 \mu\text{m}$ and $t = 100 \text{ nm}$) in homogeneous GaAs substrate and periodic Si/SiO₂ layered substrate showed the attenuation at 1 THz was 1.7 dB/mm and 2.6 dB/mm [Pahlevaninezhad2011], respectively. Zero dispersion of group velocity was observed in the homogeneous GaAs structure. Therefore, less dispersive performances of slotline can be achieved by modifying traditional slotline structure. But the fabrication process becomes complicated. The measured slotline ($W = 270 \mu\text{m}$ and $t = 200 \text{ nm}$) in air gap has an attenuation of 0.05 dB/mm at 1 THz and shows almost zero dispersion of group velocity from 0.1-1 THz [Wächter2007].

3.5.2.2 Conductor backed slotline

As in conductor backed CPW, the function of underlying metallization on reducing radiation loss will be investigated in this part. Besides the slotline mode Figure 3-35, conductor backed slotline has a parasitic microstrip mode. This is similar to the microstrip mode in the conductor backed CPW structure. EM field is mainly concentrated between the finite top conductor and bottom infinite ground plane, and the narrow slot (compared with the top metal width) is nearly neglected. Figure 3-38 demonstrates the vector EM field distributions of the microstrip mode in this type of slotline.

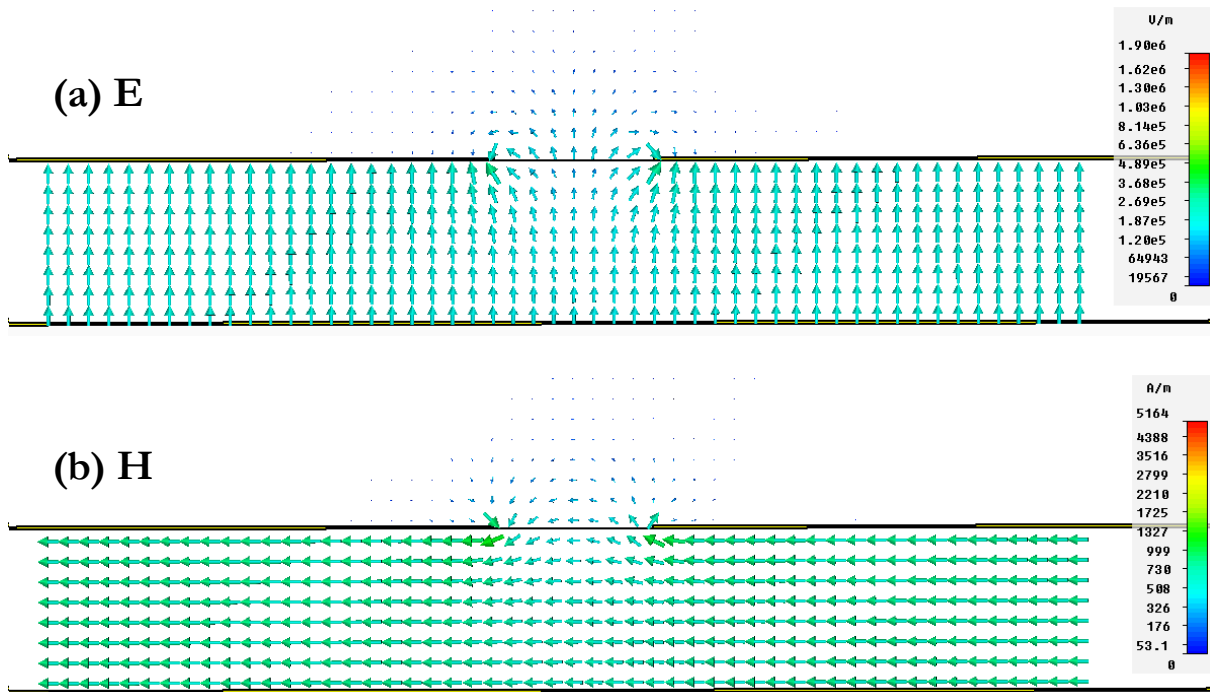


Figure 3-38: Electromagnetic vector field distribution of the parasitic Microstrip mode in a conductor backed slotline. (a): Electric field and (b): Magnetic field.

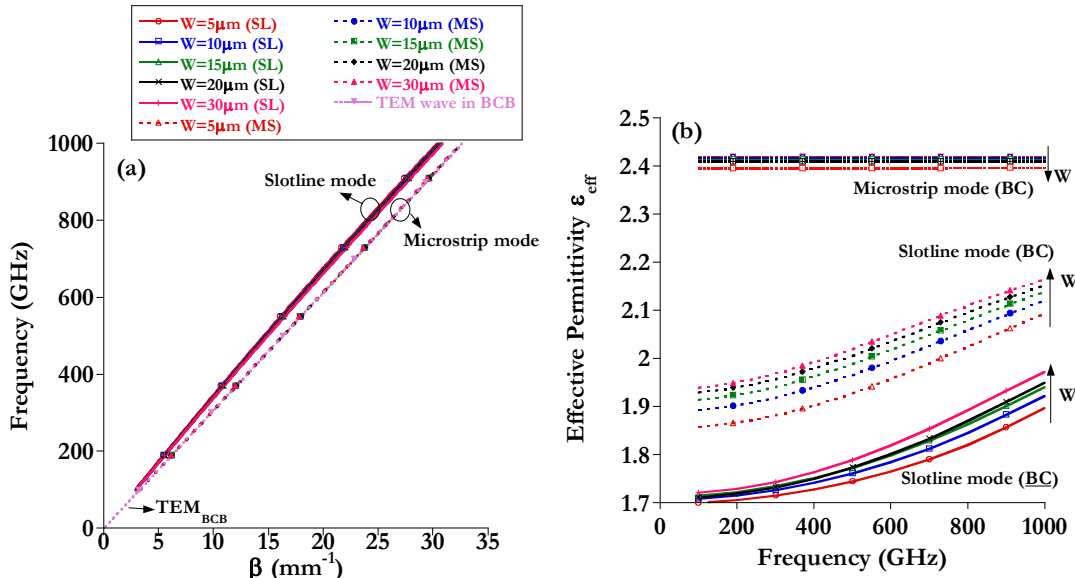


Figure 3-39: Phase constant (a), and effective permittivity (b) of slotline mode and microstrip mode in conductor backed (BC) slotline on 30 μm BCB. Cases of conventional slotline (BC) are also shown for comparisons in (b).

In conductor backed slotline, leakage of slotline mode to the parallel plate waveguide mode has been characterized [Shigesawa1988] at 10 GHz. If slot width $W = 3 \text{ mm}$, the leakage loss is about 0.5 dB per unit width and the leakage angle θ (in reference to the slot axis) is 31° ($\cos(\theta) = \beta / (\sqrt{\epsilon_r} \beta_0)$, β and β_0 are the phase constant of slotline mode and free space wave).

This leakage loss can be reduced by increasing the slot width or by increasing the substrate thickness. It can be avoided by loading the slotline with a high dielectric constant superstrate on the top, allowing the phase velocity of the slotline mode lower than that of the parallel plate mode [Das1991].

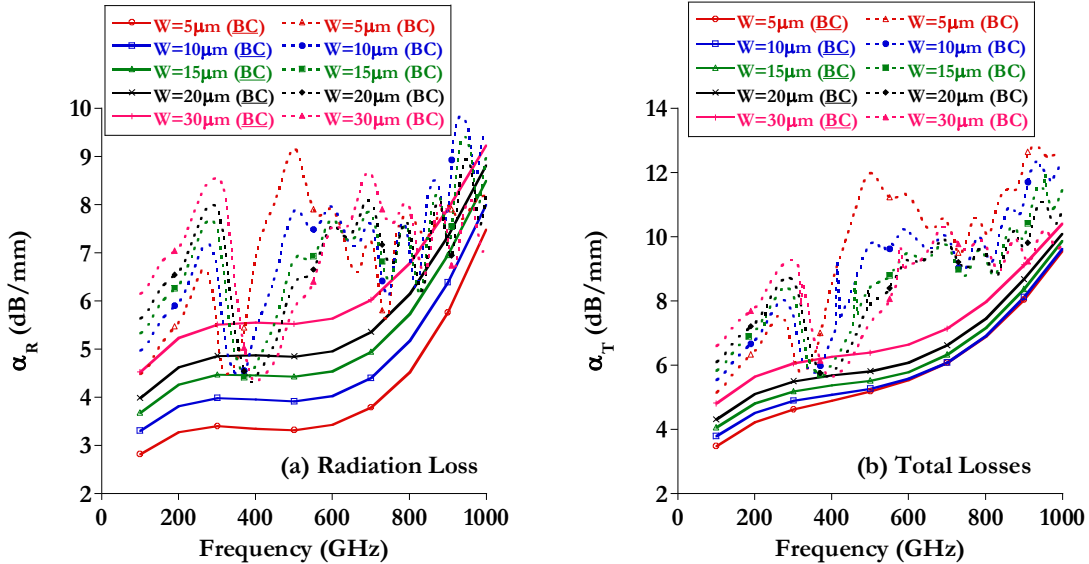


Figure 3-40: CST calculated losses of conductor backed (BC) slotline on 30 μm BCB, (a) Radiation loss and (b) Total losses. Cases of conventional slotline (BC) are also shown for comparisons

In Figure 3-39 and Figure 3-40, we compare the dispersion and losses (α_R and α_T) of conductor backed (BC) slotline with their conventional counterparts (BC). In the BC slotline, BCB with a thickness of 30 μm is modeled as in the conductor backed CPW. Figure 3-39 (a) shows that both the slotline mode and microstrip mode have no cutoff frequency. The phase constant of the microstrip mode is extremely close to the phase of the TEM wave in BCB. This can be further shown in Figure 3-39 (b), where the effective permittivity of the microstrip mode approaches the BCB permittivity (2.42) and this mode demonstrates no clear dispersion. Because most part of EM field is confined in the dielectric side and the EM field in the top air region can be neglected. With the increase of slot width, the effective permittivity of the microstrip mode decreases. Because the EM field becomes more leaky into the air region.

Effective permittivity of the dominant slotline mode is enhanced due to backed conductor and the corresponding phase velocity will be slow. This is similar to the observed increase of effective permittivity conductor backed CPW. As in the conductor backed CPW, parallel plate modes will appear at certain frequencies:

$$f_{mn} = \frac{c}{2\pi\sqrt{\epsilon_r}} \sqrt{\left(\frac{m\pi}{S}\right)^2 + \left(\frac{n\pi}{L}\right)^2} \quad (3-23)$$

Because S (0.24 mm) < L (1 mm), the resonance frequency f_{mn} is mainly determined by L and ϵ_r , in the simulated frequency range ($m = 0$). $f_{01} \approx 100$ GHz, so the resonances will appear at integral

multiple of f_{01} , as seen in the radiation and total losses in Figure 3-40. At these frequencies, the performance of conductor backed slotline mode deteriorates, making it no longer appropriate for THz transmission (increase of α_R is 3-6 dB/mm). However, outside these resonant positions, the radiation losses are comparable to those in conventional slotline, or even lower at high frequency (> 800 GHz). Concerning total losses in Figure 3-40 (b), the conductor backed slotline always has worse performance up to 1 THz (increase of α_T is 2-6 dB/mm). The backside conductor can probably introduce additional conduction and dielectric losses, as in the case of conductor backed CPW. It should be noted that the appearance of these resonances in Figure 3-40 depends on the profile of excitation plane in the simulation. This is different from the on-wafer measurement, in which the probe is only located at the metal plane (horizontal excitation). The appearances of resonances need verification in the prospective work.

3.5.3 Conclusions

In summary, the dispersions and losses of conventional and conductor backed slotline on substrate BCB have been investigated. For conventional slotline, $W=5$ μm corresponds to the minimum total attenuation among the studied dimensions ($W= [5-30]$ μm). Resonances due to the excitation of parallel plate modes in the conductor backed slotline are also observed as in the conductor backed CPW. In the high frequency region (> 800 GHz), the backed conductor helps to decrease the radiation loss in the non resonant part, which is the advantage of conductor backed slotline. Strong dispersion and high attenuation may limit the application of slotline in THz range.

Until now, four types of transmission lines have been studied separately focusing on the various parameters of geometric and material properties in THz range. In the following part of this chapter, direct numerical comparisons of these lines will be made for the first time in the [20-1000] GHz frequency range.

3.6 Optimal THz planar waveguide

3.6.1 Comparison criteria

Comparisons of dispersion and total losses between CPW and microstrip line on thin BCB film (several micrometers) over silicon substrate were conducted up to 1 THz [Schnieder2005] at the same characteristic impedance (70Ω). This impedance value can be achieved by adjustment of two geometrical parameters: S_1 and W for CPW, W and H for microstrip. However, for slotline on BCB, only the slot width W can be altered. In the section 3.5 about slotline, the characteristic impedance can be increased from 95Ω ($W = 5 \mu\text{m}$) to 160Ω ($W = 30 \mu\text{m}$). Considering the technological realization by conventional optical lithography, here we propose to compare the four simulated different types of waveguides at the same low frequency (20 GHz) characteristic impedance (100Ω). Their geometrical dimensions are illustrated in Figure 3-41 and they can be easily fabricated.

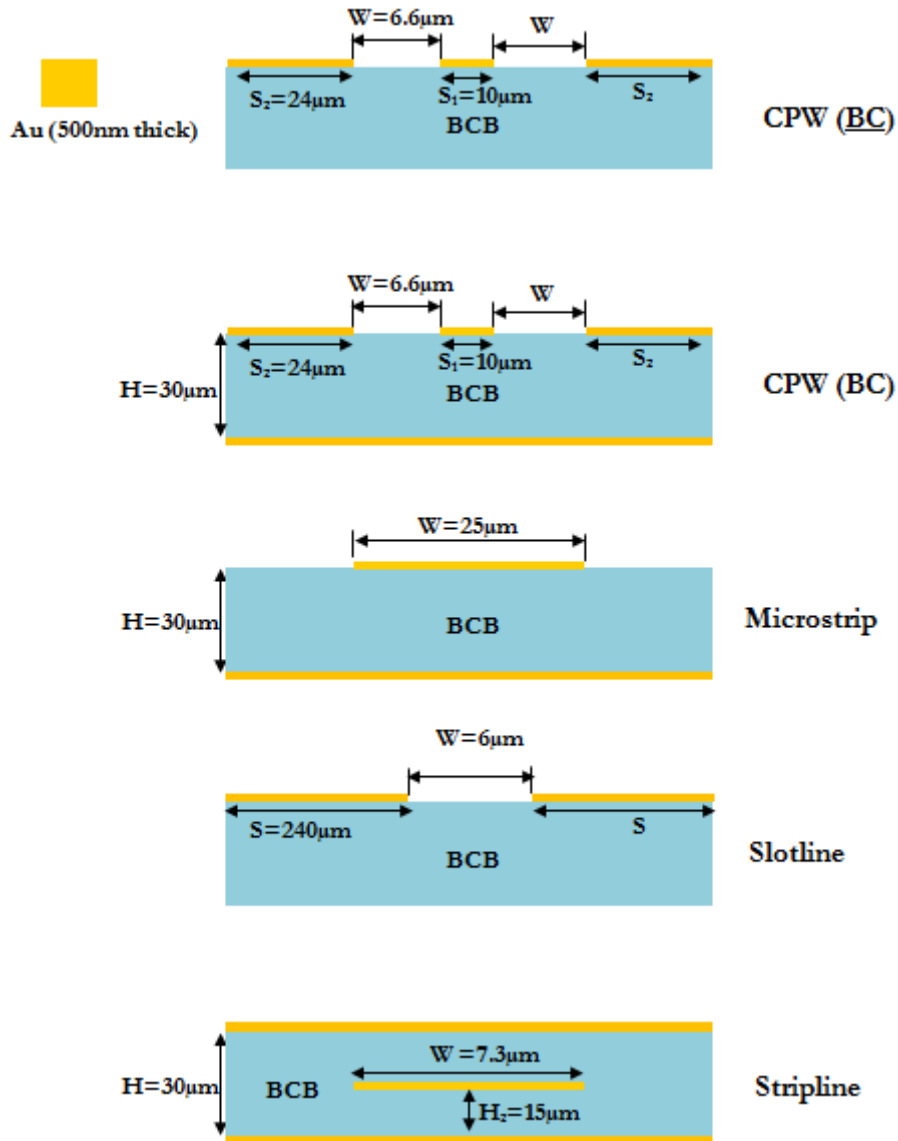


Figure 3-41: Dimensions of different 100Ω waveguides for comparisons

CPW with (BC) and without (BC) backed conductor gives similar characteristic impedance, while conductor backed slotline on 30 μm BCB at $W = 6 \mu\text{m}$ has 74 Ω impedance. It should be noted that, for CPW, the dimensions of S_1 (10 μm) and W (6.6 μm) in Figure 3-41 are not unique to achieve 100 Ω impedance. The BCB thickness (H) is assumed ideally to be infinite for CPW and slotline without backside metallization, while $H = 30 \mu\text{m}$ for microstrip and the homogeneous stripline. A thickness of 30 μm BCB can be easily deposited by a spin coating device, as seen in the section of sample fabrication.

Metal conductivity $\sigma_{\text{Au}} = 5.10^6 \text{ S/m}$ and thickness $t = 500 \text{ nm}$, and other material parameters are kept as the same as in Table 3-1. The dispersions and different types of losses will be compared among the four types of waveguides and the optimal structure suitable for THz transmission is then proposed based on the chosen comparison criteria (100 Ω characteristic impedance). Frequency domain simulation of slotline is conducted by CST MWS, and by HFSS for other three types of waveguide in the range [10-1000] GHz.

3.6.2 Dispersion and losses

3.6.2.1 Dispersion

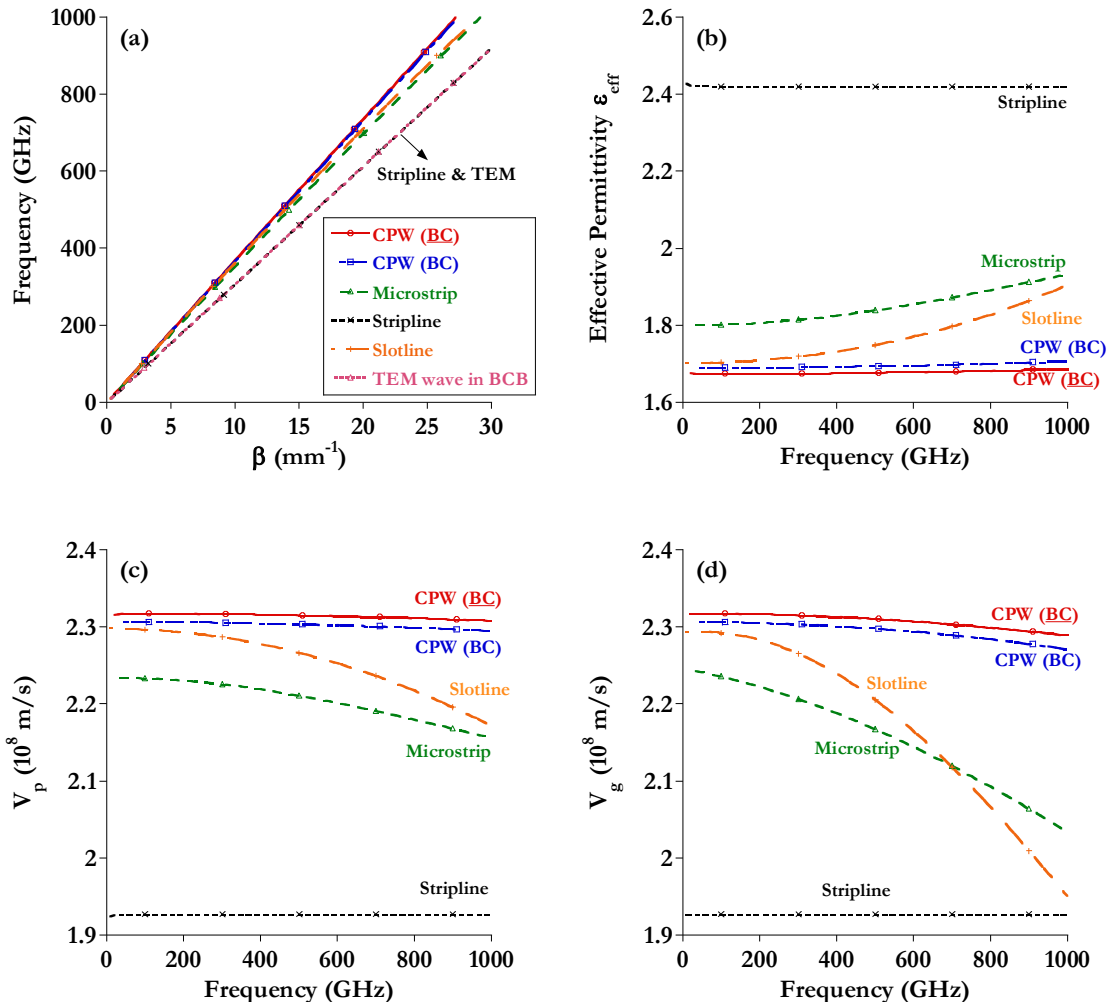


Figure 3-42: Phase constant (a), effective permittivity (b), phase (c) and group (d) velocities of the fundamental mode in the four types of waveguides. Phase constant of TEM wave in BCB is also plotted for reference

Figure 3-42 plots the phase constant, effective permittivity, phase and group velocities of the dominant mode in the four types of transmission lines on BCB substrate. The results of CPW (BC and BC) are reproduced here from the section 3.2. The slotline mode in CPW structure is not shown here. Stripline has its phase constant equal to the phase of TEM wave in homogeneous BCB, so it is the only waveguide owning TEM nature of propagation. The effective permittivity of CPW and stripline is quasi-constant with the frequency. From 10 GHz to 1 THz, the incremental value of effective permittivity is 0.0138 (CPW BC), 0.02 (CPW BC), 0.1327 (Microstrip), 0 (Stripline) and 0.203 (Slotline). As seen in section 3.2, backed conductor in CPW can increase the effective permittivity. The phase velocity (ω / β) is in the following order: CPW (BC) > CPW (BC) > Slotline > Microstrip > Stripline = TEM wave in BCB. Both the phase and group velocities of slotline demonstrate its most strong frequency dependent behavior. Among these waveguides, slotline appears as the most dispersive line and the stripline as the least

dispersive one. Microstrip is less dispersive than slotline. The four types of waveguides can be sorted by descending order of dispersion as follows: Slotline > Microstrip > CPW > stripline.

3.6.2.2 Losses

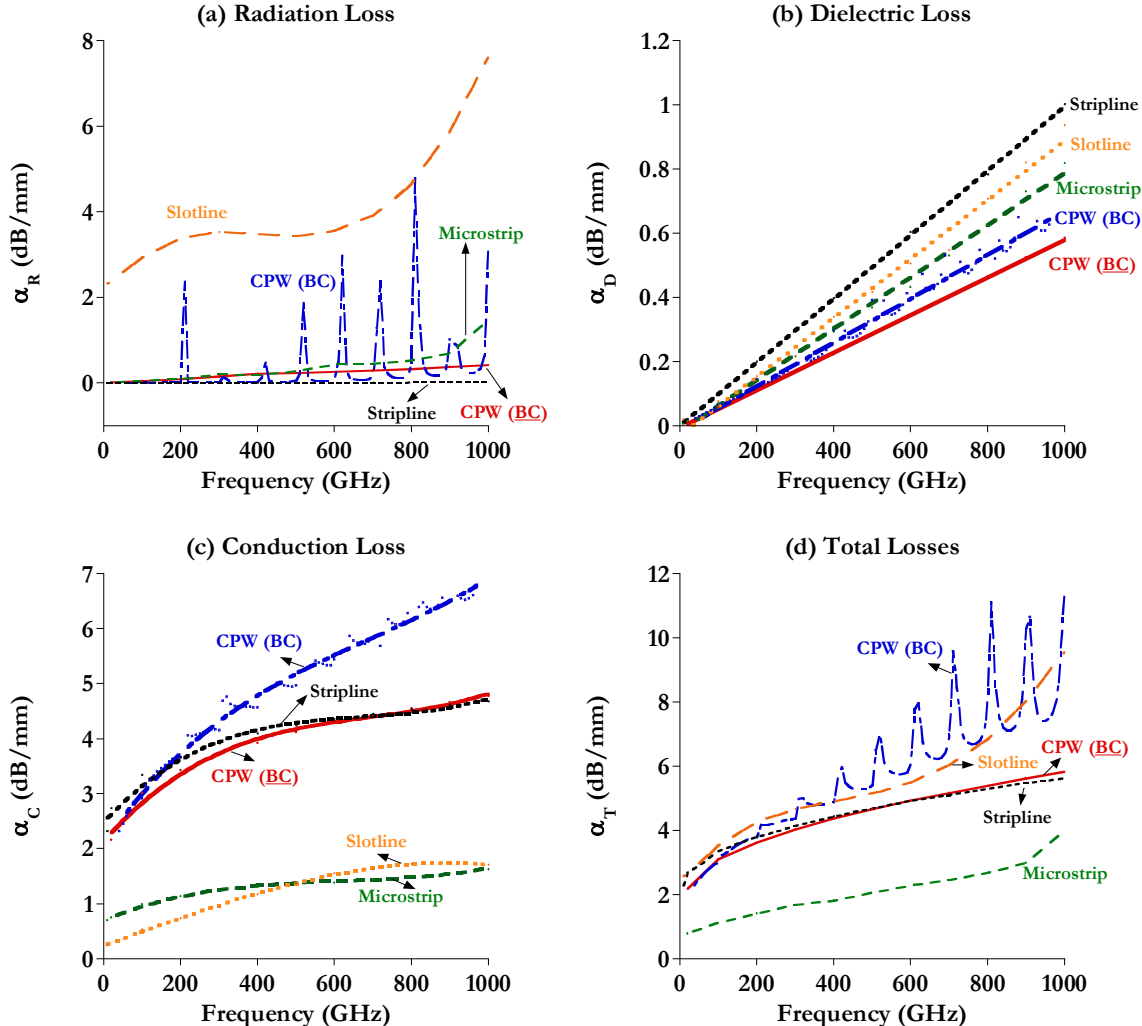


Figure 3-43: Losses of the four types of waveguides: (a) Radiation loss, (b) Dielectric loss, (c) Conduction loss ($\sigma_{Au} = 5.10^6 \text{ S/m}$), and (d) Total losses ($\sigma_{Au} = 5.10^6 \text{ S/m}$)

I Radiation loss

Losses in each line can be found in Figure 3-43. For radiation loss, the slotline has the largest attenuation (7.63 dB/mm at 1 THz) well above other three lines. The high loss can be reduced by using narrow slot, but the fabrication difficulty will increase accordingly. Unsurprisingly, stripline has quasi zero radiation until 1 THz (0.006 dB/mm). Microstrip and CPW (BC) also present satisfactory performances, with 1.48 dB/mm and 0.43 dB/mm respectively at 1 THz. CPW (BC) has radiation loss between those of stripline and CPW (BC) in the non resonant region. At resonances, its value is comparable to, but lower than that of slotline.

II Dielectric loss

Dielectric loss is related to the loss tangent in BCB and they are shown to be equivalent between different lines (note the different ordinate values). The dielectric loss is almost proportional to frequency. This result is consistent with the theory in microwave [Gupta1996]. For the four types of waveguides, the maximum loss observed is inferior to 1 dB/mm at 1 THz. We can conclude that dielectric losses are weak and comparable to the radiation losses in CPW and microstrip. Reduction of the dielectric loss is possible by employing a substrate material with lower loss tangent, such as the cyclic-olefin copolymer (COC, $\epsilon_r = 2.35$ at 10 GHz and $\tan\delta = 0.0007$ at 1 THz) [Peytavit2011].

III Conduction loss

Conduction losses in metals influence the EM field distribution outside metals via the variations of geometric dimensions of metals and the distance between them. Slotline and microstrip have the least ohmic losses (1.6 dB/mm at 1 THz) whereas CPW (BC) suffers from the highest loss (6.7 dB/mm at 1 THz). CPW (BC) and stripline have relatively high value (4.7 dB/mm at 1 THz) due to their narrow metal width or gap width. The reduction of conduction loss is possible by properly choosing the values of (S_1 , W) for CPW (BC), and (W , H) for stripline, while the characteristic impedance is maintained at 100 Ω .

IV Total losses

The total losses are compared in Figure 3-43 (d). Based on the assigned material parameters of BCB and metal, microstrip line is the optimal THz transmission line showing an attenuation of 4.0 dB/mm at 1 THz. Stripline and CPW (BC) suffer from their large conduction loss in the metals. Due to its large radiation loss, slotline is proved to be the most lossy transmission line (9.6 dB/mm at 1 THz). The attenuation in CPW (BC) presents resonances and its value is equivalent to, or even higher than that of slotline because of its great conduction loss.

At 1 THz, the phase velocity and different losses of the dominant mode in each line is summarized in Table 3-4.

***Table 3-4: Phase velocities and attenuation properties of the four types of waveguides at 1 THz.
Phase velocity in BCB is 1.93×10^8 m/s.***

	$V_p (10^8 \text{ m/s})$	$\alpha_R (\text{dB/mm})$	$\alpha_D (\text{dB/mm})$	$\alpha_C (\text{dB/mm})$	$\alpha_T (\text{dB/mm})$
CPW (<u>BC</u>)	2.31	0.43	0.59	4.77	5.84
CPW (BC)	2.29	3.82	0.63	6.74	11.71
Microstrip	2.16	1.48	0.82	1.63	4.00
Stripline	1.93	0.006	1.00	4.68	5.64
Slotline	2.17	7.63	0.94	1.71	9.60

The microstrip seems to be the best transmission according to the total losses in Table 3-4. However, the performances of the other three types of waveguide as well as the microstrip at 100 Ω still leave room to be improved, if the geometric dimensions are varied. In CPW (BC) and stripline, the conduction loss dominates in the total attenuation. By increasing the gap width in

CPW and the central strip width in stripline, the conduction loss can be reduced. For slotline, the radiation loss is high due to its strong dispersion. If the dispersion becomes weak, the radiation loss will decrease accordingly. The following section aims to optimize the attenuation in each waveguide, while the characteristic impedance is always at 100Ω .

3.6.3 Optimization of the performances of waveguides on BCB at 100Ω

In CPW without BC, the radiation loss increases with the gap width W and the central metal width S_1 , while the conduction value decreases with W . By varying S_1 and W at the same time, the characteristic impedance can be maintained at 100Ω at 20 GHz. The evolution of the total losses with the combination (S_1/W) is shown in Figure 3-44 (a). The optimal choice exists: $S_1 = 20 \mu\text{m}$ and $W = 12 \mu\text{m}$. At 1 THz, the total losses are reduced from 5.84 dB/mm to 4.83 dB/mm. For S_1 and W higher than the optimal values, the radiation loss becomes important at high frequency (> 400 GHz). If they are below the optimal values, the conduction loss dominates.

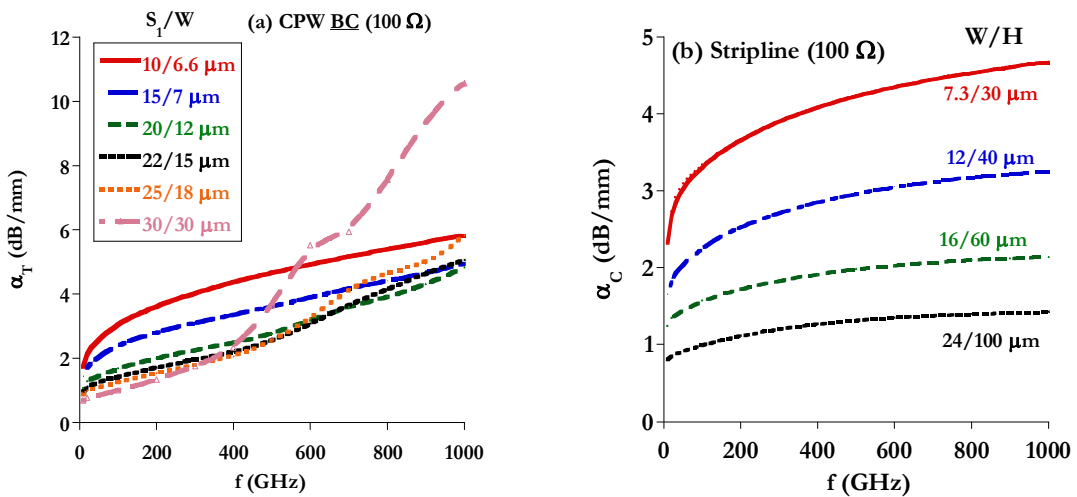


Figure 3-44: (a) Total losses of CPW (BC) at 100Ω with different combinations of S_1 and W , (b) Conduction loss of stripline at 100Ω with different combinations of W and H

In stripline at 100Ω , both the central metal width (W) and the dielectric thickness (H) should be changed. Because the radiation loss and dielectric loss do not depend on W and H , the practical method is to use wide central strip to reduce the conduction loss (or the total losses). Figure 3-44 (b) shows the conduction loss in the stripline with the variation of (W/H) . Large values of W and H are optimal. In practice, they are limited by the maximum thickness of BCB deposited over the metallic ground plane. $H = 60 \mu\text{m}$ can be easily realized in the fabrication process. The corresponded strip width is $W = 16 \mu\text{m}$. At these values, the conduction (total) losses are reduced from 4.68 (5.64) dB/mm to 2.14 (3.23) dB/mm at 1 THz. The attenuation is lower than the total losses (4 dB/mm at 1 THz) in the microstrip ($H = 30 \mu\text{m}$).

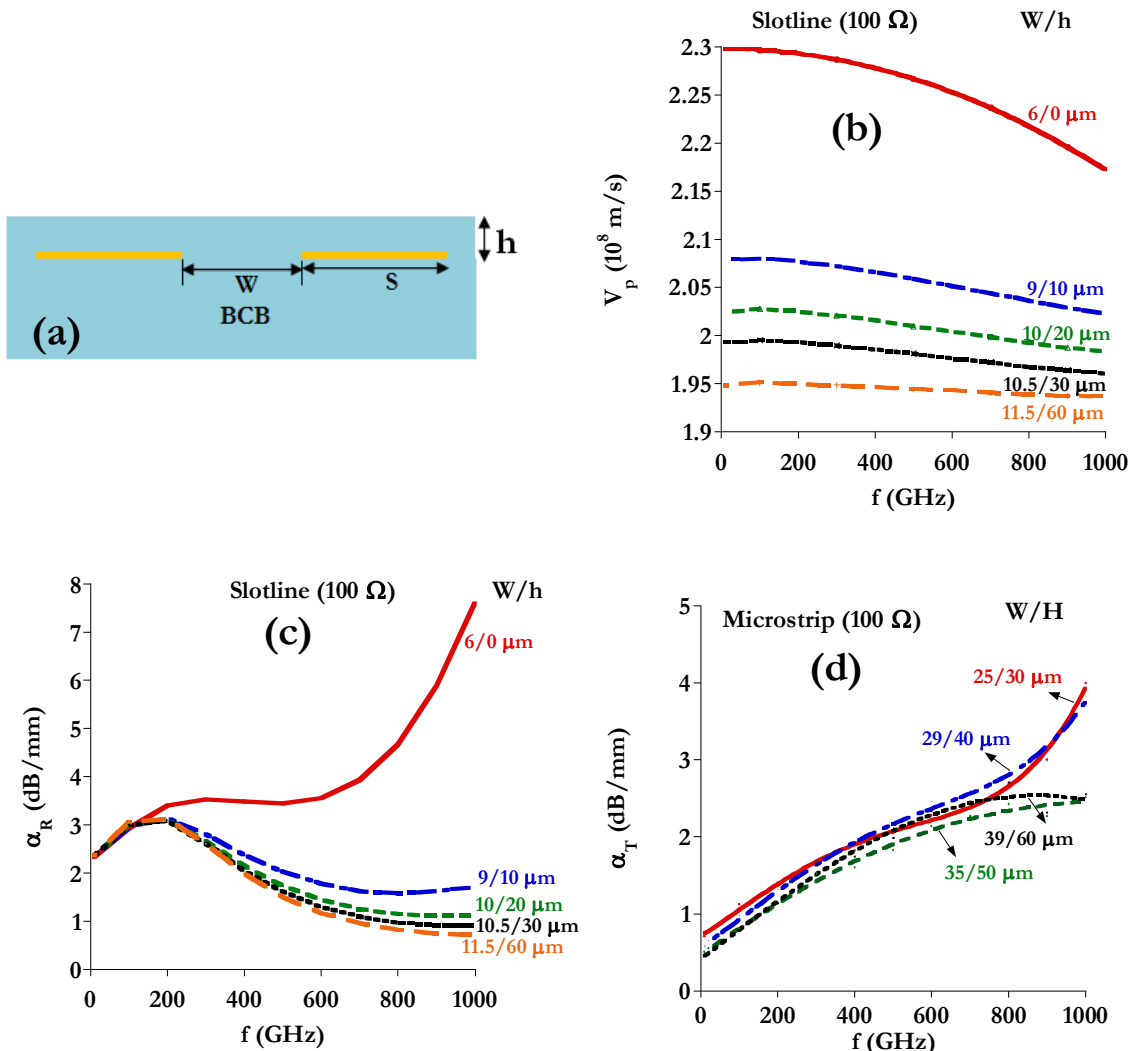


Figure 3-45: (a) Deposition of BCB (thickness h) on top of the slotline. (b) and (c) are the phase velocity and radiation loss of slotline at 100Ω with different combinations of W and h . (d) is the total losses of microstrip at 100Ω with different combinations of W and H

In slotline at 100Ω , only one parameter (W) can be changed. To add an adjustable parameter, a layer of BCB with a thickness of h is deposited on top of the structure (Figure 3-45 (a)). This step is feasible in the fabrication for the polymer BCB, while it is difficult for semiconductor material. Thick BCB (large value of h) helps to confine the EM field at the side of dielectric, particularly at high frequency (> 200 GHz). Thus, the dispersion of the phase velocity and the radiation loss become weak, shown in Figure 3-45 (b) and (c). At $H = 60 \mu\text{m}$, the radiation (total) losses are reduced from 7.63 (9.6) dB/mm to 0.7 (3.49) dB/mm at 1 THz. The radiation loss is comparable to the dielectric loss and the total losses are lower than those in microstrip at 1 THz. Results presented in Figure 3-45 (c) have to be taken with care. Such a reduction of radiation losses at high frequency requires at least further investigation.

However, the losses in microstrip at 100Ω can also be optimized via the different combination of the metal width (W) and BCB thickness (H), shown in Figure 3-45 (d). At $W = 35 \mu\text{m}$ and $H = 50 \mu\text{m}$, the total losses are lowered from 4 dB/mm to the optimal value of 2.52 dB/mm at 1

THz. This result is considered as the compromise among all the three types of loss (radiation, conduction and dielectric loss) because they are close and comparable (Table 3-4).

3.6.4 Conclusions

Assuming the same characteristic impedance (100Ω), dispersions and losses properties have been compared among the four types of waveguides on BCB.

Microstrip with BCB substrate seems as the best transmission line in the frequency range [10-1000] GHz. Stripline are not too far in term of attenuation and it possesses the unique advantage: non dispersive nature (TEM) and zero radiation loss. If the conduction loss can be decreased, CPW (BC) will also be attractive. Slotline and CPW (BC) is not suitable for THz transmission for a distance above 1 mm according to Figure 3-43. However, their performances can be improved further by choosing properly the geometrical dimensions of the metal, the gap or the dielectric thickness.

It should be noted that these quantitative results and conclusions are only based on the selected criteria. Waveguides on other substrates and dimensions may show different results.

3.7 Transition design, sample fabrication and measurements

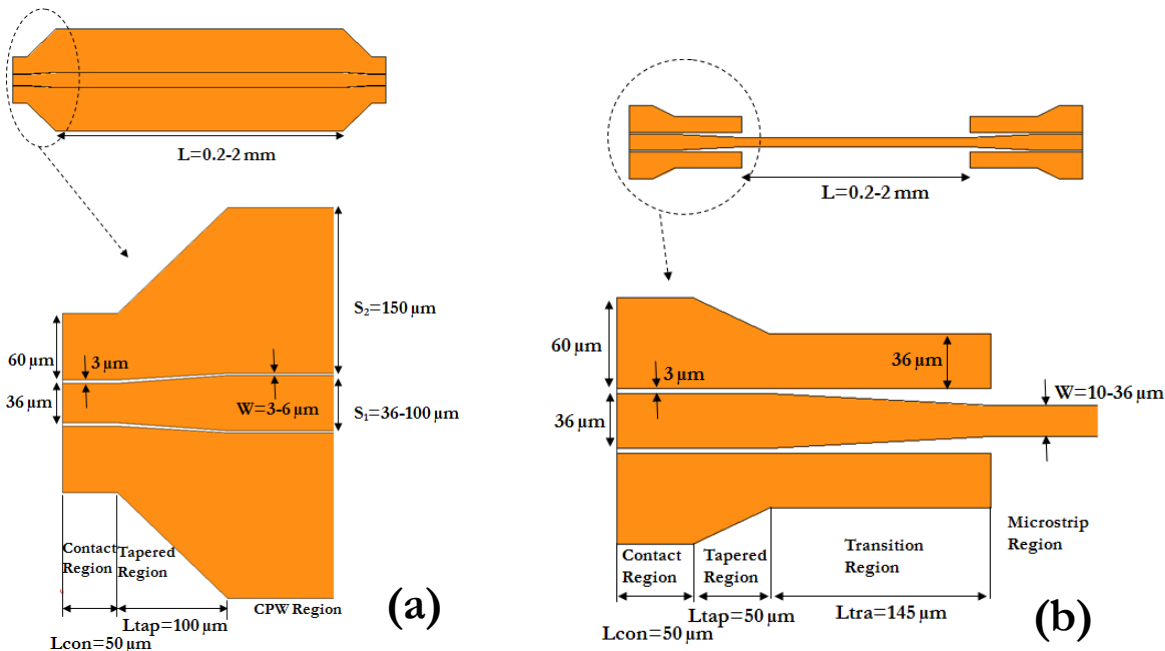
In order to validate the simulation results of planar waveguides with HFSS, experiments have been completed in the submillimeter frequency range [325-500] GHz with a vector network analyzer at the Fraunhofer Institute for Applied Solid State Physics (IAF at Freiburg, Germany). Propagation constants of four lines (conventional and conductor backed CPW, and Microstrip) on BCB film deposited on Si substrate have been measured. Both the sample fabrication technologies in the clean room and the de-embedding methods for extracting the line performances will be explained in the next sections. The stripline and slotline have not been measured.

3.7.1 Design of coupling transitions

Standard 50Ω CPW structure adapted to the 50Ω network analyzer is used to excite the corresponding waveguides under test. For efficient power coupling, specific via-less transitions should be carefully designed to smooth the impedance mismatch between the external CPW and internal lines. Table 3-5 lists the line dimensions prepared for experiments. For CPW, the first three dimensions ($(S_1, W) = (36 \mu\text{m}, 3 \mu\text{m}), (70 \mu\text{m}, 4.28 \mu\text{m})$ and $(100 \mu\text{m}, 6 \mu\text{m})$) have a characteristic impedance around 50Ω at 20 GHz, according to HFSS results of CPW on BCB. The last two CPW structures are employed to evaluate the influence of gap width (W) on the attenuation at a constant central metal width (S_1). The ground plane width is fixed at $S_2 = 150 \mu\text{m}$. For microstrip, the width of signal line is the only parameter to be varied: $W = 10, 20$ and $36 \mu\text{m}$. The line length L for all the three kinds of waveguides has four options: 0.2, 0.5, 1 and 2 mm. To achieve high coupling efficiency, we adopt different forms of transitions depending on the line type and geometry. Their transitions are illustrated in Figure 3-46.

Table 3-5: Dimensions of CPW and Microstrip

Width (μm)	CPW ($S_2 = 150 \mu\text{m}$)					Microstrip
S_1	36	70	100	36	36	$W=10, 20 \text{ and } 36 \mu\text{m}$
W	3	4.28	6	6	10	

**Figure 3-46: Design transitions for (a) CPW-CPW, and (b) CPW-Microstrip. Line dimensions are indicated**

3.7.1.1 Transition CPW-CPW

Due to the same arrangement of metals between the contact region and CPW region, the transition CPW-CPW can be realized easily. Figure 3-46 (a) shows the plan view of CPW with two symmetric transitions at each side of the waveguide. The dimensions of the contact part, on which the G-S-G probe is located, are the same for all lines in Table 3-5 to facilitate the measurement and comparison. A tapered region is used to alleviate the impedance mismatch between the two segments. Its length is chosen to be $L_{\text{tap}} = 100 \mu\text{m}$. The electric field distribution, reflection and transmission properties of a 1 mm CPW line with back-to-back transitions at the ends are shown in Figure 3-47 and Figure 3-48, respectively. Both the losses in BCB ($\tan \delta = 0.007$) and metals ($\sigma_{\text{Au}} = 5 \cdot 10^6 \text{ S/m}$) are included in the calculation. The majority of EM energy propagates through the two gaps regions and a small part extends to the outer open substrate region.

The power reflection coefficient S_{11} is maintained at least 15 dB ($-20 \log |S_{11}|$) in the anticipated experimental frequency range (325-500 GHz). Transmission coefficient S_{21} with the two transitions is below 6 dB ($-20 \log |S_{21}|$). The insertion losses of the contact region and contact region plus the tapered regions depending on CPW dimensions are shown in Figure 3-48 (b).

Each contact has losses less than 0.2 dB and the contact plus tapered parts contribute to additional attenuation below 2.7 dB.

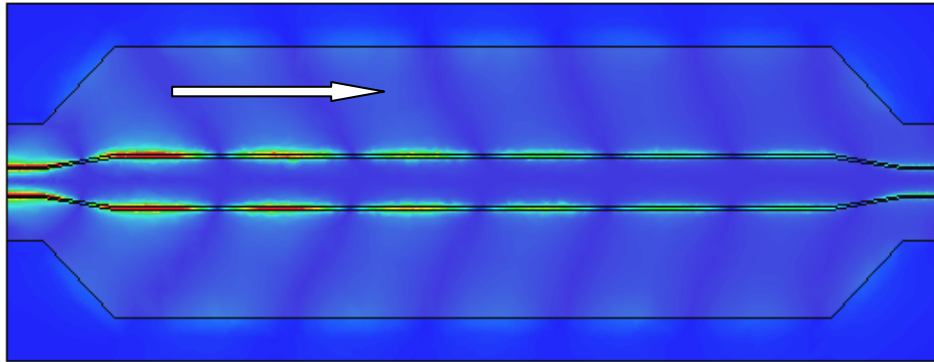


Figure 3-47: Electric field distribution along the propagation direction (white arrow) for 1 mm length of CPW ($S_1 = 70 \mu\text{m}$) with transitions at two ends

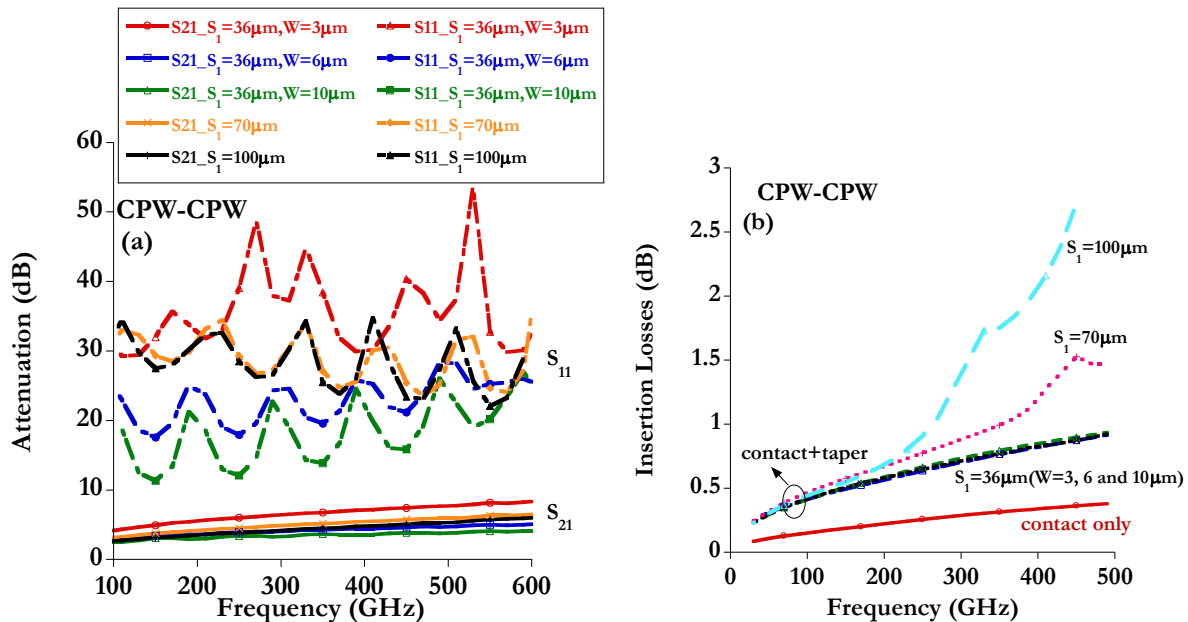


Figure 3-48: (a) Reflection (S_{11}) and transmission (S_{21}) of a 1 mm CPW with two transitions at both ends, and (b) Insertion losses in different sections of a transition (Figure 3-46 (a))

3.7.1.2 Transition CPW-Microstrip

From the side of experimental investigation of microstrip, coaxial transmission line and the CPW structure are the common methods to excite the microstrip mode. Coaxial line excitation does not apply easily in this planar structure. This excitation often requires via/holes through microstrip substrate to connect the ground planes, which introduces the fabrication difficulties. Some methods without via/holes have been proved experimentally to work at frequencies below 100 GHz [Wang2006]. In these approaches, carefully designed transition region and CPW ground plane shapes [Gauthier1998] are prerequisite conditions for efficient coupling. The via-less transition CPW to microstrip is presented in Figure 3-46 (b), as use in [Gauthier1998] for W-band measurements (70-120 GHz). The length of transition is set at $L_{tra} = 145 \mu\text{m}$, corresponding

approximately to one quarter of the guided wavelength at 400 GHz. Figure 3-49 shows the mode coupling from CPW mode to dominant mode in microstrip. Simulation results in Figure 3-50 (a) show a minimum reflection of 10 dB and a maximum transmission attenuation of 5 dB. The insertion losses of the different parts in one transition are shown in Figure 3-50 (b). Each contact has losses less than 0.2 dB and the contact plus tapered parts contribute to additional attenuation below 0.5 dB. The whole transition can introduce a loss less than 2.3 dB. The resonances at 410 GHz are due to the formation of parallel plate mode in the simulation.

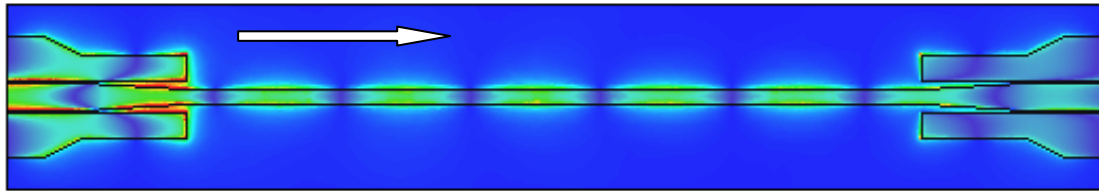


Figure 3-49: Electric field distribution along the propagation direction (white arrow) for 1 mm length of Microstrip line ($W = 20 \mu\text{m}$) with transitions at two ends

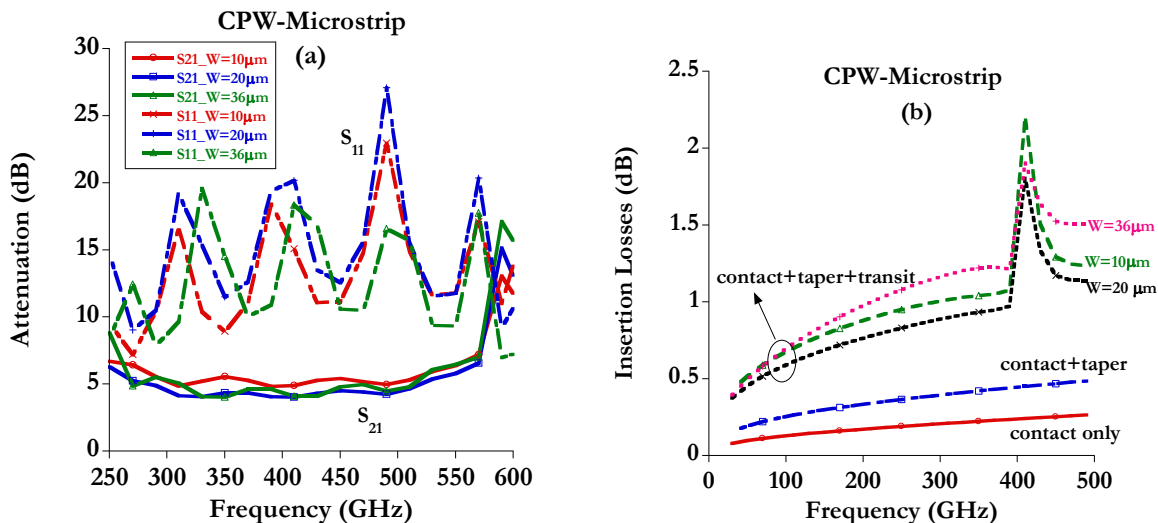


Figure 3-50: (a) Reflection (S_{11}) and transmission (S_{21}) of a 1 mm Microstrip line with two transitions at both edges, and (b) Insertion losses in different sections of a transition (Figure 3-46 (b))

The mask contains different lengths of waveguides and their corresponded open and (or) short circuits (Figure 3-51) for the follow-up de-embedding task. Region A contains the short and open circuits of the contact region for probes. Region C and B are the CPW lines and the short circuits of CPW, respectively. Region E and D correspond to Microstrip lines and their open circuits.

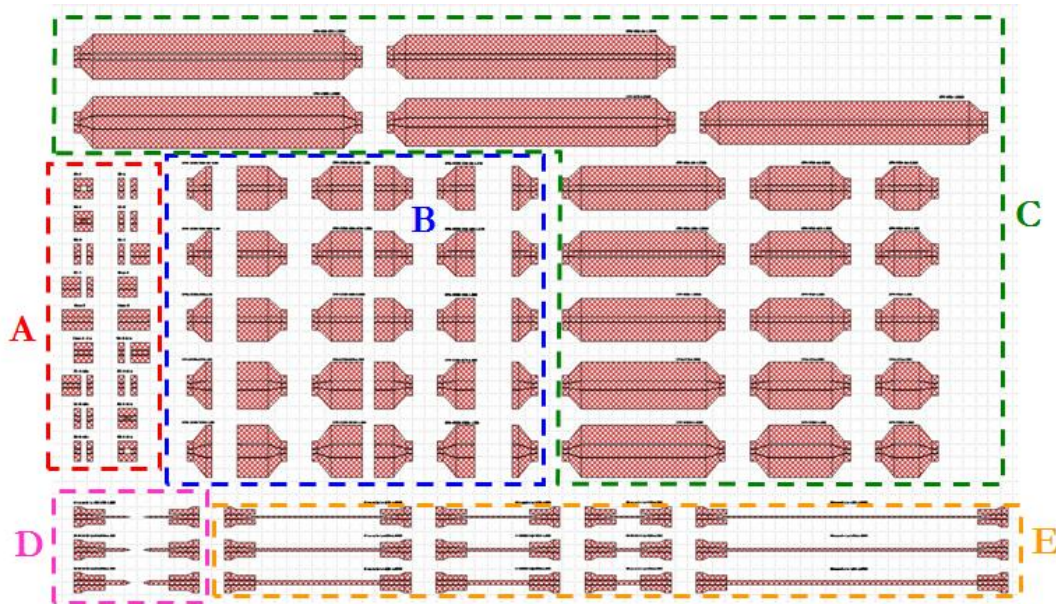


Figure 3-51: Arrangement of waveguide motif centered on a 2 inch silicon wafer

Different technological procedures have been developed to realize the waveguides on thin or thick BCB.

3.7.2 Technologies of sample fabrication

The fabrication process with conductors below the dielectric BCB (conductor backed CPW and microstrip lines) is complicated when compared with conventional CPW. Moreover, the manufacture process begins on a 2 inch silicon wafer (resistivity is [1-20] ohm-cm). To reduce the dielectric losses, BCB layer should be as thick as possible to avoid the EM field penetrating into the lossy silicon wafer. According to the product data of CYCLOTENE 3022-63 dry etch resin (BCB) provided by Dow Company (<http://www.dow.com/cyclotene/prod/302263.htm>), multiple times of deposition are needed to achieve a thickness of BCB higher than 30 μm . Finally, BCB does not have a good connection quality with most conducting metals, such as gold and aluminum. Special technique will be employed to accomplish this requirement.

Here we describe in detail the mains procedures (see Figure 3-52) for realizing the planar waveguides on thick BCB ($> 60 \mu\text{m}$), where a layer of gold conductor is present between BCB and the silicon wafer.

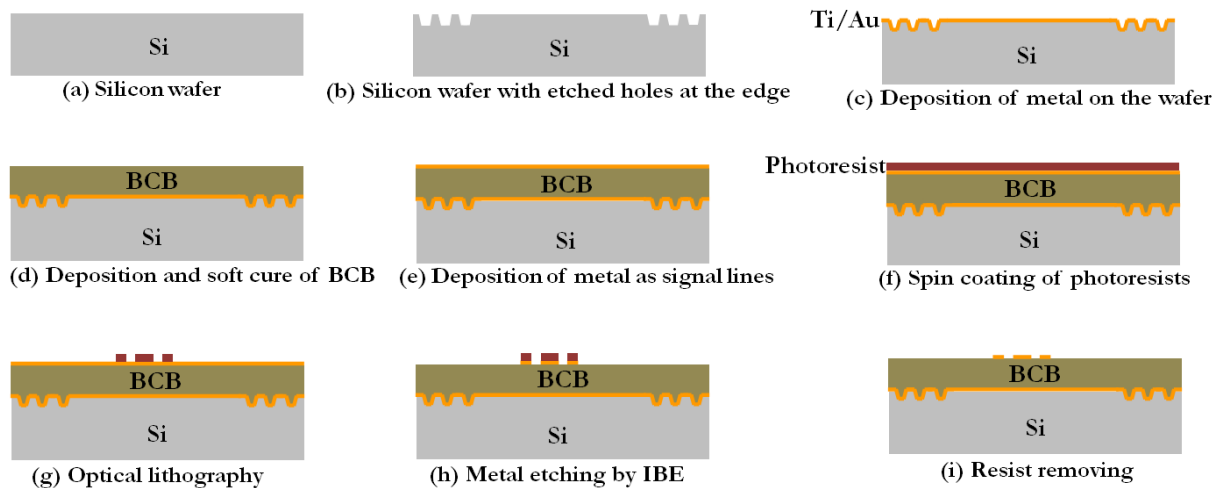


Figure 3-52: Flow chart for realization of waveguide on thick BCB with an underlying conductor layer on silicon wafer. Procedure details are described in the text

(a)-(b) Formation of holes in Si wafer

In order to improve the adhesion of BCB with the underlying metal layer, periodic holes are etched at the periphery of wafer. The step (b) can increase the contact area and make the deposition of thick BCB possible. As the waveguides locate at the center of wafer, the influences of holes on their performances are negligible.

1.3 μm photoresist Shipley S1813 from Microposit is spin coated onto the wafer. The center region of wafer is isolated from the UV beam in the optical lithography process (double-sided mask alignment system from EV group, <http://www.evgroup.com/en>). The pattern of periodic circles (10 μm diameter and 20 μm center-to-center distance) is formed at the outer 1/4 radial region. Silicon is etched at the temperature 10°C by Inductively Charged Plasma (ICP) from STS system. To achieve high etching anisotropy and high aspect ratio structure, alternating etching (SF_6) and passivation (C_4F_8) processes are used for deep silicon etching, as listed in Table 3-6. The total time is 4 minutes and the hole depth is about 10 μm .

Table 3-6: Etching and passivation processes for deep holes in silicon by ICP

	C_4F_8 (sccm)	SF_6 (sccm)	O_2 (sccm)	Pressure (mTorr)	Power (W)	Time (s)
Passivation	200	0	0	5	1500	2
Etching	20	450	45	5	2200	4

(c) Evaporation of Ti/Au on Si as the underlying conductor

Electron beam evaporation of metal layer is conducted by PLASSYS system. An adhesion layer of titanium (thickness is 10 nm, and speed is 0.1 nm/s) is used before the deposition of gold (thickness is 500 nm, and speed is 0.2 nm/s), the same thickness as in the simulations.

(d) Deposition and soft cure of thick BCB

The polymer BCB used is non photosensible, and is a part of the series CYCLOTENE 3022-63 provided by Dow Chemical Company. From the tutorial available on the Dow chemical website, a 30 μm thick BCB can be achieved at a spin speed of 700 rpm after soft cure. Two successive depositions are needed to reach the wanted thickness ($>60 \mu\text{m}$).

The adhesion promoter AP3000 from the same company is employed as the adhesion layer between Au and BCB. Then the first layer of BCB is deposited followed by a bake on a hotplate to remove solvents and avoid material flow during subsequent handling. The sample is baked for 5 minutes at 90°C. Finally, the soft or partial cure of BCB is designed to reach a 75-82% polymerization useful for multilayer structures. Table 3-7 gives the soft cure process of BCB in the oven filled with nitrogen (N_2) flux.

Table 3-7: Soft cure of BCB

Step No.	Temperature /Ramp Time	Time (min)
1	50°C/5min	5
2	100°C/15min	15
3	150°C/15min	15
4	210°C/60min	40
5	Natural cooling to environment temperature	

The second layer of BCB is deposited after the soft cure. The processes of bake and cure are reproduced for the second layer. A verification of the sample profile with electron beam microscopy shows that there is no evident boundary existing at the two adjacent BCB layers, as shown in Figure 3-53.

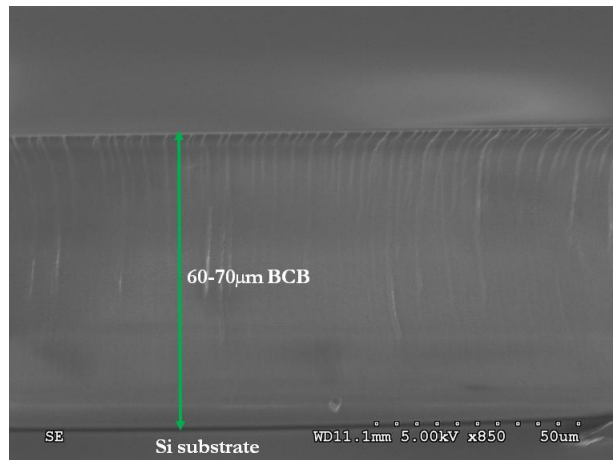


Figure 3-53: Scanning electron microscopy (SEM) image of thick BCB (60-70 μm) deposited on Si substrate

(e) Evaporation of Ti/Au on BCB as the signal lines and hard cure of BCB

As in (c), Ti(10 nm)/Au(500 nm) is evaporated on cured BCB to realize the planar waveguides from the designed mask. The hard cure is carried out as final cure to achieve 95-100% conversion

of BCB after all the polymer layers and conductor layers have been completed. Table 3-8 resents the hard cure process of BCB in the N₂ gas filled oven.

Table 3-8: Hard cure of BCB

Step No.	Temperature /Ramp Time	Time (min)
1	50°C/5min	5
2	100°C/15min	15
3	150°C/15min	15
4	250°C/60min	60
5	Natural cooling to environment temperature	

(f)-(h) Spin coating of resist and Au etching

The Au layer is covered by the resin S1813 and patterned by optical lithography. Then it is etched by the system IonSys 500 from Roth & Rau Group. Inert gas Ion Beam Etching (IBE) is conducted in 2 minutes at -10°C and followed by 1 minute of cooling to avoid the overheat of metal and to maintain the good adhesion between BCB/Au. The alternating processes are repeated 6 times to finish the etching of 500 nm Au. Table 3-9 gives the IBE parameters.

Table 3-9: Au etching by IBE

Power (W)	Beam Voltage (V)	Ar (sccm)	Pressure (mbar)	Temperature (°C)
350	300	1.5	2.2×10 ⁻⁴	-10

(i) Removing the resist

The photoresin left on the waveguide lines after the Au etching process is removed by dry etching in plasma O₂ for 5 minutes (power is 160 W and pressure is between 0.6 and 0.8 mbar). It should be noted that the resin can also be removed by acetone combined with ultrasonic cleaning, however, long time ultrasonic wave perhaps makes the adhesion between BCB and underlying Au layer weak. So the dry etching method is recommended.

The procedure for realizing waveguides on thin BCB (for example, 30 μm) and/or without underlying conductor layer can be slightly modified according to the above general descriptions in Figure 3-52.

Figure 3-54 shows the images of waveguide on 30 μm BCB without underlying Au layer and on 60 μm BCB with the existence of underlying Au layer. The right images represent the enlarged part of the ensemble of waveguides centered on the wafer (within solid white circle). The region where there are no holes in silicon wafer is indicated in Figure 3-54 (b) as be within the dashed white circle. The yellow color seen in Figure 3-55 (b) is attributed to the underlying Au layer because the BCB is over 90% transparent to visible light.

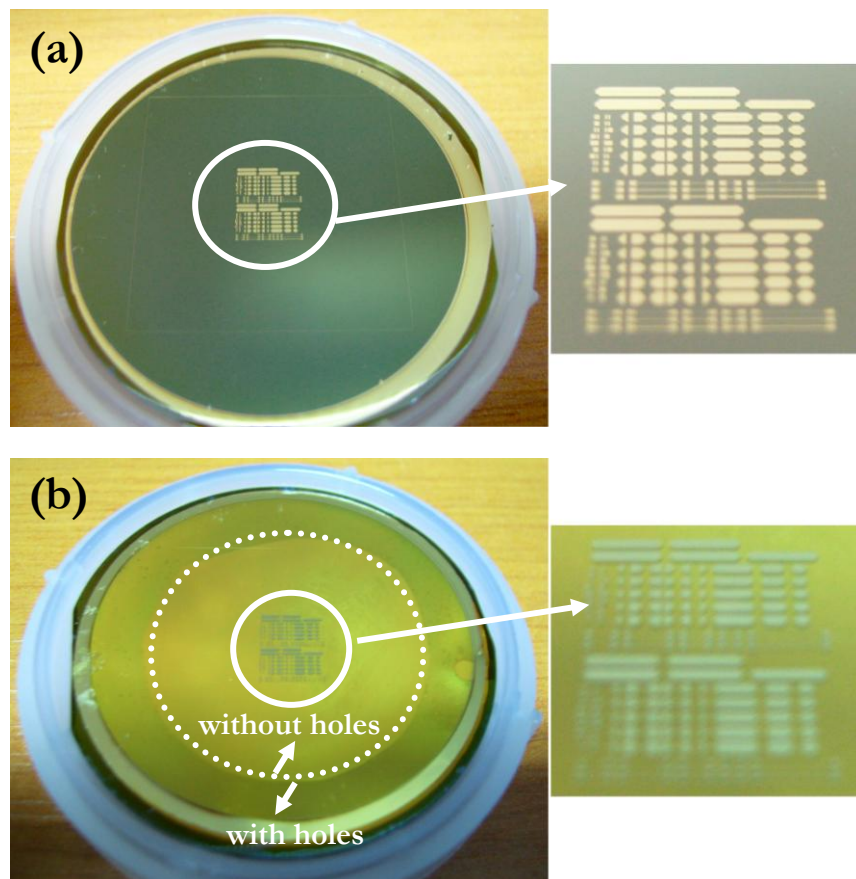


Figure 3-54: Optical microscopy images of wafer after the removal of photo resist: (a) Waveguides on thin BCB without underlying Au layer, (b) waveguides on thick BCB with underlying Au layer. The enlarged part corresponds to the designed waveguides

3.7.3 Measurements results in the frequency range [340-500] GHz

The on-wafer measurement was carried out by means of a vector network analyzer (VNA) Agilent PNA-X in [325-500] GHz at Fraunhofer Institute for Applied Solid State Physics (Fraunhofer IAF) in Freiburg (Germany). G-S-G pitch (tip spacing) is 60 μm , which matches the contact region designed on the mask. To remove repeatable errors from the VNA, probe losses and reflections, calibration was conducted by the Thru-Reflect-Line (TRL) technique [Engen1979] on an alumina substrate (ISS 138-356) from Cascade Microtech Company. A recent review of calibration methods for planar electromagnetic structures can be found in [Wu2005].

The method for extracting the complex phase constant of CPW lines are introduced in the following part.

3.7.3.1 De-embedding technique by using ADS

I Choice of de-embedding

In order to exclude contributions of unwanted portions (contact/tapered/transition parts) of the structure from the measured data, a de-embedding step is required. The common de-embedding methods in microwave frequency are based on mathematically cascade matrix manipulation, such as short-open [Zhu2002-1], short-open-load-thru (SOLT) [Zhu2002-2] and TRL techniques. The

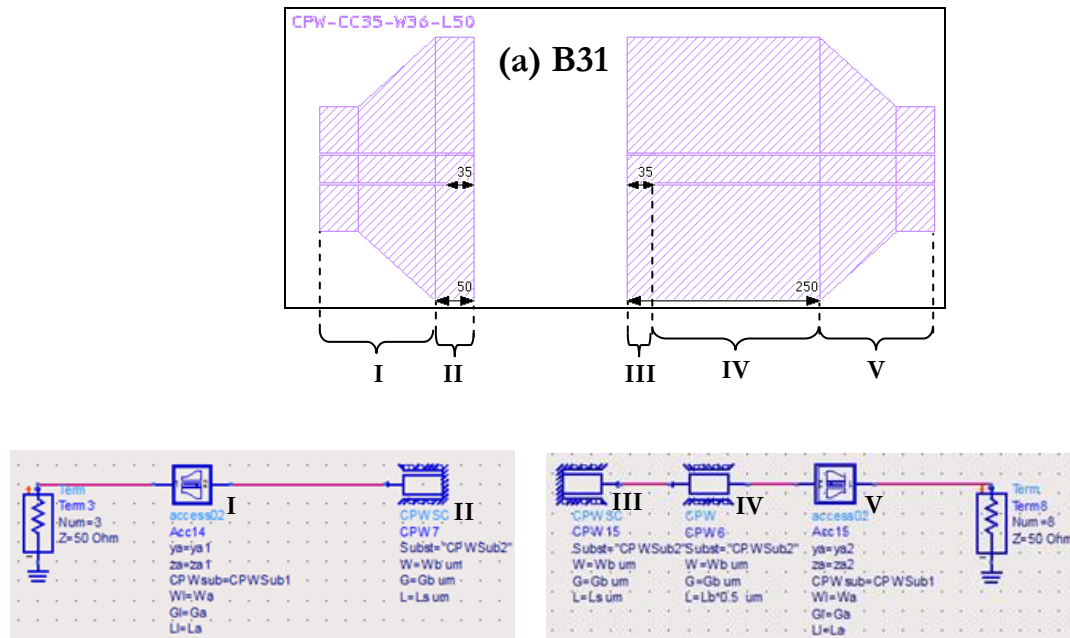
accuracy of these methods depends critically on the sensitivity of structure fluctuations and measurement errors. For all the waveguides under test in this section, the de-embedding has been done in ADS, where the standard electrical models (lumped impedance/admittance, CPW and conductor backed CPW) are used to mimic the electrical behavior of transitions and the waveguides. Direct comparisons between measurements and simulations can be done with ADS to facilitate the optimization. The main drawback of this method is the difficulty to find an appropriate electrical circuit model.

II De-embedding procedures with ADS

In this part, we describe the different steps of de-embedding by ADS. The reference structure of 50Ω CPW ($S_1 = 36 \mu\text{m}$, $W = 3 \mu\text{m}$) is used to illustrate the de-embedding method, knowing that CPW with other dimensions can be treated with the same approach.

A Electrical model of the transition

Figure 3-55 shows the "offset" short circuited CPW with different lengths at left and right sides: B31 (left/right length = $50 \mu\text{m}/250 \mu\text{m}$), B32 (250 $\mu\text{m}/150 \mu\text{m}$) and B33 (150 $\mu\text{m}/50 \mu\text{m}$). The length of all the short circuited part is 35 μm . ADS circuit model of different parts (I, II, III, IV, and V) is described in the following. The interactions of different parts (from I to V) are neglected in the ADS model.



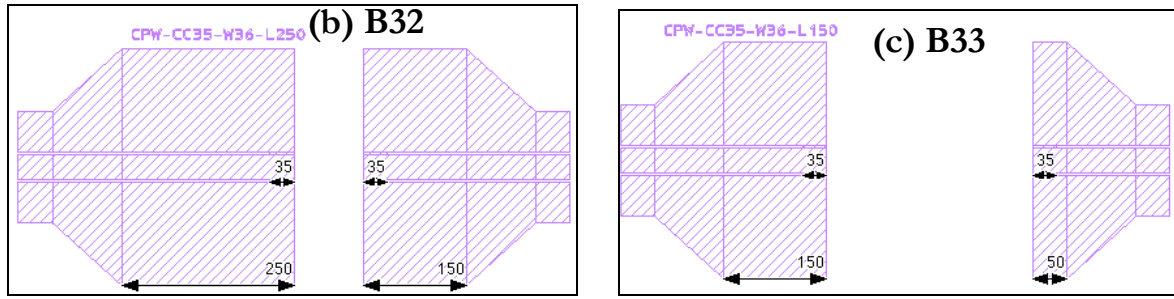


Figure 3-55: Short circuited CPW ($S_t = 36 \mu\text{m}$, $W = 3 \mu\text{m}$) for de-embedding (length of the short circuited part = $35 \mu\text{m}$) and the equivalent electrical circuit model of B31 (left length = $50 \mu\text{m}$, right length = $250 \mu\text{m}$)

(1) Part I and V: contact/access regions

They are modeled via a π network connected in series with a CPW model, as shown in Figure 3-56. This network is composed by a frequency dependent (3rd order) complex serial impedance (Z) and two parallel admittance (Y) as in [Heuermann1999, Ito2008] normalized by the standard 50Ω resistance:

$$Z = 50 \left[zr_0 + zr_1(f - f_0) + zr_2(f - f_0)^2 + j(z_i_0 + z_i_1(f - f_0) + z_i_2(f - f_0)^2 + z_i_3(f - f_0)^3) \right] \quad (3-24)$$

$$Y = 0.02 \left[yr_0 + yr_1(f - f_0) + yr_2(f - f_0)^2 + j(yi_0 + yi_1(f - f_0) + yi_2(f - f_0)^2 + yi_3(f - f_0)^3) \right] \quad (3-25)$$

Where f is the frequency, $f_0 = 400 \text{ GHz}$ (center frequency in measured data) and j is the imaginary unit. To account for the asymmetrical probe position in the measurement, the coefficients of the real (zr_0 , zr_1 and zr_2) and imaginary part (z_i_0 , z_i_1 , z_i_2 and z_i_3) of Z can be varied independently between part I and V. This is also true for the coefficients of real and imaginary part of Y .

In ADS, the substrate properties (thickness H , permittivity ϵ_r , loss tangent $\tan\delta$), metal conductivity (C_d) and structural dimensions (Central metal width W , gap width G , and length L) of CPW have to be fitted on measured data (optimization). The model used for Part I is also applied for the part V.

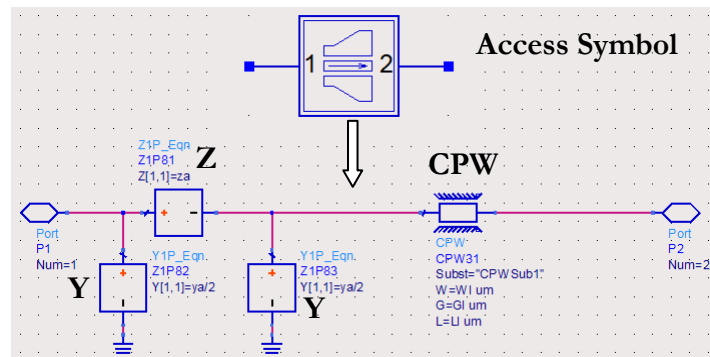


Figure 3-56: Electrical model and symbol of the access region for CPW structure

(2) Part II and III: short circuited CPW line at one end (50 μm length)

A corresponding short circuited CPW model is used. The substrate properties (H , ϵ_r and T_{and}) and line dimensions (W , G and L) are varied independently from the part I. The right part of B33 follows the same model as the left part of B31.

The short circuited part at the right of B31 owns a longer length (250 μm) and it is considered as the independent combination of a 50 μm short circuited CPW (III is the same as II) and a 200 μm homogeneous CPW line (IV). For the latter, the line dimensions (W , G and L) are optimized independently. The same treatment applies in the left part of B32.

The measured reflection data S_{11} and S_{22} of B31-B33 are used in the fitting process, while the small transmission S_{12} and S_{21} (< -25 dB) is omitted.

B Electrical model of CPW line with transitions

The electric model of 1 mm CPW line is illustrated in Figure 3-57. Its left and right transitions (contact region and tapered region) are as the same as in Figure 3-56. The central homogeneous CPW line is represented in the same way as the part IV in Figure 3-55, because they have the same dimensions (S_1 and W). Its length L is optimized between 0.9 and 1.1 mm around 1 mm to take account of the fabrication errors. Other CPW lines (500 μm and 2 mm) use the same model as in Figure 3-57. The only difference is the line length L . Ideally, the losses in the line are proportional to the line length. CPW with $L = 200 \mu\text{m}$ is not included in the fitting, because the interactions of two transitions may become important.

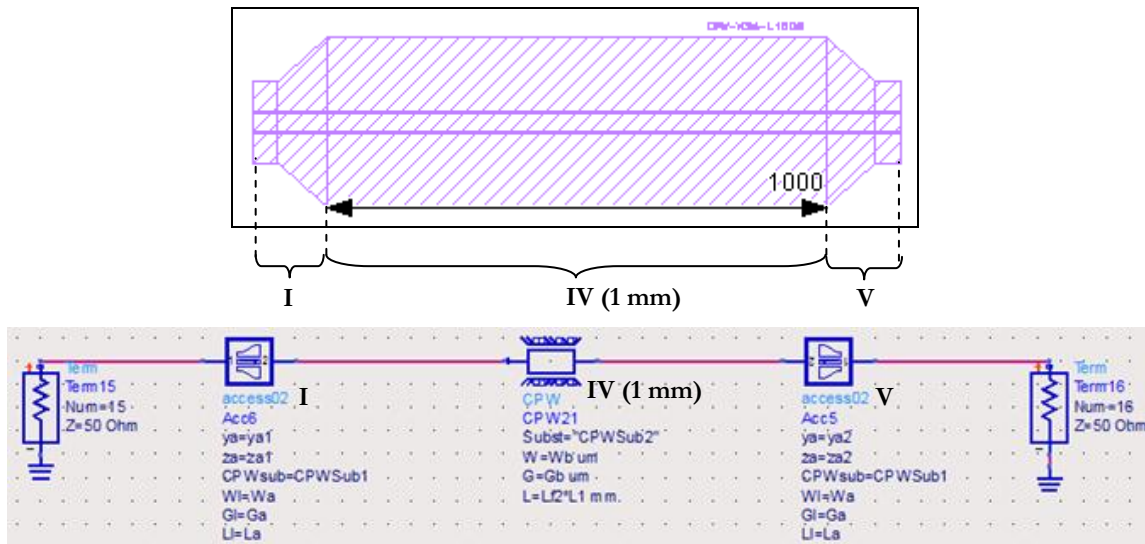


Figure 3-57: 1 mm CPW line ($S_1 = 36 \mu\text{m}$, $W = 3 \mu\text{m}$, $L = 1000 \mu\text{m}$) with two transitions and its equivalent circuit model

C Extraction of the S parameters of the transition

A parametric optimization is conducted **simultaneously** to fit the measurements S parameters (reflection coefficients for B31, B32 and B33, transmission and reflection coefficients for CPW transmission lines). One should verify that the optimized parameters (H , ϵ_r , T_{and} , C_d , W , G and

L) are in the reasonable range, particularly the line lengths. The measurement frequency below 340 GHz is not taken into account due to large noise levels in the experiments.

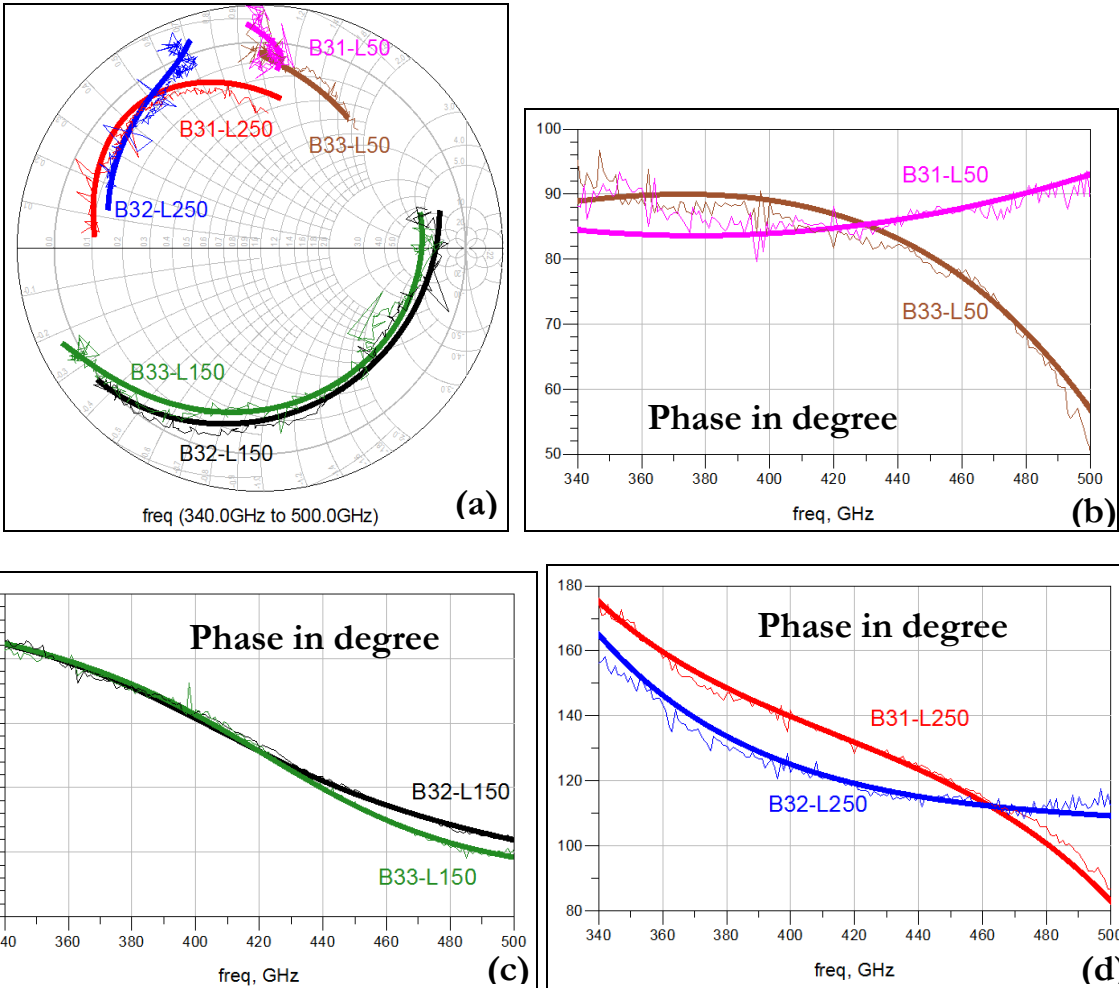


Figure 3-58: Fitting results of the reflection coefficients for the short circuited CPW (B31, B32, and B33). (a) Reflection coefficient in smith chart, phase of 50 μm (b), 150 μm (c) and 250 μm (d) short circuited CPW. The thick smooth curves represent the modeling (modeling and experiment are displayed in the same color). B31-L250 stands for the 250 μm short circuited part in B31. The rest may be deduced by analogy

Figure 3-58 and Figure 3-59 present the fitting results of the three short circuited CPW and three CPW lines in Smith charts. The phase of reflection coefficients for short circuited CPW is also displayed in Figure 3-58. Generally, the employed circuit models well represent the behavior of short circuited CPW. The average value of the absolute difference between the simulated and measured S_{11} (amplitude/phase) is 0.2 dB/3°, 0.5 dB/5° and 0.5 dB/2° for short circuited CPW with length of 50, 150 and 250 μm , respectively. The phase differences between short circuited parts with the same length (for example, B31-L50 and B33-L50) suggest that the probes are not laid symmetrically on the two contacts. For CPW transmission lines at different lengths (Figure 3-59), the transmission (T) behaviors are well simulated, while the reflection (R) coefficients are more difficult to follow. The averaged difference between the simulated and measured S_{21} and S_{11} is 0.3 dB/4° and 2 dB/10° respectively for each line. This is because the reflection coefficient is more sensitive to the probe position in each measurement. To increase the fitting accuracy, more

frequency dependent terms (4^{nd} and high orders) may be included in the impedance (Z) and admittance model (Y) for the contact region.

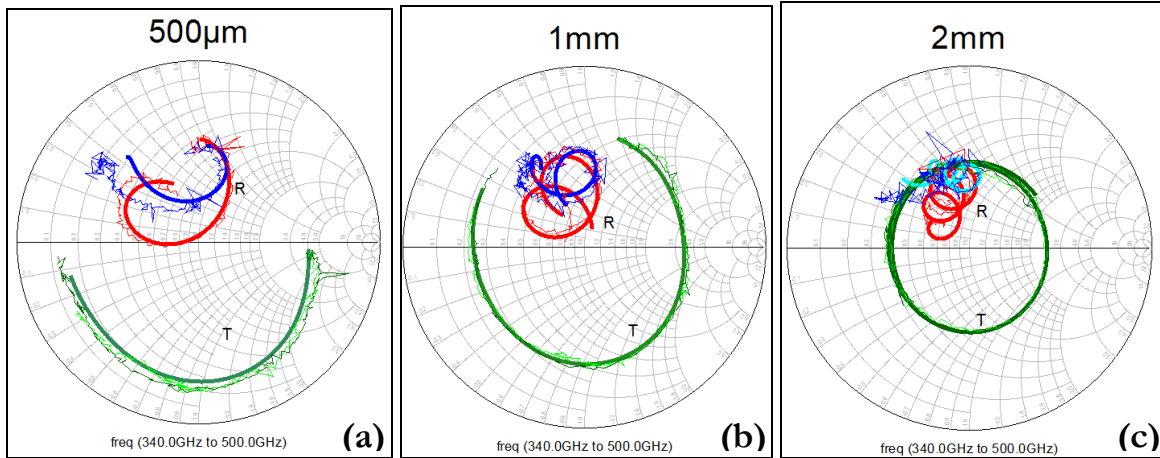


Figure 3-59: Fitting results of the transmission and reflection coefficients of CPW line ($S_1 = 36 \mu\text{m}$, $W = 3 \mu\text{m}$) at different lengths. (a) $L = 500 \mu\text{m}$, (b) $L = 1 \text{ mm}$ and (c) $L = 2 \text{ mm}$. The thick smooth curves represent the modeling (modeling and experiment are displayed in the same color)

D Extraction of the S parameters of CPW line

In order to get the S parameters of the homogeneous CPW, the functions of fitted circuit models I and V in Figure 3-55 are reversed to subtract their contributions in the measured S parameters. Figure 3-60 shows the de-embedding scheme in ADS. -I (-V) represents the reverse circuit of I (V) by replacing the line length to its negative value and by replacing both the impedance and admittance to their negative values.

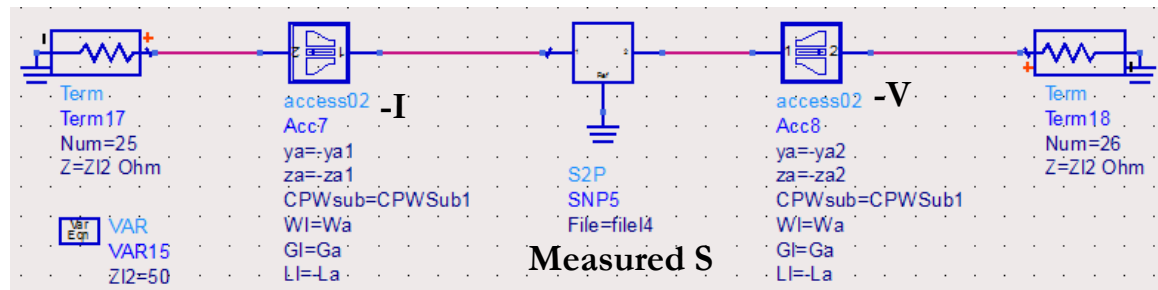


Figure 3-60: Circuit model for extracting the S parameters of CPW line ($S_1 = 36 \mu\text{m}$, $W = 3 \mu\text{m}$) based on measurement results and fitted transition models

The de-embedded S parameters (T and R) of the CPW lines are represented in Smith charts in Figure 3-61. The number of trip for T around the Smith chart is observed to be proportional to the line length: 150° ($L = 0.5 \text{ mm}$), 290° ($L = 1 \text{ mm}$) and 560° ($L = 2 \text{ mm}$).

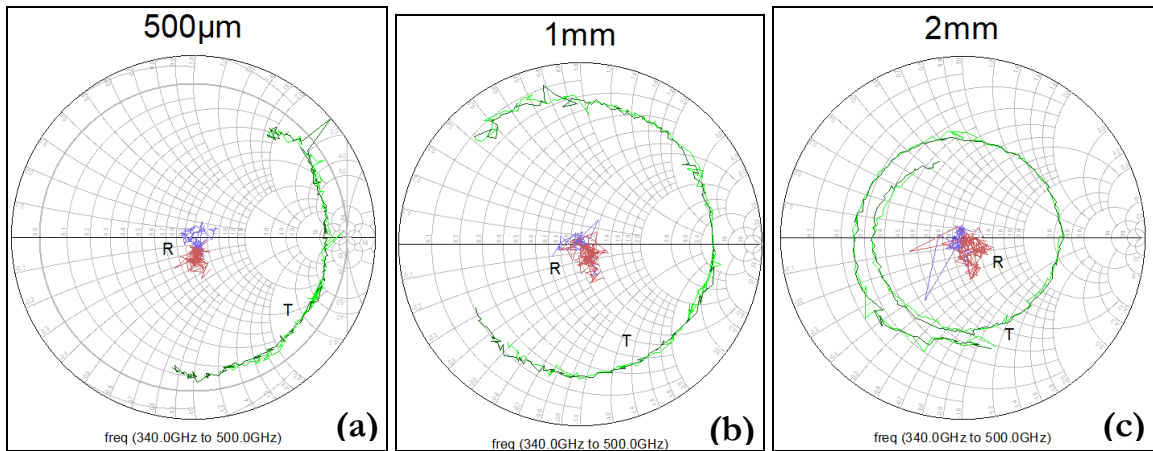


Figure 3-61: De-embedded S parameters of CPW ($S_1 = 36 \mu\text{m}$, $W = 3 \mu\text{m}$) at different lengths. (a) $L = 500 \mu\text{m}$, (b) $L = 1 \text{ mm}$ and (c) $L = 2 \text{ mm}$

E Calculation of the propagation constant of CPW line

Once the S matrix is extracted, the propagation constant $\gamma = \alpha + j\beta$ of the waveguide is given by Nicolson-Ross-Weir (NRW) method [Nicolson1970, Weir1974],

$$\gamma = -\frac{1}{L} \ln\left(\frac{S_{11} + S_{21} - \Gamma}{1 - (S_{11} + S_{21})\Gamma}\right) \quad (3-26)$$

Where the reflection coefficient $\Gamma = \frac{Z_c - Z_0}{Z_c + Z_0} = K \pm \sqrt{K^2 - 1}$ and $K = \frac{S_{11}^2 - S_{21}^2 + 1}{2S_{11}}$. The choice of + and – at each frequency is to ensure: $|\Gamma| < 1$. L is the CPW length.

In the above expression, the characteristic impedance Z_c of CPW can be evaluated directly through S parameters according to [Pozar2004],

$$Z_c^2 = Z_0^2 \left\{ \frac{\left(1 + S_{11}^2\right)^2 - S_{21}^2}{\left(1 - S_{11}^2\right)^2 - S_{21}^2} \right\} \quad (3-27)$$

Where Z_0 is the impedance of the measurement system (50Ω).

The same de-embedding procedures was applied on the others kinds of coplanar waveguides. For the conductor backed CPW, we used the associated electrical model given in ADS library. In next section, the extracted attenuation constant of the five CPW (listed in Table 3-5 with and without backed conductor) will be presented and compared with the simulations performed by HFSS. We will also point out the best CPW transmission line in the millimeter wave range.

3.7.3.2 Measurement results of the BCB THz coplanar waveguide

Up to now, as an initial test for the planar waveguides in millimeter wave frequency, only the de-embedding work of CPW has been finished. For extracting the losses in microstrip, more structures (short and open circuits, longer microstrip lines, etc.) are needed to improve the results

of de-embedding in a follow-up improvement. In this part, we only present the measurement results of CPW.

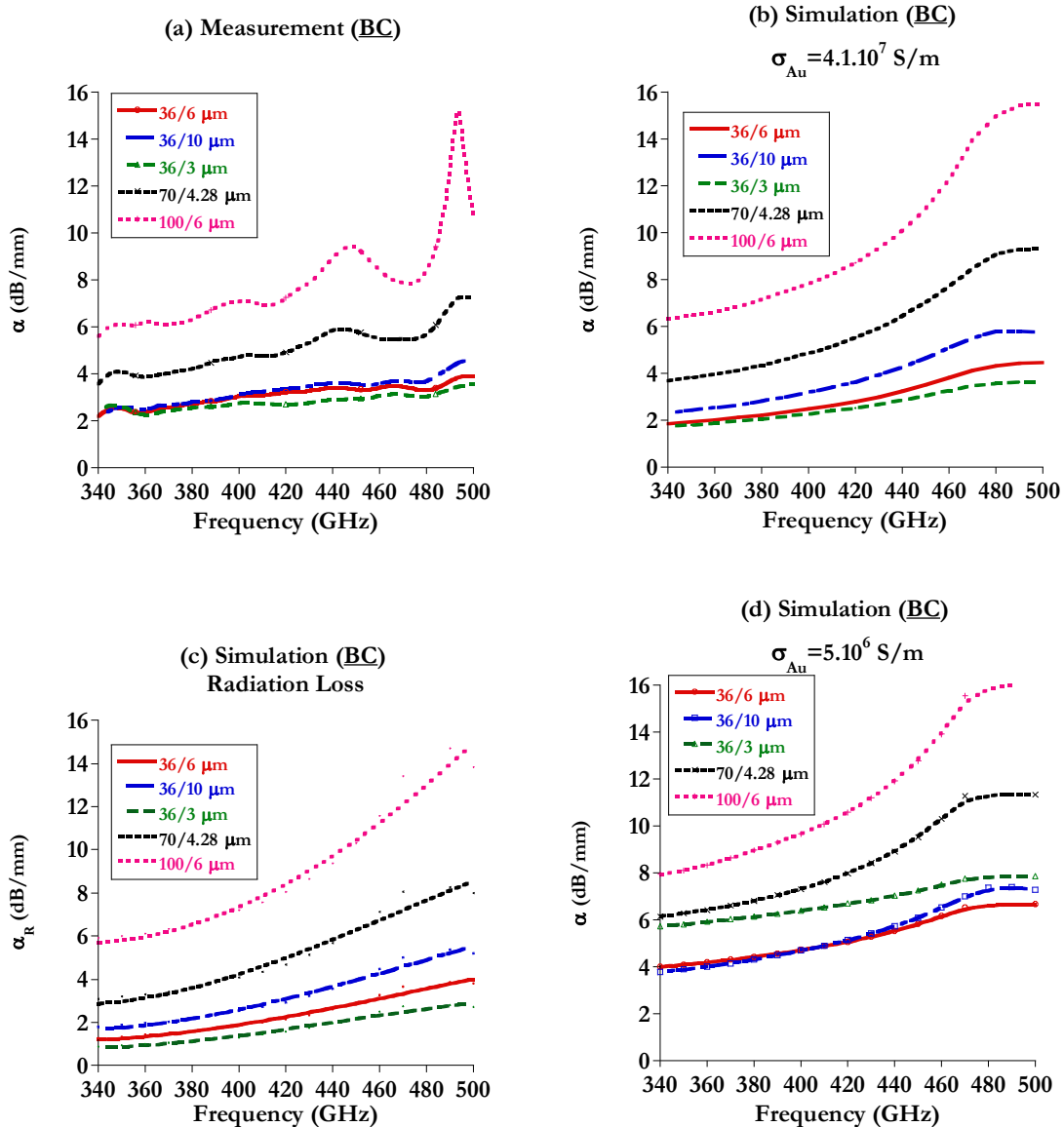


Figure 3-62: (a) Measured and (b) modeled attenuation constant α (dB/mm) of CPW without backed conductor at different dimensions (S_1/W): 36/6, 36/10, 36/3, 70/4.28 and 100/6 μm . Sample: Metal (500 nm)/BCB (~30 μm)/Si substrate (300 μm), Model: $\sigma_{Au} = 4.1 \cdot 10^7$ S/m, $\tan\delta$ (BCB) = 0.007, $\epsilon_{BCB} = 2.42$, 30 μm BCB on semi-infinite Si ($\epsilon_{Si} = 11.9$, $\sigma_{Si} = 10$ S/m). (c) is the calculated radiation loss. (d) is the simulated attenuation with $\sigma_{Au} = 5.1 \cdot 10^6$ S/m

Both conventional and conductor backed CPW have been measured. Figure 3-62 shows the measured and simulated attenuation constant α (dB/mm) of CPW on 30 μm thick BCB. In the simulation results, no fitting parameters are used. For metals: thickness $t = 500$ nm, conductivity $\sigma_{Au} = 4.1 \cdot 10^7$ S/m and $5.1 \cdot 10^6$ S/m. Metal width S_1 ($S_2 = 150$ μm) and gap width W are taken as theoretical values as indicated on the legend of each figure. For dielectric, BCB (permittivity $\epsilon_{BCB} = 2.42$ and loss tangent $\tan\delta = 0.007$) is assumed to be 30 μm on semi-infinite lossy silicon

substrate (permittivity $\epsilon_{Si} = 11.9$ and conductivity $\sigma_{Si} = 10 \text{ S/m}$). The actual conductivity of Si wafer is in the range [5-100] S/m.

As one can observe on Figure 3-62, the losses increase within the frequency range [340-500] GHz. The modeling results in Figure 3-62 (b) agree well with the measured curves of CPW with the five dimensions in Figure 3-62 (a), particularly at the narrow central metal ($S_1 = 36 \mu\text{m}$). At $S_1 = 36 \mu\text{m}$, when the gap width increases from 3 to 10 μm , the attenuation increases. As we can observe, losses follow a quasi cubic frequency law. Because radiation loss plays a major role in total attenuation compared to conduction loss with the high metal conductivity $\sigma_{Au} = 4.1 \cdot 10^7 \text{ S/m}$. This is true for the radiation loss in Figure 3-62 (c). If the conductivity decreases to $5 \cdot 10^6 \text{ S/m}$, the conduction loss in narrow gap CPW ($W = 3 \mu\text{m}$) becomes more important, as shown by the calculated total attenuation in Figure 3-62 (d). Comparing with Figure 3-62 (b), the losses are increased by 2 dB/mm at 340 GHz for all the dimensions. The metal conductivity of the measured conventional CPW can be approximated by a value around $\sigma_{Au} = 4.1 \cdot 10^7 \text{ S/m}$.

Wide central metal ($S_1 > 36 \mu\text{m}$) suffers from large attenuation (16 dB/mm at 500 GHz for $S_1 = 100 \mu\text{m}$) and this is coherent with the fact that radiation losses increases as S_1 and W increase. The fluctuations in the measured data are attributed to the experimental uncertainty at the high frequency side. Concerning the modeling in Figure 3-62 (b), we can remark that for wide metal ($S_1 = 70$ and $100 \mu\text{m}$), the simulation overestimates the attenuation from 400 GHz in comparison with the one measured for the same structure. Firstly, this is probably due to that the conductivity for gold chosen in the modeling is not the optimal value. Secondly, from the fabrication process, the structural dimensions and material properties may deviate from the values chosen for modeling: (1) the gap width cannot be defined exactly due to the resolution limitation (0.2-0.4 μm) in the photolithography. The radiation loss in CPW depends critically on the value of gap width, particularly at wide central width. (2) Metal profile in the propagation direction is inhomogeneous and irregular in the etching process as shown by the optical microscopy images in Figure 3-63. Some gaps (openings) appear both on metals in the access region (maximum depth 0.8 μm) and the CPW part (maximum depth 0.2 μm). Surface roughness also exists. (3) Metal thickness and conductivity may differ from assumed values. This will mainly influence the conduction loss. (4) BCB thickness may be inhomogeneous below the waveguides. The best structure is ($S_1 = 36 \mu\text{m}$, $W = 3 \mu\text{m}$), showing an attenuation of 2.7 dB/mm at 400 GHz and 3.5 dB/mm at 500 GHz.

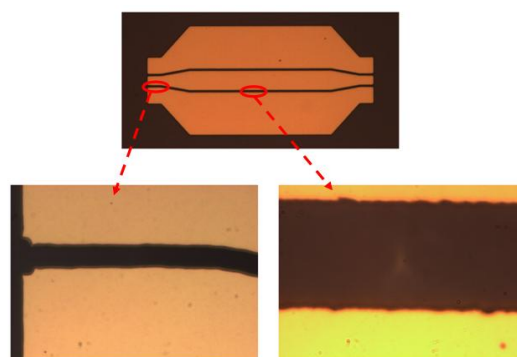


Figure 3-63: Optical microscopy images of a fabricated CPW ($S_1 = 70 \mu\text{m}$, $W = 4.28 \mu\text{m}$, $L = 500 \mu\text{m}$)

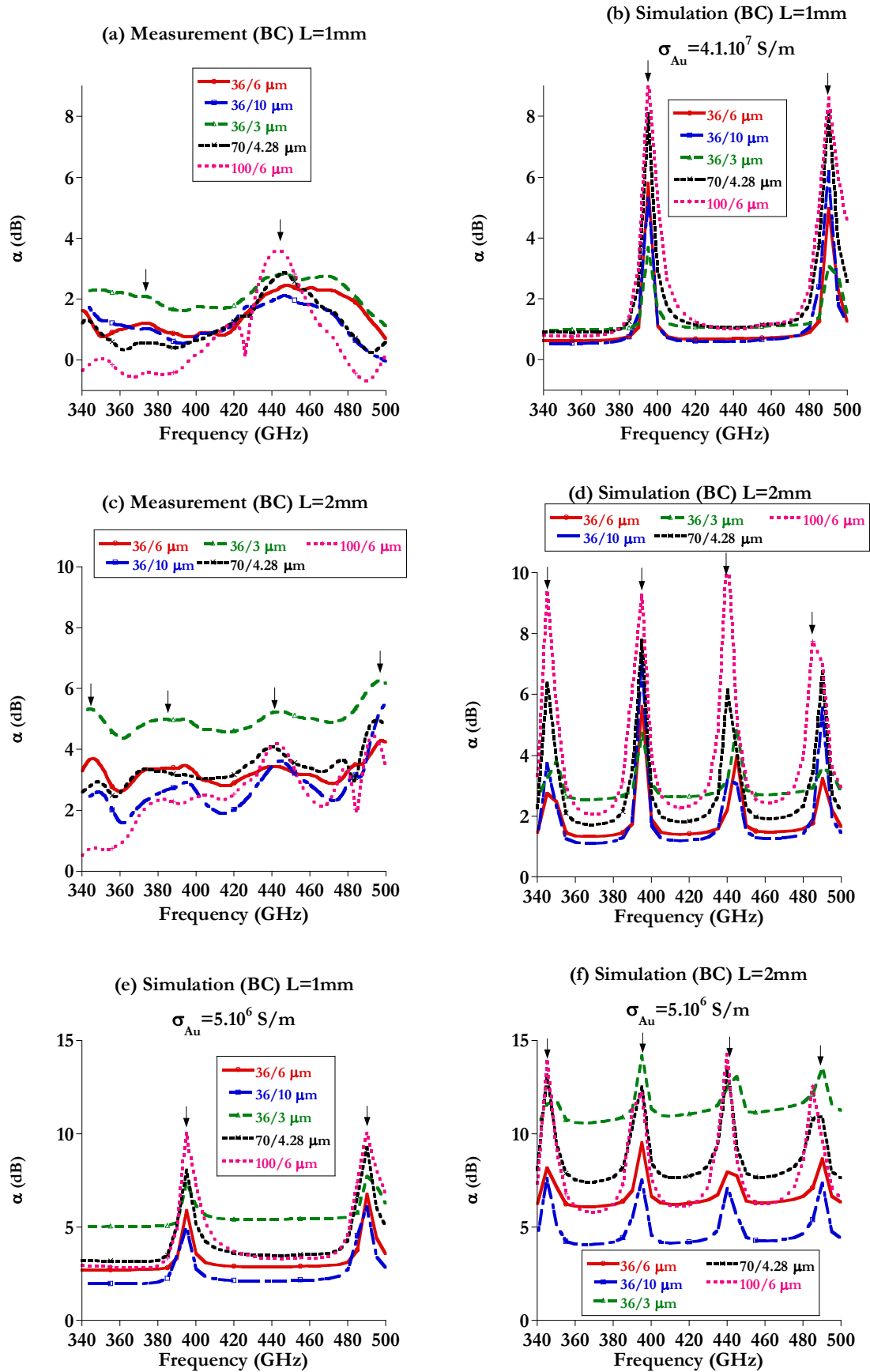


Figure 3-64: Measured (a/c) and modeled (b/d) attenuation constant α (dB) of 1/2 mm CPW with backed conductor at different dimensions (S_1/W) : 36/6, 36/10, 36/3, 70/4.28 and 100/6 μm .

Sample: Metal (500 nm)/BCB (~60 μm)/Metal (500 nm)/Si substrate (300 μm), Model: $\sigma_{Au} = 4.1 \cdot 10^7 \text{ S/m}$, $\tan\delta(\text{BCB}) = 0.007$, $\epsilon_{BCB} = 2.42$, BCB thickness is assumed to be 60 μm . (e) and (f) are the simulated attenuation for a 1 mm and 2 mm conductor backed CPW at $\sigma_{Au} = 5 \cdot 10^6 \text{ S/m}$, respectively

Figure 3-64 compares the attenuation of the 1 mm and 2 mm conductor backed CPW ($> 60 \mu\text{m}$ thick BCB). For $L = 1 \text{ mm}$ in Figure 3-64 (b), two resonances appear at 395 GHz and 490 GHz in the simulated data. As explained before in the parametric numerical study, the resonances are linked to the excitation of parallel plate mode which occurs in this kind of backed structure. In the measurement, the first resonance at low frequency is not pronounced whereas the second one is present at 445 GHz. The latter one is wider (80 GHz in average as width at half height (FWHM)) than the modeled one, whose FWHM is 15 GHz in average. The resonant frequencies in the measured data are lower, because the additional length (150 μm) of the two transitions (absent in the simulation) can cause the decrease of resonant frequency. At $L = 2 \text{ mm}$ in Figure 3-64 (c) and (d), four resonances appear in both the measured and simulated total losses.

In the region without resonances, if we compare the measured attenuation of conventional CPW in Figure 3-62 (a) and conductor backed CPW in Figure 3-64 (a), the losses are reduced apparently with the existence of backed conductor. According to the simulations in the section CPW, the reduction is mainly due to the decrease of radiation loss. In the conductor backed CPW, the total attenuation is dominated by the conduction loss. Indeed, for example, CPW with $W = 3 \mu\text{m}$ shows the largest loss among the three dimensions at $S_1 = 36 \mu\text{m}$. This is further validated in the long CPW. In the region without resonances, the simulated values underestimate the losses. It is probably due to our chosen optimistic value of the metal conductivity used in the modeling which should be slightly higher than the real case. Indeed, the simulations in Figure 3-64 (e) and (f) with low conductivity $\sigma_{Au} = 5 \cdot 10^6 \text{ S/m}$ can remarkably raise the attenuation by increasing the conduction loss. For example, the attenuation in the 1 mm CPW increases from 1 dB to 5 dB. Due to the decrease of radiation loss with backed conductor, the attenuation performances of the wide central metal CPW ($S_1 = 70$ and $100 \mu\text{m}$) are also greatly improved (below 5 dB for a length of 2 mm), as shown in Figure 3-64 (c).

At the resonances, the numerical data present more attenuation than the measured loss. For example, with $S_1 = 36 \mu\text{m}$, $W = 10 \mu\text{m}$, and $L = 1 \text{ mm}$, the resonance is more intense and reaches 6 dB rather than 2 dB obtained experimentally. Thus, the amplitudes of resonances are overestimated in the modeling. However, to summarize, a trade off should be made between the different structures to find the best one. The conductor backed waveguides with $(S_1, W) = (36 \mu\text{m}, 10 \mu\text{m})$ and $(100 \mu\text{m}, 6 \mu\text{m})$ occur as good candidates. The typical attenuations obtained for these structures are below or close to 2 dB/mm up to 500 GHz. But, additional measurements and simulations should be needed to analyze these conductor backed CPW structures.

3.7.4 Conclusions concerning measurement

The transitions CPW-CPW, and CPW-Microstrip have been designed by HFSS in the frequency range [300-500] GHz.

Technologies for realization of thick BCB ($> 60 \mu\text{m}$) on gold layer were demonstrated and samples with CPW and Microstrip have been fabricated in the clean room (CTU/MINERVE) at IEF.

De-embedding technique based on electrical models in ADS was shown to extract the S parameters of CPW at different lengths. Complex phase constant and characteristic impedances were calculated based on S parameters. Preliminary measured results show that the conductor backed CPW can reduce greatly the line attenuation in the frequency range [340-500] GHz. The conventional CPW ($S_1 = 36 \mu\text{m}$, $W = 3 \mu\text{m}$) has losses below 3.5 dB/mm at 500 GHz. The conductor backed CPW is also attractive due to the drop of radiation loss. Numerical model based on lots of assumptions can predict well the losses of conventional CPW as a function of frequency and dimensions.

3.8 Conclusions of Chapter 3

In this chapter, quantitative evaluations of the propagation constant of four types of waveguide (CPW, Microstrip, Slotline and Stripline) and optimizations among them based on the same characteristic impedance (100Ω) have been conducted up to 1 THz by HFSS and CST.

Four types of CPW configuration have been investigated at three gap width ($W = 1.6, 6.6$ and $12 \mu\text{m}$). Airbridges used in this work are proved to attenuate slotline mode and hardly affect the other modes for $W = 1.6$ and $6.6 \mu\text{m}$. While at $W = 12 \mu\text{m}$, this advantage is weakened and additional losses contribute to the CPW mode at $f > 1 \text{ THz}$. The backed conductor makes the phase velocity of the dominant CPW mode slower and introduces parallel plate resonances in the losses, which may deteriorate the waveguide performance. The observed resonant frequencies are well predicted by theoretical formula. Then different losses (radiation, conduction and dielectric loss) are studied separately with the variation of gap width (W) on low permittivity BCB and high permittivity InP substrate. CPW on BCB has lower losses, and notably less radiation loss, in comparison with a waveguide on InP substrate. With the increase of W , conduction loss decreases and radiation loss increases. The attenuation in the dielectric does not depend strongly on W .

Microstrip lines with metal width of 5-30 μm on 30 μm thick BCB substrate are compared. Wide metal width contributes to large radiation and low conductivity loss. The dielectric loss is comparable to the radiation loss and the conduction loss dominates in the total losses.

Conventional slotline with slot width of 5-30 μm on semi-infinite BCB shows large dispersion and high attenuation loss. Conduction loss can be reduced by increasing gap width or the metal conductivity. As in the conductor backed CPW, conductor backed slotline has also resonances which mainly depend on the line length.

Stripline (central metal width = 5-30 μm) in 30 μm low permittivity BCB shows nearly zero radiation and zero dispersion, as well as in high permittivity semiconductor substrate. When the material is inhomogeneous, radiation loss is no longer quasi zero due to the non TEM nature of the dominant mode. Resonances have also been observed.

Then a comparative study of the four types of waveguides at the same characteristic impedance (100Ω) was done. Microstrip line in THz frequency has minimum attenuation, although suffers from weak dispersion. stripline has comparable total losses but shows no dispersion. The attenuation in CPW without backed conductor can be comparable to microstrip line if the metal conductivity is improved. Slotline and conductor backed CPW suffer from the extremely large radiation loss and Slotline shows the most dispersive behavior. Methods have been proposed and demonstrated to ameliorate the losses in each type of waveguide at 100Ω .

Technologies for sample fabrication on thick BCB dielectric in the clean room and transition design for coupling with the measurement system were introduced. De-embedding technique for extracting the S matrix, propagating constant and characteristic impedances of CPW waveguide was presented in detail.

Finally, measurement results of CPW with and without backed conductor were shown in the frequency range [340-500] GHz. Parallel plate resonances were observed in the conductor backed CPW, which has lower attenuation (below 2 dB/mm for $S_1 = 36 \mu\text{m}$ and $W = 10 \mu\text{m}$) compared to a CPW without backed conductor (4.5 dB/mm for $S_1 = 36 \mu\text{m}$ and $W = 10 \mu\text{m}$). Numerical results agree with the experimental attenuations of conventional CPW, while they underestimate the losses in conductor backed CPW in the region without resonances. The large resonances in the numerical modeling for conductor backed CPW need further investigation.

One perspective of the part of THz waveguide is to take into account other planar transmission lines, like planar Goubau line (PGL). It has simple structure and owns surface plasmon mode as the dominant mode. In addition, the dispersion of slotline, CPW and microstrip at high frequency can be improved by covering the top metal layer with a finite thickness of BCB to reach monomode propagation in the considered frequency range.

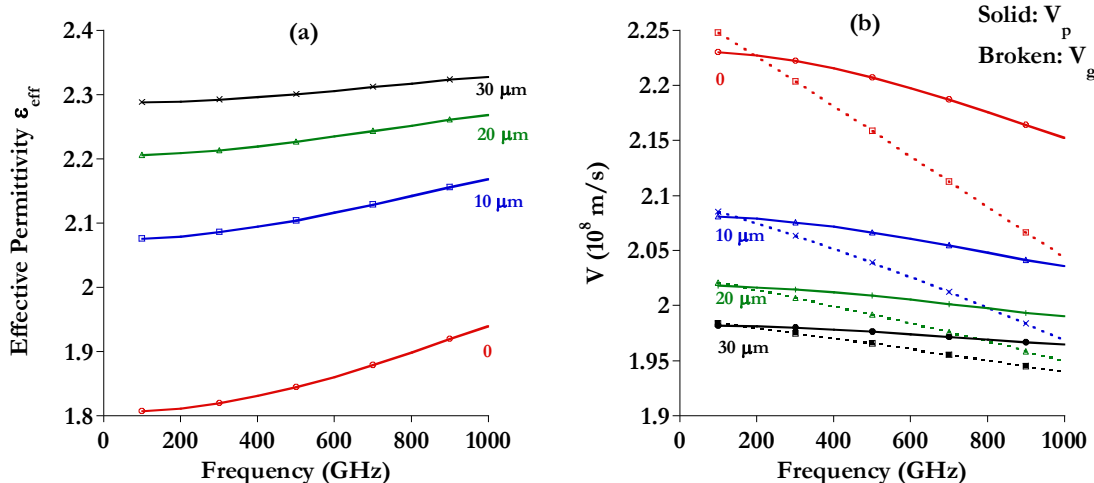


Figure 3-65: (a) Effective permittivity, (b) phase and group velocities of microstrip ($W = 30 \mu\text{m}$) with signal line buried in different thickness of BCB ([10-30] μm) by HFSS. 0 corresponds to conventional microstrip with signal line in air

Figure 3-65 shows the effective permittivity (a), phase and group velocities (b) of the dominant mode in an encapsulated $30 \mu\text{m}$ wide microstrip line on $30 \mu\text{m}$ thick BCB substrate. With the

increase of upper BCB thickness from 10 to 30 μm , the effective permittivity is improved and its curve becomes flat in function of the frequency. The velocity difference $|V_g - V_p|$ at 1 THz is reduced from $0.11 \times 10^8 \text{ m/s}$ in conventional microstrip (red curve) to $0.02 \times 10^8 \text{ m/s}$ for covered microstrip in 30 μm BCB (black curve). The line becomes less dispersive. The same treatment can be applied to other types of waveguide, like CPW and slotline.

Chapter 4 Conclusions and Perspectives

4.1 Conclusions

This PhD work allows to, quantitatively analyze and optimize the detection and propagation of THz signal in the frequency range [10-1000] GHz. Numerical modeling, sample fabrication and characterization were lead together.

4.1.1 THz detection

In chapter 2, plasmonic heterostructures were studied for THz detection. Both commercial software HFSS and indigenously developed CWM code were compared. They solved the problem of metallic grating assisted Plasmon-Polariton (PP) absorption of THz radiation in four materials (AlGaN/GaN, InAlN/GaN, SiGe/Si/SiGe and AlGaAs/GaAs) and they have shown a good agreement. For homogeneous 2DEG system, the parametric study (incident angle, electron density, barrier thickness, metal width, grating period and temperatures) showed that nitride based materials demonstrate the maximum absorption at room temperature without doping. The absorption in other two structures can be improved at cryogenic temperature, but the modulation doping is required to reach high electron concentration (10^{16} m^{-2}). The resonant frequency can be tuned in [0.3-3] THz via grating period (L) in [0.5-5] μm and metal width (W). From the side of dispersion, the grating screened PP has asymptotic behaviors: beyond $W/L = 0.6$, the PP dispersion approaches that of PP with continuous metal layer (totally screened), while below $W/L = 0.5$, it is near that of open surface PP (unscreened). Experimental FTIR transmission results of the sample AlGaN/GaN/Sapphire with various W ($W/L = 0.25, 0.5, 0.6$ and 0.75) and temperatures (300 K, 78 K and 10 K) have validated the simulated one: the resonant amplitude and frequency depend on W/L , and the absorption at $W/L = 0.75$ and 10 K is maximum.

For the case of inhomogeneous 2DEG, both natural and forced modulated electron density in AlGaAs/GaAs were studied numerically. Natural modulation without biasing on the metallization is due to the differences between the barrier height at metal/semiconductor interface and the Fermi level pinning at air/semiconductor interface. Step distribution function of electron density of 2DEG below and between metal fingers was as accurate as more complex distribution models, like linear and parabolic functions. This type of modulation causes the slight decrease of both absorption amplitude and frequency of PP, compared with the homogeneous 2DEG case in AlGaAs/GaAs. The other type is the modulation by biasing. It can greatly tune the PP absorption by altering the electron concentration below metal fingers. When reaching the regime of strong modulation, the plasma oscillation is located under the gap part ($W_G = L-W$). The PP absorption amplitude is comparable to the case of homogeneous 2DEG and can be reinforced at narrow W_G . Its resonant position is higher than that of the totally screened, but lower than that of the unscreened strongly modulated 2DEG system. Metallic grating is indispensable for efficient coupling between incident THz radiation and 2D plasmons with both homogeneous and inhomogeneous electron concentration.

In the view of application, the comparative results among the four heterostructures can provide both theoretical and technical references for tunable resonant THz detection, because the parameters used in the simulation are based on reported practical values. The grating can be integrated in a transistor structure to serve as the gate electrode and to realize efficient coupling

when 2D plasmons are used as the active layer. Frequency tunability is feasible by voltage bias. Moreover, THz emission and amplification are also possible application areas.

4.1.2 THz transmission

The chapter 3 contributed to the optimization of THz transmission in planar waveguide structures through numerical code HFSS and CST MWS. Four types of waveguide on BCB were investigated separately from the aspects of dispersions and attenuations. (1) CPW on BCB benefits smaller radiation and conduction losses in reference to InP substrate. Airbridges are useful to attenuate parasitic slotline mode. Backed conductor is helpful in reducing the radiation loss, but introduces resonances at frequencies of parallel plate mode and results in additional conduction and dielectric losses. Wide gap contributes to high radiation loss and low conduction loss. Among the three values of W (1.6, 6.6 and 12 μm), CPW on BCB at W = 6.6 μm is the optimal one. (2) Microstrip on BCB has the radiation loss comparable to the dielectric loss. Conduction loss dominates in the total losses. For strip width in the range [5-30] μm , W = 30 μm shows the minimum attenuation. (3) stripline has the unique nature of TEM wave propagation and zero radiation loss in low permittivity BCB, and also in high dielectric permittivity medium. For stripline in inhomogeneous dielectric, the propagation mode is no longer TEM and the radiation grows. Stripline in homogeneous BCB with a 30 μm wide central strip has the least losses (W = [5-30] μm), mainly coming from the lowest conduction loss. (4) In Slotline, the radiation occupies a major part in the total attenuation and increases with slot width (W = [5-30] μm). It has high dispersion even at narrow slot (W = 5 μm). The conductor backed slotline demonstrated resonant behaviors in the frequency dependent losses and had worse transmission performance than the conventional one. (5) Comparisons of the four types of waveguide on BCB at a characteristic impedance of 100 Ω showed the microstrip at strip width W = 25 μm is the best transmission line (4 dB/mm at 1 THz) from the aspect of attenuation. Stripline at central strip width W = 7.3 μm is the optimal line from the aspect of dispersion, but it suffers from large conduction loss. CPW has the overall moderate performances of both attenuation and dispersion. Slotline is the most dispersive line and has the largest attenuation (9.6 dB/mm at 1 THz). Dielectric loss is proportional to the product of frequency and loss tangent ($f \tan \delta$). The value of dielectric loss in BCB at 1 THz is below 1 dB/mm. The total losses for each waveguide at 100 Ω can be reduced below 5 dB/mm at 1 THz by the optimization of geometric dimensions. Monomode propagation is possible for BCB waveguide up to 1 THz. These numerical values can provide references for characterizing planar waveguide in THz range in both time and frequency domain.

Experimental characterization of CPW (W = [3-10] μm and S₁ = [36-100] μm) and microstrip (W = [10-36] μm) have been finished by a Vector Network Analyzer (VNA) in the frequency range [340-500] GHz. Preliminary results of conventional CPW agree with the simulation performed by HFSS. Among the five dimensions of CPW, S₁ = 36 μm / W = 3 μm is the optimal structure for conventional CPW with an attenuation of 2.7 dB/mm at 400 GHz. For conductor backed CPW, the two structures with large gap width (S₁ = 36 μm / W = 10 μm and S₁ = 100 μm / W = 6 μm) are better. Resonances were observed in the conductor backed CPW.

4.2 Future Work

The follow-up works are expected for the purpose of performance improvement and possible applications.

- (1) Transmission spectrum using the Drude type permittivity of 2DEG in the numerical simulation agrees well with the FTIR measured results for the sample AlGaN/GaN. To further improve the accuracy of the modeled results, the local permittivity model of 2D plasmon can be replaced by a more rigorous and complex non-local permittivity $\varepsilon(\omega, k)$ which depends on both the frequency ω and the wave vector k . Moreover, for practical device application in THz detection and emission, the number of metallic grating should be finite in size and area. It is preferred to know the minimum number of metal strips to coupler effectively THz radiation.
- (2) The dispersion of non TEM propagation mode in THz waveguide can be possibly reduced by depositing a finite thickness of substrate material to embody upper conductor layer. This improvement needs further investigation in waveguides, like microstrip, slotline, CPW and planar Goubau line.

Appendix A: Surface waves in a planar waveguide

Surface waves exist at the dielectric waveguide slab. For CPW with large substrate thickness and high permittivity, the cutoff frequencies maybe locate at the interested frequency range and deteriorate the line performance [Shigesawa1990]. It is necessary to study this type of wave for all types of planar waveguide on finite substrate, especially for high frequency applications. Here the existence or not of the surface waves in the three configurations (semi-infinite air/semi-infinite dielectric, semi-infinite air/finite dielectric/semi-infinite air, and semi-infinite air/finite dielectric with backed conductor) will be investigated theoretically. Analytic expressions of the cutoff frequency in each configuration are presented.

A.1 Air/dielectric

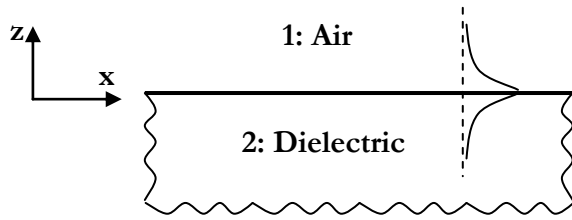


Figure A-1: Interface between semi infinite air and semi infinite dielectric

Supposing the plane wave propagates along x direction, the semi infinite air and dielectric is separated by the $z = 0$ plane, in the y direction, the dielectric is homogeneous (no variations of all the EM components, hence the propagation constant $k_y = 0$). If there are surface waves, the field components should attenuate to zero along the increasing direction of the absolute z value in both the two materials.

For TM polarization, only E_x , E_z and H_y exist, and their expressions are written as,

$$\begin{aligned} H_{y,1} &= H_1 \exp(-\alpha_1 z) \exp(jk_x x) \\ E_{x,1} &= \frac{j\alpha_1}{\omega\epsilon_0} H_1 \exp(-\alpha_1 z) \exp(jk_x x) \end{aligned} \quad (\text{A-1})$$

in air($z > 0$), and

$$\begin{aligned} H_{y,2} &= H_2 \exp(-\alpha_2 z) \exp(jk_x x) \\ E_{x,2} &= \frac{-j\alpha_2}{\omega\epsilon_0\epsilon_r} H_2 \exp(\alpha_2 z) \exp(jk_x x) \end{aligned} \quad (\text{A-2})$$

in the dielectric ($z < 0$).

Where $\alpha_1 = \sqrt{k_x^2 - \omega^2/c^2} > 0$ and $\alpha_2 = \sqrt{k_x^2 - \epsilon_r \omega^2/c^2} > 0$ are the attenuation constants in the air and dielectric, ϵ_r is the relative dielectric permittivity, k_x is the propagation constant in x direction, H_1 and H_2 are constant values decided by the initial conditions or excitation source values. The time dependent factor $e^{-j\omega t}$ is omitted in the derivation.

The continuity of the magnetic tangential component H_y and electric tangential component E_x at the interface $z = 0$ gives the dispersion relation:

$$\alpha_2 = -\epsilon_r \alpha_1 \quad (\text{A-3})$$

Because the appearance of surface wave requires $\alpha_2 > 0$, $\alpha_1 > 0$ and $\epsilon_r > 0$, the above relation does not hold. We conclude that there is no TM wave in this configuration.

Similarly, for TE polarization, we have only H_x , H_z and E_y components,

$$\begin{aligned} E_{y,1} &= E_1 \exp(-\alpha_1 z) \exp(jk_x x) \\ H_{x,1} &= \frac{-j\alpha_1}{\omega\mu_0} E_1 \exp(-\alpha_1 z) \exp(jk_x x) \end{aligned} \quad (\text{A-4})$$

in air, and

$$\begin{aligned} E_{y,2} &= E_2 \exp(\alpha_2 z) \exp(jk_x x) \\ H_{x,2} &= \frac{j\alpha_2}{\omega\mu_0} E_2 \exp(\alpha_2 z) \exp(jk_x x) \end{aligned} \quad (\text{A-5})$$

in the dielectric.

According to the continuity of H_x and E_y at the two interfaces, the dispersion relation reads,

$$\alpha_2 = -\alpha_1 \quad (\text{A-6})$$

This equation also has no solution, so the TE wave does not exist. Both TM and TE polarizations surface waves are not supported in semi infinite air/semi infinite substrate. In real cases, the substrate thickness is definitely finite, which is discussed in the following two types of structures.

A.2 Air/ dielectric slab/Air

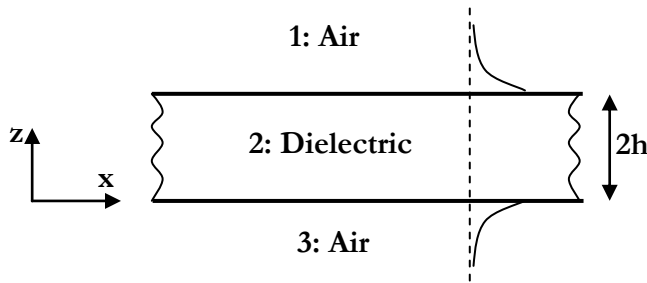


Figure A-2: A dielectric slab with thickness $2h$ sandwiched between semi infinite air.

For TM polarization, the field components in the three materials,

$$\begin{aligned} H_{y,1} &= H_1 \exp(-\alpha_1 z) \exp(jk_x x) \\ E_{x,1} &= \frac{j\alpha_1}{\omega\epsilon_0} H_1 \exp(-\alpha_1 z) \exp(jk_x x) \end{aligned} \quad (\text{A-7})$$

in upper air ($z > 2h$),

$$\begin{aligned} H_{y,2} &= (H_2 \exp(j\alpha_2 z) + H'_2 \exp(-j\alpha_2 z)) \exp(jk_x x) \\ E_{x,2} &= \frac{\alpha_2}{\omega\epsilon_0\epsilon_r} (H_2 \exp(j\alpha_2 z) - H'_2 \exp(-j\alpha_2 z)) \exp(jk_x x) \end{aligned} \quad (\text{A-8})$$

in the dielectric ($0 < z < 2h$) and,

$$\begin{aligned} H_{y,3} &= H_3 \exp(\alpha_3 z) \exp(jk_x x) \\ E_{x,3} &= \frac{-j\alpha_3}{\omega\epsilon_0} H_3 \exp(\alpha_3 z) \exp(jk_x x) \end{aligned} \quad (\text{A-9})$$

in lower air ($z < 0$)

The attenuation constants in the three dielectrics are defined as: $\alpha_1 = \alpha_3 = \sqrt{k_x^2 - \omega^2/c^2} > 0$ and $\alpha_2 = \sqrt{\epsilon_r \omega^2/c^2 - k_x^2} \geq 0$.

From this point, two cases could be distinguished: TM even and TM odd, according to the symmetry of H_y at the middle plane $z=h$ in the dielectric layer.

TM even mode (symmetric type, $\left. \frac{\partial H_y}{\partial z} \right|_{z=h} = 0$ or the equivalent perfect electric wall at $z = h$):

The boundary condition at the interfaces $z = 0$ and $z = 2h$ arrives

$$\epsilon_r(\alpha_1 h) = (\alpha_2 h) \tan(\alpha_2 h) \quad (\text{A-10})$$

Another natural relation between the attenuation constant by the definitions of the attenuation constants,

$$(\alpha_1 h)^2 + (\alpha_2 h)^2 = (\epsilon_r - 1)(k_0 h)^2 \quad (\text{A-11})$$

Where $k_0 = \omega/c$ is the wave number in air.

By letting $\alpha_2 h = n\pi$ and $\alpha_1 h = 0$, the cutoff frequency of the surface wave is determined as

$$\frac{h}{\lambda_0} = \frac{n}{2\sqrt{\epsilon_r - 1}}, \lambda_0 = \frac{c}{f}, n = 0, 1, 2, \dots \quad (\text{A-12})$$

TM odd mode (asymmetric type, $\left. H_y \right|_{z=h} = 0$ or the equivalent perfect magnetic wall at $z=h$):

Using the above derivation procedures, the cutoff frequency is calculated by

$$\frac{2h}{\lambda_0} = \frac{2n+1}{2\sqrt{\epsilon_r - 1}}, \lambda_0 = \frac{c}{f}, n = 0, 1, 2, \dots \quad (\text{A-13})$$

In combination of the two cases, the cutoff frequency for TM mode can be combined into one uniform formula,

$$\frac{2h}{\lambda_0} = \frac{n}{2\sqrt{\epsilon_r - 1}}, \lambda_0 = \frac{c}{f} \quad (\text{A-14})$$

Where $n = 0, 2, 4, \dots$ corresponds to TM even modes and $n = 1, 3, 5, \dots$ corresponds to TM odd mode.

For TE polarization, we also have two cases: TE even and TE odd modes (in reference to the symmetry of E_y at the middle plane $z = h$). Their cutoff frequencies are as the same as the TM cases.

$$\frac{2h}{\lambda_0} = \frac{n}{2\sqrt{\epsilon_r - 1}}, \lambda_0 = \frac{c}{f} \quad (\text{A-15})$$

Where $n = 0, 2, 4, \dots$ corresponds to TE even modes and $n = 1, 3, 5, \dots$ corresponds to TE odd mode.

A.3 Air/ dielectric slab back conducted

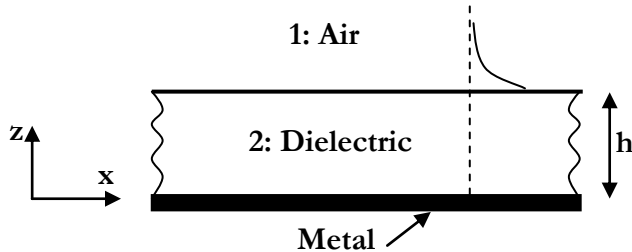


Figure A-3: Interface between semi infinite air and a dielectric slab with thickness h backed conducted with a metal layer.

If the metal is considered as PEC, which requires the tangential component of E being vanishing at the surface of metal layer,

$$E_x|_{z=0} = E_y|_{z=0} = 0 \quad (\text{A-16})$$

When comparing with the Figure A-2, we see that in the backed conductor condition, only TM even ($0, 2, 4, \dots$) and TE odd ($1, 3, 5, \dots$) modes are supported in this type of waveguide. The cutoff frequencies can be calculated by the above expressions (A-14) and (A-15).

Appendix B: Coupling coefficients in CPW

Table B-1: Coupling coefficient between mode CPW and mode Slotline in conventional CPW without air bridges (AB/BC).

f (THz)	W = 1.6 μm	W = 6.6 μm	W = 12 μm
	C(CPW/Slot)	C(CPW/Slot)	C(CPW/Slot)
0.6	0.0006	0.0066	0.0049
0.7	0.0004	0.0036	0.0045
0.8	0.0002	0.0032	0.0065
0.9	0.0004	0.0029	0.0036
1.0	0.0003	0.0028	0.0047
1.1	0.0005	0.0025	0.0040
1.2	0.0012	0.0011	0.0044
1.3	0.0005	0.0024	0.0043
1.4	0.0006	0.0010	0.0039
1.5	0.0003	0.0008	0.0033

Table B-2: Coupling coefficient between mode CPW and mode Slotline in conventional CPW with air bridges (AB/BC).

f (THz)	W = 1.6 μm	W = 6.6 μm	W = 12 μm
	C(CPW/Slot)	C(CPW/Slot)	C(CPW/Slot)
0.6	0.01449	0.0042	0.0041
0.7	0.01477	0.0045	0.0070
0.8	0.0090	0.0020	0.0059
0.9	0.0066	0.0022	0.0032
1.0	0.0030	0.0014	0.0054
1.1	0.0029	0.0021	0.0026
1.2	0.0008	0.0004	0.00002
1.3	0.0007	0.0031	0.0080
1.4	0.0019	0.0041	0.0060
1.5	0.0106	0.0005	0.0039

Table B-3: Coupling coefficient between mode CPW and mode Slotline or Microstrip in conductor backed CPW without air bridges (AB/BC).

f (THz)	W = 1.6 μm	W = 6.6 μm		W = 12 μm	
	C(CPW/Slot)	C(CPW/Slot)	C(CPW/Mstrp)	C(CPW/Slot)	C(CPW/Mstrp)
0.8				0.0156	
0.9	0.0119	0.0084		0.0170	0.7156
1.0	0.0066	0.0026		0.0052	0.1925
1.1	0.0090	0.0053		0.0055	0.0616
1.2	0.0116	0.0007		0.0058	0.0179
1.3	0.0130	0.0003		0.0023	0.0004
1.4	0.0117	0.0009	0.0155	0.0067	0.0007
1.5	0.0109	0.0002	0.0533	0.0114	0.0003

Table B-4: Coupling coefficient between mode CPW and mode Slotline or Microstrip in conductor backed CPW with air bridges (AB/BC).

f (THz)	W=1.6μm		W=6.6μm		W=12μm	
	C(CPW/Slot)	C(CPW/Slot)	C(CPW/Mstrp)	C(CPW/Slot)	C(CPW/Mstrp)	
0.8				0.0010		
0.9	0.0745	0.0138		0.0024	0.8781	
1.0	0.0449	0.0099		0.0045	0.1199	
1.1	0.0284	0.0073		0.0042	0.0155	
1.2	0.01991	0.0058		0.0024	0.0226	
1.3	0.01381	0.0002		0.0040	0.0344	
1.4	0.01396	0.0043	0.1078	0.1569	0.0018	
1.5	0.01596	0.0026	0.0410	0.2377	0.0007	

References

- [Ager1991] C.D.Ager, and H.P.Hughes, "Optical properties of stratified systems including lamellar grating", Physical Review B, Vol.44, No.24, pp.13452-13465, 1991.
- [Ager1992-1] C.D.Ager, R.J.Wilkinson, and H.P.Hughes, "Periodic grating-gate screening of plasmons in heterojunction structures", J.Appl.Phys., Vol.71, No.3, pp.1322-1326, 1992.
- [Ager1992-2] C.D.Ager, and H.P.Hughes, "Screening of plasmons in modulated 2DEGs by grating gates", Solid State Communications, Vol.83, No.8, pp.627-633, 1992.
- [Aggarwal2010] M.D.Aggarwal, A.K.Batra, P.Guggilla, M.E.Edwards, B.G.Penn, and J.R.Currie, Jr., "Pyroelectric materials for uncooled infrared detectors: processing, properties, and applications", NASA/TM, 216373 (<https://www2.sti.nasa.gov/>), pp.1-71, 2010.
- [Akalin2006] Tahsin Akalin, Anthony Treizebré and Bertrand Bocquet, "Single-Wire Transmission Lines at Terahertz Frequencies", IEEE Transaction on Microwave Theory and Techniques, Vol.54, No.6, pp.2762-2767, 2006.
- [Allen1977] S.J.Allen, Jr.,D.C.Tsui and R.A.Logan, "Observation of the Two-Dimensional Plasmon in Silicon Inversion Layers", Physical Review Letters, Vol.38, No.17, pp.980-983, 1977.
- [Ambacher1998] O. Ambacher, "Growth and applications of group III-nitrides", J. Phys .D: Appl. Phys., Vol.31, pp.2653-2710, 1998.
- [Ambacher1999] O.Ambacher, J.Smart, J.R.Shealy, N.G.Weimann, K.Chu, M.Murphy, W.J.Schaff, L.F.Eastman, R.Dimitrov, L.Wittmer, M.Stutzmann, W.Rieger, and J.Hilsenbeck, "Two-dimensional electron gases induced by spontaneous and piezoelectric polarization charges in N- and Ga-face AlGaN/GaN heterostructures ", Journal of Applied Physics, Vol.85, No.6, pp.3222-3232, 1999.
- [Ambacher2000] O.Ambacher, B.Foutz, J.Smart, J.R.Shealy, N.G.Weimann, K.Chu, M.Murphy, A.J.Sierakowski, W.J.Schaff, L.F.Eastman, R.Dimitrov, A.Mitchell, and M.Stutzmann, "Two dimensional electron gases induced by spontaneous and piezoelectric polarization in undoped and doped AlGaN/GaN heterostructures ", Journal of Applied Physics, Vol.87, No.1, pp.334-344, 2000.
- [Angerer1997] H.Angerer, D.Brunner, F.Freudenberg, O.Ambacher, M.Stutzmann, R.Höpler, T.Metzger, E.Born, G.Dollinger, A.Bergmaier, S.Karsch, and H.-J. Körner, "Determination of the Al mole fraction and the band gap bowing of epitaxial $\text{Al}_x\text{Ga}_{1-x}\text{N}$ films", Applied Physics Letters, Vol.71, No.11, pp.1504-1506, 1997.
- [Aniel1996] F.Aniel, A.Sylvestre, Y.Jin, P.Crozat, A.de Lustrac, and R.Adde, "Enhancements and degradations in ultrashort gate GaAs and InP HEMTs properties at cryogenic temperatures: an overview", Journal de physique IV, Vol.6, pp.145-149, 1996.
- [Aniel2000] F.Aniel, N.Zerounian, R.Adde, M.Zeuner, T.Hackbarth, U.König, "Low temperature analysis of 0.25 μm T-Gate strained Si/Si_{0.55}Ge_{0.45} N-MODFET's", IEEE Transactions on Electron Devices, Vol.47, No.7, pp.1477-1483, 2000.
- [Asada2008] Masahiro Asada, Safumi Suzuki and Naomichi Kishimoto, "Resonant Tunneling Diodes for Sub-Terahertz and Terahertz Oscillators", Japanese Journal of Applied Physics, Vol. 47, No. 6, pp. 4375–4384, 2008.

- [Ashcroft1976] Neil W. Ashcroft and N. David Mermin, "Solid State Physics", Harcourt College Publishers, ISBN: 0-03-083993-9, 1976.
- [Bahl1977] I.J.Bahl, and Ramesh Garg, "Simple and accurate formulas for microstrip with finite strip thickness", Proceedings of the IEEE, Vol. 65, pp. 1611-1612, 1977.
- [Beard2001] Matthew C.Beard, Gordon M.Turner, and Charles A.Schmuttenmaer, "Subpicosecond carrier dynamics in low-temperature grown GaAs as measured by time-resolved terahertz spectroscopy", Journal of Applied Physics, Vol.90, No.12, pp.5915-5923, 2001.
- [Ben1966] Adi Ben-Israel, "A newton-raphson method for the solution of systems of equations", Journal of Mathematical analysis and applications, Vol.15, No.2, pp.243-252, 1966.
- [Bernardini1997] Fabio Bernardini, Vincenzo Fiorentini and David Vanderbilt, "Spontaneous polarization and piezoelectric constants of III-V nitrides", Physical Review B, Vol.56, No.16, pp.R10024-R10027, 1997.
- [Blin2012] Stéphane Blin, Frédéric Teppe, Lucie Tohme, Shintaro Hisatake, Kazuki Arakawa, Philippe Nouvel, Dominique Coquillat, Annick Pénarier, Jérémie Torres, Luca Varani, Wojciech Knap, and Tadao Nagatsuma, "Plasma-wave detectors for terahertz wireless communication", IEEE electron device letters, Vol. 33, No. 10, pp.1354-1356, 2012.
- [Brennan1999] Kevin F.Brennan, "The physics of semiconductors with applications to optoelectronic devices", Cambridge, England: Cambridge University Press, ISBN: 0-52-159350-6, 1999.
- [Burchett1993] M.Hugh Burchett, Steve R.Pennock, and Peter R.Shepherd, "A rigorous analysis of uniform stripline of arbitrary dimensions", IEEE Transactions on Microwave and Techniques, Vol. 41, No.12, pp.2074-2080, 1993.
- [Byrne2008] M.B.Byrne, J.Cunningham, K.Tych, A.D.Burnett, M.R.Stringer, C.D.Wood, L.Dazhang, M.Lachab, E.H.Linfield, and A.G.Davies, "Terahertz vibrational absorption spectroscopy using microstrip-line waveguides", Applied Physics Letters, Vol. 93, 182904, 2008.
- [Chamberlain2004] J.M.Chamberlain, "Where optics meets electronics: recent progress in decreasing the terahertz gap", Phil.Trans.R.Soc.Lond.A, Vol.362, pp.199-213, 2004.
- [Chen1991] Yi Chen, Steven Williamson, Tim Brock, F.W.Smith, and A.R.Calawa, "375-GHz-bandwidth photoconductor detector", Appl. Phys. Lett., Vol. 59, No.16, pp.1984-1986, 1991.
- [Chen2006] Li-Jin Chen, Hung-Wen Chen, Tzeng-Fu Kao, Ja-Yu Lu, and Chi-Kuang Sun, "Low-loss subwavelength plastic fiber for terahertz waveguiding", Optics Letters, Vol. 31, No.3, pp.308-310, 2006.
- [Cheng1994] H. Cheng, J.F.Whitaker, T.M.Weller, and L.P.B.Katehi, "Terahertz-bandwidth pulse propagation on a coplanar stripline fabricated on a thin membrane", IEEE microwave and guided wave letters, Vol. 4, No.3, pp.89-91, 1994.
- [Cohn1955] Seymour B.Cohn, "Problems in strip transmission lines", IRE transactions on microwave theory and techniques, Vol. 3, pp.119-126, 1955.
- [Cohn1968] Seymour B.Cohn, "Slot line on a dielectric substrate", IEEE Transactions on microwave theory and techniques, Vol. MTT-17, pp.768-778, 1969.
- [Collier1999] R.J.Collier, "Coupling between coplanar waveguides and substrate modes", in 29th European Microwave Conference, pp.382-385, Munich 1999.

- [Collin1960] Robert E.Collin, "Field Theory of Guided Waves", New York: McGraw-Hill,1960.
- [Cunningham2008] J.Cunningham, M.Byrne, P.Upadhyra, M.Lachab, E.H.Linfield, and A.G.Davies, "Terahertz evanescent field microscopy of dielectric materials using on-chip waveguides", Applied Physics Letters, Vol. 92, 032903, 2008.
- [Das1991] Nirod K.Das, and David M.Pozar, "Full-wave spectral-domain computation of material, radiation, and guided wave losses in infinite multilayered printed transmission lines", IEEE Transactions on microwave theory and techniques, Vol. 39, No.1, pp.54-63, 1991.
- [Denlinger1971] E.J.Denlinger, "A frequency dependent solution for microstrip transmission lines", IEEE transactions on microwave theory and techniques, Vol. 19, pp.30-39, 1971.
- [Dexheimer2008] Susan L.Dexheimer, "Terahertz spectroscopy: principles and applications", CRC Press-Taylor & Francis Group, ISBN: 978-0-8493-7525-5, 2008.
- [Dragoman2004] D.Dragoman and M.Dragoman, "Terahertz fields and applications", Progress in Quantum Electronics, Vol.28, pp.1-66, 2004.
- [Dyakonov1993] Mikhail Dyakonov and Michael Shur, "Shallow Water Analogy for a Ballistic Field Effect Transistor: New Mechanism of Plasma Wave Generation by dc Current ", Physical Review Letters, Vol.71, No.15, pp.2465-2468, 1993.
- [Dyakonov1996-1] Mikhail Dyakonov and Michael Shur, "Detection, Mixing, and Frequency Multiplication of Terahertz Radiation by Two-Dimensional Electronic Fluid ", IEEE Transactions on Electron Devices, Vol.43, No.3, pp.380-387, 1996.
- [Dyakonov1996-2] Michael I.Dyakonov, and Michael S.Shur, "Plasma wave electronics: novel terahertz devices using two dimensional electron fluid", IEEE Transactions on Electron Devices, Vol.43, No.10, pp.1640-1645, 1996.
- [Eguiluz1975] Adolfo Eguiluz, T.K.Lee, J.J.Quinn, and K.W.Chiu, "Interface excitations in metal-insulator-semiconductor structures", Physical Review B, Vol.11, No.12, pp. 4989-4993, 1975.
- [Engen1979] Glenn F.Engen, and Cletus A.Hoer, ""Thru-Reflect-Line": An improved technique for calibrating the dual six-port automatic network analyzer", IEEE transactions on microwave theory and techniques, Vol. MTT-27, No.12, pp.987-993, 1979.
- [Fateev2010] D.V.Fateev, V.V.Popov, and M.S.Shur, "Transformation of the plasmon spectrum in a grating-gate transistor structure with spatially modulated two-dimensional electron channel", Semiconductors, Vol.44, No.11, pp.1406-1413, 2010.
- [Fatimy2006] A.El Fatimy, S.Boubanga Tombet, F.Teppe, W.Knap, D.B.Veksler, S.Rumyantsev, M.S.Shur, N.Pala, R.Gaska, Q.Fareed, X.Hu, D.Seliuta, G.Valusis, C.Gaquiere, D.Theron and A.Cappy, "Terahertz detection by GaN/AlGaN transistors", Electronics Letters, Vol.42, No.23, 2006.
- [Finlay1988] Hugh J.Finlay, Rolf H.Jansen, John A.Jenkins, and Ian G.Eddison, "Accurate characterization and modeling of transmission lines for GaAs MMIC's", IEEE Transactions on microwave theory and techniques, Vol. 36, No.6, pp.961-967, 1988.
- [Fischer1984] R.Fischer, T.Henderson, J.Klem, W.T.Masselink, W.Kopp, H.Morkoç, and C.W.Litton, "Characteristics of GaAs/AlGaAs MODFETs grown directly on (100) silicon", Electronics Letters, Vol.20, No.22, pp.945-947, 1984.

- [Frankel1991] Michael Y.Frankel, Shantanu Gupta, Janis A.Valdmanis and Gerard A.Mourou, "Terahertz Attenuation and Dispersion Characteristics of Coplanar Transmission Lines", IEEE Transaction on Microwave Theory and Techniques, Vol.39, No.6, pp.910-916, 1991.
- [Gallot2000] G.Gallot, S.P.Jamison, R.W.McGowan and D.Grischkowsky, "Terahertz Waveguides", J.Opt.Soc.Am.B, Vol.17, No.5, pp.851-863, 2000.
- [Garg1976] Ramesh Garg, and K.C.Gupta, "Expressions for wavelength and impedance of a slotline", IEEE transactions on microwave theory and techniques, Vol.24, p.532, 1976.
- [Gauthier1998] Gildas P. Gauthier, Linda P. Katehi, and Gabriel M. Rebeiz, "W-Band Finite Ground Coplanar Waveguides (FGCPW) to Microstrip Line Transition", IEEE MIT-S Digest, pp.107-109, 1998.
- [Golay1947] Marcel J.E.Golay, "Theoretical Consideration in Heat and Infrared Detection, with Particular Reference to the Pneumatic Detector", Review of Scientific Instruments, Vol.18, No.5, pp.347-356, 1947.
- [Gondermann1993] Jörg Gondermann, Elard G.Stein von Kamienski, Hartmut G.Roskos, and Heinrich Kurz, "Al-SiO₂-Al sandwich microstrip lines for high-frequency on-chip interconnects", IEEE Transactions on microwave theory and techniques, Vol. 41, No.12, pp.2087-2091, 1993.
- [Goubau1950] Georg Goubau, "Surface Waves and Their Application to Transmission Lines", Journal of Applied Physics, Vol.21, pp.1119-1128, 1950.
- [Granet1996] G.Granet, and B.Guizal , "Efficient implementation of the coupled-wave method for metallic lamellar grating in TM polarization", J.Opt.Soc.Am.A, Vol.13, No.5, pp. 1019-1023, 1996.
- [Griffiths2007] Peter R.Griffiths, and James A.de Haseth, "Fourier transform infrared spectrometry", John Wiley & Sons, Inc., 2nd edition, ISBN: 978-0-471-19404-0, 2007.
- [Grimault2012] Anne-Sophie Grimault-Jacquin, Bouchra Tissafi, Etienne Perret and Frédéric Aniel, "Considering to minimize losses in terahertz coplanar waveguide on indium phosphide", Microwave and Optical Technology Letters, Vol. 54, No.1, pp.213-219, 2012.
- [Grimes1976] C.C.Grimes and Gregory Adams, "Observation of Two-Dimensional Plasmons and Electron-Ripplon Scattering in a sheet of Electrons on Liquid Helium", Physical Review Letters, Vol.36, No.3, pp.145-148, 1976.
- [Grischkowsky1987] D. Grischkowsky, I.N. Duling, III, J.C. Chen, and C.C. Chi, "Electromagnetic shock waves from transmission lines", Physical Review Letters , Vol.59, No.15, pp.1663-1666, 1987.
- [Grischkowsky1988] Daniel R. Grischkowsky, Mark B. Ketchen, C.-C. Chi, Irl N. Duling, III, Naomi J. Halas, Jean-Marc Halbout, and Paul G. May "Capacitance free generation and detection of subpicosecond electrical pulses on coplanar transmission lines", IEEE journal of quantum electronics, Vol.24, No.2, pp.221-225, 1988.
- [Gupta1996] K.C.Gupta, Ramesh Garg, Inder Bahl and Prakash Bhartia, "Microstrip Lines and Slotlines", 2nd edition, Artech House, ISBN: 0-89006-766-X, 1996.
- [Hache1993] P.Hache, T.Detchprohm, K.Hiramatsu, and N.Sawaki, "Schottky barrier on n-type GaN grown by hydride vapor phase epitaxy", Applied Physics Letters, Vol.63, No.18, pp.2676-2678, 1993.
- [Haus1991] Hermann A.Haus and WeiPing Huang, "Coupled-Mode Theory", Proceedings of the IEEE, Vol. 79, No.10, pp.1505-1518, 1991.

- [Haydl2000] William H.Haydl, "Resonance Phenomena and Power Loss in Conductor-Backed Coplanar Structures", IEEE Microwave and Guided Wave Letters, Vol.20, No.12, pp.514-516, 2000.
- [Heiliger1997] H.-M.Heiliger, M.Nagel, H.G.Roskos, H.Kurz, F.Schnieder, W.Heinrich, R.Hey, and K.Ploog, "Low-dispersion thin-film microstrip lines with cyclotene (benzocyclobutene) as dielectric medium", Applied Physics Letters, Vol. 70, No.17, pp.2233-2235, 1997.
- [Heinrich2000] Wolfgang Heinrich, Frank Schnieder, and Thorsten Tischler, "Dispersion and radiation characteristics of conductor-backed CPW with finite ground width", IEEE MTT-S Digest, pp.1663-1666, 2000.
- [Hesler2007] Jeffrey L.Hesler, and Thomas W.Crowe, "Responsivity and noise measurements of zero-bias schottky diode detectors", Proceedings of 18th Intl. Symp. Space Terahertz Techn., Pasadena, March 2007.
- [Heuermann1999] Holger Heuermann, "Calibration procedures with series impedances and unknown lines simplify on-wafer measurements", IEEE transactions on microwave theory and techniques, Vol.47, No.1, pp.1-5, 1999.
- [Hirakawa1995] K.Hirakawa, K.Yamanaka, M.Grayson, and D.C.Tsui, "Far-infrared emission spectroscopy of hot two-dimensional plasmons in AlGaAs/GaAs heterojunctions", Applied Physics Letters, Vol.67, pp.2326-2328, 1995.
- [Hirata 2009] Akihiko Hirata, Hiroyuki Takahashi, Naoya Kukutsu, Yuichi Kado, Hidehiko Ikegawa, Hiroshi Nishikawa, Toshihiro Nakayama and Tomonori Inada, "Transmission Trial of Television Broadcast Materials Using 120-GHz-band Wireless Link", NTT Technical Review, Vol.7, No.3, pp.1-6, 2009.
- [Hsu1997] L.Hsu, and W.Walukiewicz, "Electron mobility in Al_xGa_{1-x}N/GaN heterostructures", Physical Review B, Vol.56, No.3, pp.1520-1528, 1997.
- [Huang2004] Feng Huang, Brian Schuklin, Hakan Altan, John F.Federici, Dale Gary, Robert Barat, David Zimdars, Minghan Chen, and D.B.Tanner, "Terahertz study of 1,3,5-trinitro-s-triazine by time-domain and Fourier transform infrared spectroscopy", Applied Physics Letters, Vol.85, No.23, pp.5535-5537, 2004.
- [Hübers2005] H-W Hübers, S G Pavlov, and V N Shastin, "Terahertz lasers based on germanium and silicon", Semiconductor Science and Technology, Vol.20, pp.S211-S221, 2005.
- [Hübers2008] Heinz-Wilhelm Hübers, "Terahertz heterodyne receivers", IEEE journal of selected topics in quantum electronics, Vol.14, No.2, pp.378-391, 2008.
- [Ismail1995] K.Ismail, M.Arafa, K.L.Saenger, J.O.Chu, and B.S.Meyerson, "Extremely high electron mobility in Si/SiGe modulation-doped heterostructures", Applied Physics Letters, Vol.66, No.9, pp.1077-1079, 1995.
- [Ito2008] Hiroyuki Ito, and Kazuya Masu, "A simple through-only de-embedding method for on-wafer S-parameter measurements up to 110 GHz", IEEE MTT-S, pp. 383-386, 2008.
- [Itoh1973] T.Itoh, and R.Mittra, "Spectral-domain approach for calculating dispersion characteristics of microstrip lines", IEEE transactions on microwave theory and techniques, Vol.21, pp.496-499, 1973.
- [Jackson1986] Robert W. Jackson, "Considering in the Use of Coplanar Waveguide For Millimeter-Wave Integrated Circuits", IEEE Transaction on Microwave Theory and Techniques, Vol. MTT-34, No.12, pp.1450-1456, 1986.

- [Jamison2000] S.P.Jamison, R.W.McGowan, and D.Grischkowsky, "Single-mode waveguide propagation and reshaping of sub-ps terahertz pulses in sapphire fibers ", Applied Physics Letters, Vol.76, No.15, pp.1987-1989, 2000.
- [Jang2006] Jae Hyuk Jang, Norimasa Ishitobi, Bruce C.Kim, and Seung Gyo Jeong, "Effects of microstructural defects in multilayer LTCC stripline", IEEE Transactions on Advanced Packaging, Vol. 29, No.2, pp.314-319, 2006.
- [Jelley1958] J.V.Jelley, "Cerenkov Radiation and Its Applications", Pergamon Press, New York, ISBN: 0-08-013127-1, 1958.
- [Jena2000-1] Debdeep Jena, Arthur C.Gossard, and Umesh K.Mishra, "Dislocation scattering in a two-dimensional electron gas", Applied Physics Letters, Vol.76, No.13, pp.1707-1709, 2000.
- [Jena2000-2] Debdeep Jena, Arthur C.Gossard, and Umesh K.Mishra, "Dipole scattering in polarization induce III-V nitride two-dimensional electron gases", Journal of Applied Physics, Vol.88, No.8, pp.4734-4738, 2000.
- [Kadoya2008] Yutaka Kadoya, Masayuki Onuma, Shinji Yanagi, Tetsuya Ohkubo, Naoko Sato, and Jiro Kitagawa, "THz wave propagation on strip lines: devices, properties, and applications", Radioengineering, Vol. 17, No.2, pp.48-55, 2008.
- [Karasik2011] Boris S.Karasik, and Robin Cantor, "Demonstration of high optical sensitivity in far-infrared hot-electron bolometer", Appl. Phys. Lett., Vol. 98, 193503, 2011.
- [Kasai2009] Shintaro Kasai, Akihiro Tanabashi, Kosuke Kajiki, Takeaki Itsuji, Ryoji Kurosaka, Haruko Yoneyama, Masatsugu Yamashita, Hiromasa Ito, and Toshihiko Ouchi, "Micro Strip Line-based on-chip terahertz integrated devices for high sensitivity biosensors", Applied Physics Express, Vol. 2, 062401, 2009.
- [Kasilingam1983] Dayalan P.Kasilingam and David B.Rutledge, "Surface-Wave Losses of Coplanar Transmission Lines", IEEE MITT-S Digest, pp.113-115, 1983.
- [Kato1991] Kiyoko Kato, Toshihiro Kusunoki, Chisato Takenaka, Toshiyuki Tanahashi, and Kazuo Nakajima, "Reduction of dislocations in InGaAs layer on GaAs using epitaxial lateral overgrowth", Journal of Crystal Growth, Vol.115, pp.174-179, 1991.
- [Keil1992] Ulrich D.Keil, Douglas R.Dykaar, A.F.J.Levi, Rose F.Kopf, L.N.Pfeiffer, Sheldon B.Darack and K.W.West, "High-Speed Coplanar Transmission Lines", IEEE Journal of Quantum Electronics, Vol.28, No.10, pp.2333-2342, 1992.
- [Kemp2006] Michael C Kemp, "Millimeter Wave and Terahertz Technology for the Detection of Concealed Threats - A Review", Proc. of SPIE, Vol.6402, 64020D, 2006.
- [Kim1998] Juno Kim, Hai-Young Lee, and Tatsuo Itoh, "Novel microstrip-to-stripline transitions for leakage suppression in multilayer microwave circuits", Proceedings of IEEE 7th Topical Meeting on Electrical Performance of Electronic Packaging, pp.252-255, 1998.
- [Kitazawa1973] T.Kitazawa, Y.Fujiki, Y.Hayashi, and M.Suzuki, "Slot line with thick metal coating", IEEE transactions on microwave theory and techniques, Vol.21, pp.580-582, 1973.
- [Knap2002-1] W.Knap, Y.Deng, S.Rumyantsev and M.S.Shur, "Resonant detection of subterahertz and terahertz radiation by plasma waves in submicron field-effect transistors", Applied Physics Letters, Vol.81, No.24, pp.4637-4639, 2002.

- [Knap2002-2] W.Knap, V.Kachorovskii, Y.Deng, S.Rumyantsev, J.-Q. Lü, R.Gaska, M.S.Shur, G.Simin, X.Hu, M.Asif Khan, C.A.Saylor, and L.C.Brunel, "Nonresonant detection of terahertz radiation in field effect transistors", Journal of Applied Physics, Vol.91, No.11, pp. 9346-9353, 2002.
- [Knap2009] Wojciech Knap, Mikhail Dyakonov, Dominique Coquillat, Frederic Teppe, Nina Dyakonova, Jerzy Lusakowski, Krzysztof Karpierz, Maciej Sakowicz, Gintaras Valusis, Dalius Seliuta, Irmantas Kasalynas, Abdelouahad El Fatimy, Y.M.Meziani, and Taiichi Otsuji , "Field effect transistors for terahertz detection: physics and first imaging applications", J Infrared Milli Terahz Waves, Vol.30, pp.1319-1337, 2009.
- [Knorr1975] Jeffrey B.Knorr and Klaus-Dieter Kuchler, "Analysis of coupled slots and coplanar strips on dielectric substrate", IEEE transactions on microwave theory and techniques, Vol.23, No.7, pp.541-548, 1975.
- [Komiyama2000] S.Komiyama, O.Astafiev, V.Antonov, T.Kutsuwa and H.Hirai, "A single-photon detector in the far-infrared range", Vol.43, pp.405-407, 2000.
- [Kukushkin1988] I.V.Kukushkin, and V.B.Timofeev, "Magneto optics of two-dimensional electrons under the conditions of the fractional quantum Hall effect. Coulomb gaps and a critical temperature of an incompressible Fermi liquid", Sov.Phys.JETP, Vol.67, No.3, pp.594-599, 1988.
- [Leahy2009] Megan R.Leahy-Hoppa, Michael J.Fitch, and Robert Osiander, "Terahertz spectroscopy techniques for explosives detection", Anal Bioanal Chem, Vol.395, pp.247-257, 2009.
- [Lee1999] Jongjoo Lee, Heeseok Lee, Woopoung Kim, Jaehoon Lee and Joungho Kim, "Suppression of Coupled-Slotline Mode on CPW Using Air-Bridges Measured by Picosecond Photoconductive Sampling", IEEE Microwave and Guided Wave Letters, Vol.9, No.7, pp.265-267, 1999.
- [Lee2005] Minjoo L.Lee, Eugene A.Fitzgerald, Mayank T.Bulsara, Matthew T.Currie, and Anthony Lochtefeld, "Strained Si, SiGe, and Ge channels for high-mobility metal-oxide-semiconductor field-effect transistors", Journal of Applied Physics, Vol.97, pp.011101:1-27, 2005.
- [Leib2010] Mario Leib, Michael Mirbach, and Wolfgang Menzel, "An ultra-wideband vertical transition from microstrip to stripline in PCB technology", Proceedings of IEEE International Conference on Ultra-Wideband, pp.1-4, 2010.
- [Li1993] Lifeng Li, "Multilayer modal method for diffraction grating of arbitrary profile, depth, and permittivity ", J.Opt.Soc.Am.A, Vol.10, No.12, pp. 2581-2591, 1993.
- [Li1996] Lifeng Li, "Use of Fourier series in the analysis of discontinuous periodic structures", J.Opt.Soc.Am.A, Vol.13, pp.1870-1876, 1996.
- [Lo1993] Wen-Teng Lo, Ching-Kuang C. Tzuang, S.-T. Peng, Ching-Cheng Tien, Chung-Chi Chang, and Jenq-Wen Huang, "Resonant Phenomena in Conductor-Backed Coplanar Waveguides (CPCPW's)", IEEE Transactions on Microwave Theory and Techniques, Vol.41, No.12, pp.2099-2108, 1993.
- [Loewen1997] Erwin G.Loewen, and Evgeny Popov, "Diffraction grating and applications", Marcel Dekker Inc., ISBN: 0-8247-9923-2, 1997.
- [Lok2008] L.B.Lok, C.-J.Hwang, H.M.-H.Chong, K.Elgaid, and I.G.Thayne, "Measurement and modeling of CPW transmission lines and power dividers on electrically thick GaAs substrate to 220 GHz", Proceedings of 33rd IRMMW-THz, Pasadena, CA (USA) , 2008.

- [Lü1998] Jian-Qiang Lü, Michael S.Shur, Jeffrey L.Hesler, Liangquan Sun, and Robert Weikle II, "A resonant terahertz detector utilizing a high electron mobility transistor", International Electron Device Meeting, pp. 453-456, 1998.
- [Ma1999] Kuang-Ping Ma, Yongxi Qian, and Tatsuo Itoh, "Analysis and applications of a new CPW-slotline transition", IEEE Transactions on microwave theory and techniques, Vol. 47, No.4, pp.426-432, 1999.
- [Machado2011] A.Gamez-Machado, D.Valdes-Martin, A.Asensio-Lopez, and J.Gismero-Menoyo, "Microstrip-to-stripline planar transitions on LTCC", Proceedings of IEEE MTT-S International Microwave Workshop Series on Millimeter Wave Integration Technologies, pp.1-4, 2011.
- [Mackens1984] U.Mackens, D.Heitmann, L.Prager, J.P.Kotthaus, and W.Beinvogl, "Minigaps in the plasmon dispersion of a two-dimensional electron gas with spatially modulated charge density", Physical Review Letters, Vol.53, No.15, pp.1485-1488, 1984.
- [Majumdar2010] Payal Majumdar, and A.K.Verma, "Modified closed-form dispersion and loss models of slot-line with conductor thickness", J Infrared Milli Terahz Waves, Vol.31, pp.271-287, 2010.
- [Maloratsky2003] Leo G.Maloratsky, "Passive RF and Microwave Integrated Circuits", Newnes Elsevier, New York, ISBN: 075067699X, 2003.
- [Manasreh2005] Omar Manasreh, "Semiconductor Heterojunctions and Nanostructures", McGraw-Hill Professional, 1st edition, ISBN: 0-07-145228-1, 2005.
- [Marchais2006] C.Marchais, G.Le Ray, and A.Sharaifa, "Stripline slot antenna for UWB communications", IEEE antennas and wireless propagation letters, Vol. 5, pp.319-322, 2006.
- [Masaki1989] Kazuo Masaki, Chihiro Hamaguchi, Kenji Taniguchi, and Masao Iwase, "Electron mobility in Si Inversion Layers", Japanese Journal of Applied Physics, Vol.28, No.10, pp.1856-1863, 1989.
- [Matov1993] O.R.Matov, O.V.Polischuk, and V.V.Popov, "Electromagnetic emission from two-dimensional plasmons in a semiconductor-dielectric structure with metal grating: Rigorous Theory", International J of Infrared and Milli Waves, Vol.14, No.7, pp.1455-1470, 1993.
- [Matov1998] O.R.Matov, O.F.Meshkov, and V.V.Popov, "Spectrum of plasma oscillations in structures with a periodically inhomogeneous two-dimensional electron plasma", J. of Experimental and Theoretical Physics, Vol.86, No.3, pp.538-544, 1988.
- [Matov2002] O.R.Matov, O.V.Polischuk, and V.V.Popov, "The plasma oscillations spectrum of a periodically inhomogeneous 2D electron system near the perforation threshold", J. of Experimental and Theoretical Physics, Vol.95, No.3, pp.505-510, 2002.
- [McGowan1999] R.W.McGowan, G.Gallot, and D.Grischkowsky, "Propagation of ultrawideband short pulses of terahertz radiation through submillimeter-diameter circular waveguides ", Optics Letters, Vol.24, No.20, pp.1431-1433, 1999.
- [McGrath1995] William R. McGrath, "Hot-electron bolometer mixers for submillimeter wavelengths: an overview of recent developments", Sixth International Symposium on Space Terahertz Technology, pp.216-228, 1995.

- [Meissner1976] G.Meissner, H.Namaizawa, and M.Voss, "Stability and image-potential-induced screening of electron vibrational excitations in a three-layer structure", Physical Review B, Vol.13, No.4, pp. 1370-1376, 1976.
- [Mendis2000] R.Mendis, and D.Grischkowsky, "Plastic ribbon THz waveguides", Journal of Applied Physics, Vol. 88, No.7, pp.4449-4451, 2000.
- [Mendis2001] R.Mendis, and D.Grischkowsky, "Undistorted guided-wave propagation of subpicosecond terahertz pulses", Optics Express, Vol. 26, No.11, pp.846-848, 2001.
- [Mikhailov1998] S.A.Mikhailov, "Plasma instability and amplification of electromagnetic waves in low-dimensional electron systems", Physical Review B, Vol.58, No.3, pp.1517-1532, 1998.
- [Mishra1997] J.K.Mishra, A.K.Panda, and G.N.Dash, "An extremely low noise heterojunction IMPATT", IEEE transactions on electron devices, Vol.44, No.12, pp.2143-2148, 1997.
- [Muravjov2010] A.V.Muravjov, D.B.Veksler, V.V.Popov, O.V.Polischuk, N.Pala, X.Hu, R.Gaska, H.Saxena, R.E.Peale and M.S.Shur, "Temperature dependence of plasmonic terahertz absorption in grating-gate gallium-nitride transistor structures", Applied Physics Letter, 96, 042105, 2010.
- [Nadar2010] S.Nadar, H.Videlier, D.Coquillat, F.Teppe, M.Sakowicz, N.Dyakonova, W.Knap, D.Seliuta, I.Kasalynas and G.Valusis, "Room temperature imaging at 1.63 and 2.54 THz with field effect transistor detectors", Journal of Applied Physics, 108, 054508, 2010.
- [Naftaly2007] Mira Naftaly, and Robert E.Miles, "Terahertz Time-Domain Spectroscopy for material characterization", Proceedings of the IEEE, Vol.95, No.8, pp.1658-1665, 2007.
- [Nakayama1974] M. Nakayama, "Theory of surface waves coupled to surface carriers", Journal of the Physical Society of Japan, Vol.36, No.2, pp. 393-398, 1974.
- [Nelson1993] S.F.Nelson, K.Ismail, J.O.Chu, and B.S.Meyerson, "Room temperature electron mobility in strained Si/SiGe heterostructures", Appl.Phys.Lett., Vol.63, pp.367-369, 1993.
- [Nghiem1992] David Nghiem, Jeffery T.Williams, David R.Jackson, and Arthur A.Oliner, "Leakage of the stripline dominant mode produced by a small air gap", IEEE MTT-S International Microwave Symposium Digest, Vol. 1, pp.491-494, 1992.
- [Nicolson1970] A.M.Nicolson, and G.F.Ross, "Measurement of the Intrinsic Properties of Materials by Time Domain Techniques", IEEE transactions on Instrumentation and Measurement, Vol. 19, No.4, pp.377-382, 1970.
- [Nishizawa1979] J.Nishizawa, K.Motoya, and Y.Okuno, "Submillimeter wave oscillation from GaAs TUNNETT diode", Proceedings of 9th European Microwave Conference, pp.463-467, September 1979.
- [Oh2012] Jungwoo Oh, Kanghoon Jeon, Se-Hoon Lee, Jeff Huang, P.Y.Hung, Injo Ok, Barry Sassman, Dae-Hong Ko, Paul Kirsch, and Raj Jammy, "High mobility CMOS transistors on Si/SiGe heterostructure channels", Microelectronic Engineering, Vol.97, pp.26-28, 2012.
- [Okisu1986] Noriyuki Okisu, Yasuo Sambe, and Takeshi Kobayashi, "Far-infrared emission from two dimensional plasmons in AlGaAs/GaAs heterointerfaces", Applied Physics Letters, Vol. 48, No.12, 1986.

- [Ordal1983] M.A.Ordal, L.L.Long, R.J.Bell, S.E.Bell, R.R.Bell, R.W.Alexander, Jr., and C.A.Ward, "Optical properties of the metals Al, Co, Cu, Au, Fe, Pb, Ni, Pd, Pt, Ag, Ti, and W in the infrared and far infrared", Applied Optics, Vol.22, No.7, pp. 1099-1120, 1983.
- [Ozgur2005] A.Ozgur, W.Kim, Z.Fan, A.Botchkarev, A.Salvador, S.N.Mohammad, B.Sverdlov, and H.Morkoc, "High transconductance-normally-off GaN MODFETs", Electronics Letters, Vol.31, No.16, pp.1389-1390, 1995.
- [Pahlevaninezhad2010] Hamid Pahlevaninezhad, Thomas Edward Darcie, and Barmak Heshmat, "Two-wire waveguide for terahertz", Optics Express, Vol. 18, No.7, pp.7415-7420, 2010.
- [Pahlevaninezhad2011] Hamid Pahlevaninezhad, Barmak Heshmat, and Thomas Edward Darcie, "Efficient terahertz slot-line waveguides", Optics Express, Vol. 19, No.26, pp.B41-B55, 2011.
- [Paul2004] Douglas J Paul, "Si/SiGe heterostructures: from material and physics to devices and circuits", Semiconductor Science and Technology, Vol.19, pp.R75-R108, 2004.
- [Peytavit2011] E.Peytavit, C.Donche, S.Lepilliet, G.Ducournau, and J.-F.Lampin, "Thin-film transmission lines using cyclic olefin copolymer for millimeter-wave and terahertz integrated circuits", Electronics Letters, Vol.47, No.7, 2011.
- [People1984] R.People, J.C.Bean, D.V.Lang, A.M.Sargent, H.L.Störmer, K.W.Wecht, R.T.Lynch, and K.Baldwin, "Modulation doping in $\text{Ge}_x\text{Si}_{1-x}/\text{Si}$ strained layer heterostructures", Applied Physics Letters, Vol.45, No.11, pp.1231-1233, 1984.
- [Peralta2002] X.G.Peralta, S.J.Allen, M.C.Wanke, N.E.Harff, J.A.Simmons, M.P.Lilly, J.L.Reno, P.J.Burke, and J.P.Eisenstein, "Terahertz photoconductivity and plasmon modes in double-quantum-well field-effect-transistors", Appl. Phys. Lett., Vol.81, No.9, pp.1627-1629, 2002.
- [Perret2008] Etienne Perret, Nicolas Zerounian, Sylvain David and Frédéric Aniel, "Complex permittivity characterization of benzocyclobutene for terahertz applications", Microelectronic Engineering, Vol.85, pp.2276-2281, 2008.
- [Petit1980] R.Petit, "Electromagnetic theory of grating", Springer-Verlag Berlin Heidelberg New York, ISBN: 3-540-10193-4, 1980.
- [Pfeifer1994] T.Pfeifer, H.-M. Heiliger, E.Stein von Kamienski, H.G.Roskos, and H.Kurz, "Fabrication and characterization of freely positionable silicon-on-sapphire photoconductive probes", J.Opt.Soc.Am.B, Vol.11, No.12, pp.2547-2552, 1994.
- [Phatak1990] D.S.Phatak and A.P.Defonzo, "Dispersion Characteristics of Optically Excited Coplanar Striplines: Pulse Propagation", IEEE Transaction on Microwave Theory and Techniques, Vol.38, No.5, pp.654-661, 1990.
- [Pines1952] David Pines and David Bohm, "A Collective Description of Electron Interactions: II. Collective vs Individual Particle Aspects of the Interactions", Physical Review, Vol.85, No.2, pp.338-353, 1952.
- [Poisson2006] M.A.di Forte-Poisson, M.Magis, N.Sarazin, M.Tordjman, and J.di Persio, "III-Nitrides semiconductor compounds for microwave devices", Phys.Stat.Sol.(a), Vol.203, No.1, pp.185-193, 2006.
- [Poisson2010] M.-A.di Forte Poisson, N.Sarazin, M.Magis, M.Tordjman, J.Di Persio, R.Langer, E.Iliopoulos, A.Georgakilas, P.Kominou, M.Guziewicz, E.Kaminska, A.Piotrowska, C.Gaquiére, M.Oualli,

- E.Chartier, E.Morvan, and S.Delage, "LP MOCVD growth of InAlN/GaN HEMT heterostructure: comparison of sapphire, bulk SiC and composite SiCopSic substrates for HEMT device applications ", Phys.Status Solidi C, Vol.7, No.5, pp.1317-1324, 2010.
- [Popov2003] V.V.Popov, O.V.Polischuk, T.V.Teperik, X.G.Peralta, S.J.Allen, N.J.M.Horing and M.C.Wanke, "Absorption of terahertz radiation by plasmon modes in a grid-screened double-quantum-well field-effect transistor", J. of Applied physics, Vol.94, No.5, pp.3556-3562, 2003.
- [Popov2005] V.V.Popov, O.V.Polischuk, and M.S.Shur, "Resonant excitation of plasma oscillations in a partially gated two-dimensional electron layer", Journal of Applied Physics, 98, 033510, 2005.
- [Popov2008-1] V.V.Popov, G.M.Tsymbalov and M.S.Shur, "Plasma wave instability and amplification of terahertz radiation in field-effect-transistor arrays", J. Phys.: Condens. Matter, Vol.20, 384208, 2008.
- [Popov2008-2] V.V.Popov, A.N.Koudymov, M.Shur and O.V.Polischuk, "Tuning of unscreened plasmons by a gate in the field-effect transistor with two-dimensional electron channel", Journal of Applied physics, Vol.104, 024508, 2008.
- [Popov2010] V.V.Popov, "Plasmonic devices for detection of terahertz radiation", Terahertz plasmonics, Vol.5, No.4, pp.140-146, 2010.
- [Popov2011] Viacheslav V.Popov, "Plasmon excitation and plasmonic detection of terahertz radiation in the grating-gate field-effect-transistor structures", J Infrared Milli Terahz Waves, Vol.32, pp.1178-1191, 2011.
- [Pozar2004] David M. Pozar, "Microwave engineering", 3rd edition, ISBN: 0470631554, John Wiley & Sons Inc., 2004.
- [Pucel1968] Robert A.Pucel, Daniel J.Massé, and Curtis P.Hartwig, "Losses in microstrip", IEEE transactions on microwave theory and techniques, Vol.MTT-16, No.6, pp. 342-350, 1968. Correction in IEEE transactions on microwave theory and techniques, Vol.MTT-16, p. 1064, 1968.
- [Pucel1981] Robert A.Pucel, "Design considerations for monolithic microwave circuits", IEEE Transactions on microwave theory and techniques, Vol. MTT-29, No.6, pp.513-534, 1981.
- [Rao1979] J.S.Rao, and B.N.Das, "Analysis of asymmetric stripline by conformal mapping", IEEE Transactions on Microwave and Techniques, Vol. MIT-27, No.4, pp.299-303, 1979.
- [Riaziat1990] Majid Riaziat, Reza Majidi-Ahy and I-Jaung Feng, "Propagation Modes and Dispersion Characteristics of Coplanar Waveguides", IEEE Transaction on Microwave Theory and Techniques, Vol.38, No.3, pp.245-251, 1990.
- [Richard2004] Soline Richard, Frédéric Aniel, and Guy Fishman, "Energy-band structure of Ge,Si, and GaAs: A thirty-band k· p method", Physical Review B, Vol.70, 235204, 2004.
- [Richard2005] Soline Richard, Nicolas Zerounian, Philippe Boucaud, Jean-Michel Ortega, Thomas Hackbarth, Hans-Joest Herzog, and Frederic Aniel, "Detection of THz electromagnetic radiation with Si/SiGe HFET", Proceeding of ESSDERC, France, pp.363-366, 2005.
- [Richards1994] P.L.Richards, "Bolometers for infrared and millimeter waves", Journal of Applied Physics, 76, pp.1-24, 1994.

- [Rizzi2002] A.Rizzi, and H.Lüth, "III-V semiconductor interface properties as a knowledge basis for modern heterostructure devices", *Applied Physics A: Materials Science & Processing*, Vol.75, pp.69-77, 2002.
- [Rogalski2010] Antoni Rogalski, "Infrared Detectors", 2nd edition, CRC Press-Taylor&Francis Group, ISBN-10: 142007671X, 2010.
- [Roskos1991] Hartmut Roskos, Martin C.Nuss, Keith W.Goossen, David W.Kisker, Alice E.White, Ken T.Short, Dale C.Jacobson, and John M.Poate, "Propagation of picosecond electrical pulses on a siliconbased microstrip line with buried cobalt silicide ground plane", *Applied Physics Letters*, Vol. 58, No.23, pp.2604-2606, 1991.
- [Rozzi1990] Tullio Rozzi, Franco Moglie, Antonio Morini, Emilio Marchionna, and Marco Politi, "Hybrid modes, substrate leakage, and losses of slotline at millimeter-wave frequencies", *IEEE transactions on microwave theory and techniques*, Vol. 38, No.8, pp.1069-1077, 1990.
- [Rutledge1983] D.B. Rutledge, D.P. Neikirk, and D.P. Kasilingam, "Integrated circuit antennas", *infrared and millimeter waves*, Vol. 10, Academic Press, New York, 1983.
- [Schäffler1992] F.Schäffler, D.Többen, H-J Herzog, G.Abstreiter, and B.Holländer, "High-electron-mobility Si/SiGe heterostructures: influence of the relaxed SiGe buffer layer", *Semiconductor Science and Technology*, Vol.7, pp.260-266, 1992.
- [Schneider1969] M.V.Schneider, "Microstrip lines for microwave integrated circuits", *The bell system technical journal*, pp.1421-1444, 1969.
- [Schnieder2005] Frank Schnieder and Wolfgang Heinrich, "Thin-film microstrip lines and coplanar waveguides on semiconductor substrates for sub-mm wave frequencies", *Frequenz*, Vol. 59, 5-6, pp.1-4, 2005.
- [Schüppert1988] Bernd Schüppert, "Microstrip/slotline transitions: modeling and experimental investigation", *IEEE Transactions on microwave theory and techniques*, Vol. 36, No.8, pp.1272-1282, 1988.
- [Schuster2011] Franz Schuster, Dominique Coquillat, Hadley Videlier, Maciej Sakowicz, Frédéric Teppe, Laurent Dussopt, Benoît Giffard, Thomas Skotnicki, and Wojciech Knap, "Broadband terahertz imaging with highly sensitive silicon CMOS detectors", *Optics Express*, Vol.19, No.8, pp.7827-7832, 2011.
- [Shi2009] Jinglin Shi, Kai Kang, Yong Zhong Xiong, and Fujiang Lin, "Investigation of CMOS on-chip transmission lines CPW, SCPW and CPWG up to 110 GHz", *Proceedings of IEEE international symposium on radio-frequency integration technology*, Singapore, 2009.
- [Shigesawa1988] H.Shigesawa, M.Tsuji, and A.A.Oliner, "Conductor-backed slot line and coplanar waveguide: dangers and full-wave analysis", *IEEE Transactions on microwave theory and techniques*, Vol. MTT-S Digest, pp.199-202, 1988.
- [Shigesawa1990] Hiroshi Shigesawa and Mikio Tsuji, "A new mode-coupling effect on coplanar waveguides on finite width", *IEEE MTT-S Digest*, pp.1063-1066, 1990.
- [Shur2003] Michael S.Shur, and Victor Ryzhii, "Plasma wave electronics", *International Journal of High Speed Electronics and Systems*, World Scientific Publishing Company, Vol.13, No.2, pp.575-600, 2003.

- [Siegel1999] Peter H.Siegel, R.Peter Smith, Michael C.Gaidis and Suzanne C.Martin, "2.5-THz GaAs Monolithic Membrane-Diode Mixer", IEEE Transactions on Microwave Theory and Techniques, Vol.47, No.5, pp.596-604, 1999.
- [Siegel2002] Peter H.Siegel, "Techhertz Technology", IEEE Transactions on Microwave Theory and Techniques, Vol.50, No.3, pp.910-928, 2002.
- [Smorchkova2001] I.P.Smorchkova, L.Chen, T.Mates, L.Shen, S.Heikman, B.Moran, S.Keller, S.P.DenBaars, and J.S.Speck, "AlN/GaN and (Al,Ga)N/AlN/GaN two-dimensional electron gas structures grown by plasma-assisted molecular-beam epitaxy", Journal of Applied Physics, Vol.90, No.10, pp.5196-5201, 2001.
- [Snider1990] G.L.Snider, I-H.Tan, and E.L.Hu, "Electron states in mesa-etched one-dimensional quantum well wires", Journal of Applied Physics, Vol.68, No.6, pp.2849-2853, 1990.
- [Stern1967] Frank Stern, "Polarizability of a two-dimensional electron gas", Physical Review Letters, Vol.18, No.14, pp.546-548, 1967.
- [Stern1992] Frank Stern, and Steven E.Laux, "Charge transfer and low-temperature electron mobility in a strained Si layer in relaxed Si_{1-x}Ge_x", Applied Physics Letters, Vol.61, No.9, pp.1110-1112, 1992.
- [Sugii1998] N.Sugii, K.Nakagawa, Y.Kimura, S.Yamaguchi, and M.Miyao, "High electron mobility in stained Si channel of Si_{1-x}Ge_x/Si/Si_{1-x}Ge_x heterostructure with abrupt interface", Semiconductor Science and Technology, Vol.13, pp.A140-A142, 1998.
- [Sun1997] Nai-Hsiang Sun, Jerome K.Butler, Gary A.Evans, Lily Pang, and Phil Congdon, "Analysis of Grating-Assisted Directional Couplers Using the Floquet-Bloch Theory", Journal of Lightwave Technology, Vol.15, No.12, pp.2301-2315, 1997.
- [Takakuwa1986] Hidemi Takakuwa, Kuninobu Tanaka, Yoshifumi Mori, Michio Arai, Yoji Kato, and Seiichi Watanabe, "A low-noise microwave HEMT using MOCVD", IEEE transactions on electron devices, Vol.ED-33, No.5, pp.595-600, 1986.
- [Tan1990] I-H.Tan, G.L.Snider, L.D.Chang, and E.L.Hu, "A self-consistent solution of Schrödinger-Poisson equations using a nonuniform mesh", Journal of Applied Physics, Vol.68, No.8, pp.4071-4076, 1990.
- [Theis1978] T.-N. Theis, J.P.Kotthaus, and P.J.Stiles, "Wavevector dependence of the two-dimensional plasmon dispersion relationship in the (100) silicon inversion layer", Solid State Communications, Vol.26, pp.603-606, 1978.
- [Thomas2011] Thomas Kleine-Ostmann and Tadao Nagatsuma, "A Review on Terahertz Communications Research", J.Infrared Milli Terahz Waves, 32, pp.143-171, 2011.
- [Tonouchi2007] Masayoshi Tonouchi, "Cutting-edge terahertz technology", Nature photonics, Vol. 1, pp.97-105, 2007.
- [Tucker1985] John R.Tucker and Marc J.Feldman, "Quantum detection at millimeter wavelengths", Review of Modern Physics, Vol.57, No.4, pp.1055-1113, 1985.
- [Tyson1994] R.E.Tyson, D.E.Bangert, and H.P.Hughes, "Oscillations in the frequencies and coupling strengths of two-dimensional plasmons induced by grating couplers", J.Appl.Phys., Vol.76, No.10, pp.5509-5515, 1994.

- [Vendelin1970] G.D.Vendelin, "Limitations on stripline Q", *Microwave Journal*, Vol. 13, pp.63-69, 1970.
- [Wächter2007] Markus Wächter, Michael Nagel, and Heinrich Kurz, "Metallic slit waveguide for dispersion-free low-loss terahertz signal transmission", *Applied Physics Letters*, Vol. 90, 061111, 2007.
- [Wang2004] Kanglin Wang, and Daniel M.Mittleman, "Metal wires for terahertz wave guiding", *Nature*, Vol. 432, No.17, pp.376-379, 2004.
- [Wang2006] Yi Wang, and Michael J. Lancaster, "Coplanar to microstrip transitions for on-wafer measurements", *Microwave and Optical Technology Letters*, Vol.49, No.1, pp.100-103, 2006.
- [Wang2012] Lin Wang, Weida Hu, Jun Wang, Xiaodong Wang, Shaowei Wang, Xiaoshuang Chen, and Wei Lu, "Plasmon resonant excitation in grating-screened AlN barrier transistors at terahertz frequency", *Appl. Phys. Lett.*, Vol. 100, 123501, 2012.
- [Weir1974] William B.Weir, "Automatic Measurement of Complex Dielectric Constant and Permeability at Microwave Frequencies", *Proceedings of the IEEE*, Vol. 62, No.1, pp. 33-36, 1974.
- [Welch1966] J.D.Welch, and H.J.Pratt, "Losses in microstrip transmission systems for integrated microwave circuits", *NEREM Rec.*, Vol. 8, pp. 100-101, 1966.
- [Wen1969] C.P.Wen, "Coplanar Waveguide: A Surface Strip Transmission Line Suitable for Non-Reciprocal Gyromagnetic Device Application", *IEEE Trans.*, Vol. MTT-17, pp.1087-1090, 1969.
- [Wendler1999] L. Wendler, T. Kraft, "Theory of grating-coupler-assisted infrared spectroscopy of lower dimensional electron systems: Local optics of anisotropic multilayer systems with grating", *Physica B*, Vol. 271, pp. 33-98, 1999.
- [Wendler2005] L.Wendler, N.Finger and E.Gornik,"Grating-coupler assisted infrared spectroscopy on anisotropic multilayer systems: A comparative study", *Infrared Physics & Technology*, Vol.46, pp.291-307, 2005.
- [Wheeler1964] Harold A.Wheeler, "Transmission-line properties of parallel wide strips by a conformal-mapping approximation", *IEEE Transactions on Microwave and Techniques*, pp.280-289, 1964.
- [Wheeler1978] Harold A.Wheeler, "Transmission-line properties of a strip line between parallel planes", *IEEE Transactions on Microwave and Techniques*, Vol. MTT-26, No.11, pp.866-876, 1978.
- [Williams2007] Benjamin S.Williams, "Terahertz quantum-cascade lasers", *Nature Photonics*, Vol.1, pp.517-525, 2007.
- [Wright1997] A.F.Wright, "Elastic properties of zinc-blende and wurtzite AlN, GaN, and InN", *Journal of Applied Physics*, Vol.82, No.6, pp.2833-2839, 1997.
- [Wu1995] Q.Wu and X.C.Zhang, "Free-space electrooptic sampling of terahertz beams", *Applied Physics Letters*, 67, pp.3523-3525, 1995.
- [Wu1996] Q.Wu, T.D.Hewitt and X.C.Zhang, "Two-dimensional electrooptic imaging of THz beams", *Applied Physics Letters*, Vol.69, pp.1026-1028, 1996.
- [Wu1997-1] Q.Wu, and X.C.Zhang, "7 terahertz broadband GaP electro-optic sensor", *Applied Physics Letters*, Vol. 70, No. 14, pp.1784-1786, 1997.

- [Wu1997-2] Q.Wu, and X.C.Zhang, "Free-space electro-optics sampling of mid-infrared pulses", Applied Physics Letters, Vol. 71, No.10, pp.1285-1286, 1997.
- [Wu2005] Ke Wu, and Lin Li, "Numerical calibration and de-embedding techniques for CAD and equivalent circuit models of electromagnetic structures", Microwave Review, pp.7-19, June 2005.
- [Yamashita1979] Eikichi Yamashita, Kazuhiko Atsuki, and Tomio Ueda, "An approximate dispersion formula of microstrip lines for computer-aided design of microwave integrated circuits", IEEE Transactions on microwave theory and techniques, Vol. MTT-27, No.12, pp.1036-1038, 1979.
- [Yilmazoglu2008] Oktay Yilmazoglu, Kabula Mutamba, Dimitris Pavlidis, and Tamer Karaduman, "First observation of bias oscillations in GaN Gunn diodes on GaN substrate", IEEE transactions on electron devices, Vol.55, No.6, pp.1563-1567, 2008.
- [Yu1993-1] L.S.Yu, D.J.Qiao, Q.J.Xing, S.S.Lau, K.S.Boutros, and J.M.Redwing, "Ni and Ti Schottky barriers on n-AlGaN grown on SiC substrates", Applied Physics Letters, Vol.73, No.2, pp.238-240, 1993.
- [Yu1993-2] Ming Yu, Ruediger Vahldieck and Jifu Huang, "Comparing Coax Launcher and Wafer Probe Excitation for 10mil Conductor Backed CPW with Via Holes and Airbridges", IEEE MTT-S Digest, pp.705-708, 1993.
- [Yutani1997] A.Yutani, and Y.Shiraki, "Hybrid MBE growth and mobility limiting factors of n-channel Si/SiGe modulation-doped systems", Journal of Crystal Growth, Vol.175/176, pp.504-508, 1997.
- [Zhang1999] D.H.Zhang, "Metal contacts to n-type AlGaAs grown by molecular beam epitaxy", Materials Science and Engineering, Vol.B60, pp. 189-193, 1999.
- [Zhao2002] G.Zhao, R.N.Schouten, N.van der Valk, W.Th.Wenckebach, and P.C.M.Planken , "Design and performance of a THz emission and detection setup based on a semi-insulating GaAs emitter", Review of Scientific Instruments, Vol.73, No.4, pp.1715-1719, 2002.
- [Zheng1990] Lian Zheng, W.L.Schaich, and A.H.MacDonald, "Theory of two-dimensional grating couplers", Physical Review B, Vol.41, No.12, pp. 8493-8499, 1990.
- [Zheng1991] Lian Zheng, and W.L.Schaich, "Theory of a grating coupler of finite thickness", Physical Review B, Vol.43, No.5, pp. 4515-4518, 1991.
- [Zheng2003] Xuemei Zheng, Ying Xu, Roman Sobolewski, Roman Adam, Martin Mikulics, Michael Siegel, and Peter Kordos, "Femtosecond response of a free-standing LT-GaAs photoconductive switch", Applied Optics, Vol.42, No.9, pp.1726-1731, 2003.
- [Zhu2002-1] L.Zhu, and K.Wu, "Short-open calibration technique for field theory-based parameter extraction of lumped elements of planar integrated circuits", IEEE transactions on microwave theory and techniques, Vol. 50, issue 8, pp.1861-1869, 2002.
- [Zhu2002-2] L.Zhu, and K.Wu, "Comparative investigation on numerical de-embedding techniques for equivalent circuit modeling of lumped and distributed microstrip circuits", IEE microwave and guided wave letters, Vol.12, No.2, pp.51-53, 2002.

Publications and Conferences

L. Cao, A.-S. Grimault-Jacquin, and F. Aniel, "Optimal structure for Resonant THz Detection of Plasmons-Polaritons in the 2D Quantum Wells", Applied Physics A, Vol. 109, No. 4, pp. 985-991, 2012.

L. Cao, A.-S. Grimault-Jacquin and F. Aniel, "Optimal structure for Resonant THz Detection of Plasmons-Polaritons in the 2D Quantum Wells", in Proc. EuMiC2012, Amsterdam, The Netherlands, Oct. 2012.

L. Cao, A.-S. Grimault-Jacquin and F. Aniel, "Optimal structure for Resonant THz Detection of Plasmons-Polaritons in the 2D Quantum Wells", in Proc. Meta2012, Paris, Apr. 2012.

L. Cao, A.-S. Grimault-Jacquin and F. Aniel, "Resonant terahertz detection of 2DEG with grating coupler", in Proc. IRMMW-THz, Paper M2C.2.1, Houston, Oct. 2011.